UNIVERSITÀ DEGLI STUDI DI PAVIA
DOTTORATO DI RICERCA IN FISICA – XXX CICLO

A local view on Spin and Charge correlations in Iron Based Superconductors

Matteo Moroni

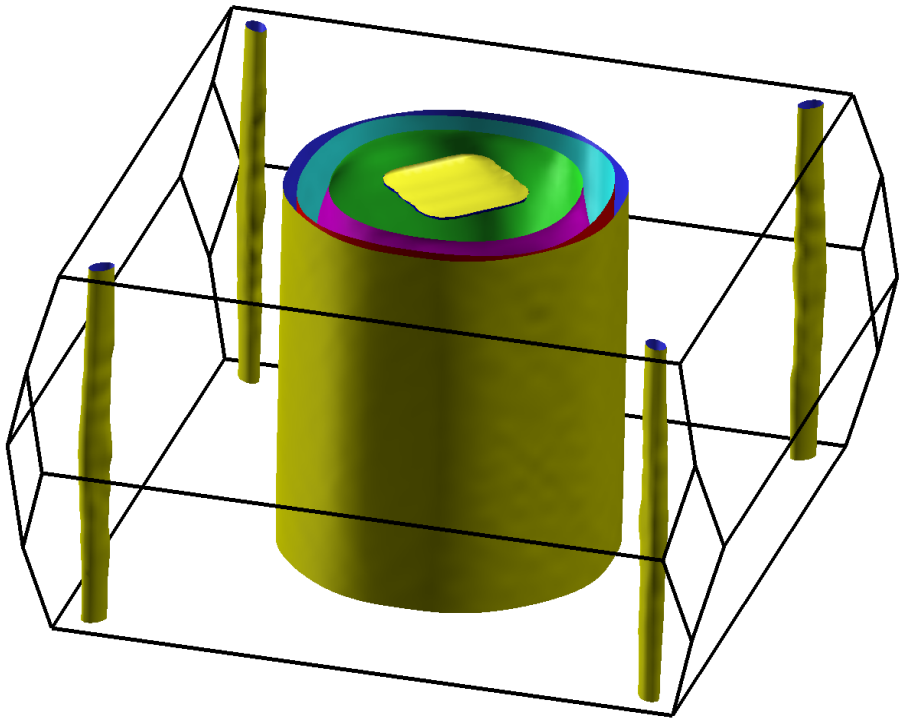

Tesi per il conseguimento del titolo

Full title:
A local view on Spin and Charge correlations in Iron Based Superconductors

Short title for the side if necessary:
Spin and Charge correlations in Iron Based Superconductors

Matteo Moroni

2018

Dipartimento di Fisica
Dottorato di Ricerca in Fisica – XXX Ciclo
2017

A local view on Spin and Charge correlations in Iron Based Superconductors

dissertation submitted by

Matteo Moroni

in partial fulfillment of the requirements for the degree of

Dottore di Ricerca in Fisica
Doctor of Philosophy in Physics

supervisor:

Prof. P. Carretta

Cover: $RbFe_2As_2$ Fermi Surface calculated using the ELK software package.

A local view on Spin and Charge correlations in Iron Based Superconductors

Matteo Moroni
PhD thesis - University of Pavia
Pavia, Italy, January 2018

Contents

Introduction

High Temperature Superconductivity has been a fascinating conundrum in solid state physics since the discovery [1] of the cuprates superconductors in the mid-eighties. Despite the immense experimental and theoretical efforts which have been devoted to the study of these materials, the nature of the pairing remains elusive to date.

In 2008 the discovery [2] of superconductivity in fluorine doped LaFeAsO opened a new chapter in the fundamental research on High Temperature Superconductivity. Other compounds based on similar crystalline structures where then quickly discovered, marking the birth of a new family of superconducting materials. While the strong iron magnetic moment is detrimental for superconductivity several superconducting compounds containing Fe have been known for a long time (e.g. U_6Fe and $Lu_2Fe_3Si_5$) and even metallic iron is a superconductor at low temperature (< 2 K) and very high pressure (10 GPa), where ferromagnetism is suppressed [3]. However the newly discovered Iron Based Superconductors (IBS), with a maximum T_c of about 55 K (in bulk samples at atmospheric pressure), are the materials with the highest T_c outside the cuprates family and constitute an utterly important new class of High Temperature Unconventional Superconductors.

The common feature characterizing these iron based compounds is their tetragonal FeAs layered structure, similar to the CuO_2 based two-dimensional lattice geometry of the cuprates. The superconducting phase arise, upon charge doping, in correspondence to the suppression of the AF phase, where strong magnetic fluctuations are still present. The IBS phase diagram is extremely rich, with relevant qualitative differences from one sub-family to the other. The parent compounds are characterized, as is also the case for the cuprates, by a long range antiferromagnetic (AF) order.

Theoretical band structure calculations and Angle Resolved Photoemission Spectroscopy (ARPES) revealed a strongly nested Fermi surface and the magnetic fluctuations at the nesting vector are thought to be an essential ingredient for the appearance of superconductivity. However, in analogy with the cuprates, a mechanism capable of conclusively explaining the nature of the pairing has not been found yet.

In this thesis the Iron Based Superconductor have been studied using local probe techniques: Nuclear Magnetic Resonance (NMR), Nuclear Quadrupole Resonance (NMR) and Muon Spin Rotation (μSR). These experimental techniques have been widely used in the study of unconventional superconductors and of strongly correlated electrons systems since they are sensitive to both static and dynamic susceptibilities, making it possible to probe a wide range of phenomena, from spin and orbital fluctuations to magnetism and charge order.

The thesis is divided in four chapters:

- **Chapter 1:** The first chapter is a general introduction to Iron Based Superconductivity. A significant section of this brief review is devoted to the analysis of the differences between the various families of High Temperature Superconductors.

- **Chapter 2:** This chapter covers a few basic aspects of NMR and μSR which are essential to understand the experimental results reported in the following chapters. Several important NMR-μSR results on iron based superconductors are also presented.

- **Chapter 3:** This chapter presents the results of NMR and NQR experiments carried out on electron (Sections 3.1, 3.2) and hole doped (Section 3.3) Iron based superconductors.

  The most striking result reported in Section 3.1 is the observation of low energy fluctuations in electron (Rh) doped $BaFe_2As_2$, which confirms that they are a widespread feature of IBS materials. In the following section (Sec. 3.2) we studied the evolution of these low energy fluctuations in presence of uniaxial strain.

  Section 3.3 instead is dedicated to the fascinating phenomenology observed in (Rb,Cs)Fe_2As_2, where NQR-NMR measurements revealed the presence of a charge ordered phase coexisting with superconductivity.

- **Chapter 4:** In the last chapter we discuss the effect of impurities in iron based superconductors. In the first Section we focused on the effect of magnetic Mn impurities in F doped LnFeAsO (Ln = La, Sm,Y) superconductors, while the second Section is devoted to the effect of proton irradiation in Rh doped $BaFe_2As_2$.

  The most important result reported in the first Section is the extremely fast suppression of the superconducting ground state upon introducing Mn in optimally fluorine doped $LaFe_{1-x}Mn_xAsO_{0.89}F_{0.11}$ and the simultaneous recovery of the stripe ($\mathbf{Q} = (0,\pi)$ or $(\pi,0)$) antiferromagnetic phase present in the undoped compound.

  The second section deals with several intriguing results about the effects of irradiation induced defects in $Ba(Rh_xFe_{1-x})_2As_2$. In particular we discovered that, in the optimally doped sample, proton irradiation

induces ferromagnetic correlations revealed by the Curie-Weiss temperature dependence of the ^{75}As NMR line width.

Chapter 1

Introduction to the Iron Based Superconductors

The mechanism responsible for superconductivity remained a mystery for forty years, from its discovery (Kamerlingh Onnes, 1911) until the development of the BCS theory by Bardeen, Cooper and Schrieffer (BCS) in 1957 [4]. During the sixties and the seventies several experiments (e.g. isotope effect, ultrasonic attenuation, specific heat experiments, the Little-Park experiment in 1962 [5] and the Hebel-Slichter experiment in 1957 [6]) confirmed the BCS theory and most of the physicists began to consider superconductivity as a solved problem. Furthermore the highest observed critical temperature (23.2 K in Nb_3Ge) did not increased significantly between 1950 and 1980 (see Fig. 1.1), leading to the widespread belief, corroborated by a theoretical study by McMillan [8] who estimated the maximum T_c of the compounds under study at the end of the sixties, that higher critical temperatures could only be achieved in metallic hydrogen [7] and other hydrogen based compounds at very high pressure, as recently confirmed by the discovery of high temperature superconductivity in H_2S [9] (203 K for pressures higher than 150 GPa).

This quiet period came to an abrupt end in the eighties, first with the emergence of the Heavy-Fermion (e.g. $CeCu_2Si_2$ [11]) and organic ($(TMTSF)_2ClO_4$ [12]) superconductors, and then, few years later, with the groundbreaking discovery of the cuprates superconductors [1]. The cuprates critical temperature can reach values well above 100 K in several compounds (e.g. $Bi_2Sr_2Ca_22Cu_3O_{10}$ and $HgBa_2Ca_2Cu_3O_8$). Such a high T_c is incompatible with the phononic coupling within the BCS theory and until the discovery of the HTSC it was widely believed that these values were unreachable (see Fig. 1.1). Similarly to what happened in the first half of the twentieth century for the conventional superconductors understanding the mechanism responsible for high temperature superconductivity proved to be very difficult and up to now, more than 30 years after this discovery, no general consensus has emerged yet.

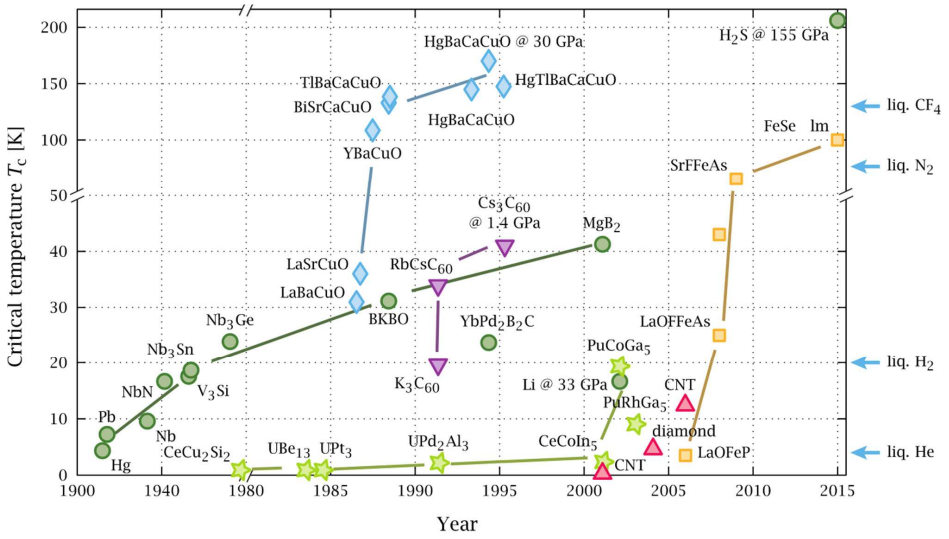

Figure 1.1: Evolution of the maximum value of T_c for the various families of superconductors [10]. Cuprates are denoted by blue diamonds, iron-pnictides by yellow squares, BCS superconductors by dark green circles, heavy fermions by green stars and organic superconductors by magenta triangles.

When in 2008 the Hosono Group discovered [2] that the fluorine doped LaFeAsO is a superconductor with a relatively high T_c of 26 K for the optimally doped compound ($LaFeAsO_{0.89}F_{0.11}$), a huge research effort began around the world. Several other compounds of the same family were quickly discovered and T_c reached up to 55 K ($SmFeAsO_{0.7}F_{0.3}$). Since the beginning it was clear that the newly discovered iron pnictides superconductors (Iron Based Superconductors: IBS) are the only known family of HTSC compounds beside the cuprates. The discovery of a second family of high T_c materials raised a big hope to finally understand the nature of high temperature superconductivity. However it soon became clear that while the cuprates share several common features with the iron based superconductors, both being strongly correlated quasi-2D materials close to a magnetic ground state, the symmetry of the superconducting order parameter is different and the nature of the pairing mechanism, while likely involving the spin fluctuations in both the HTSC families, could also be different. A plethora of models aimed at explaining the superconducting gap symmetry and the pairing mechanism have been proposed but a conclusive experimental evidence capable of discriminating among them is still lacking.

While we are still quite far from the complete understanding both of the cuprates and of the IBS in the last few years various substantial advancement have been made and several important points are now well understood and agreed upon. This first chapter deals with the crystalline structure of the iron-pnictides, their electronic properties, and the comparison with the order families of unconventional superconductors: the cuprates and the heavy fermion compounds.

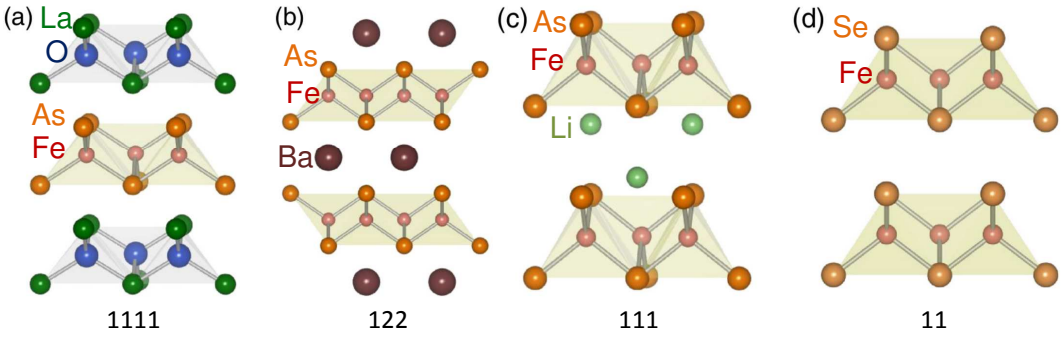

Figure 1.2: Structure of the 4 iron based superconductors families considered in this thesis: (a): 1111, (b) 122 (c) 111 (d) 11. Image adapted from Ref. [13]

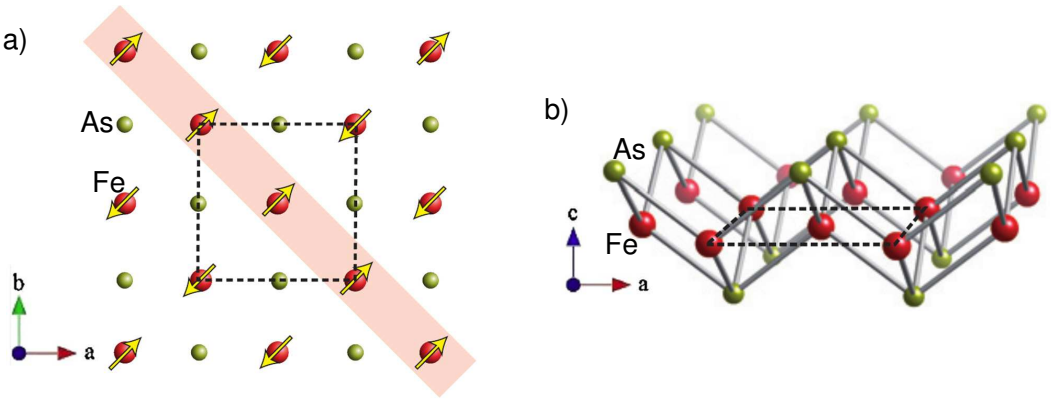

Figure 1.3: Structure of a FeAs plane seen from two different prospectives: from along the *c*-axis (a) and from inside the FeAs *ab*-plane (b). The *c*-axis is perpendicular to the FeAs plane. The black dashed lines indicates the FeAs unit cell. The yellow arrows in (a) represents the orientation of the Fe moments in the magnetic stripe phase. Image adapted from Ref. [14].

1.1 Iron-based Superconductors: crystalline and electronic structure

The IBS are characterized by a planar 2D structure of iron-arsenic (FeAs) or iron-selenium (FeSe) layers, where superconductivity takes place (see Fig. 1.2, 1.3). The iron-pnictogen layers have a tetragonal crystalline structure at high temperature and in the non superconducting compounds a tetragonal to orthorhombic (TO) transition is often present at low temperature (< 200 K).

The TO transition usually takes place together with a magnetic transition towards a stripe antiferromagnetic ordered phase ($\mathbf{Q} = (0, \pi)$ or $(\pi, 0)$ static spin density wave, SDW). Superconductivity emerge when the magnetic order is suppressed upon charge doping or by applying an hydrostatic pressure [2, 15].

Since the iron-pnictogen group is common to all the FeAs based IBS, their are also called *iron-pnictides*. The bidimensionality is a feature shared with cuprates, ruthenates and cobaltates and seems to be a leitmotif of the unconventional high-T_c superconductors.

Several families of IBS have been discovered during the years and new ones are still being discovered. Four important and widely studied families of IBS (1111, 122, 111 and 11, see Fig. 1.2) are presented here in order of discovery. Each family differs significantly from the others both in chemical composition and in the crystalline structure, however all the four families show the IBS's customary FeAs(Se) layered structure.

Many other families of iron based superconductors still exit since, while the FeAs layer is essential for superconductivity, a huge variety of intercalating elements and compounds can be used in order to obtain new materials (e.g. $Sr_3Sc_2O_5Fe_2As_2$ [16], $Ba_2Ti_2Fe_2As_4O$ [17]) with different properties (self-doping, chemical pressure, interlayer separation, etc).

1.1.1 1111 compounds (L*n*FeAsO)

The 1111 was the first family of IBS to be discovered. Their parent compound, LaFeAsO, is not a superconductor itself but instead it is characterized by an antiferromagnetic stripe phase ($\mathbf{Q} = (0, \pi)$) below $\sim$ 150 K. Together with the magnetic transition also a tetragonal to orthorhombic structural phase transition (*P4/nmm* $\rightarrow$ *Cmma*) takes place.

The general stoichiometric formula can be written as RTMPnO (R: rare earth, TM: transition metal, Pn: pnictogen group atom, O: oxygen). The presence of oxygen is one of the peculiar characteristics of this family. In fact the compounds of the other families do not contain oxygen and in general this element, differently from the case of the cuprates, is not essential for the rise of superconductivity in the IBS.

All the compounds of the 1111 family share a ZrCuSiAs-like (*P4/nmm*) crystalline structure. Due to their chemical composition all the samples of this family can easily be synthesized in form of powder or in small submillimeter crystals, while larger crystals are much more difficult to grow.

Superconductivity shows up in correspondence with the suppression of the magnetic order upon electron doping LaFeAsO with fluorine [2] ($LaFeAsO_{1-x}F_x$). The maximal critical temperature was found to be 26 K [2] ($x = 0.11$, see Fig. 1.4a). However it can be increased up to 43 K [15] applying an hydrostatic pressure to the sample and up to 55 K [19] ($SmFeAsO_{1-x}F_x$, $x = 0.3$) by substituting La with another rare earth characterized by a smaller atomic radius, such as Sm (Fig. 1.4b), Pr, Ce or Y (partial substitution). Interestingly for Sm1111 it was observed, through μSR experiments, that superconductivity and magnetism coexist over a sizable region of the under-doped side of the phase diagram. Superconductivity can also be obtained by doping the superconducting FeAs layer, for example substituting Fe with Co (electron doping Fig. 1.4d).

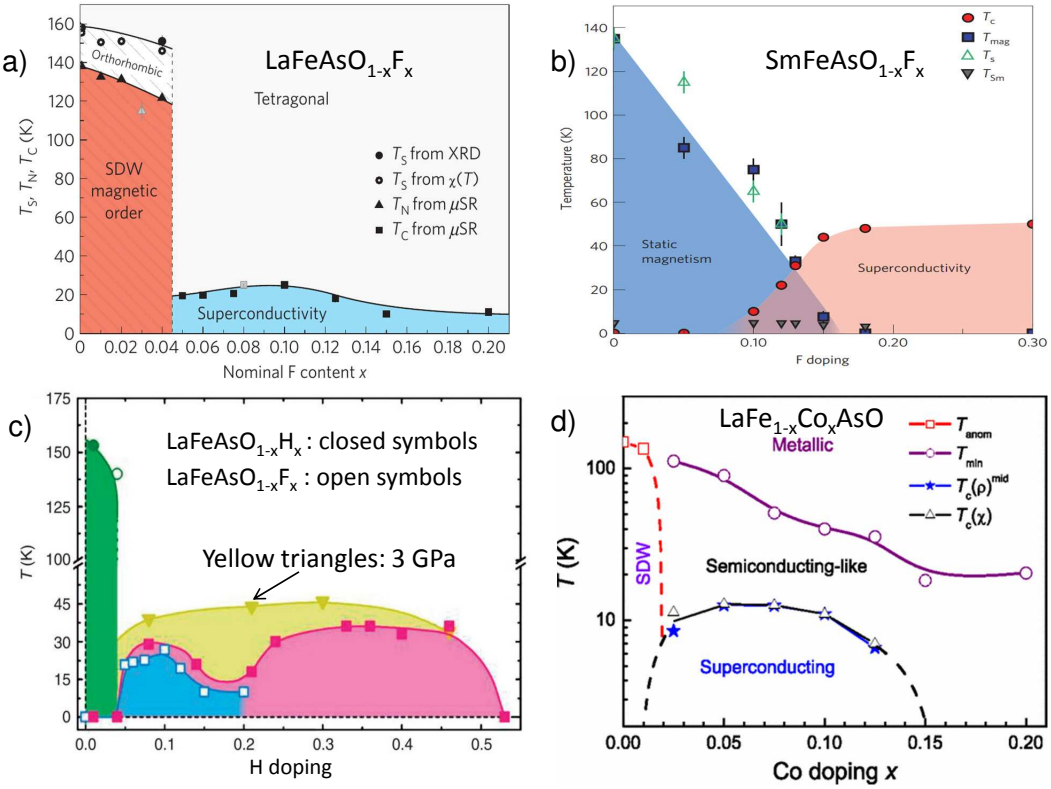

Figure 1.4: Phase diagram of four representative 1111 compounds: a) F-doped LaFeAsO [18], b) F-doped SmFeAsO [19] (c) H-doped LaFeAsO [20] (d) Co doped LaFeAsO [21]. In (c) the filled-square symbols represent T_c of $LaFeAsO_{1-x}H_x$ at ambient pressure and the yellow filled inverted triangular symbols represent T_c under an external pressure of 3 GPa. The blue symbols indicates $LaFeAsO_{1-x}F_x$ (for comparison).

It is also possible to induce superconductivity by doping LaFeAsO (and related compounds) with hydrogen [22] or by creating oxygen vacancies [23] ($LaFeAsO_{1-x}$). In the case of $LaFeAsO_{1-x}H_x$ a second superconducting dome peak is present at $x = 0.3$ with $T_c = 36$ K [22](Fig. 1.4c).

1.1.2 122 compounds ($BaFe_2As_2$)

The first compound of this family to show superconductivity, $Ba_{1-x}K_xFe_2As_2$ (T_c ~40K), was discovered [27] just a few months after the discovery of superconductivity in $LaFeAsO_{1-x}F_x$. The parent compound, $BaFe_2As_2$ (Ba122), is a strongly correlated metal with a magnetic (stripe) and structural (tetragonal to orthorhombic) phase transition around 140 K and just like LaFeAsO it is not a superconductor itself.

The 122 materials can either be electron (e.g. with Rh and Co) or hole doped (e.g. with K). All the compounds have the same I4/*mmm* AFe_2As_2 (A: Ba, Sr, Ca, Rb, Cs, K) unit cell. In correspondence with the structural

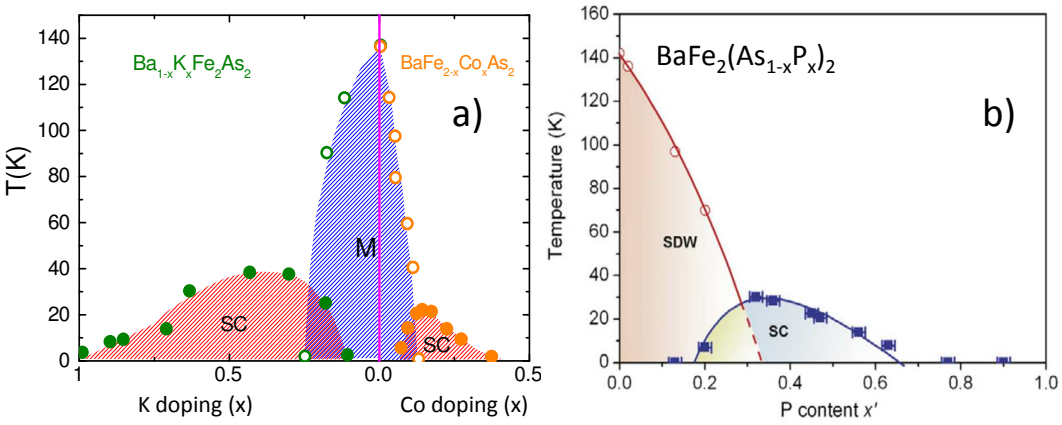

Figure 1.5: Phase diagrams of the Ba122 compounds. a) Charge doping phase diagram: K doping [24] (left side) corresponds to hole doping while Co doping [25] (right side) corresponds to electron doping. b) Phosphorus doped Ba122 phase diagram [26]. Isovalent P for As substitutions allow one to increase the chemical pressure.

transition the space group changes from *I4/mmm* to *Fmmm*. In analogy with the 1111 family superconductivity arise when magnetism is suppressed by doping (see Fig. 1.5). The highest T_c is $\sim$ 23 K for the electron doped compound and $\sim$ 39 K for the hole doped one [24, 25] (see Fig. 1.5a). Similar values of T_c can also be obtained through isovalent P for As substitutions (see Fig. 1.5b). This type of substitutions does not introduce charge doping into the material but it increase the chemical pressure. In 2016 it was discovered that the critical temperature of $CaFe_2As_2$ can be raised up to 49 K [28, 29] by doping the sample with a rare earth (La, Ce, Pr, or Nd). This is the new T_c record for the 122 family.

All the components of the 122-type superconductors are metallic elements and thus the synthesis of the sample is somewhat easier in comparison with the 1111 family. Furthermore it is relatively simple to grow large crystals (>10 mm^2), making it easier to conduct experiments which require a particular orientation of the FeAs layers.

1.1.3 111 compounds (LiFeAs)

LiFeAs was the first 111 compound to be discovered [30, 31]. The compounds of this family share a Cu_2Sb-type tetragonal structure (*P4/nmms*). Differently from the parent compounds of 1111 and 122 families, LiFeAs, the parent compound of the 111 family, is itself a superconductor with $T_c \sim 18$ K, although its superconductivity is only filamentary [31]. Another widely studied compound belonging to this family is NaFeAsO [32]. In these compounds lithium/sodium atoms interlaced between the FeAs layers act as a charge reservoir (self-doping).

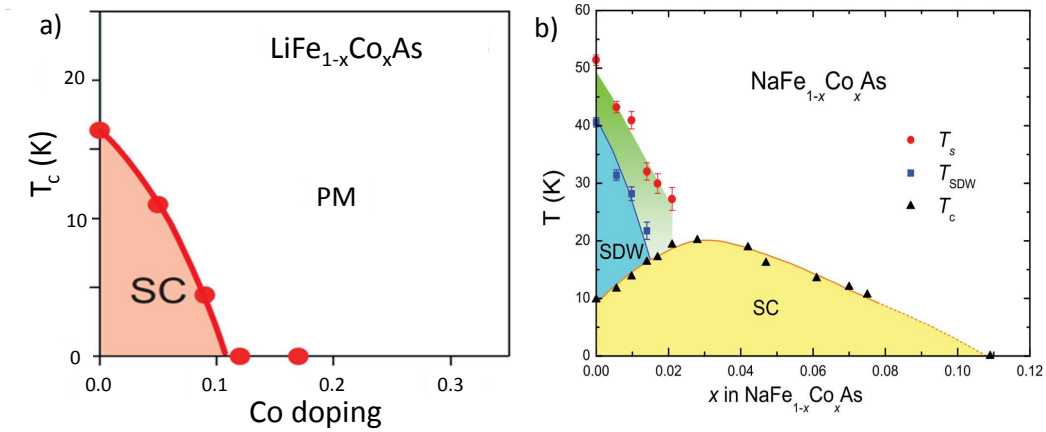

Figure 1.6: Phase diagrams for electron (Co) doped LiFeAs [33] (a) and NaFeAs [32] (b).

As can be seen by looking at the phase diagram reported in Fig. 1.6a in LiFeAs no magnetic phase is present [33] and T_c is suppressed both by charge doping and by applying an external hydrostatic pressure. Conversely NaFeAs exhibit both the structural TO transition and the magnetic stripe order (Fig. 1.6b). Moreover in NaFeAs it is possible to enhance T_c both by electron doping (Fig. 1.6b) and by applying an external pressure (Fig. 1.7c), in close analogy with the other IBS. Superconductivity coexist with magnetism in the underdoped region of the NaFeAs phase diagram and ^{23}Na and ^{75}As NMR measurements proved that the two states coexist microscopically and not as separated phases [34].

1.1.4 11 compounds (FeSe)

The iron chalcogenide $Fe(Te_{1-x}Se_x)$, discovered at the end of 2008 [38], is the simplest of the iron based superconductors (see Fig. 1.2). Even if FeSe is a chalcogenide (Se instead of As in the superconducting iron layers) the crystalline structure (αPbO-type) is quite similar to that of the other families, displaying the layered structure common to all the IBS.

The parent compound of this family is the antiferromagnetic monoclinic FeTe (Neel order, $\mathbf{Q} = (\pi, \pi)$ in the single Fe BZ). All the compounds from FeTe to FeSe can be synthesized, with pure FeSe being a superconductor without the need of chemical substitutions or of external hydrostatic pressure. In FeSe superconductivity can be enhanced by Se-deficiency or by substituting Se with Te.

A structural phase transition from a high temperature tetragonal phase to a low temperature orthorhombic phase is also present in $FeSe_{1-x}$ like in other familes of IBS. However the case of FeSe is rather unique since it is the only IBS compound where the structural transition is not followed by a magnetic transition towards the SDW order.

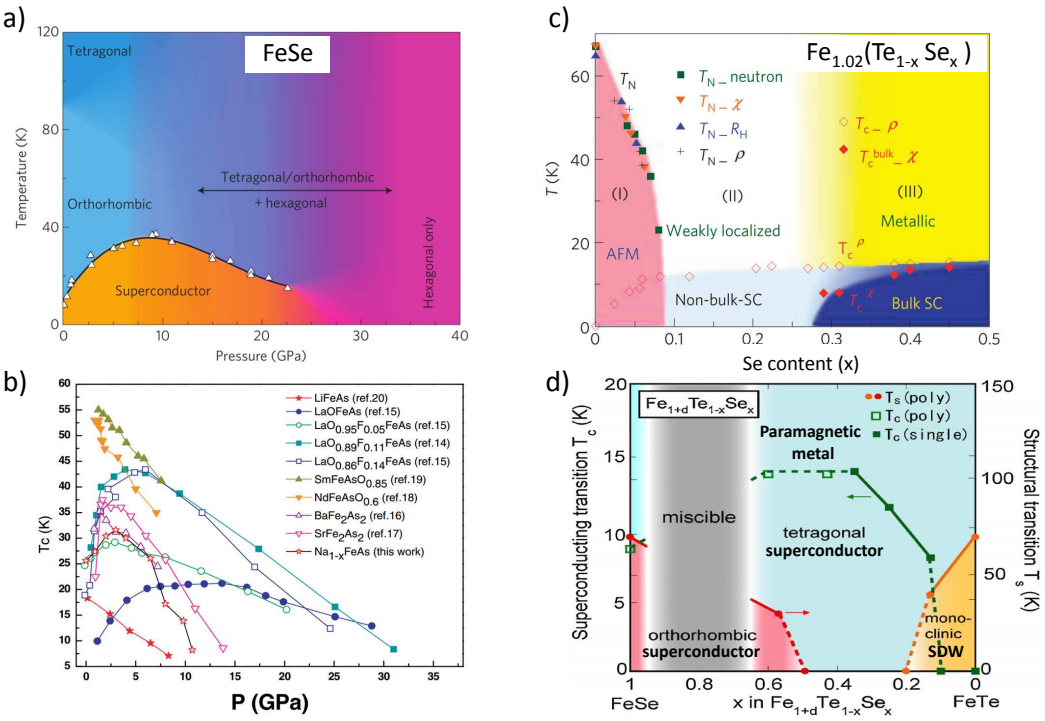

Figure 1.7: a) Phase diagram as a function pressure for FeSe [35]. b) Phase diagram as a function of pressure for several other iron based compounds (for comparison). c) Phase diagram of $Fe(Te_{1-x}Se_x)$ for $x < 0.5$ [36]: three regions are present. Region I is antiferromagnetic and monoclinic ($T < 70$ K), region II is weakly localized, tetragonal and non superconducting, region III is orthorhombic and superconducting. d) Full phase diagram of $Fe(Te_{1-x}Se_x)$ [37]. The gray shaded patch of the phase diagram indicates a miscible region extending for $0.7 < x < 0.95$ which makes the phase diagram impossible to draw in this region.

While T_c is fairly low in the Se deficient compound (T_c ~9 K), it can be raised up to 36.7 K applying an high pressure (8.9 GPa) to the sample (see Fig. 1.7a). In fact FeSe is the IBS compound where pressure has the greatest effect on T_c (Fig. 1.7b). The partial substitution of Se with Te can also enhance T_c up to 15 K in $Fe(Te_{1-x}Se_x)$ [39] (see Fig. 1.7 (c) and (d)). As shown in Fig. 1.7d the highest T_c is reached for $x \sim 0.5$.

Remarkably the strain induced by a substrate on mono-layer FeSe can enhance T_c by almost an order of magnitude (claims of $T_c \sim 109$ K in a FeSe monolayer grown on a $SrTiO_3$ (001) substrate have been reported [40]).

1.1.5 Sample growth methods

The sample preparation methods of the various families differ significantly from each other, since, as described in the previous section, the sample chemical properties vary widely from family to family. Here we will only give a

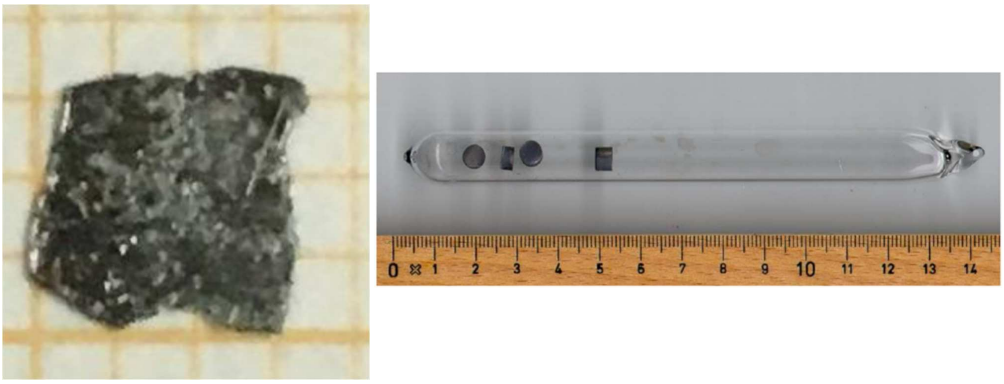

Figure 1.8: Left: $Ba(Fe_{89.3}Rh_{10.7})_2As_2$ mono-crystal. Right: $LaFeAsO_{1-x}F_x$ powder in pellets [41].

brief explanation of the standard growth method used for the samples studied in this thesis (L*n*FeAsO and AFe_2As_2).

Polycrystalline samples of $LaFeAsO_{1-x}F_x$ are prepared using a two step solid state method [42] [13]. In the first step Fe powder and As powder are milled, mixed and pressed into pallets. The pallets of mixed iron and arsenic powder are then annealed first at a temperature of 500°C for 2 hours and then at 700°C for 10 hours in a previously evacuated silica tube. The pellets of FeAs powder are now extracted and milled, the resulting powder being mixed with lanthanum powder, annealed La_2O_3 powder and anhydrous LaF_3 powder in order to finally obtain the desired stoichiometric proportions. All preparation steps are carried out under argon atmosphere.

The mixed FeAs-La-La_2O_3-LaF_3 powder is now pressed into pellets at high pressure (~1GPa). The pallets must now be re-sealed into an evacuated silica tube and annealed first at 940°C for 8 h and then at 1150 °C for 40 h. The samples obtained are now pallets of compressed $LaFeAsO_{1-x}F_x$ powder (see Fig. 1.8b) with a typical grain size of some tens of micrometers.

The preparation of 122 samples (such as $Ba(Fe_{1-x}Rh_x)_2As_2$) differs significantly from that of $LaFeAsO_{1-x}F_x$ since the 122 family components are more metallic than the ones of the 1111 family, which means that self-growth flux techniques can be applied, as extensively described in Ref. [43, 44].

In the flux method single crystals are self-grown in a very slow-cooling supersaturated solution. The flux is a metallic "solvent" with low melting point used to dissolve the reactants. In the growth of 122 samples usually Sn flux or FeAs flux (self-flux) are used. Since Sn grown samples always contain sizable (~ 1 %) traces of Sn, the self-flux method is usually preferred [45] even if FeAs melts at rather high temperatures (1042 K). FeAs is obtained by reacting the mixture of the elements in powdered form in an evacuated quartz tube at around 1000 K for several hours after a slow heating procedure. Other precursor powder, such as CoAs for Co doped Ba122 [43], can be obtained in a similar way. In order to obtain $BaFe_2As_2$ small Ba chunks and FeAs powder are mixed together according to the ratio Ba:FeAs=1:4.

The mixture is then placed into an alumina crucible. A second catch crucible containing quartz wool is placed on top of this growth crucible and both are sealed in a quartz tube under Ar gas. The sealed quartz tube is heated up to 1180 °C, kept at 1180 °C for 2 h, and then cooled to 1000 °C over 36 h. Once the furnace reach 1000 °C, the excess of FeAs is decanted from the platelike single crystals. This procedure results in flat single-crystals (see Fig. 1.8a) which is very useful for experiments where the sample orientation is important. In Fig. 1.8 examples of both 1111 ($LaFeAsO_{1-x}F_x$) and 122 (Rh doped $BaFe_2As_2$) samples are shown.

1.2 Electronic structure, magnetism, fluctuations and superconductivity

Understanding the non trivial electronic structure of the iron based superconductors is essential in order to grasp many of the exotic properties of these materials. In this section we will focus mainly on the 1111 and 122 families since the experimental section of this thesis deals mainly with these two families.

The iron based superconductors are weakly correlated materials so the standard Density Functional Theory method (DFT-LDA/GGA) is not completely adequate for describing these systems since it is not able to correctly take into account the electron-electron correlations. More advanced methods such as Dynamical mean-field theory (DMFT) or GW-DFT give more precise results, at the cost of being much more computationally demanding and thus difficult to apply to very complicated systems or supercells. However, even in presence of significant correlations, as is the case for strongly hole doped Ba122 ($Ba_{1-x}K_xFe_2As_2$), the results provided by simple DFT-GGA often gives a fair enough description of many important properties of the materials, such as the density of states at the Fermi energy and the shape of the Fermi surface [46, 44].

The electronic structure measurements from various experimental techniques, mainly Angle Resolved Photoemission Spectroscopy (ARPES), Scanning transmission Microscopy (STM) and Resonant Inelastic X-Ray Scattering (RIXS) can be compared with ab-initio calculations in order to validate them.

1.2.1 Band structures and Fermi Surfaces

We already pointed out in the previous sections that the primitive cell of the IBS is body-centered-tetragonal for the 122 family (bct, I4/*mmm*), and primitive tetragonal (pt, P4/*nmm*) for the 11, 111 and 1111 families. The corresponding Brillouin zones (BZ) and the relevant high symmetry points are reported in Fig. 1.9a and 1.9b. It is important to note that it is common in literature to use two different types of BZ, denoted as "folded" and "unfolded" Brillouin zones. The "folded" BZ of the Fe_2 lattice is the actual BZ calculated

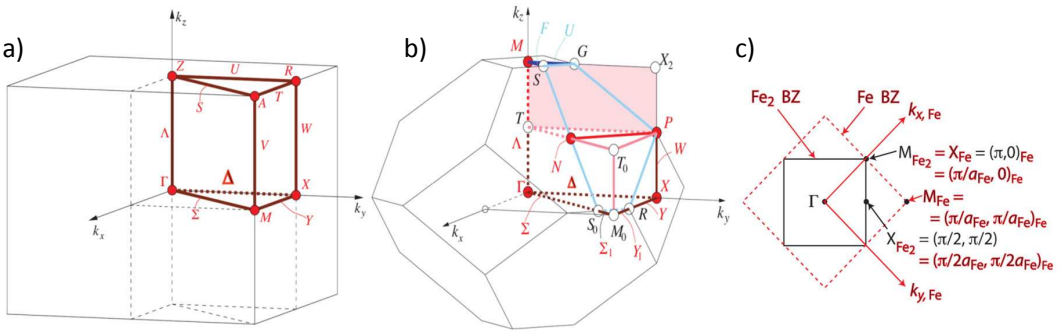

Figure 1.9: a): First Brillouin zone ("folded") for 1111 family (primitive tetragonal P4/nmm space group). b): First Brillouin zone for 122 family (body-centred tetragonal I4/mmm space group). c) Top view of the "unfolded" Fe BZ for the Fe square lattice containing one Fe atom per cell (red dashed box), and the tetragonal "folded" Fe_2 unit cell containing two Fe atoms per unit cell per layer (black solid box). Figures adapted from Ref. [47] and [48].

by the direct lattice. Conversely the folded BZ, often called single Fe BZ or simply "magnetic cell" is the BZ one obtains when the direct lattice is considered to be a simple Fe square lattice, with only one Fe atom per unit cell, and neglecting the presence of other atoms (As/Se). In this thesis, as it is also customary in the literature [48, 49], we will use the standard Fe_2 BZ when dealing with the Fermi surfaces and the electronic structure while we will refer to the single Fe BZ when dealing with the magnetic structure since in this case the notation is much more intuitive. In Fig. 1.9c a top view comparison of the two BZ is shown together with the coordinates of the relevant symmetry points in the single Fe Brillouin zone.

In case of a transition metal cation (Fe) surrounded by four anions (As) usually one should expect the Fe 3d orbitals to split into a set of two low energy e_g orbitals and three high energy t_{2g} orbitals due to the crystalline field. This effect is clearly observable in several type of oxides [48]. However both ab-initio calculation and experimental results (ARPES) confirmed that in the IBS the five $3d$ orbitals are nearly degenerate. This results in an overlap in the bands formed by them in proximity of the Fermi energy [48, 44]. Additionally we know from the DFT calculations that the density of state at the Fermi energy (E_f) is strongly dominated by these Fe $3d$ orbitals, with the As $4p$ orbital giving a much smaller contribution to the DOS (see Fig. 1.10b for the LaFeAsO case). Since the states at E_f are predominantly the Fe ones it means that the main electronic conduction mechanism is direct Fe–Fe hopping. Also most of the macroscopic properties, such as the specific heat, depends mostly from the $3d$ iron bands. Conversely the As $4p$ orbitals lie very deep below the Fermi energy, in agreement with the commonly accepted oxidation number for As (-3) [48, 51, 52].

Differently from what happens for the parent compound of the cuprates superconductors, which are Mott insulators, the parent compounds of the

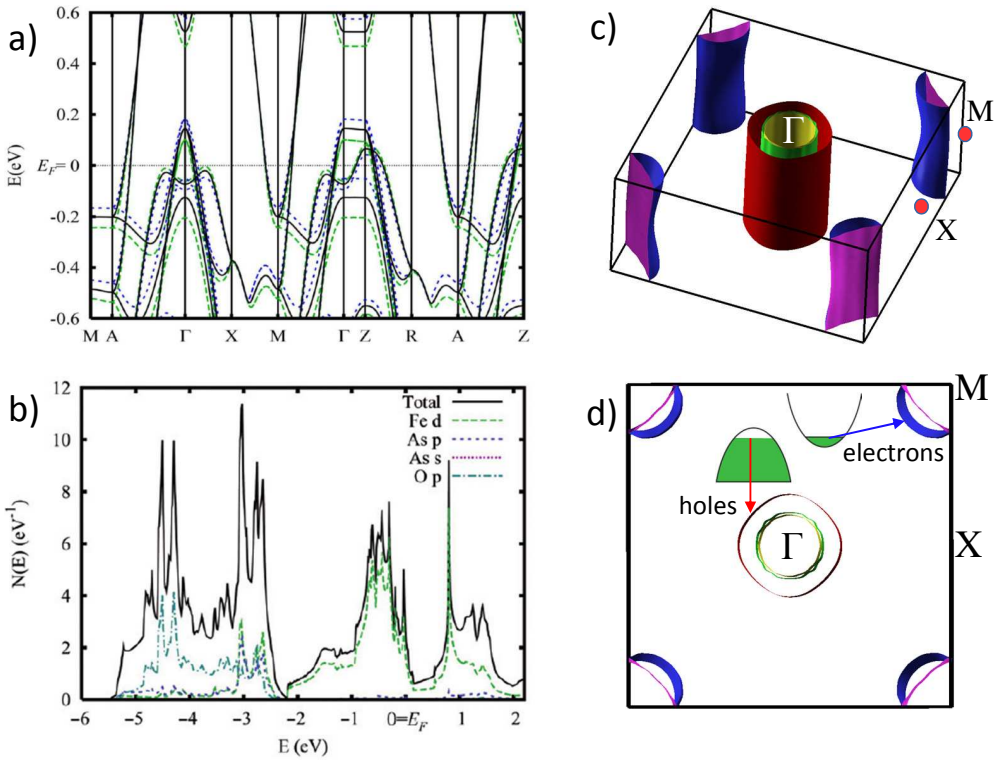

Figure 1.10: a): Band structure from DFT-LDA calculations in LaFeAsO. The solid black curves give the band structure for the experimental (X-Rays) crystal structure, while the blue dotted lines and green dashed lines are for the As planes (hypothetically) shifted by 0.035 Å towards or away from the Fe planes, respectively. b): corresponding DOS. (a) and (b) are from Ref. [50]. On the left side (c) and top (d) view of the Fermi surface (FS) of undoped LaFeAsO. The holes pockets are the red/yellow/green sheets at Γ while the electron pockets are the blue/magenta sheets at the corner (M) of the Brillouin Zone. Inset: sketch of the bands. The FS in (c) and (d) was calculated by us using the Full Potential Augmented Plane Wave method (FP-LAPW) as implemented in the Elk code with the GGA (Generalized Gradient) approximation.

iron based superconductors show a strongly correlated metal behavior. More precisely ARPES [54] and band structure calculations showed that they are 2D semimetals, which means that they have a completely filled valence band (at $T = 0$) and no gap between valence and conduction bands. The conduction band is at a different position in the momentum space (M) with respect to the valence band (Γ). Since there is a very small overlap of the bands the electrons "spill over" in the conduction band until the energy of highest occupied state is the same (Fig. 1.10d inset). This results in the presence of small electron (hole) pockets at M (Γ). FeAs-based parent compounds are thus "fully compensated" metals, where the electron (in the conduction band) and hole (in the valence band) concentrations are exactly the same at all temperatures.

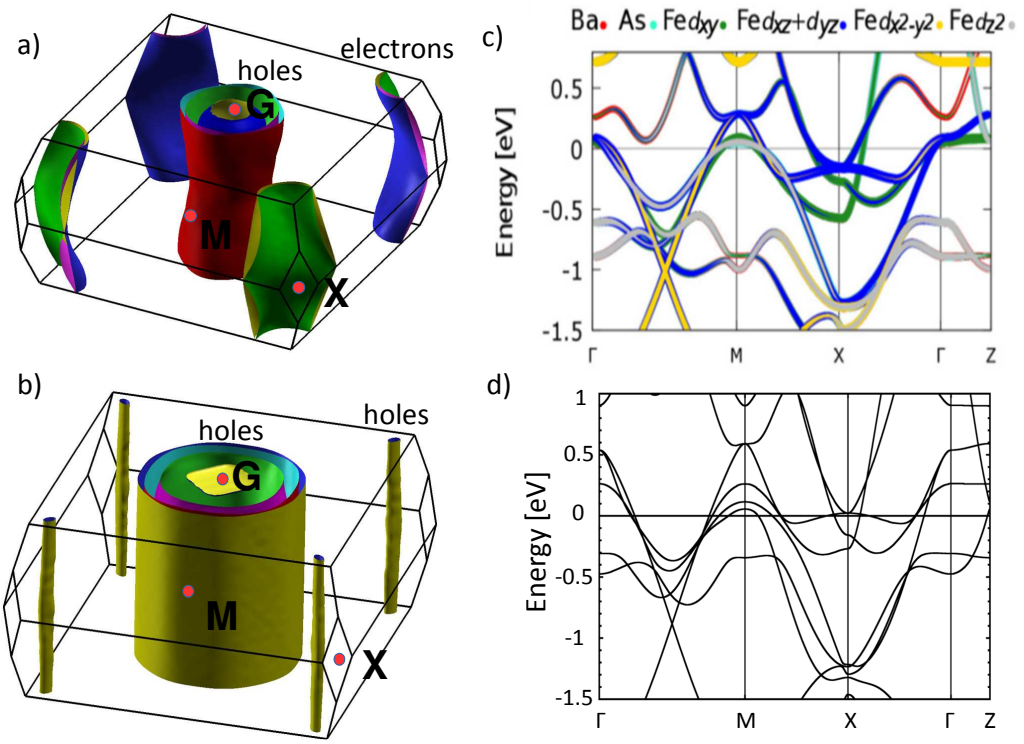

Figure 1.11: Fermi surface of $BaFe_2As_2$ (a) and $RbFe_2As_2$ (b) calculated using the FP-LAPW method (Elk code). AFe_2As_2 (A: K, Rb, Cs) correspond to the "fully" hole doped compound since Ba is completely substituted. All the carrier pockets in $RbFe_2As_2$ are holes pockets. In (c) and (d) the corresponding band structures are reported. All the calculations have been carried out by us, except for panel (c) which is adapted from Ref. [53] and displays the $BaFe_2As_2$ orbital character of the bands calculated using WIEN2K.

The electronic structure for LaFeAsO, the 1111 family's parent compound, was first calculated by Sing et al. [50] (see Fig. 1.10). The band plot clearly shows three hole bands near the Fermi energy E_f at the Γ point of the first Brillouin zone and two electron bands at the M point. ARPES spectroscopy revealed that a significant dispersion occurs along k_z and implies a rather strong coupling between contiguous FeAs planes. As can be seen in Fig. 1.10a the bands, and accordingly the Fermi surface, are strongly dependent from the position of the As ion with respect to the Fe-Fe plane. This is in good agreement with the experimental observation that T_c is also strongly affected by the value of this parameter with the highest transition temperature being observed when the $FeAs_4$ tetrahedrons are regular [55].

The band structure calculations for the 122 family compounds yield similar qualitative results with the difference that this time the electron pockets are at the X point of the Brillouin zone and not at the M point (see Fig. 1.11). However for the 122 family the M point of the primitive tetragonal crystalline structure is equivalent to the body-centred-tetragonal X point due to a 45°

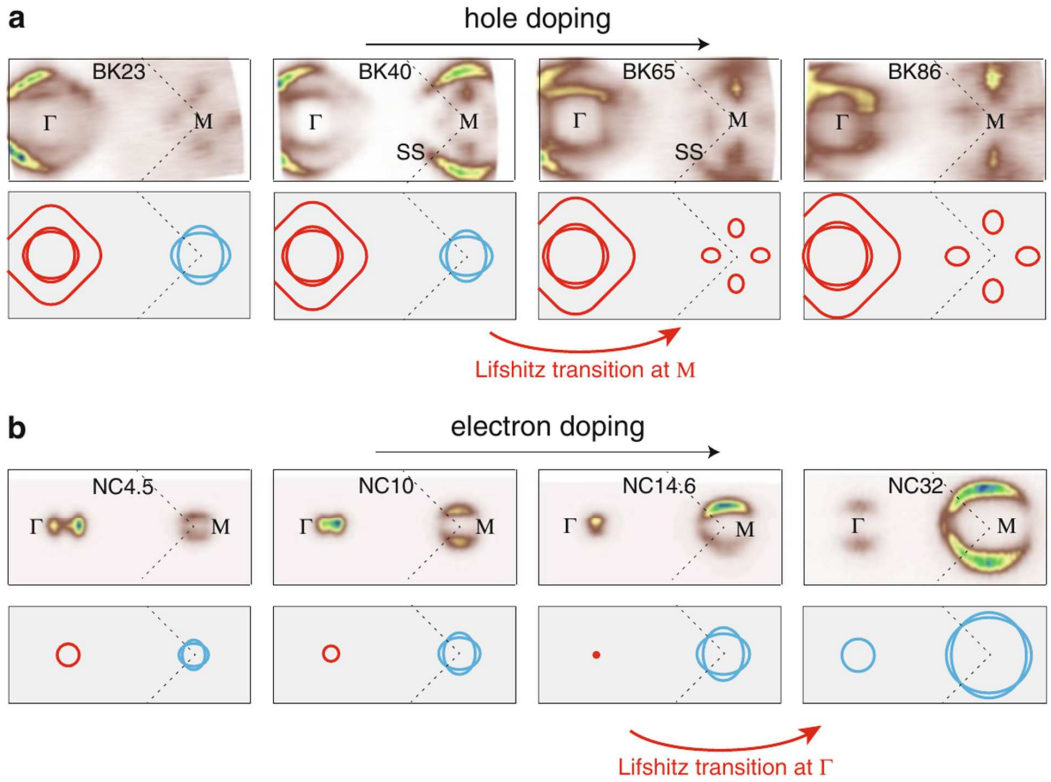

Figure 1.12: (a) The doping dependence of Fermi surface topology measured in $Ba_{1-x}K_xFe_2As_2$. The upper panels are the photoemission intensity distribution at the Fermi energy. The low panels are the obtained Fermi surface. SS is the abbreviation of surface state. The red and blue lines illustrate the hole pockets and electron pockets, respectively. (b) is the same as panel (a), but taken in $NaFe_{1-x}Co_xAs$. Figure adapted from [44].

rotation of the bct reciprocal lattice with respect to the primitive tetragonal 1111 reciprocal lattice. Thus the position of the pockets in the 122 and 1111 families is completely equivalent. In order to have a consistent notation for all the IBS the X point of the 122 family is often simply re-labelled as M in many ARPES works [44].

The introduction of carriers, for example through chemical doping, results in the shift of the bands. In $Ba_{1-x}K_xFe_2As_2$ the K for Ba substitution (hole doping) results in the rigid shift of the bands and thus in the expansion of the hole pockets at the center of the BZ (Γ point) and the shrinking of the electron pockets at M (see Fig. 1.12). Conversely electron (Co) doping enlarges the electron pockets and shrinks the hole ones. If the central hole pockets sink below the Fermi energy a Lifshitz transition [56], an abrupt change in the topology of the Fermi surface, takes place and an electron pocket appears at Γ. The opposite type of Lifshitz transition takes place at M in case of hole doping. This effect has been both theoretically predicted and extensively studies by imaging the Fermi surface with ARPES [44, 54] upon

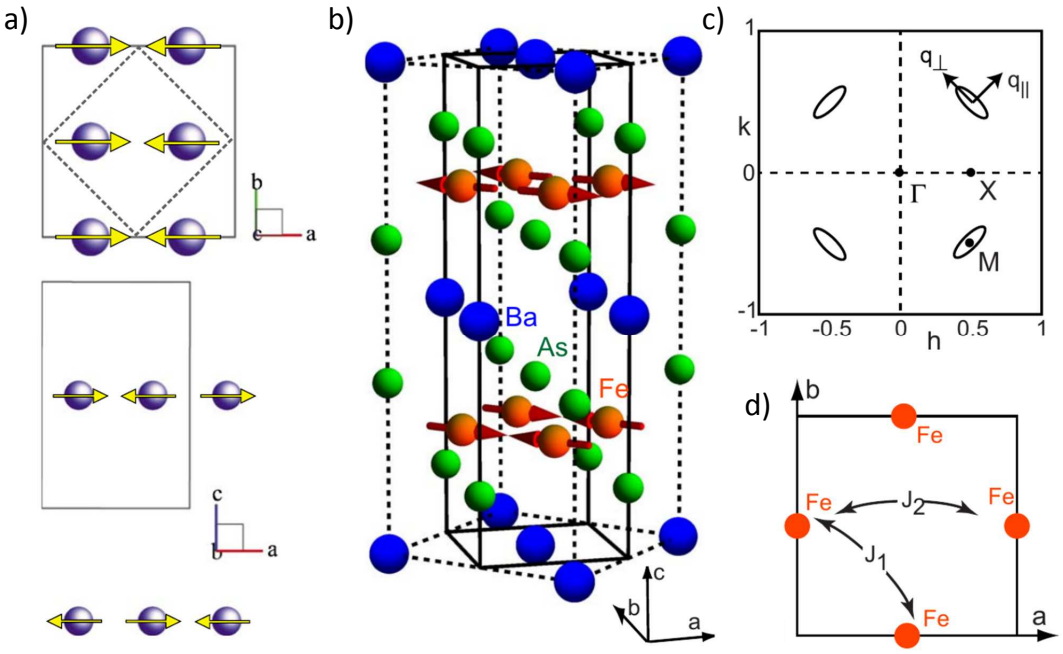

Figure 1.13: (a) Top: The magnetic structure only showing the Fe ions in the orthorhombic unit cell (straight line). The dashed line depicts the tetragonal cell. Bottom: Alternation of the moment direction along the c axis. (b) Antiferromagnetic structure of the parent compound $BaFe_2As_2$. Solid lines denote the tetragonal unit cell. (c) Schematic illustration of reciprocal space of a 2D square lattice. The wave vectors are used to define the spin-wave velocities. (d) Exchange couplings (J_1, J_2) between Fe atoms. Figure adapted from [57] and [58].

changing the charge doping (see Fig. 1.12).

Superconductivity can be induced in the IBS through charge doping, similarly to what also happens in cuprates superconductors. Since the electrons forming the Cooper pairs are those occupying the states very close to E_f it is reasonable to expect a strong dependence of T_c from the topology of the Fermi surface, especially in correspondence of the Lifshitz transition.

1.2.2 Magnetism and superconductivity

Just a few months after the discovery of the IBS it was hypothesized that the superconducting pairing is due to the inter-pocket interaction between the central hole and the corner electron pockets [59, 60].

In this picture superconductivity is mediated by the spin fluctuations which are characterized by a rich phenomenology. In particular, in LaFeAsO, three sources of spin fluctuations are present [60]: (1) from theoretical calculations the system is relatively near a Stoner [61] instability, (2) there is a nearest-neighbor antiferromagnetic (AFM) super-exchange [62], (3) there

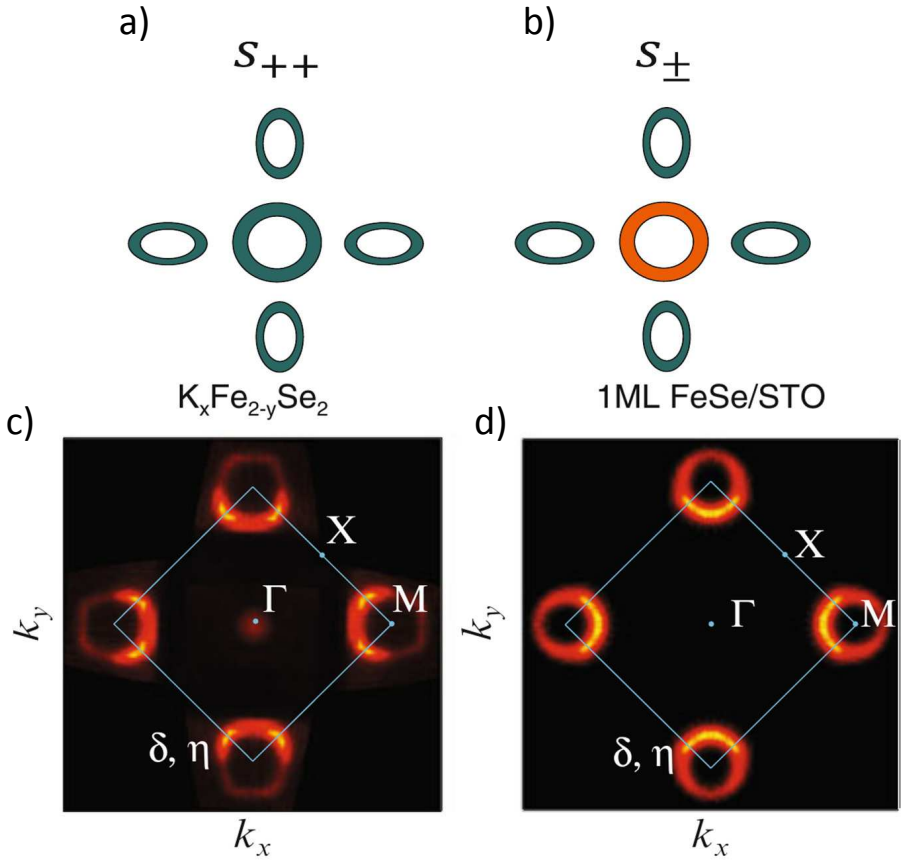

Figure 1.14: Top: Schematic 2D projection of the FS of IBS, the possible gap symmetries are indicated as colored regions on the Hole/electron pockets: (a) s^{++} symmetry, no sign change of the order parameter from Γ to M); (b) $s^{\pm}$ the order parameter changes sign at the corners of the BZ [63]. In this sketch no node is present, however the topology of the Fermi surface strongly suggest the presence of accidental nodes (see [14]. Bottom: Fermi surface (top view) of $K_xFe_{2-y}Se_2$ and mono-layer FeSe grown on $SrTiO_3$. The central hole pocket is just barely visible in (c) [64] and completely absent in (d) [65].

are nesting related antiferromagnetic spin-density-wave-type spin fluctuations near wave vectors connecting the electron and hole pockets [60].

The component resulting from nesting has been shown to be the strongest one for both the 1111 and the 122 families [60]. The corresponding interaction connects the well-separated FS pockets located around the Γ and M points. Though repulsive in the singlet channel this interaction results in a strong pairing if the superconducting order parameters on the Fermi Surface hole/electron pockets have opposite signs. Since the superconducting gap is s-wave but its sign changes on the two pockets of the FS this pairing symmetry is usually referred to as $s^{\pm}$.

The nesting wave vector between the electron and hole pockets is $\mathbf{Q_{nesting}} = (\pi/2, \pi/2)$ for the standard Fe_2 BZ (taking $a \equiv 1$) while it is

$\mathbf{Q_{nesting}} = (0, \pi)$ with the Fe-Fe distance $a_{Fe} \equiv 1$, in the notation of the single Fe Brillouin zone.

However the parent compounds (LaFeAsO and $BaFe_2As_2$) are magnetic and no superconductivity is present since the two states (magnetism and superconductivity) compete for the same electrons. Nuclear magnetic resonance (^{75}As [66, 67, 68]) and neutron diffraction measurements [57] showed a static antiferromagnetic orthorhombic structure with a "stripe" type configuration in the FeAs planes (see Fig. 1.13). The antiferromagnetic vector is $\mathbf{Q} = (0, \pi)$ or $(0, \pi)$ (unfolded BZ) which corresponds to the electron-hole Fermi surface nesting vector, strongly suggesting that the antiferromagnetic ordering is due to the spin density wave (SDW) [13] at the nesting vector.

The underdoped compounds share various electronic properties of the parent compounds, in particular the Fermi energy characterized by hole and electron pockets and the stripe magnetic order. However the static SDW is suppressed upon charge doping (see e.g. Fig.1.5a) due to the shrinking of the electron/hole pockets which weakens the nesting. When static magnetism is suppressed superconductivity appears. This is in good agreement with the model described above: the spin fluctuations are still strong when static magnetism disappears and they provide the glue for the Cooper pairs. In this scenario however the presence both of the central hole and of the corner electron pockets is required for superconductivity. This is in good agreement with the experiments since when the electron/hole pockets disappear in the over-doped regime, in corrispondence of the Lifshitz transition (see Fig. 1.12 for $Ba_{1-x}K_xFe_2As_2$, $NaFe_{1-x}Co_xAs$), T_c drops to zero.

It must be noted that other kinds of gap symmetries and pairing mechanisms have been proposed besides the $s^{\pm}$ spin fluctuations picture (see Fig. 1.14). Photoemission experiments on moderately doped IBS have shown [69, 63, 70, 71] that the pairing state is s-wave. However theoretical calculations revealed that also orbital fluctuations could give rise to a strong s-wave pairing interaction, without sign change of the order parameter (s^{++} symmetry [72]). This model is consistent with experimentally observed robustness of superconductivity against the introduction of impurities [72, 73, 74, 75, 76].

Finally we would like to remark that, while the $s^{\pm}$ model is in good agreement with the phenomenology observed in most of the IBS compounds, recent ARPES experiments on 11 iron-chalcogenides ($K_xFe_{2-y}Se_2$ [64] and mono-layer FeSe grown on $SrTiO_3$ with T_c above 50 K [40, 65], see Fig. 1.14) found that only corner electron pockets exist in the Brillouin zone, without any center hole pocket. This new finding implies that the presence of holes is not necessary for superconductivity in some IBS, thus casting a shadow on the general validity of the $s^{\pm}$ model.

1.2.3 The puzzle of the Fe magnetic moment

The theoretically calculated (DFT) Fe magnetic moment (1.75 μ_B/Fe in $BaFe_2As_2$, see Ref. [77]) for the SDW ground state of the IBS was found to be much larger than the experimental one, which is typically smaller than 1 μ_B/Fe (0.63 μ_B in LaFeAsO from Neutron scattering [57] and Mössbauer [78, 79], 0.4–1 μ_B in $BaFe_2As_2$ [80, 27, 81, 82]). The local Hund's coupling is primarily responsible for the large magnetic moment found by the DFT calculations [83].

This discrepancy with the experimental value could, in part, be a computational artifact caused by the strong dependency of the Fe magnetic moment from the As position in the lattice (see Fig. 1.10 for effect of the As position on the bands). In fact the experimental position of the As atoms does not correspond to the energy minimum found in the calculations. If the minimum energy of the compounds is calculated one gets a more reasonable value for the magnetic moment but also a wrong value for the distance of the As atom from the Fe plane.

In general a very strong coupling is present between the magnetic state of the Fe atom and the structure of the compound. For example in $CaFe_2As_2$ calculations (see Ref.[84]) predict a difference of 1.1 Å in the interlayer distance if the Fe atom is considered non magnetic. However it is also possible that the discrepancy is due to the fact that DFT calculations do not take into account the quantum fluctuations. These materials in fact have long be known to be close to a Stoner instability, suggesting the presence of intrinsic itinerant magnetism (SDW instability of the Fermi Surface, see Section 1.2.2) and related quantum fluctuations, which could explain the overestimate of the ordered Fe moment [14] (weak-coupling approach).

The presence of the magnetic order can also be explained in the framework of the $J_1 - J_2$ (strong-coupling approach) model with $2J_2 > J_1$. Here J_1 is the superexchange interaction developing between a pair of nearest-neighbor Fe spins while J_2 is the interaction between next-nearest-neighbor Fe spins (see Fig. 1.13). Even if this model is only suited to deal with localized electrons systems (e.g. the vanadates) and not metallic ones (the iron pnictides), it is still able to grasp several import aspect of the physic of the IBSs [14], such as the presence of the collinear magnetic order in the undoped compounds and its suppression by charge doping. In this framework the presence of magnetic frustration is a natural way to explain the anomalously low Fe moment [14, 85]. However it has been shown by Fang *et al.* [78] that, in a quantum Heisenberg spin-localized model, frustration may not be enough to justify the small measured μ_{Fe}.

It must be remarked that there are significant differences in the values of the magnetic moment obtained with different experimental techniques. In particular in $BaFe_2As_2$ it was found that while static techniques, such as μSR and Mössbauer spectroscopy, reveal a magnetic moment of ~0.4 μ_B/Fe [27, 81, 82], inelastic neutron scattering finds μ_{Fe} ~0.9–1 μ_B [81] while Resonant Inelastic X-Ray Scattering (RIXS) finds

that the iron moment is ~1.3 μ_B [86]. This is a strong confirmation that the "missing" magnetic moment is mostly due to the time-averaging effect of the quantum fluctuations which results in the masking of the real "bare" value of μ_{Fe} [86]. Since RIXS is much faster than the other experimental methods (femtosecond range), it is able to take snapshots of the real magnetic moment and thus reveals higher values than the slower techniques.

The anomalous Fe magnetic moment however is still a subject of great interest and it is widely studied with neutron scattering [57, 80, 81, 87], X-Rays [86, 88, 89] and NMR [66, 67].

1.3 Nematicity and Spin fluctuations

In most IBS superconductivity emerges close to the disruption of the stripe magnetically orderer state. This led to the early hypothesis [60, 94, 95] that the magnetic fluctuations may play a key role in the pairing mechanism, as explained in the previous sections. However another non superconducting phase is present close to the magnetic one [93]. In fact at a certain temperature T_{nem}, above the magnetic transition temperature T_m, the system spontaneously breaks the symmetry between the x and y directions in the Fe-plane, resulting in the point group symmetry of the lattice changing from tetragonal to orthorhombic (T-O transition). A transition in which the rotational symmetry is broken and the time reversal one is preserved is often referred to as nematic, in analogy with the nematic phase found in liquid crystals [96]. In the nematic phase no spin order is present $\langle \vec{S} \rangle = 0$ but a strong q-dependence (nematic order) of the spin correlation function appears (see Fig. 1.16d). Both for the cuprates [97] and for the IBS [98] it has been proposed that the nematic fluctuations could have a strong influence on the superconducting state, and may be responsible for the very high T_c observed in these materials.

While for a few compounds (e.g. hole doped $BaFe_2As_2$) $T_m = T_{nem}$, for the most of the materials (e.g. Co doped $BaFe_2As_2$ and F doped LaFeAsO) the two temperatures are significantly different and T_m is always lower than T_{nem} (see Fig. 1.15).

In the first case ($T_m = T_{nem}$) the transition is of the first order while both the nematic and the magnetic transitions are of the second order if $T_m < T_{nem}$ [99, 91, 92, 100, 101]. In general T_{nem} tracks T_n across all the phase diagram, from the underdoped compound up to the optimally doped one. For higher doping no magnetic/nematic transition is present above T_c (see Fig. 1.15).

A notable exception is FeSe where no magnetic transition is present even if the nematic transition has been observed for a broad range of chemical doping levels and external hydrostatic pressure values (see Section 1.1.4, Fig. 1.7). However very strong spin fluctuations have been observed at low

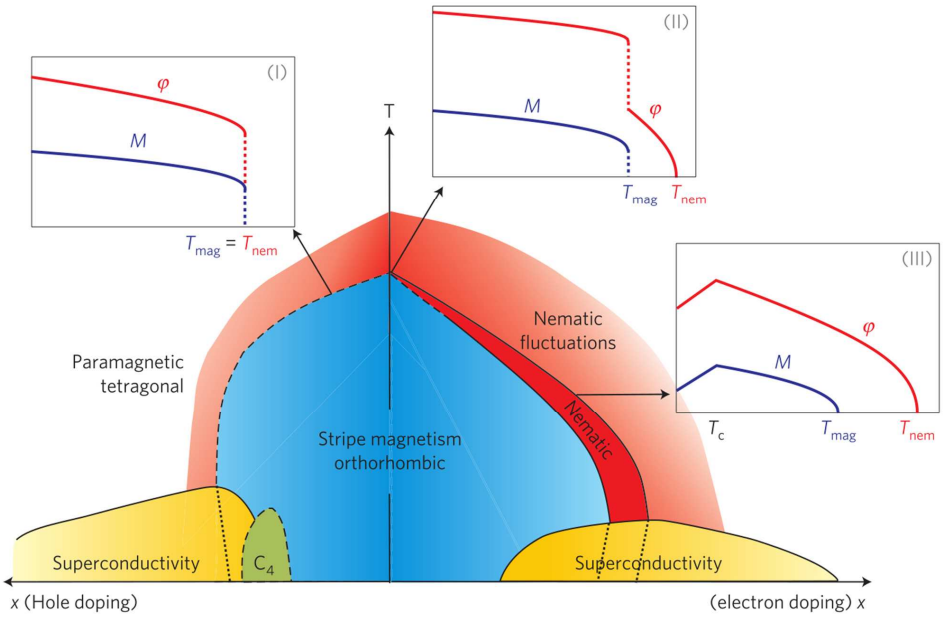

Figure 1.15: Scheme of the phase diagram of the Ba122 compounds (see Fig. 1.5 for the actual experimental phase diagram). The dark red region in the hole doped side indicates the orthorhombic paramagnetic state while in the blue area stripe antiferromagnetism and orthorhombicity coexist. Superconductivity is in yellow while the green area corresponds to a possible magnetically ordered state that preserves the tetragonal (C_4) symmetry [90]. The shaded/light red region indicates the presence of nematic fluctuations. The insets show the temperature-dependence of the orthorhombic (ϕ) and magnetic (M) order parameters in different regions of the phase diagram: in region (I) the first-order magnetic and nematic transitions are simultaneous while in region (II) the transitions are second-order nematic, first-order magnetic and take place at different temperatures. In region (III) the transitions are second-order and at different temperatures. At $x = 0$ the transitions are split, like in region (II), but their separation is very small [91, 92]. Figure adapted from [93].

temperature indicating that also this compound is very close to a magnetic transition [102].

Understanding the nematic transition is thus extremely important in order to explain the origin of the magnetic order and of the superconducting state. Recently it has been proposed that the nematic phase could also exist in other unconventional superconductors, such as cuprates and Heavy Fermions, suggesting an other link between these fascinating systems [96].

It must be remarked that the nematic transition is not a regular phonon-driven tetragonal to orthorhombic transition. In fact it has been proposed, from theoretical calculations [78, 103], that the transition is probably driven by some electronic degree of freedom. This is confirmed by the shape of the phase diagram, where magnetism always follows the structural transition

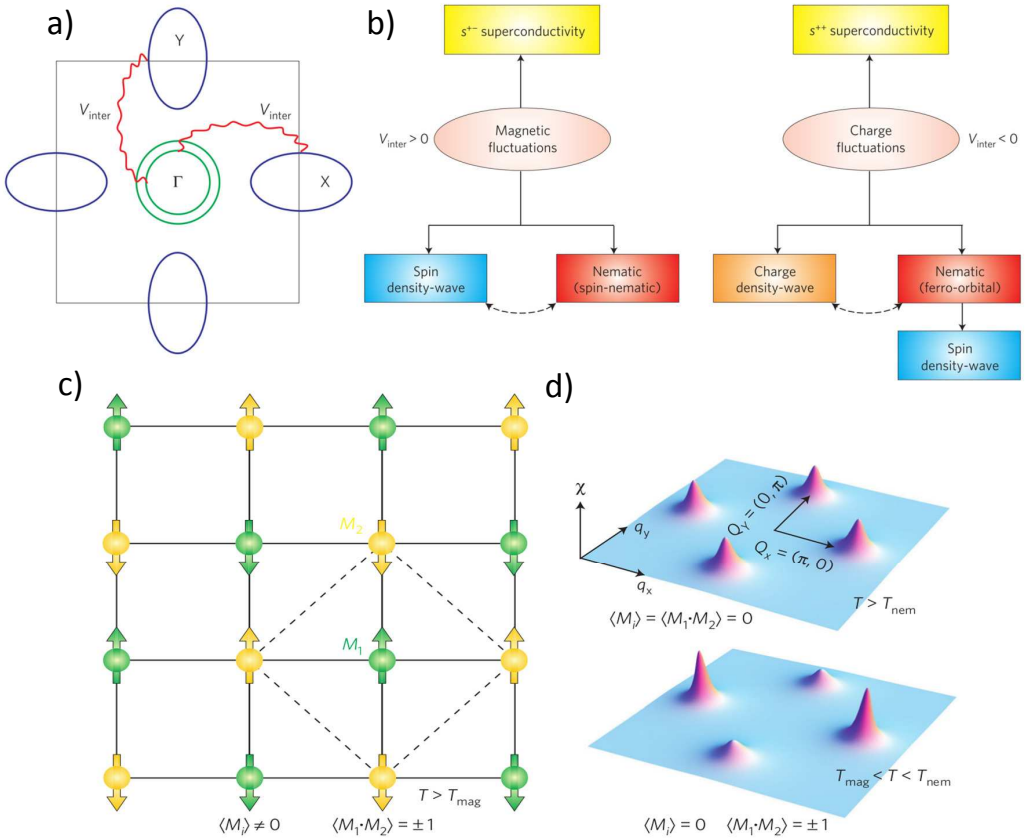

Figure 1.16: (a) Sketch of the Fermi Surface (top view, along k_z). V_{inter} is the inter-pocket interaction (see text). (b) Depending on the sign of V_{inter}, either spin fluctuations ($V_{inter} > 0$, repulsion) or orbital fluctuations ($V_{inter} > 0$ attraction) dominate (see text). (c) Stripe magnetic configuration in real space. It can be interpreted as two inter-penetrating Néel sublattices (green and yellow) with staggered magnetization M_1 and M_2. (d) Magnetic susceptibility $\chi(q)$ across the first BZ, above and below the nematic transition temperature. Figure adapted from [93].

and, quite strikingly, by dc resistivity measurements which showed a much larger $x-y$ anisotropy than the one observed for the lattice parameters. This strong anisotropy effect was also revealed by thermopower [104], optical conductivity [105, 106] and ARPES measurements [107]; evidence of strong magnetic anisotropy has also been found by NMR [108]. Interestingly X-Ray diffraction provided one of the most clearcut evidence of the electronic character of the nematic transition by observing that the orthorhombic distortion is strongly suppressed in the superconducting phase [109], where the two states compete for the same electrons.

Three main experimental manifestations of nematicity have been found: (1) the structural transition, (2) the occupations of the d_{xz} and d_{yz} Fe-orbitals become different [107] and (3) the static spin susceptibility $\chi(q)$ becomes

different along the q_x and q_y directions before the appearance of the static stripe state (see Fig. 1.16). The unbalance between the d orbitals populations (2) is usually associated with divergent charge fluctuations (orbital degrees of freedom) while the magnetic order (3) is usually associated with spin fluctuations.

Since we can exclude the phonons (see previous paragraph) as the drivers of the nematic phase this leaves us with just two alternatives: orbital fluctuations and spin fluctuations [93]. However since both the orbital and the magnetic order parameter can give rise to the structural and to the magnetic phase transition it not easy to understand which of the two order parameters is driving the other one.

Discriminating between the two is very important for the understanding of superconductivity in IBS, in fact charge/orbital fluctuations favor the s^{++} gap symmetry whereas spin fluctuations favor the $s^{\pm}$ symmetry.

In the spin fluctuations scenario the stripe magnetic order emerge from the spin-driven orthorhombic nematic phase. In case of dominant orbital fluctuations instead a charge density-wave emerges from the charge-nematic phase and the stripe magnetic order is only as a secondary consequence of the orbital order. The superconducting state is s^{++} (same-sign gaps).

From the theoretical point of view the problem can be treated using the itinerant approach (weak correlations) by assuming the presence of an interband interaction (V_{inter}), which is a combination of the Hubbard and Hund interactions dressed up by coherence factors associated with the transformation from the orbital to the band basis (see Ref. [110, 111, 93]). If $V_{inter} > 0$ the magnetic fluctuations will be dominant while for $V_{inter} < 0$ the nematic state will be driven by the charge/orbital fluctuations (see Fig. 1.16b).

1.3.1 Experimental studies of the nematic fluctuations

Since the order parameters are correlated it is very difficult to find a conclusive experimental evidence discriminating among the two models. Notwithstanding significant advances have been achieved through the study of the spin fluctuations by NMR and neutron scattering. In particular NMR revealed that the spin fluctuations are very strong between T_{nem} and T_m [112] and that they extend well into overdoped region of the phase diagram [113, 114]. Also the comparison between the NMR $1/T_1$ (proportional to the nematic susceptibility) and the shear modulus C_s (proportional to the non critical renormalized lattice susceptibility) revealed a robust scaling between $1/T_1$ and C_s [93, 115], providing strong support for the spin-fluctuation model. A review of the most important NMR results in the IBS material is presented in the following chapter.

Inelastic neutron scattering (INS) is often used in tandem with NMR in order to probe both magnetic order and spin fluctuations. The technique uses the neutron magnetic moment as a probe of the electronic magnetic moments in the sample.

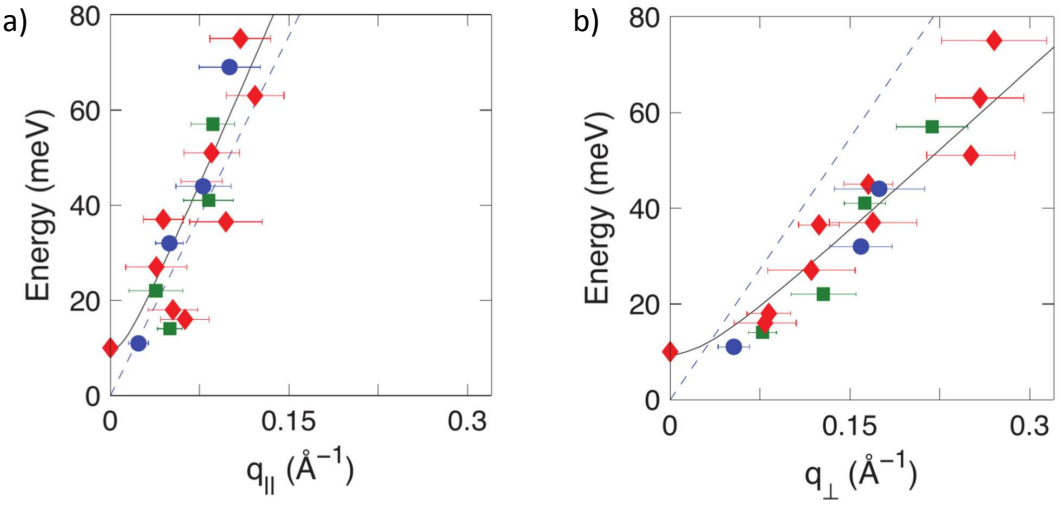

Figure 1.17: The dispersion of the magnetic excitations in $Ba(Fe_{1.935}Co_{0.065})_2As_2$ for $T = 7$ K measured with Inelastic Neutron Scattering. The comparison between $q_{||}$ and $q_{\perp}$ reveals a strong anisotropy up to 80 K. Figure adapted from [58].

Anisotropic spin excitations were observed by INS in the undoped parent compounds along the two orthorhombic a and b axes, as expected for an anisotropic $\chi(q)$ (see Fig. 1.16d). Lester et al. [58] observed spin wave-like excitations in the paramagnetic tetragonal structure of superconducting $Ba(Fe_{1.935}Co_{0.065})_2As_2$ single crystals [58] demonstrating that the anisotropy of the spin fluctuations persists also when the nematic and magnetic phases are vanishing. This implies that the anisotropy of the parent compound persist in the superconducting samples even for significant doping levels. From the Heisenberg model they also extracted the nearest neighbour $J_1 = 43 \pm 7$ meV and the next nearest neighbour $J_2 = 30 \pm 3$ meV exchange couplings. Even if the system does not show a static order it is quite near to the antiferromagnetic quantum critical point since it can be shown that a stripe-like order develops in iron-pnictides if $J_2/J_1 > 0.5$ [116] (see Fig. 1.13).

It should however be noted that a 2011 theoretical paper from Park *et al.* [117] proposed a different interpretation for the neutron scattering results. They calculated both the one-particle and the magnetic two-particle excitation spectra of $BaFe_2As_2$ using DFT in combination with the dynamical mean-field theory method and showed that the results fit pretty well the neutron scattering data in the whole temperature range, without the need of introducing any nematic order.

Below T_c inelastic neutron scattering measurements observe a magnetic neutron scattering peak called "spin-resonance mode". This resonance mode, with an energy gap, evolves out of the antiferromagnetic spin fluctuation background in the normal phase upon cooling below T_c and has the same

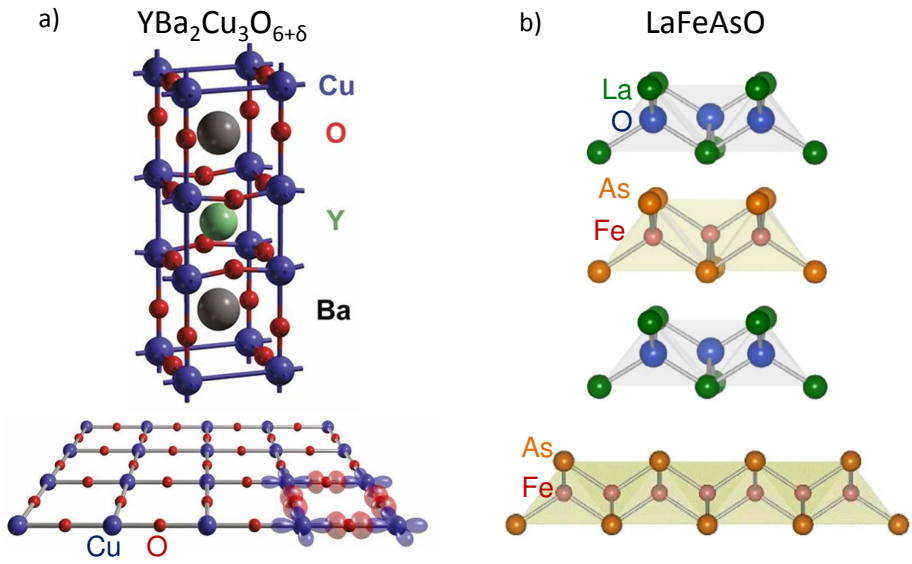

Figure 1.18: Comparison of the lattice structure of cuprates (a) and iron based (b) superconductors. The crystal structure in (a) is that of YBCO (adapted from Ref. [119]) while the one in in (b) is LaFeAsO (adapted from Ref. [13]). At the bottom of the two panels is shown the different structure of the superconducting layers.

in plane $(0, \pi)$ wave-vector of the neutron scattering peak above T_c arising from nesting between electron and hole-pockets. The presence of this spin-resonance suggests a sign difference in the superconducting gap $\Delta(k)$ between different parts of the Fermi surface, in good agreement with what expected in case of $s^{\pm}$ pairing [48, 118].

The study of the nematic fluctuations is thus a central topic in the IBS research and significant experimental and theoretical efforts are still going on.

1.4 Pnictides, Cuprates and Heavy Fermion materials: analogies and differences

In this section we briefly discuss analogies and differences between the iron based superconductors and some of the other unconventional superconductors: the cuprates and the Heavy Fermion (HF) compounds.

1.4.1 Pnictides and cuprates

Both the cuprates and the iron pnictides are strongly 2D materials as it can be immediately grasped by looking at their lattice structure (see Fig.1.18). Superconductivity takes place in the CuO layer in the cuprates and in the

FeAs layer in the iron-pnictides while the intercalating layers act as a charge reservoir and decouple the adjacent conducting layers. While the CuO layer is a perfectly flat square lattice of Cu atoms, each surrounded by four O atoms, the FeAs plane displays a tetragonal structure with four Fe atoms at the corners of the base and the As atom at center but shifted above the Fe plane. In the FeAs layer conduction takes place along the Fe-Fe directions ($3d$ orbitals) while the As $4p$ orbitals give rise to levels lying well below the Fermi surface [48, 51, 52]. Conversely in the CuO planes the carriers have to hop from Cu to O to Cu, which results in a big contribution of the O $2p$ orbitals to the density of state at the Fermi energy and in a sizable superexchange antiferromagnetic interaction between the Cu spins. This difference in structure results in a very different ground state for the two materials: the undoped cuprates are Mott insulators while the IBS are metals or semimetals with sizable electronic correlations. Furthermore, while just one band cross the Fermi energy in the cuprates, the IBS are characterized by 5 bands crossing the Fermi level originating from the 5 Fe d orbitals, which can give rise to exotic orbital dependent behaviours [120].

Strong correlations are universally understood to be be driving force of the cuprates phase diagram and the essential physics of the system is often described by the Hubbard model in the strong coupling limit (t-J model). Conversely the IBS are in an "intermediate" correlation strength regime which makes their theoretical treatment much more challenging [44, 121, 122, 48].

The most striking similarity between cuprates and IBS is the shape of phase diagram. In both cases the parent compounds are magnetic in their ground state and superconductivity can be induced upon charge doping [121, 44] or by applying pressure. The magnetic fluctuations, persisting after the suppression of the static magnetism, are the leading candidates for the pairing interaction in both the systems [60, 122, 44]. However the magnetic order in the cuprates is of the Néel type (the Cu^{2+} spins are anti-parallel along both the crystallographic directions of the CuO plane) while, as thoroughly discussed in the previous sections, in the IBS the magnetic order is collinear (the Fe^{2+} spins are anti-parallel along a (b) and parallel along b (a), see Fig. 1.19c and d). The magnetic state is typically much more robust in cuprates (T_m <150 K for the IBS and above 300 K in cuprates). Not only the magnetic order is different but also the superconducting state displays a different gap symmetry (d wave in the cuprates [121] and $s^{\pm}$ in the IBS [14]), which is not unexpected for a spin driven superconducting state.

Another significant difference is the absence of the pseudogap region from the phase diagram of the IBS. The pseudogap phase is characterized by a non completely open gap at the Fermi energy (some regions of the FS become gapped while other parts retain their conducting properties) which has the same d symmetry of the superconducting gap and was observed to evolve smoothly in the SC gap by lowering temperature or increasing the

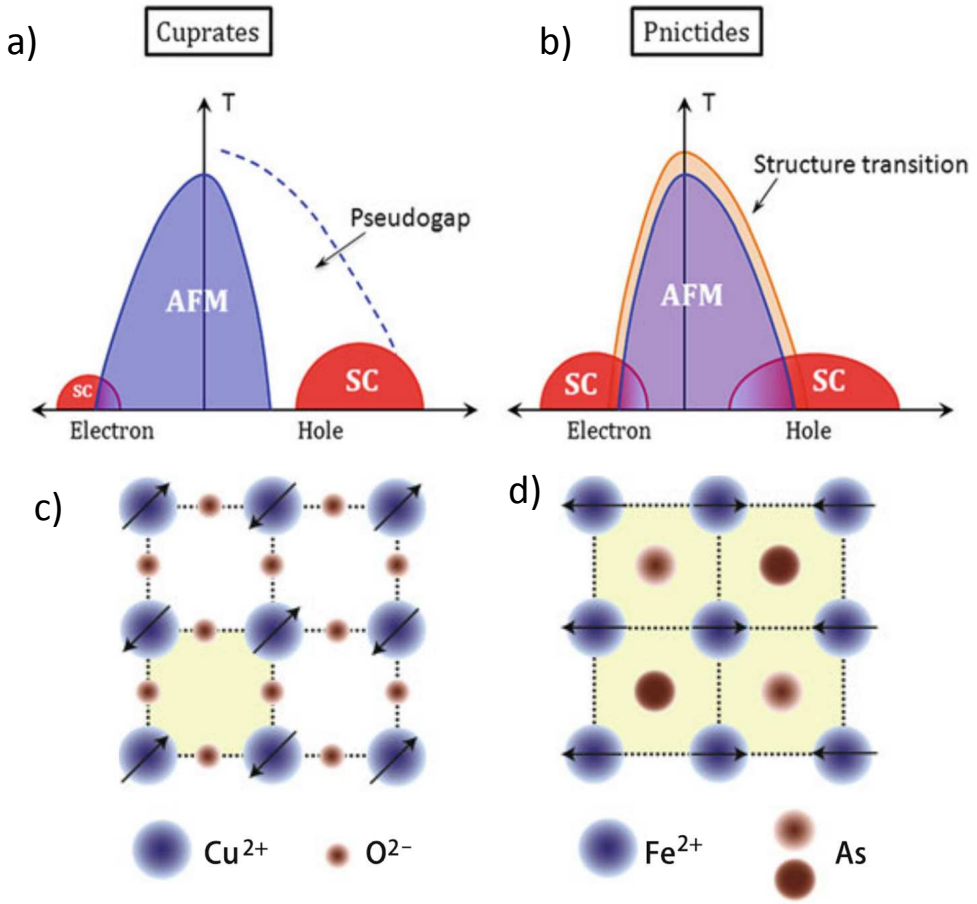

Figure 1.19: Sketch of the phase diagrams of cuprates (a) and iron based superconductors (b). In (c) and (d) the typical real space configuration of the spins in the magnetic phase is reported for the two class of materials. In (d) the light/dark shaded As atoms lie below/above the Fe plane. Figure adapted from Ref. [44].

doping level [123]. Despite several studies (NMR, specific heat, ARPES) no conclusive evidence of this feature has been found in the IBS [48].

Moreover neutron scattering [125], resonant inelastic X-Ray scattering (RIXS) [126, 127, 128], scanning-tunnelling microscopy STM [129] and high-field NMR [124] revealed the presence of a charge ordered phase (charge density wave, CDW) developing close to optimal doping (see Fig. 1.20) in several cuprates compounds.

While this CDW modulation is usually dynamic, it can be frozen down and studied with NMR by applying a large enough magnetic field [124]. Recent experiments indicate that the charge ordered phase coexists with superconductivity for a very wide charge doping range [128, 129] and another novel NMR study by Reichardt *et al.* [130] suggests that the oxygen satellite line splitting in $YBa_2Cu_3O_{6+y}$, initially attributed to the orthorhombic distortion, is instead due to a charge density modulation.

While the CDW is usually considered to be in competition with the super-

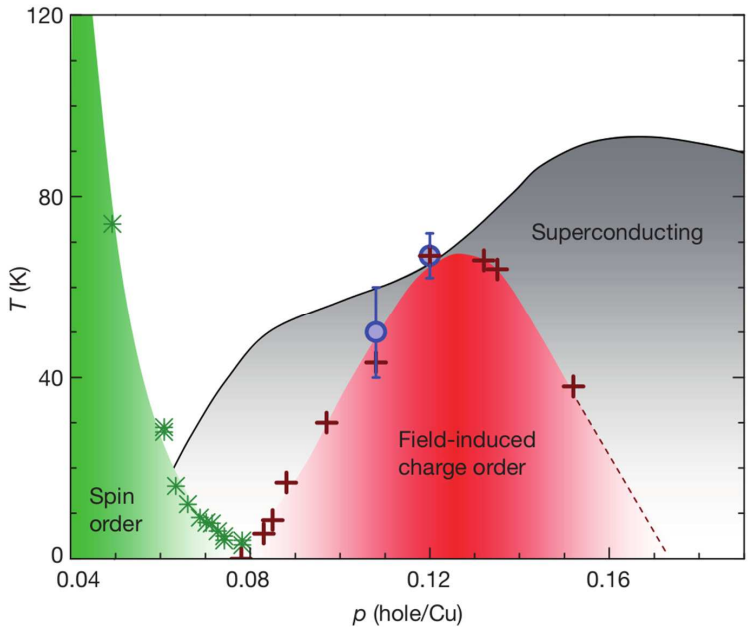

Figure 1.20: $YBa_2Cu_3O_y$ phase diagram. The red region indicates charge order. The charge ordering temperatures measured with NMR are indicated by blue dots (H>28.5 T) and the ones measured using Hall effect by red plus symbols. The green stars indicate the magnetic transition temperature obtained from μSR measurements. The continuous line represents the superconducting transition temperature T_c. Figure adapted from Ref. [124].

conducting state, its relation with both superconductivity and the pseudogap state is still object of a considerable research effort [128].

We will thoroughly discuss the possible presence of a charge ordered phase in hole doped IBS in Section 3.3.

1.4.2 Pnictides and Heavy Fermions

Their metallic ground state, characterized by significant electronic correlations, makes the parent compound of iron based superconductors quite similar to the heavy fermion materials (see Ref. [133]).

The heavy fermions are a big class of materials, containing actinides and rare earths, which are characterized by the presence of quasi-localized f electrons. Their are commonly named heavy fermions owning to their huge electron effective mass (100 - 1000 larger [134] than the free electron mass) resulting in the gigantic Sommerfeld coefficient characterizing their low temperature specific heat. The significant electronic correlations lead to several other exotic behaviors which are strongly material dependent (See Ref. [134] for a review). However many of these compounds display a phase transition, driven from an external parameter such as pressure, doping or disorder, from a strongly correlated antiferromagnetic phase to a more weakly correlated

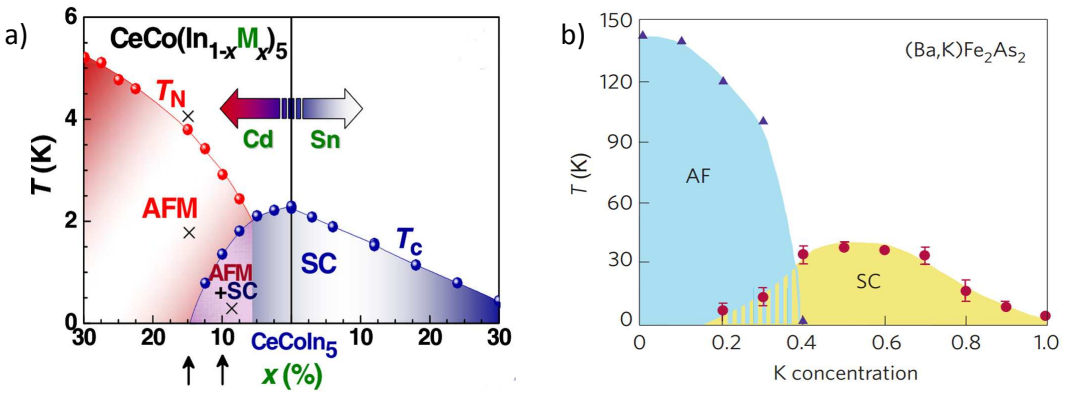

Figure 1.21: Comparison of the phase diagram of K doped $BaFe_2As_2$ (right) with the one of Cd/Sn doped $CeCoIn_5$ HF superconductor (left). Figure adapted from Ref. [131] ($CeCoIn_5$) and Ref. [132] (K doped $BaFe_2As_2$).

Fermi liquid phase. In correspondence of the Quantum Critical Point (QCP) separating the two phases a superconducting dome is often observed. In fact the HF were the first class of materials were superconductivity was observed in presence of large magnetic moments (from the f electrons) [11]. It is generally accepted that the critical fluctuations near the QCP are responsible for the superconducting state. In this region the behavior of the materials is quite complex and small perturbations can lead to a completely different ground state [131].

In some HF compound, such as $CeCoIn_5$, it was shown that the AF phase, which is absent at ambient pressure, can be restored by Cd doping, while Sn doping slightly suppress the superconductivity [131]. The resulting phase diagram is extremely similar to the one commonly observed in charge doped cuprates and IBS. Even if the electronic ground state is quite different (no f electrons, completely different Fermi Surface) several attempt have been made to treat the IBS as heavy fermions systems with the quasi localized Fe $3d$ electrons playing the role of the f electrons [133, 135, 87].

Chapter 2

Experimental techniques: NMR and μSR

In this chapter we will give a brief review of the main experimental techniques used in this thesis: Nuclear Magnetic Resonance and Muon Spin Rotation. The following description of the techniques is mainly based on the books from C.P. Slichter [136] and A. Abragam [137] for the NMR section and on the reviews from Blundell [138] and P. D. de Reotier [139] for the μSR one.

2.1 Nuclear Magnetic Resonance

Nuclear Magnetic Resonance (NMR) is a type of radio-frequency (rf) spectroscopy which deals with the magnetic dipole transitions between the nuclear spin magnetic energy levels split by the Zeeman interaction.

The magnetic moment of the nuclei is so small that it is completely undetectable using static methods, in fact the small nuclear magnetic moment is completely masked by the electronic contribute which is roughly six order of magnitude stronger. However it is possible to study the nuclear magnetism using the resonant method: when the system is put inside a static magnetic field the nuclei will absorb rf radiation at a characteristic frequency ω_L (Larmor frequency) whose energy ($\hbar\omega_L$) corresponds to the Zeeman splitting between the nuclear spin levels. The radio-frequency response allows one to retrieve informations on the local spin-charge environment in which the nuclei are immersed since the splitting between the levels and the transition probabilities are affected by the electronic environment through to the hyperfine interaction.

Nuclear Magnetic Resonance is a local technique, in fact each nucleus only probe its immediate surroundings and the results of the experiments will be the sum of the contributions resulting from nuclei probing the distribution of electronic and magnetic environments present into the sample.

Furthermore NMR is also sensible to the presence of low energy spin dynamics in the kHz-MHz range, since they affect the transition probabilities between the nuclear energy levels and thus modify the nuclear spin relaxation rates.

Differently from other techniques (e.g. Neutron Scattering, μSR, RIXS), which require complex and expensive facilities, for NMR only relatively cheap rf equipment is needed, making the technique particularly attractive and widespread. Effectiveness, versatility and cheapness have contributed to the huge success of NMR in solid state physics, chemistry, pharmaceutics and industrial processes quality control.

2.1.1 The quantum interpretation of NMR

Most of the elements of the periodic table have at last an isotope with a non zero nuclear spin **I** and all these isotopes are NMR active. The nuclear spin gives rise to a nuclear magnetic moment $\boldsymbol{\mu}$:

$$\boldsymbol{\mu} = \frac{g\mu_N}{\hbar}\mathbf{I} = \gamma\mathbf{I} \ . \tag{2.1}$$

Here g denotes the Lande g-factor of the nucleus and $\mu_N = e\hbar/m_p = 5.05 \cdot 10^{-27}$ A·m^2 is the nuclear magneton (m_p: proton rest mass). The gyromagnetic ratio γ combines all the prefactors in Eq. 2.1 in an isotope-specific constant, ranging from $\gamma/2\pi = 42.579$ MHz/T for hydrogen (^{1}H) to $\gamma/2\pi = 0.7291$ MHz/T for ^{197}Au.

The nuclear moment $\boldsymbol{\mu}$ couples to an external magnetic field $\mathbf{H}_0$ via the nuclear Zeeman interaction described by the Hamiltonian:

$$\mathcal{H}_z = -\boldsymbol{\mu} \cdot \mathbf{H}_0 \ . \tag{2.2}$$

Assuming that the external field is aligned along the z-direction ($\mathbf{H}_0 = H_0\hat{z}$) and taking into account Eq. 2.1, one can write Eq. 2.2 as:

$$\mathcal{H}_z = -\gamma H_0 \mathbf{I}_z \ , \tag{2.3}$$

where $\mathbf{I}_z$ is the z component of the angular momentum operator. The energy of the corresponding $2I + 1$ equidistant levels (see Fig. 2.1) can be written as:

$$E_m = \langle I, m|\mathcal{H}_z|I, m\rangle = -\gamma H_0 \langle I, m|\hat{I}_z|I, m\rangle = -m\gamma\hbar H_0 \ , \tag{2.4}$$

where the possible values of m are $m = -I, -I + 1, \ldots, I - 1, I$. Since the matrix elements between states $|I, m\rangle$ and $|I, m'\rangle$ of the operator $\mathbf{I}_z$ vanish unless $m' = m \pm 1$, only the transitions that follows the selection rule $\Delta m = \pm 1$ (magnetic dipole transitions) are allowed. To undergo such a transition, the system has to absorb the energy $\Delta E = \hbar\omega_0$ where $\omega_0 = \gamma H_0$ is the so called Larmor frequency for the magnetic field $\mathbf{H}_0$.

The previous treatment holds for a single nuclear spin. For an NMR experiment however we need at least 10^{16} nuclear spins in order to obtain an

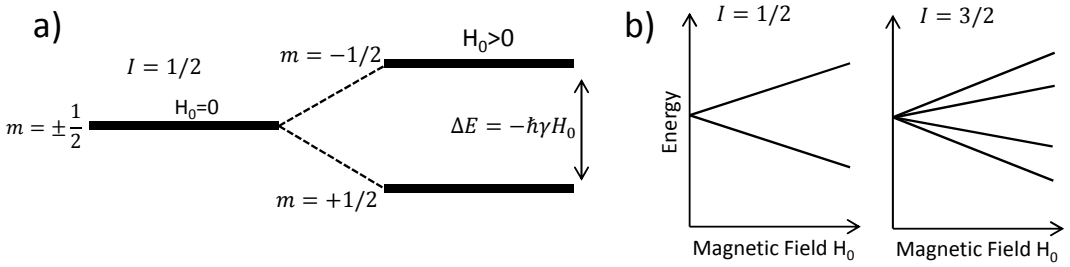

Figure 2.1: Sketch of the Zeeman splitting of the levels for different values of the nuclear spin. a) Zeeman splitting ($I = 1/2$) of the levels in an external magnetic field. b) the evolution of the Zeeman splitting with increasing magnetic field for $I = 1/2$ and $I = 3/2$.

acceptable signal-to-noise ratio. For an ensemble of spins in thermodynamic equilibrium the occupancy of the nuclear magnetic energy levels E_m (see 2.4) follows the the Boltzmann distribution. The unequal occupancy of the levels results in a nuclear spin polarization $\langle \mathbf{I}_z \rangle$ and thus in a total nuclear magnetic moment M_z:

$$M_z = N\gamma\langle \mathbf{I}_z \rangle = N\gamma \frac{\sum_{m=-I}^{m=+I} \hbar m \exp(-E_m/k_B T)}{\sum_{m=-I}^{m=+I} \exp(-E_m/k_B T)} \approx \frac{N\gamma^2\hbar^2 I(I+1)}{3k_B T} H_0 = \chi_0 H_0 \,, \tag{2.5}$$

where N denotes the number of nuclear spins and χ_0 is the static nuclear susceptibility. In agreement with equation 2.5 one can increase M_z (and thus the intensity of the NMR signal) by raising the external magnetic field, by lowering temperature or by increasing the size of the sample (raising N).

The static nuclear susceptibility is smaller than the electronic one by a factor of $10^{-6} - 10^{-8}$ as can be seen from Eq. 2.5. This huge difference between the nuclear and electronic spin susceptibility is pivotal for the NMR technique, in fact, since the nuclear and electronic spin systems are coupled by the hyperfine Hamiltonian (see following section), it is possible to obtain information on the electronic spins by observing the nuclear spin system but the perturbation of the nuclear system during the NMR measurement will only give rise to a completely negligible effect on the electronic system under study.

2.1.2 Interactions

Up to this point we have studied the behavior of the nuclear spin system with all the interactions, save for the Zeeman interaction, turned off. The interactions among the nuclear spins and with their electronic environment

shift and broaden the nuclear magnetic energy levels E_m and drive the relaxation of the nuclear magnetization following an external perturbation. The complete Hamiltonian can be written as:

$$\mathcal{H} = \mathcal{H}_z + \mathcal{H}_{n-n} + \mathcal{H}_{n-e} + \mathcal{H}_{EFG} \ . \tag{2.6}$$

Here $\mathcal{H}_z$ denotes the Zeeman interaction, $\mathcal{H}_{n-n}$ is the interaction between n-neighbours nuclear spins (nucleus-nucleus interaction), $\mathcal{H}_{n-e}$ is the interaction between the nuclear spins and the spin and orbital momenta of the electrons and $\mathcal{H}_{EFG}$ is the electric quadrupole interaction between the elettric quadrupole moment of non spherical nuclei and the Elettric Field Gradient resulting from the electron density $n(\mathbf{r})$ in the material. For a summary of the effects of the interactions on the NMR spectrum see Fig 2.3.

2.1.2.1 Nucleus-nucleus interaction

The nucleus-nucleus dipolar interaction is extremely important in solid-state NMR since very often it is the main contribute responsible for the line-width and thus for the length of the spin-spin relaxation time T_2. The $\mathcal{H}_{n-n}$ Hamiltonian describing the nucleus-nucleus interaction consists of two terms: the direct coupling and the indirect coupling ($\mathcal{H}_{n-n} = \mathcal{H}_{n-n}^{direct} + \mathcal{H}_{n-n}^{indirect}$). The $\mathcal{H}_{n-n}^{direct}$ term is due to the magnetic dipole coupling between the nuclei and is given by [137, 136]:

$$\mathcal{H}_{n-n}^{direct} = \sum_{j<k}^{N} \frac{\hbar^2\gamma^2}{r_{jk}^3} \left[\mathbf{I}^j \cdot \mathbf{I}^k - 3\frac{(\mathbf{I}^j \cdot \mathbf{r}_{jk})(\mathbf{I}^k \cdot \mathbf{r}_{jk})}{r_{jk}^2} \right] \ . \tag{2.7}$$

The sum is performed on couples of nuclei jk which are at a distance r_{jk}. The dipolar *n-n* interaction is the origin of the homogeneous broadening of the NMR lines. Without this term the lines would be similar to Dirac deltas, their width being only determined by the spontaneous emission term, which is exceedingly small for the NMR frequencies ($\Gamma \propto \omega^3$). The dipolar term is usually of the order of a few Gauss and is independent from the applied field (see Ref. [137] and [140]). This means that $\mathcal{H}_{n-n}^{direct}$ can be treated as a perturbation of the Zeeman Hamiltonian $\mathcal{H}_z$ and the energy correction explicitly calculated using the first order perturbation theory. In order to calculate explicitly the NMR line broadening in a solid the approximated Method of Moments is also commonly used [137].

The indirect coupling $\mathcal{H}_{n-n}^{indirect}$ between the nuclei is mediated by the electrons. The mechanism of the interaction is the following: a nuclear spin interacts with a surrounding electron via the hyperfine interaction then another nucleus interacts with the same electron leading to an indirect coupling between the two nuclear spins. Depending on the material being studied this indirect coupling can lead to a narrowing or a broadening of the resonance line.

2.1.2.2 Electron nucleus hyperfine interaction

The third term in equation 2.6, $\mathcal{H}_{n-e}$, indicates the electron nucleus hyperfine interaction, which is the coupling of the nuclear magnetic moment with the magnetic fields generated by the spin and orbital angular moments of the electrons. The $\mathcal{H}_{n-e}$ interaction results in an extra magnetic field at the nuclear site and correspondingly in a shifts of the NMR line with respect to the bare nucleus resonance frequency (often called Knight shift [141]). The Hamiltonian resulting from the Zeeman and hyperfine interactions thus takes the form:

$$\mathcal{H}_z + \mathcal{H}_{n-e} = -\gamma\hbar\mathbf{I}(\mathbf{H}_0 + \mathbf{H}_{el}) = -\gamma\hbar\mathbf{I}(\mathbf{H}_0 + A_{hyp}\langle\mathbf{S}\rangle) = -\gamma\hbar\mathbf{I}(1+\mathbf{K})\mathbf{H}_0\,, \quad (2.8)$$

where $\mathbf{H}_{el}$ is the local field due to the electrons, $\langle\mathbf{S}\rangle$ is the spin polarization, A_{hyp} is the hyperfine interaction tensor and $\mathbf{K}$ is the shift tensor. If $\mathbf{H}_0 \parallel \hat{z}$ the resonance frequency is shifted from the expected Larmor frequency of a bare nucleus $\omega_0 = \gamma H_0$ to an observed frequency $\omega_{obs} = (1 + K_z)\omega_0$, where K_z is the shift. The different contributions results in a Knight shift of the form:

$$K = K_{dia} + K_{orb} + K_s\,, \quad (2.9)$$

where K_{dia} is the diamagnetic contribute, K_{orb} is the orbital shift and K_s is the spin shift. The diamagnetic shift K_{dia} (shielding) is due to the diamagnetism created by current loops in closed inner electronic shells and to the Landau diamagnetism of the conduction electrons. Its magnitude is usually very small ($\Delta\omega/\omega \sim 10^{-5}$) and is observable only in in high resolution NMR of liquids. In the following we will always neglect K_{dia}. In this framework the hyperfine Hamiltonian is given by [136, 137]:

$$\mathcal{H}_{n-e} = \gamma_n\gamma_e\hbar^2\mathbf{I}\cdot\left[\overbrace{\left(3\frac{(\mathbf{S}\cdot\mathbf{r})\mathbf{r}}{r^5} - \frac{\mathbf{S}}{r^3}\right)}^{K_{dip}} + \overbrace{\frac{8\pi}{3}\mathbf{S}\delta(\mathbf{r})}^{K_{contact}} + \overbrace{\frac{\mathbf{L}}{r^3}}^{K_{orb}}\right]. \quad (2.10)$$

$\mathcal{H}_{n-e}$ represents the interaction between a nuclear spin $\mathbf{I}$ and the spin ($\mathbf{S}$) and the orbital momentum ($\mathbf{L}$) of an electron being at a distance $\mathbf{r}$ from the nucleus. The first two terms of the Hamiltonian are responsible for the spin shift ($K_s = K_{dip} + K_{contact}$) while the last one gives rise to the orbital shift K_{orb} (see Appendix A.4).

2.1.2.3 Electric Quadrupole Interaction

All the nuclei with $\mathbf{I} > 1/2$ are characterized by a non spherical nuclear charge distribution. These nuclei thus posses a electric quadrupole moment $eQ \neq 0$ while their electric dipole moment is zero. The quadrupole moment interacts with the electric field gradient (EFG) generated by the electronic charge distribution $n(\mathbf{r})$ surrounding the nucleus. In presence of an EFG

described by the tensor $V_{\alpha\beta}$ the quadrupole interaction Hamiltonian is given by:

$$\mathcal{H}_Q = \frac{1}{6}\sum_{\alpha,\beta} V^i_{\alpha,\beta} Q^i_{\alpha,\beta}\,, \quad \text{where} \quad V_{\alpha\beta} = \frac{\partial^2 V}{\partial x_\alpha \partial x_\beta}\,, \tag{2.11}$$

with V the electrostatic potential. It is always possible to find a coordinate system (X,Y,Z) in which $V_{\alpha,\beta}$ is diagonal. The principal axis Z is chosen to be the one along which the magnitude of the EFG is greater. Since V has to satisfy the Laplace's equation $\nabla^2 V = 0$ than the trace of the EFG is zero. In the principal axes reference frame the EFG is thus completely defined by two parameters: V_{ZZ} and the asymmetry η, where:

$$\eta = \frac{V_{XX} - V_{YY}}{V_{ZZ}} \geqslant 0\,. \tag{2.12}$$

Using the quantum mechanical operators for the angular momenta the quadrupolar Hamiltonian can be written as [137, 136, 142]:

$$\mathcal{H}_Q = \sum_i \mathcal{H}^i_Q = \sum_i \frac{e^2 q Q}{4I(2I-1)}\left[3I_Z^2 - I(I+1) + \frac{1}{2}\eta(I_+^2 - I_-^2)\right]\,, \tag{2.13}$$

where $eq = V_{ZZ} = \partial^2/\partial z^2$ and $I_\pm$ are raising/lowering operators $(I_\pm = I_X \pm iI_Y)$.

Now we will discuss the effect of $\mathcal{H}_Q$ on the nuclear magnetic energy levels in case of zero external magnetic field and in case of a strong external magnetic field.

No Magnetic Field If $H_0 = 0$ only the $\mathcal{H}_Q$ term is present and the Hamiltonian can be easily diagonalized using the eigenfunction of the I_z operator. The resulting $2I+1$ energy levels are given by (if $\eta = 0$) [136, 142]:

$$E_m = \frac{eQV_{ZZ}}{4I(2I-1)}[3m^2 - I(I+1)]\,, \tag{2.14}$$

where m are the usual I_z quantum numbers $(m = -I, -I+1, \ldots, I-1, I)$ and the magnetic dipole transition rules apply $(\Delta m = \pm 1)$. Resonant transitions between these energy levels can be induced by applying an alternating magnetic field (radio frequency) along the principal EFG axis. This type of experiment is called Nuclear Quadrupole Resonance (NQR). If $\eta = 0$ the quadrupolar frequency ν_Q is:

$$\nu_Q = \frac{3eV_{ZZ}Q}{2I(2I-1)h}\,. \tag{2.15}$$

If $I = 3/2$ (see Fig. 2.2), as is the case for the ^{75}As nucleus widely studied with NQR in iron based superconductors, ν_Q is given by:

$$\nu_Q = \frac{eQV_{ZZ}}{2h}\left(1 + \frac{\eta^2}{3}\right)^{1/2}\,. \tag{2.16}$$

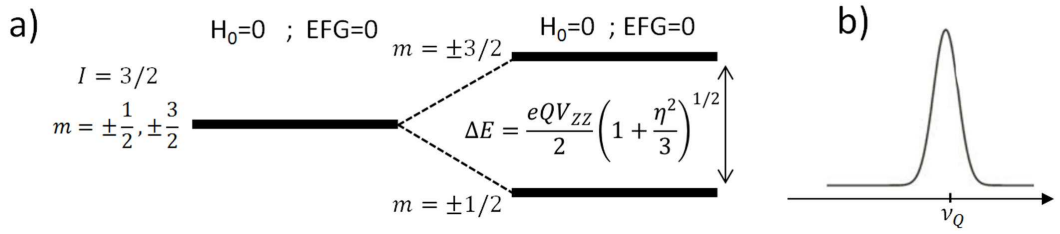

Figure 2.2: a) Sketch of the nuclear spin levels ($I = 3/2$) in presence of an EFG without any external magnetic field. b) The corresponding NQR line at frequency Δ/h.s

Strong magnetic field If the external magnetic field $\mathbf{H}_0$ is strong, as is typically the case for a NMR experiment, the strength of the quadrupolar interaction is usually much smaller than the Zeeman interaction ($\nu_Q \ll \nu_0$) and $\mathcal{H}_Q$ can be treated as perturbation of the Zeeman Hamiltonian $\mathcal{H}_z$. At the first order the energy correction for the m-th level is given by [137, 142]:

$$E_m^{(1)} = \frac{eQV_{zz}}{4I(2I-1)}[3m^2 - I(I+1)]\,, \tag{2.17}$$

where V_{zz} is the component of the EFG parallel to the direction of the applied magnetic field. This results in a splitting of the NMR resonance line into $2I$ resonance lines, where adjacent lines are separated by a frequency proportional to ν_Q. The shifted NMR spectrum resulting from the quadrupolar interaction, at he first order, can be written as [137, 143]:

$$\Delta\nu^{(1)}_{m\to m-1} = -\frac{\nu_Q}{2}\left(3\cos^2\theta - 1 + \eta\sin^2\theta\cos 2\phi\right)\left(m - \frac{1}{2}\right)\,, \tag{2.18}$$

where θ is the angle between the magnetic field and the principal Z-axis of the EFG, while ϕ is the angle between the projection of the magnetic field on the XY plane and the X-axis of the EFG. It can be noted that at the first correction to the central $-1/2 \to +1/2$ transition frequency is zero. The second order correction is proportional to ν_Q^2 and is different from zero only for the central $(+1/2 \to -1/2)$ line. If the EFG has a cylindrical symmetry ($\eta = 0$), as is the case for all the samples studied in this thesis, the second order correction is given by:

$$\nu^{(2)}_{+\frac{1}{2}\to-\frac{1}{2}} = -\frac{-\nu^2}{16\nu_L}\left(I(I+1) - \frac{3}{4}\right)(1-\cos^2\theta)(9\cos^2\theta - 1)\,. \tag{2.19}$$

In case of a large η additional ϕ and η dependent factors must be inserted in Eq. 2.19 (see e.g. [143]).

2.1.3 Classical approach

The classical treatment of nuclear spins is still widely used by the NMR community since it offers a very intuitive way to describe the evolution of the

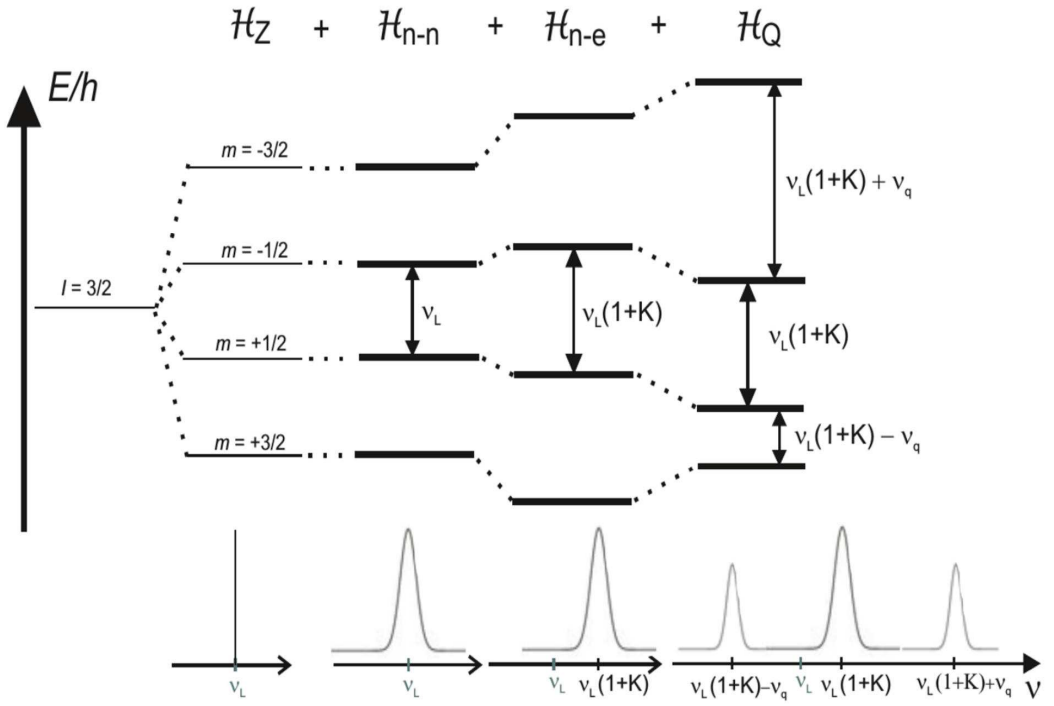

Figure 2.3: The nuclear levels evolution in presence of the various interactions and the resulting NMR spectra for a $I = 3/2$ system. In absence of magnetic field the nuclear levels are degenerate. When a static field is applied, the Zeeman interaction removes the degeneracy, and gives rise to equispaced levels. The application of the dipolar nucleus-nucles interaction $\mathcal{H}_{n-n}$ results in a line broadening, while the electron-nucleus hyperfine interaction shifts the line. Finally the quadrupolar interaction generates three different lines correcting the level spacing so that now three transitions with different energy are possible. Figure adapted from [143].

magnetization during an NMR experiment. Furthermore for non interacting and weakly interacting spins the classical approach gives the same results of the correct quantum mechanical treatment [136]. This approach has been introduced and extensively used by Bloch [144] who found the set of phenomenological equations (the Bloch equations) describing the temporal evolution of the longitudinal and transverse components of nuclear magnetization.

For simplicity we will start by considering a single free spin. The angular momentum of the system will be $\mathbf{L} = \mathbf{I}\hbar$ and thus its magnetic moment is $\boldsymbol{\mu} = \gamma(\mathbf{I}\hbar)$ where γ is a constant called *gyromagnetic ratio*. Now we turn on a static magnetic field $H_0 \parallel \hat{z}$. The magnetic moment $\boldsymbol{\mu}$ will experience a torque $\mathbf{N} = \boldsymbol{\mu} \times \mathbf{H}_0$ in agreement with the laws of electromagnetism. Using the second cardinal equation of dynamics,

$$\frac{d\mathbf{L}}{dt} = \mathbf{N}\,, \quad \text{one obtains that:} \quad \frac{d\boldsymbol{\mu}}{dt} = \gamma\boldsymbol{\mu} \times \mathbf{H}_0\,. \tag{2.20}$$

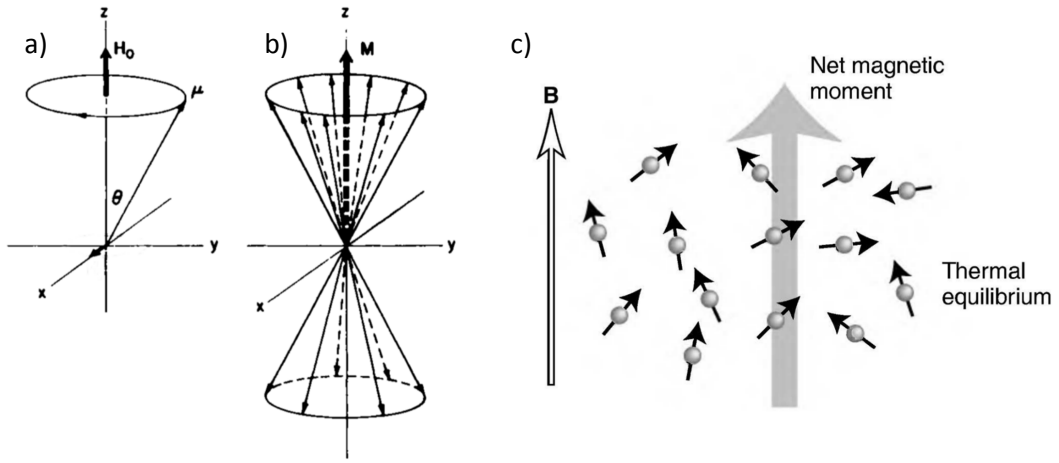

Figure 2.4: (a) Precession of a magnetic moment μ about a fixed magnetic field $\mathbf{H}_0$. (b) Precession of an ensemble of identical magnetic moments of nuclei with $I = 1/2$. (c) The net macroscopic magnetization is oriented along the direction of the field $\mathbf{H}_0 \parallel z$. Figure adapted from [145] and [146].

Equation 2.20 describes a clockwise precession of frequency $\omega_0 = -\gamma \mathbf{H}_0$. Now we will consider a system of several magnetic moments $\boldsymbol{\mu}_i$. The macroscopic magnetization $\mathbf{M}$ of N spins is $\mathbf{M} = \sum_i \boldsymbol{\mu}_i$, and thus the evolution of the magnetization can be written as:

$$\frac{d\mathbf{M}}{dt} = \frac{\sum_i d\boldsymbol{\mu}_i}{dt} = \gamma \sum_i \boldsymbol{\mu}_i \times \mathbf{H}_0 = \gamma \mathbf{M} \times \mathbf{H}_0 \,, \tag{2.21}$$

This means that a single magnetic moment has the same behavior of the macroscopic magnetization of a system of non-interacting spins (see Fig. 2.4).

However the nuclear spins in a solid are not an ensemble of non-interacting spins. When the static magnetic field $\mathbf{H}_0$ is turned on the spins orient themselves preferably in the direction of the field in order to minimize the magnetic energy $U = -\boldsymbol{\mu} \cdot \mathbf{H}$, thus giving rise to the equilibrium magnetization $\mathbf{M}_0 = \chi_0 \mathbf{H}_0$, where χ_0 is the susceptibility describing the response of the system. The presence of the magnetization is due to the interaction of the spins with the thermal bath. In fact the interactions of the nuclear spins with the quasi-particle excitation of the lattice and of the electrons system (phonons, magnons etc) allow the transitions between the nuclear Zeeman levels. The occupancy of the levels is described by a Boltzmann distribution and at finite temperature there are obviously more nuclei in the lower energy state, which is the one in whose their spin is oriented along the external field direction ($\mathbf{H}_0 \parallel z$ by convention). Accordingly a macroscopic magnetization arise along z.

From Eq. 2.21 it is clear that if $\mathbf{M} \parallel z$ than $d\mathbf{M}/dt = 0$, while if $\mathbf{M}$ is not parallel to $\mathbf{H}_0$ (e.g. $\mathbf{M} \parallel x$) than $\mathbf{M}$ would in principle precess forever. However

the interactions with the thermal bath will obviously prevent this and the magnetization will always return parallel to the equilibrium direction z after a finite time. Furthermore we have to consider that, in a real systems, each spin will interact with the local magnetic field which will be slight different from site to site due to the inhomogeneity of the external applied field, to the distribution of internal fields resulting from the dipole nucleus-nucleus interaction $\mathcal{H}_{n-n}$ and to other process (see section 2.1.5). This will result in the dephasing of the precessing spins and thus in the decay of the magnetization in the xy plane ($\mathbf{M}_{xy}$).

To take these considerations into account Bloch [144] proposed to treat the relaxation towards $\mathbf{M} \parallel z$ and in the xy plane as first order processes with characteristic relaxation times respectively T_1 and T_2. The resulting Bloch equations are[1]:

$$\frac{d\mathbf{M}_z}{dt} = \gamma(\mathbf{M} \times \mathbf{H}_0)_z + \frac{M_0 - M_z}{T_1} , \tag{2.22}$$

$$\frac{d\mathbf{M}_{x,y}}{dt} = \gamma(\mathbf{M} \times \mathbf{H}_0)_{x,y} - \frac{M_{x,y}}{T_2} . \tag{2.23}$$

It must be noted that $\mathbf{M}$ is not a rigid vector whose modulus remains the same at any time (which would require $T_1 = T_2$) and there is often a substantial difference between the two relaxation times. However it must be noted that T_1 and T_2 are not completely uncorrelated quantities, in fact it can be shown that [136, 137] $2T_1 \geqslant T_2$.

T_1 is called spin-lattice relaxation time and is responsible for the relaxation due to energy transfer from the spin system to the thermal reservoir (the lattice). The decay of $\mathbf{M}_{xy}$ instead is governed by the T_2 spin-spin relaxation time. Differently from spin-lattice relaxation the T_2 spin-spin relaxation does not involve an exchange of energy between the spin system and the lattice. For this reason T_2 is sometimes called dephasing, or decoherence time.

2.1.4 Fourier Transform NMR and the Free Induction Decay (FID) experiment

Now we will briefly describe how a very basic Fourier Transform NMR (pulsed NMR) experiment is carried out. The sample is put inside a coil and immersed in a strong static magnetic field $\mathbf{H}_0$ with the axis of the coil perpendicular to the field (Fig. 2.5b). A series of radiofrequency pulses is then sent to the coil. Due to magnetic induction a variable magnetic field $2H_1 \cos\omega t\, \hat{x}$ develops inside the coil during a rf pulse. The rf frequency is chosen equal to the Larmor frequency. The linear variable magnetic field can be written as the sum of two counter rotating magnetic fields [147]. In the rotating frame the field component rotating clockwise will be stationary

[1] A more prcise and complete treatment of the Bloch equations can be found in Ref. [137][136]

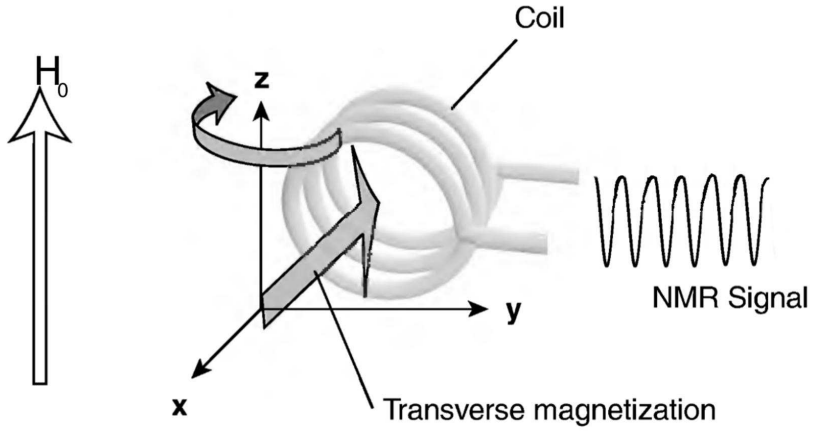

Figure 2.5: Simplified sketch of a NMR experiment. Figure adapted from [146].

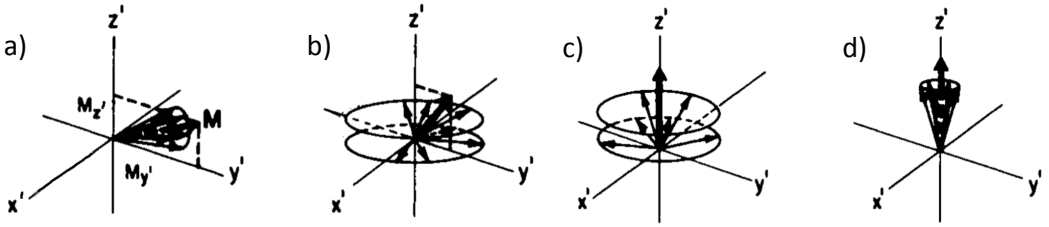

Figure 2.6: Sketch of the relaxation process described in the text. (a) Tipping of the nuclear moments and thus of the magnetization. (b) Dephasing of the nuclear moments through spin-spin relaxation. (c) $\mathbf{M}_{xy}$ has now vanished. (d) Re-establishment of $\mathbf{M}_z$ at its equilibrium value $\mathbf{M}_0$. Figure adapted from [145].

while the other component will rotate with a frequency 2ω and thus it will have no effect on the magnetization (see Section A.1).

If we choose H_1 small enough (usually < 1, mG see Eq.A.9) the magnetization will not precess around $\mathbf{H}_1 \parallel x$ as we expect for a system of free spins but instead it will form a constant angle θ with $\mathbf{H}_0$. This is due to the presence of spin-lattice relaxation processes that will strive to bring the magnetization back along z. This condition is used for continuous wave (CW) NMR experiments. In these experiment the radiofrequency irradiation is continuous. By detecting the radio-frequency response induced by the rotating M_{xy} component in a detection coil orthogonal to the irradiation coil and by sweeping the irradiation frequency or the magnetic field it is possible to directly measure the susceptibility $\chi(\omega)$. While the first NMR experiments were carried out using the CW method nowadays CW NMR has been nearly completely supplanted by the Fourier Transform (FT) NMR method which allows much faster experiments and has much higher signal to noise ratio.

In a pulsed FT-NMR experiment H_1 is chosen big enough so that Eq A.9 is not satisfied and thus $\mathbf{M}$ will precess around $\hat{x}$ as described in section A.1. If the radiofrequency is applied for time interval τ, usually in the μs range, the magnetization will be rotated by an angle $\theta = -\gamma H_1 \tau$ (see Eq. A.4).

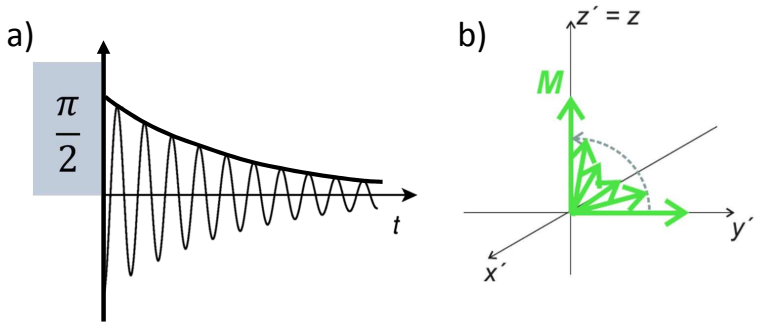

Figure 2.7: a) RF pulse and the time evolution of the FID signal. Panels b) show the relaxation of the nuclear magnetization M back to its equilibrium value $M_z = M_0$ after being disturbed by a 90° pulse (rotating frame). b) is adapted from [143]. See also Ref. [148].

Free Induction Decay (FID) The simplest type of FT-NMR experiment is the Free Induction Decay (FID) experiment. In order to carry out this measurement a single rf pulse is sent to the coil and its length τ is chosen so that $\theta = -\gamma H_1 \tau = \pi/2$. (see Eq. A.4). In this condition the rf pulse rotates the magnetization $\mathbf{M}$ of 90° around x and thus at the end of the pulse $\mathbf{M} \parallel y$. From Eq. 2.22 and 2.23 (the Bloch equations) follows that, if $\mathbf{M} \perp \mathbf{H}_0$ at $t = 0$, the magnetization will spiral out of the xy plane and return to be parallel to z (Fig. 2.6, Fig 2.7b). The evolution of $\mathbf{M}_z(t)$ will be an exponential recovery:

$$\mathbf{M}_z(t) = \mathbf{M}_0 \left[1 - \exp\left(\frac{-t}{T_1}\right)\right] \ . \tag{2.24}$$

Together with the reforming of the magnetization along z one also observes a suppression of the $\mathbf{M}_{xy}$ component due to the dephasing of the precessing spins. $\mathbf{M}_{x,y}$ will decay also in absence of spin lattice relaxation processes. In fact every nucleus will sense a slightly different magnetic field $\mathbf{H}_0 + \mathbf{H}_{loc}$ and thus precess at a different frequency $\omega = -\gamma(\mathbf{H}_0 + \mathbf{H}_{loc})$. The difference in frequency will result in a $\Delta\omega t$ phase difference between nuclear spins after a time t. The different $\mathbf{H}_{loc}$ is due to the inhomogeneities of the external magnetic field and by the local fields generated by electronic spins and by the neighboring nuclear spins. As time passes the spins orientations become completely random and $\mathbf{M}_{x,y} = 0$ goes to zero. Since the decay is exponential, as can be easily inferred from Eq. 2.23, the time evolution of the modulus of the transverse magnetization component is given by:

$$M_{x,y}(t) = M_0 \exp\left(\frac{-t}{T_2^*}\right) \ . \tag{2.25}$$

Since the coil is along x the rotating $\mathbf{M}_{xy}$ component of the magnetization will generate in the solenoid, through magnetic induction, an exponentially decaying voltage oscillating at the Larmor frequency (FID signal, see Fig. 2.7). A sketch of the process described here can be seen in Fig 2.7.

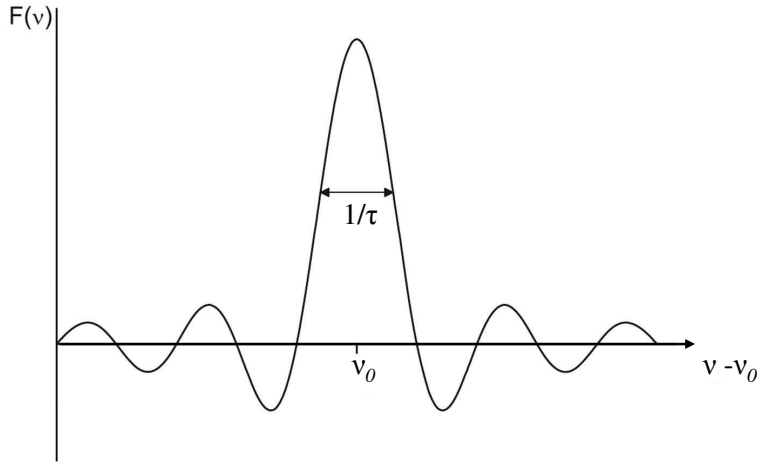

Figure 2.8: Fourier transform of a rf pulse with frequency ν_0. Figure adapted from Ref. [143].

The FID signal is modulated in accordance with the slightly different Larmor frequencies of the nuclear spins, originating from the local inhomogeneities of the external magnetic field, by the direct and indirect nucleus-nucleus interaction and possibly by the intrinsic distribution of local magnetic fields in the sample (for example in presence of magnetic impurities). In fact the squared rf pulse at the Larmor frequency that we are using to irradiate the sample contains not only ν_0 but the whole frequency range centered at ν_0 and with width $\Delta\nu_{irr} \sim 1/\tau$ where τ is the length of the pulse. In fact the Fourier transform of a squared pulse is given by [149]:

$$F(\nu) = \frac{\sin[\pi(\nu - \nu_0)\tau]}{\pi(\nu - \nu_0)\tau} \tag{2.26}$$

whose FWHM is $\sim 1/\tau$ (see Fig. 2.8). Thus if the length of the pulse is short enough and the NMR spectrum is narrower than $\Delta\nu_{irr}$ it is possible to irradiate the whole NMR spectrum and to evaluate the response function $\chi(\omega) = \chi'(\omega) + i\chi''(\omega)$ by calculating the Fourier transform of the FID signal. The largest obtainable $\Delta\nu_{irr}$ in realistic situations is around 100 kHz.

2.1.5 Spin-spin relaxation time T_2

The T_2 relaxation time measure the transverse nuclear magnetization decay in the xy plane. Several different processes are at the origin of the decay and can be divided in extrinsic and intrinsic mechanisms.

The extrinsic mechanisms are those creating a static inhomogeneous distribution of resonance frequencies, such as the inhomogeneity of the static external magnetic field or the presence of magnetic impurities giving rise to a distribution of frequency shifts. These effects results in a dephasing of the precessing spins.

The intrinsic processes instead are due to the interactions of the nuclear spins with the the magnetic moments of the other nuclei and to local magnetic field fluctuations. The combined relaxation time due to all these contributions is usually called T_2^*:

$$\frac{1}{T_2^*} = \overbrace{\frac{1}{T_2^{dip}} + \frac{1}{T_2^{indirect}} + \underbrace{\frac{1}{T_2^{Redfield}}}_{\propto 1/T_1}}^{\text{intrinsic}} + \overbrace{\frac{1}{T_2^{inhomog}}}^{\text{extrinsic}}, \tag{2.27}$$

where $1/T_2^{dip}$ and $1/T_2^{indirect}$ are respectively the dipolar and indirect components of the coupling between nuclear spins (see Sec. 2.1.2.1), $1/T_2^{Redfield}$ is a term taking into account the effect of longitudinal field fluctuations (the Redfield contribute [150] depends on T_1) and $1/T_2^{inhomog}$ is the decay due to the distribution of local magnetic fields. The spin-spin relaxation rate is usually defined as the sum of the first three components (the intrinsic ones). The magnitude of the extrinsic $1/T_2^{inhomog}$ component in fact depend on the type of magnet used for the experiment and not only on the studied sample.

When $T_2^{inhomog}$ is very short, for example in presence of magnetic impurities, it is quite difficult to measure T_2 since the extrinsic component will dominate the decay of the FID signal. This problem is solved by using echo techniques. The famous Hahn echo will be discussed in the following section while a brief description of the CPMG method can be found in Appendix A.

In solids an ubiquitous mechanism responsible for the T_2 decay is the dipolar nucleus-nucleus interaction. In fact, if a nucleus is at distance r from its nearest neighbor, it will experience a local field $H_{loc} \sim \mu_N/r^3 \sim 1$ G ($r = 2$ Å, $\mu_N = 10^{-3}\mu_B$) which can be either parallel or anti-parallel to $\mathbf{H}_0$. Thus the two nuclei will precess at different frequencies with $\Delta\omega \sim \gamma H_{loc}$. Since there are many nuclei, each with n neighbors, this will results in large accumulated phases. A rough estimation of T_2 is given by [136]: $T_2 \sim \frac{1}{\gamma \mathbf{H}_{loc}} = \frac{r^3}{\gamma^2 \hbar}$.

2.1.5.1 Hahn Spin Echo

In solids strong local magnetic fields due to the hyperfine interaction or to magnetic impurities are often present. Furthermore the external field inhomogeneity is an always present problem for NMR, even with the new superconducting magnets which have very high field homogeneity ($\delta H < 1$ ppm/cm^2). Sometimes in solids containing magnetic impurities or with strong hyperfine fields the FID signal decay is so fast that it can barely be measured.

In order to overcome this problem Hahn [151] invented a very clever pulse sequence. First a $\pi/2$ pulse is applied along the x-axis, flipping the magnetization from its equilibrium position ($\mathbf{M} \parallel z$) into the xy plane. Due

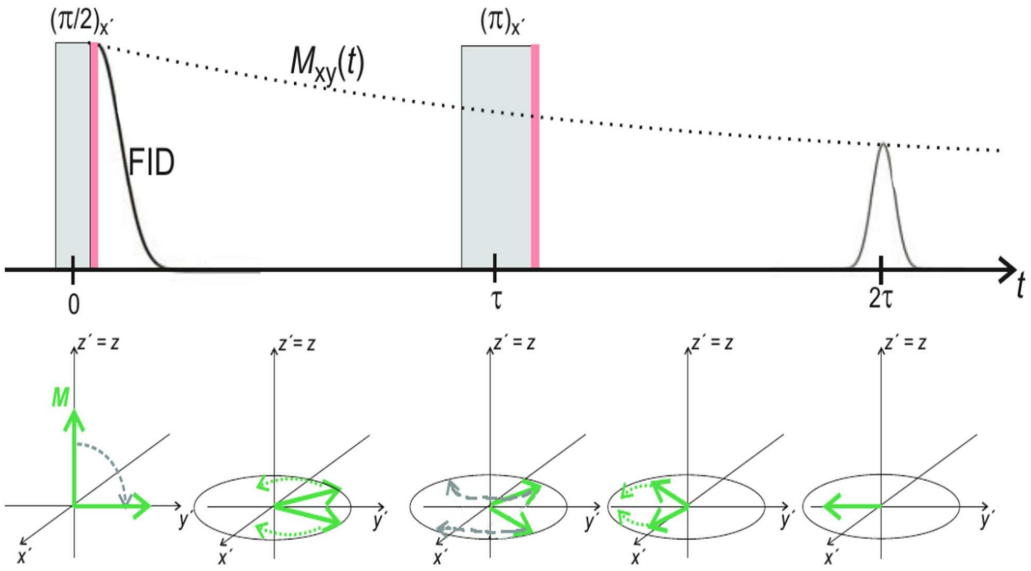

Figure 2.9: Hahn echo sequence and the correspondent evolution of the magnetization in the rotating frame. The signal at 2τ is shown to be positive. This is true only if π pulse is applied along $+y$. Figure adapted from [143].

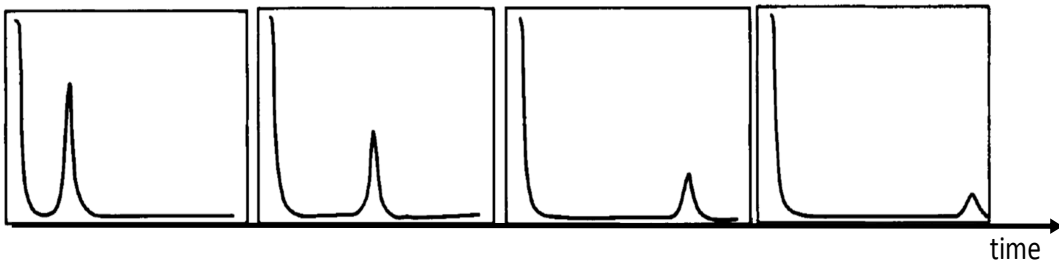

Figure 2.10: The result of a series of Hahn echoes with different values of τ. Figure adapted from [145].

to spin-spin interactions and local field inhomogeneities the individual moments rotate with different speeds within the plane and thus begin to dephase. Since a distribution of static magnetic fields is present each spin will probe a magnetic field which is either slightly larger than the nominal one, thus precessing a little bit faster and rotating clockwise in the rotating frame, or slightly smaller, thus rotating anticlockwise. After waiting for a time τ a π impulse is applied to the system, again along x. This pulse flips the components of the transverse magnetization within the xy plane, such that they will refocus at the time 2τ and give rise to the so-called spin echo. The echo generated in this way will have an intensity related to the magnitude of $M_{xy}(2\tau)$ without the influence of the local fields inhomogeneities which have been wiped out by the refocusing. At this point in order to retrieve the value of T_2 one can simply repeat the Hahn echo sequence for different values of τ (see

Fig. 2.10) and than fit the magnitude of the echoes (the maximum height, or the area under the peak) with an exponential decay law:

$$M_{x,y}(2\tau) = M_0 \exp\left(-\frac{2\tau}{T_2}\right) . \tag{2.28}$$

A better fit can sometimes be obtained separating the spin-spin relaxation rate component due to the nucleus-nucleus interaction (this component of the relaxation rate is usually indicated with $1/T_{2G}$ in cuprates and IBS, where the spin exchange is quenched [152]) from the one due to the Redfield component originating from the spin lattice relaxation ($1/T_2^{Redfield} \sim 1/2T_1$ [153, 154]). The decay term governed by $1/T_{2G}$ can be shown to be Gaussian and the total transverse magnetization decay is thus given by [155, 143]:

$$M_{x,y}(2\tau) = M_0 \exp\left(-\frac{2\tau}{T_2^{Redfield}} - \frac{(2\tau)^2}{T_{2G}^2}\right) . \tag{2.29}$$

2.1.6 Spin lattice relaxation time T_1

The spin-lattice relaxation time T_1 is the mean time of the M_z recovery. The spin-lattice relaxation is caused by the energy exchange between the spin system and the lattice.

The relaxation process is due to magnetic and EFG fluctuations (for the quadrupolar nuclei). The magnetic fluctuations arise from nuclear spin-spin interactions, electronic spin fluctuations and from interactions with the conduction electrons while the EFG fluctuations are due to phonons and charge fluctuations. Measuring T_1 thus yields useful informations about these dynamics. It can be shown (see Appendix A.5) that for purely magnetic fluctuations the spin lattice relaxation rate takes the form:

$$\frac{1}{T_1} = \frac{\gamma^2 k_B T}{2\hbar\omega_0 N} \sum_{\mathbf{q}\in BZ} |\mathbf{A}_q|^2 \chi''(\mathbf{q}, \omega_0) , \tag{2.30}$$

where χ'' is the imaginary part of the spin susceptibility. For a good metal (3D Fermi gas), $1/T_1$ is mainly determined by the the contact interaction of the nucleus with the conduction electrons [156]. From Eq. 2.30 can be obtained that the spin lattice relaxation rate is given by (Korringa relation [157]):

$$\frac{1}{T_1} = \left(\frac{16}{3}\right)^2 \pi^3 \hbar^2 \gamma^2 \mu_B^2 (\mid \psi(0) \mid^2)_{FS} D^2(E_F) k_B T \tag{2.31}$$

Hence T_1^{-1} is proportional to the temperature and to the square of the density of state at the Fermi energy $D^2(E_F)$. Also the relation $K^2 T_1 T = const$ holds since the shift is proportional to the contact interaction.

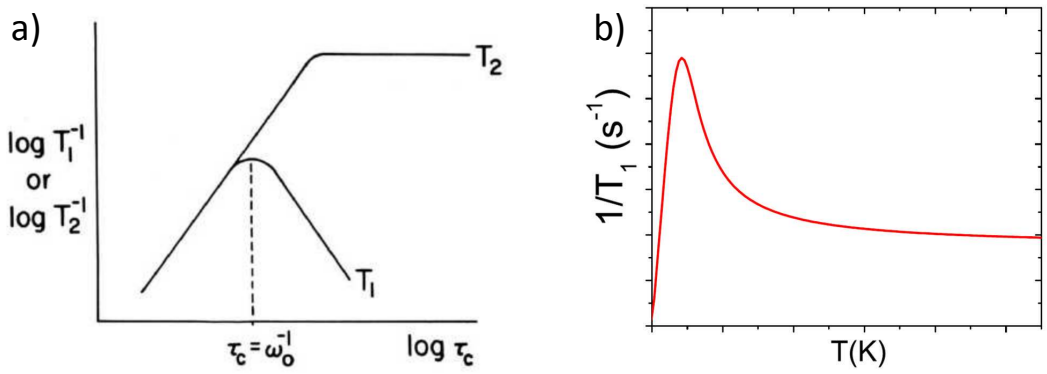

Figure 2.11: a) Dependence of the relaxation rates $1/T_1$ and $1/T_2$ on the correlation time τ_c. Figure adapted from [136]. b) Sketch of the temperature dependence of the spin lattice relaxation rate $1/T_1$ in the framework of the BPP theory and in presence of an activated τ_c.

2.1.6.1 The Bloembergen-Purcell-Pound theory

In 1947 Bloembergen, Purcell, and Pound [158, 136] proposed a theory (usually referred to as BPP theory in their honour) to explain the relaxation rate observed in liquid compounds, where the presence random motions influences the spin-lattice relaxation. However the results of the BPP theory are much more general and can also be used to describe the effect of spin fluctuations in magnetic materials.

It can be shown [136] that when the fluctuating field $\mathbf{h}(t)$ takes on either of two values $\pm h_0$ and the fluctuations from one value to the other occurs at a rate that is independent from the time elapsed since the previous transition, the correlation function takes the form:

$$\langle h_+(t)h_-\alpha(0)\rangle = \langle \Delta h_\perp^2\rangle e^{-t/\tau_c} \,, \tag{2.32}$$

This correlation function can basically describe any fluctuating local magnetic field. From Eq. 2.30, $1/T_1$ is thus given by:

$$\frac{1}{T_1} = \frac{\gamma^2}{2}\langle \Delta h_\perp^2\rangle \frac{2\tau_c(T)}{1+\omega_0^2\tau_c^2(T)} \,, \tag{2.33}$$

It is possible to identify three different dynamic regimes:

Slow motion regime: $\omega_0\tau_c \gg 1$, equation 2.33 becomes:

$$\frac{1}{T_1} = \gamma^2\langle \Delta h_\perp^2\rangle \frac{1}{\tau_c} \,. \tag{2.34}$$

Fast motions regime: $\omega_0\tau_c \ll 1$, the denominator of Eq. 2.33 is ~ 1 and $1/T_1$ becomes:

$$\frac{1}{T_1} = \gamma^2\langle \Delta h_\perp^2\rangle \tau_c \,. \tag{2.35}$$

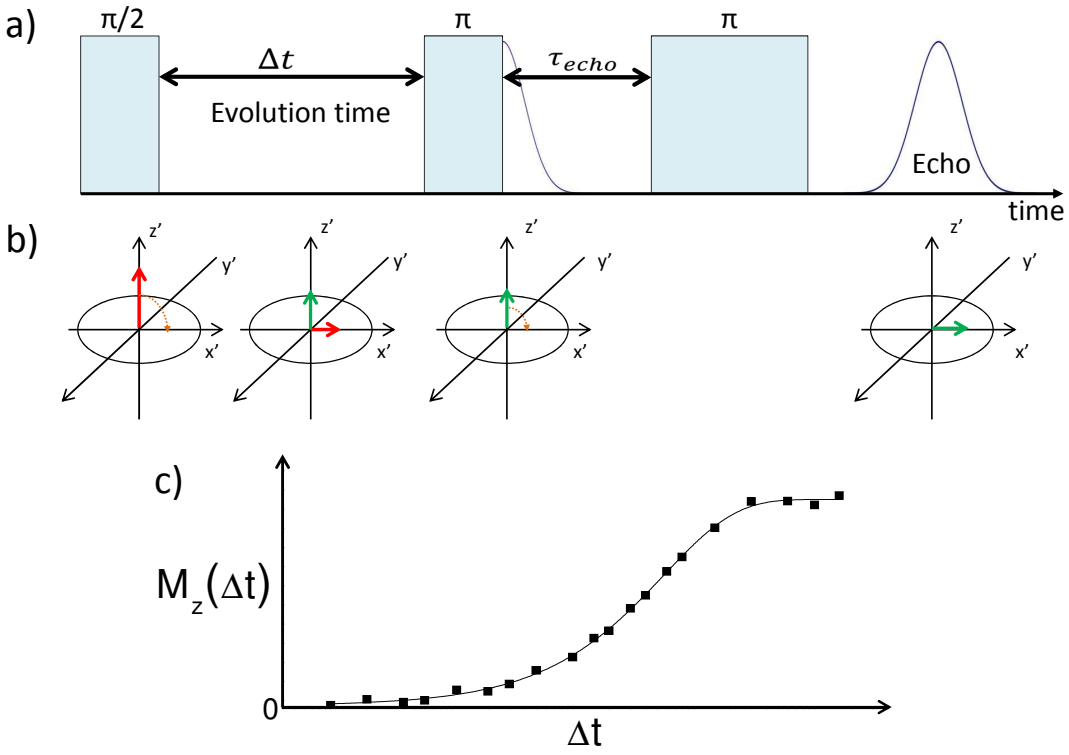

Figure 2.12: a) Sketch of the saturation recovery pulse sequence. b) evolution of the magnetization during the sequence. c) dependence of intensity of the measured echo Δt from the length Δt of the free evolution time.

BPP peak regime $\omega_0\tau_c = 1$, the function shows a maximum when the characteristic frequency of the fluctuations (τ_c^{-1}) matches the Larmor frequency.

The effective correlation time τ_c often shows an activated temperature dependence :

$$\tau_c = \tau_0 \exp(E_a/k_B T) \ . \tag{2.36}$$

where E_a is the activation energy of the fluctuations and τ_0 is the correlation time at high temperatures. A sketch of the $1/T_1$ temperature evolution obtained in this case is shown in Fig. 2.11b.

2.1.6.2 Measuring $1/T_1$

The two most common pulse sequence used in order to measure T_1 are the inversion recovery and the saturation recovery sequences. Regardless of their peculiar characteristics all the T_1 sequence have the same building blocks:

1) The preparation phase of the magnetization.

2) The free evolution of the magnetization for a variable time

3) The detection.

The detection step usually is a simple FID or a Spin Echo sequence. What really differentiates the sequences is the first step, the preparation of the magnetization. Here we will describe the saturation recovery sequence, which is the sequence used for all the $1/T_1$ measurements reported in the following chapters.

The preparation step of this sequence consist in a simple $\pi/2$ pulse along the x axis that will tip the magnetization in the xy-plane. After the pulse the magnetization will be left free to evolve under the influence of the spin-lattice interactions for a time interval Δt. The T_1 relaxation process causes a partial (or total, depending the duration of Δt) recovery of the magnetization along z. To detect this $M_z(\Delta t)$ component a second $\pi/2$ pulse is applied again along x, in order to turn $M_z(\Delta t)$ back into the plane. At this point a π pulse is applied along y and after an other short wait time τ_{echo} an Hahn echo arise, whose magnitude will be proportional to $M_z(\Delta t)$. Repeating this sequence for various durations of Δt the T_1 recovery curve can be reconstructed. The sequence is called saturation recovery because the first $\pi/2$ pulse is strong enough to make the population of the levels equal, a situation called saturation. Since the two levels have the same population after the pulse the magnetization along z will be zero. A sketch of the saturation recovery sequence is presented in Fig 2.12.

The shape of the magnetization recovery curve depends on the considered transition and on the nature of the dynamics responsible for the relaxation [160]. For example in the case of a spin 1/2 nucleus only the $+\frac{1}{2} \rightarrow -\frac{1}{2}$ transition is possible and since the quadrupolar moment of spin 1/2 nuclei is always zero only the magnetic fluctuations will contribute to T_1, giving rise to a simple exponential magnetization recovery law:

$$\mathbf{M}_z(t) = \mathbf{M}_0 \left(1 - \exp\left(\frac{-t}{T_1}\right)\right) . \tag{2.37}$$

Conversely for the common case of a spin 3/2 (e.g. ^{75}As) nucleus, if the quadrupolar coupling is significant, as is always the case in the iron based superconductors, the spin lattice relaxation rates for the $+\frac{1}{2} \rightarrow -\frac{1}{2}$ and the $\pm\frac{3}{2} \rightarrow - \pm \frac{1}{2}$ transitions can be measured separately. For the central line ($+\frac{1}{2} \rightarrow -\frac{1}{2}$) it can be shown that, if only magnetic fluctuations are present, the recovery law takes the form [160]:

$$M_z(t) = M - 0[1 - f(0.1 \cdot e^{-(\tau/T_1)} + 0.9 \cdot e^{-(6\tau/T_1)})] . \tag{2.38}$$

2.2 NMR studies on Iron Based Superconductors

In this section we present a tiny review of some important NMR results obtained on Iron based superconductors. Since the literature is quite exterminate we will focuses on the 1111 and 122 families and on the results which are particularly relevant for the experimental part of this thesis. Complete reviews can be found for example in Ref. [48] and [162].

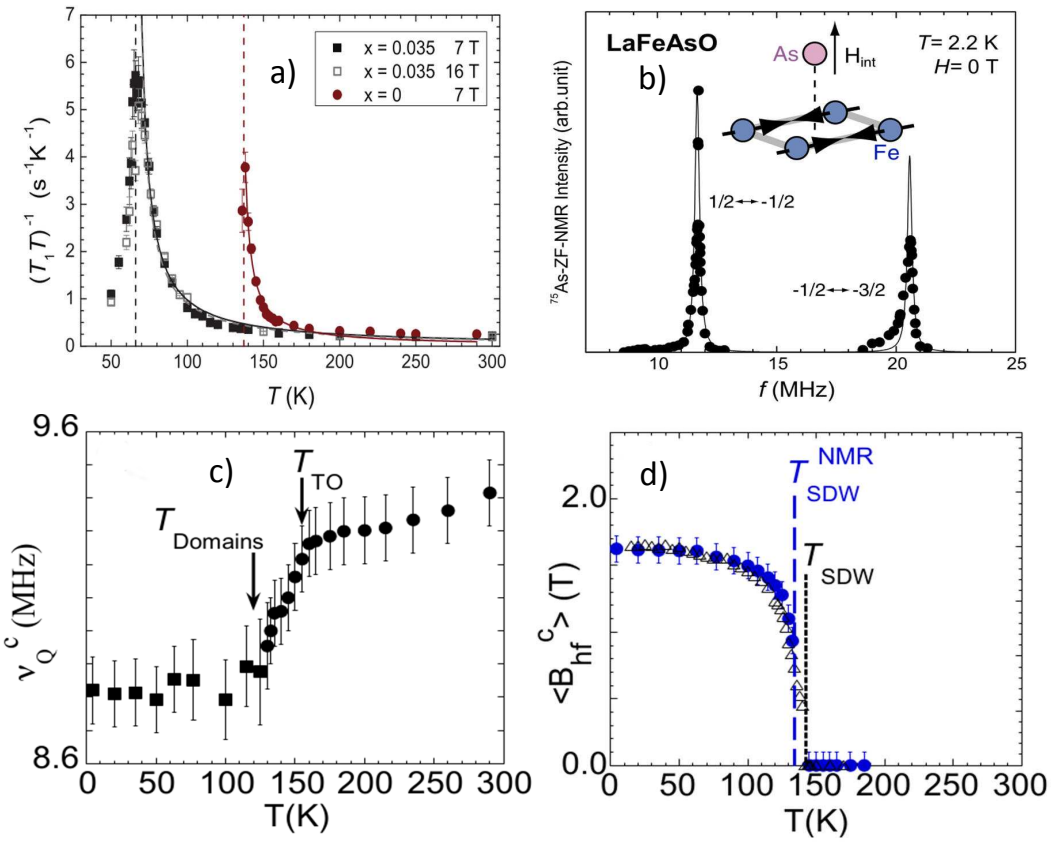

Figure 2.13: a) ^{75}As $(T_1T)^{-1}$ Temperature dependence in undoped (red) and underdoped (black) $LaFeAsO_{1-x}F_x$. The solid lines are fits to a Curie Weiss function. (Adapted from Ref. [161]) b) ^{75}As Zero Field NMR spectrum of polycrystalline LaFeAsO measured well below T_m (2.2 K). c) Temperature evolution of the ^{75}As NQR frequency (ν_Q) of single crystal LaFeAsO (Adapted from Ref. [68]). d) The corresponding evolution of the internal field on the As site (blue dot). Black triangles: magnetic Bragg scattering intensity normalized for T = 4.2 K. Adapted from Ref. [108].

2.2.1 1111 family

In undoped and underdoped $LaFeAsO_{1-x}F_x$ compounds a magnetic transition towards an antiferromagnetic stripe type ordered state takes place around 140 K (T_m). The transition can be clearly seen in the temperature evolution of ^{75}As and ^{139}La $1/T_1$ which diverge at T_m. In the case of ^{139}La the $1/T_1$ temperature behaviour can be fitted with the Moriya SCR [164] theory for spin fluctuations in a 3D itinerant antiferromagnet [165] ($(T_1T)^{-1} \propto 1/\sqrt{T-T_m}$) while for ^{75}As a simple Curie Weiss law can be used ($(T_1T)^{-1} \propto 1/T-T_m$, see Fig. 2.13a).

The magnetic order can be directly probed by measuring the ^{75}As Zero Field NMR (ZF-NMR). In fact the internal field generated by the magnetic order on the As site depends on which type of ordering is present and it

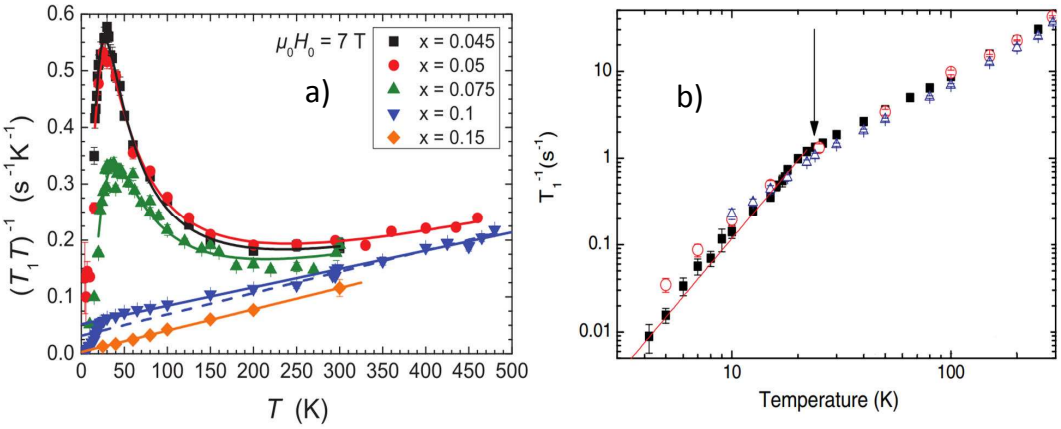

Figure 2.14: a) Temperature dependence of $(T_1T)^{-1}$ in F doped La1111 for different values of doping. b) Low temperature ^{75}As T^{-1} in optimally F doped LaFeAsO (x = 0.1). The solid red line is a fit to $1/T_1 \sim T^3$. The measurements where carried out on the two horns (blue: 41.8°; black: 90°) and at the centre (red) of the central line powder spectrum. Adapted from Ref. [163].

is given by $\mathbf{H}_{int} = \sum_i \mathbf{A}_i \mathbf{m}_i$, where $\mathbf{A}_i$ are the components of the hyperfine tensor and $\mathbf{m}_i$ the moments of the four neighbouring Fe atoms. The stripe order, differently from other types of magnetic orders, gives rise to a strong magnetic field at the As site ($\mathbf{H}_{int} \sim 1.6$ T), oriented along c and whose direction change sign from one site to the neighbouring one. The resulting ZF-NMR spectrum was first measured by Mukuda *et al.* [68] and is reported in Fig. 2.13b. The two observed lines are simply the central ($\frac{1}{2} \rightarrow -\frac{1}{2}$) and upper satellite (-$\frac{1}{2} \rightarrow -\frac{3}{2}$) lines for a NMR experiment in a $\sim$ 1.6 T magnetic field. The lower satellite is instead very difficult to measure since it lies at very low frequency (< 2 MHz) and a special NMR set up is needed. It must be remarked that no other type of magnetic order is consistent with this spectrum.

The magnetic state can also be studied with an external applied field. In this case, however, difficult to grow single crystals samples are preferable since the strong internal field gives rise to a very wide (> 20 MHz) powder spectrum which partially overlaps with that of ^{139}La. Fu *et al.* [108] measured the field swept spectrum NMR spectrum ($H_0 \parallel c$ = 8 T) of very high quality LaFeAsO single crystals. In these conditions the NMR spectrum is doubled since for half of the As nuclei the total field is the sum of the internal and external fields while for the second half it is the difference. The internal field can be obtained by measuring the shift of the central line below T_m and its value is in excellent agreement with the ZF-NMR one (see Fig. 2.13b and 2.13c). The temperature evolution of the NQR frequency, which correspond to the frequency separation between the central and the satellite line, is also extremely important since ν_Q is very sensitive to the geometry of the lattice and thus its measurement allows us to directly detect the tetragonal to orthorhombic transition ($T_{TO} > T_m$). As can be seen in

Fig. 2.13c, $\nu_Q \sim 8.8$ MHz in the orthorhombic magnetic phase and ~ 9.4 MHz in the tetragonal phase with a rather sharp step indicating the T-O transition.

NMR measurements can also give very important clues regarding the physic of the superconducting samples. The normal phase temperature dependence of $(T_1T)^{-1}$ is reported in Fig. 2.14 [161]. While the for optimally and over doped samples ($x > 0.1$) $(T_1T)^{-1}$ displays a simple linear behaviour down to T_c in the more underdoped (but still superconducting) samples a very well defined peak is observed well above T_c. Hence this feature cannot be an Hebel-Slichter coherence peak and it is not correlated to the motion of the vortex lattice lines since they appear only below T_c.

The $(T_1T)^{-1}$ linear temperature dependence is interesting on its own. The behaviour is roughly consistent with the Korringa $1/T_1 \propto T$ dependence in metals since the Knight shift is also proportional to the temperature (see Eq. 2.31 and the following paragraph). However this phenomenology cannot be explained by the presence of a pseudogap akin to that observed in cuprates superconductors since activated fits fails to describe this behaviour and no pseudogap peak is observed up to 500 K.

While a complete theoretical explanation of the peak is still lacking its existence is probably correlated to the proximity of the underdoped samples to the magnetic phase. It is possible to fit the temperature behaviour using the BPP formula (see Eq. 2.33) with a temperature activated τ_c. The BPP behaviour was confirmed by measurements carried out with different magnetic fields which revealed that the intensity of the peak is indeed inversely proportional to the strength of the magnetic field. This fit strongly suggest that the presence of the peak is due to very slow spin fluctuations that weakens upon increasing electron doping and fully disappear at optimal doping. However the nature of the fluctuations has not been clarified yet and it is also not clear if they promote or compete with superconductivity. This topic with be greatly expanded in the experimental part of this thesis.

The study of $1/T_1$ below T_c can give important clues about the symmetry of the superconducting gap. As shown in Fig. 2.14b $1/T_1$ exhibit a drop at T_c with no evidence of a Hebel-Slichter peak. Below T_c the spin lattice relaxation follows the power law $1/T_1 \sim T^3$ temperature dependence and in general in IBS the power law exponent is between 3 and 5 [162]. This behaviour indicates the presence of nodes in the superconducting gap and is in contrast with the exponential behaviour expected for an isotropic gap. However it was shown that both the $s^{\pm}$ and the s^{++} gap symmetry can give rise to this $1/T_1$ trend if the superconducting gap is anisotropic and some impurity effect is present [162].

Finally we present some ^{75}As NQR result which will be useful to better understand the following chapters. We already pointed out in Section 2.1.2.3 that the quadrupolar frequency (see Eq. 2.16) depend on the EFG at the position of the nuclei and since the EFG is strongly influenced even by tiny modification of the electron density, measuring the NQR spectrum of a sample is a good method to check its composition (line position) and to quantify

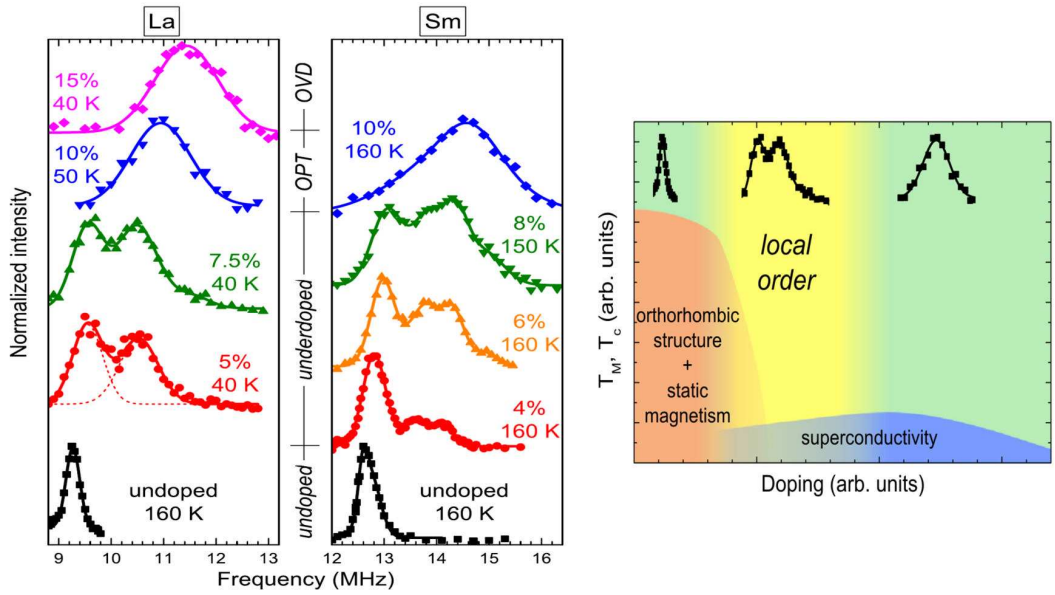

Figure 2.15: Right: ^{75}As NQR spectra of $RFeAsO_xF_{1-x}$ (R = La, Sm). The solid lines are fits carried out using or more Gaussian functions. Left: Sketch of the electronic phase diagram of the 1111 IBS. The local order develops in the underdoped region. Figure adapted from Ref. [166].

the disorder (line width). However it is also possible to study the intrinsic inhomogeneities of the system such as those originating due to orbital or charge ordering.

In $LaFeAsO_{1-x}F_x$ detailed studies of the NQR spectrum as a function of doping have been carried out by Lang *et al.* [166, 168]. This investigation unveiled the presence of two charge environments coexisting at the nanoscale in underdoped (F doping) La1111 compounds. The coexisting electronic environments give rise to two peaks in the NQR spectra whose relative intensities are nearly temperature independent. This nanoscopic separation (local order) was attributed to the presence of low-doping-like (LD-like) and high-doping-like (HD-like) regions with the HD regions being linked to the appearance of superconductivity while the LD regions are closely associated to the development of orthorhombicity and static stripe magnetism. The appearance of this nanoscopic separation is concomitant with the suppression of static magnetism and the emergence of superconductivity.

The typical shape of the NQR spectra as a function of doping is presented in Fig 2.15.

2.2.2 122 family

The underdoped compounds of the 122 family also display a magnetic transition below 150 K (see Chapter 1). Again the transition is marked by a divergence in $1/T_1$ as can be seen in Fig. 2.17a. Just like in the 1111 family

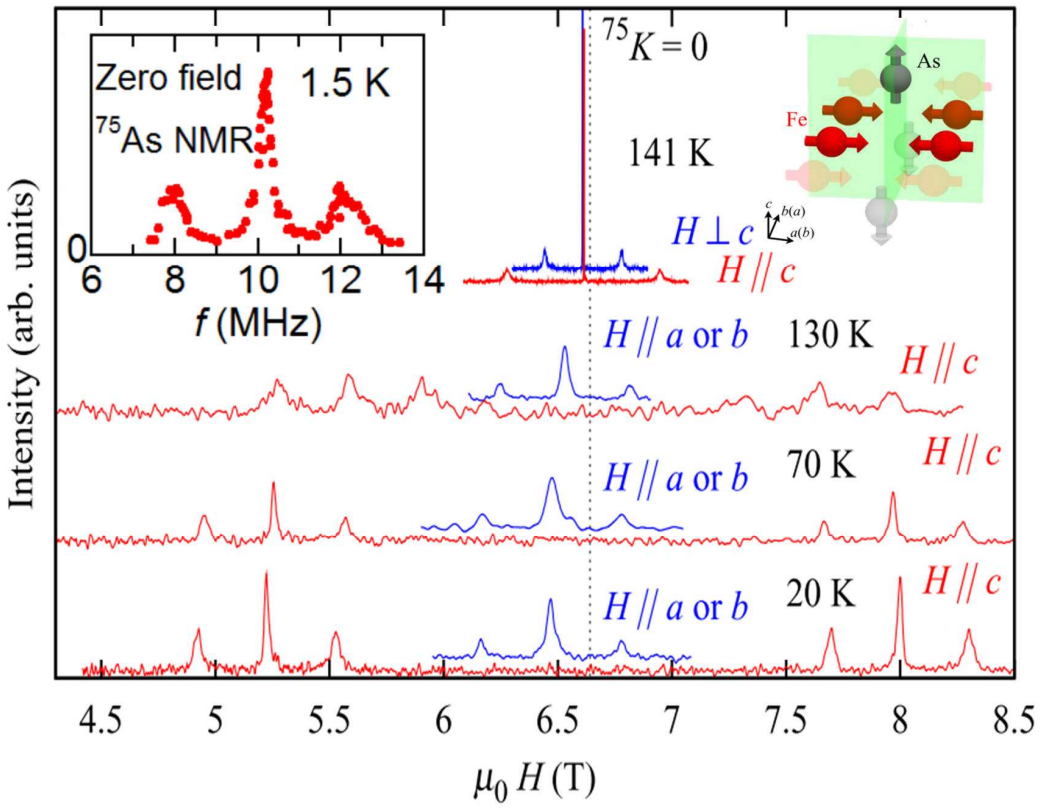

Figure 2.16: Field sweep NMR spectrum of undoped $BaFe_2As_2$ for different temperature values. Left inset: ZF-NMR spectrum measured for T=1.5 K, adapted from Ref. [167]. Right inset: sketch of the stripe antiferromagnetic order, the red arrows indicates the direction of the Fe moments while the grey arrows represent the direction of the internal field at the As site. Adapted from Ref. [66].

it is possible to investigate the nature of the magnetic state by measuring the NMR spectra both with [66] and without [167] an external magnetic field (see Fig. 2.16, $BaFe_2As_2$). The results are perfectly consistent with the stripe $\mathbf{Q} = (\pi, 0); (0, \pi)$ magnetic order also observed by neutron scattering. As can be seen in Fig. 2.16, $\nu_Q \sim 2.21$ MHz in the Ba122 family, much smaller than in La1111 ($\nu_Q \sim 8.8$ MHz below T_m) and the full ZF-NMR spectrum can be observed. Similarly to the case of La1111 a ν_Q jump to lower frequencies is observed in correspondence of the T-O transition ($\nu_Q > 2.4$ in the tetragonal phase). Kitagawa *et al.* [66] also found a marked enhancement in the $1/(T_1T)$ of $BaFe_2As_2$, depending on the orientation of the sample with respect to the field, with $(T_1T)^{-1}$ being enhanced for $H_0 \parallel ab$ with respect to the $H \parallel c$ orientation.

Ning *et al.* [169] measured the spin relaxation rate of Co doped Ba122 for doping levels ranging from zero to extremely overdoped (Fig. 2.17a). They found that very strong spin correlation persist in the superconducting region and give rise to a Curie-Weiss behaviour of $(T_1T)^{-1}$ which completely disappears only for very high doping ($x = 26\%$). The $(T_1T)^{-1}$ temperature

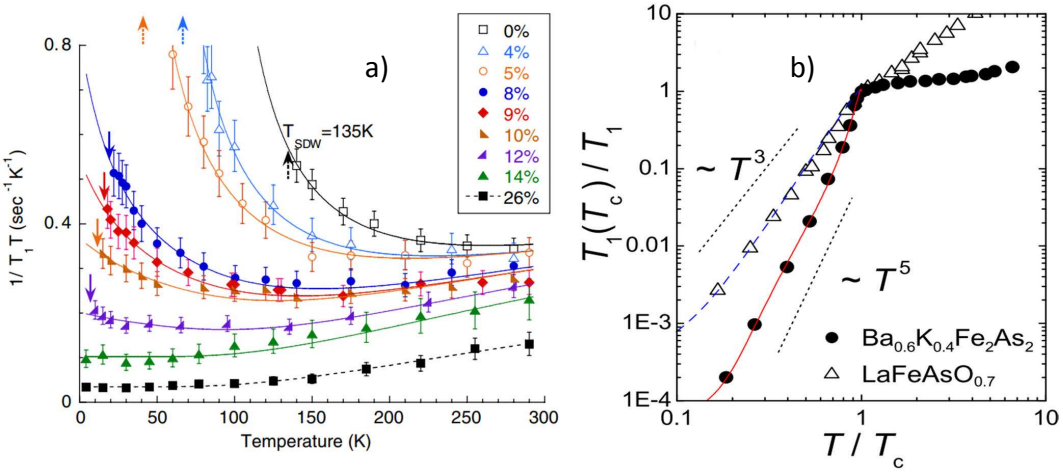

Figure 2.17: a) $1/T_1$T measured in $Ba(Fe_{1-x}Co_x)_2As_2$ for various doping concentrations x. The magnetic field is applied in the ab plane. Solid and dashed arrows mark T_c and T_m ,respectively. The solid lines are fits to a Korringa law plus a Curie-Weiss term, which completely disappear in the overdoped $x = 26\%$ sample. Adapted from Ref. [169]. b) T dependence of ^{57}Fe $1/T_1$ for $Ba_{0.6}K_{0.4}Fe_2As_2$. The solid line is a fit to a two anisotropic gap $s^{\pm}$ model. Adapted from Ref. [170].

dependence after the disappearance of the fluctuations can be fitted to a simple Korringa relation. Since the fluctuations are still very strong at optimal doping it is extremely unlikely that they compete with the superconducting state, on the contrary the data suggest that they might support it.

Below T_c the observed temperature behaviour of the relaxation rate is pretty similar to that observed in the 1111 compounds ($1/T_1 \sim T^n$ with $n \sim 3$ - 5). In particular a ^{57}As NMR study from Yashima *et al.* revealed that the $1/T_1$ temperature evolution can be fitted to an anisotropic $s^{\pm}$ two component gap in both the materials (see Fig. 2.17b).

Now we turn our attention to the study of $1/T_2$ in the Ba122 subfamily. While most of the NMR relaxation studies have been focused on $1/T_1$ which is sensitive to transverse field fluctuations (Eq. 2.30) also the the spin-spin relaxation time T_2 is a very versatile tool to investigate the low-frequency spin dynamics. In particular $1/T_2$ is sensitive to the spin fluctuations that affects the longitudinal component of the local field probed by the nucleus. A first T_2 study was reported by Mukhopadhyay *et al.* [172] for K doped $BaFe_2As_2$. They observed a very long T_2 which could not be justified in terms of dipolar interaction. This peculiar effect could be due to the presence of a strong indirect $n-n$ interaction leading to a spin diffusion in a local inhomogeneous field.

Furthermore the value of T_2 measured with the CPMG sequence is much longer than the one found using the Hahn spin-echo sequence, akin to what is usually observed in systems where a diffusion dynamic is present. Conversely, in $CaFe_2As_2$ T_2 is shorter and in much better agreement with dipolar calculations.

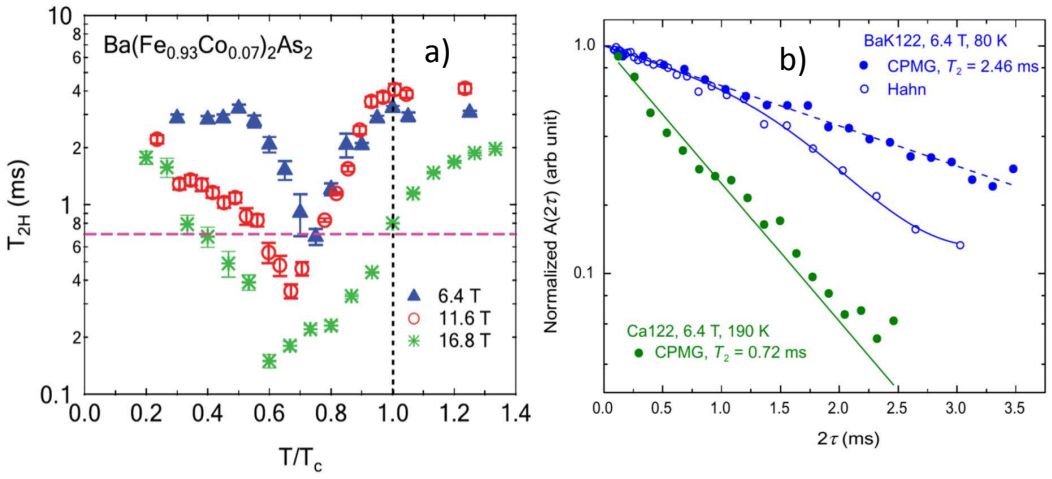

Figure 2.18: a) T_2 temperature evolution in $Ba(Fe_{0.93}Co_{0.07})_2As_2$ measured with the Hahn Spin Echo sequence ($H_0 \parallel c$) for different values of the external field. Adapted from Ref. [171]. b) Spin Echo decay measuerd with the CPMG and Hanh spin echo sequence in hole doped $Ba(Fe_{1-x}K_x)_2As_2$ ($x = 0.45$) and undoped $CaFe_2As_2$ Adapted from Ref. [172].

Oh *et al.* [171] studied the the temperature evolution of T_2 in $Ba(Fe_{0.93}Co_{0.07})_2As_2$. As can been seen in Fig. 2.18 the spin-spin relaxation display a strong dip below T_c which has been attributed by the author to the freezing of vortex lattice lines. However the onset of the dip for high external field ($H_0 > 11$ T) is at temperatures significantly higher than T_c, casting a shadow on this interpretation.

In the next Chapter will extensively study the $1/T_2$ behaviour in Rh doped Ba122.

2.3 Muon Spin Rotation (μSR)

Muon Spin Rotation (μSR) is another technique widely used in this thesis in order to study both the magnetic and the superconducting properties of the Iron Based Superconductors. Like NMR, Muon Spin Rotation is a local technique which is able to study the electronic environment through its coupling with the spin of a probe particle.

While in NMR the probes are the nuclear spins, μSR probes the evolution of the spins of μ^+ muons, created in a particle accelerator, and implanted into the sample in order to carry out the experiment. Once the positive muon is implanted in the specimen it will behave like a light proton and its spin will probe the same interactions described in the previous section (nucleus-nucleus interaction and hyperfine *n-e* interaction). The modification of the system due to the presence of injected muons can usually be neglected [138].

The results obtained from μSR experiments are often complementary to those provided by NMR. Since μSR is extremely sensitive to local fields (internal fields lower than 0.1 G can be detected) it is an excellent tool for the study of spatial magnetic inhomogeneities like those present in disordered magnetic samples or the field distribution due to the presence of fluxons in the superconducting phase [148, 173]. A significant advantage of μSR on NMR is that the technique can be used on all the materials independently from their composition. Furthermore the experiments can also be carried out with zero external field since the spins of the implanted muons are 100% polarized. This allows one to study the intrinsic magnetism of the sample without the need of a large polarizing magnetic field. On the other side determining the position of the muon site is often challenging or impossible, which makes it difficult to correctly interpret the data.

2.3.1 Muon production and implantation

Muons are spin 1/2 leptons whose mass is roughly 200 times the electron mass ($m_\mu = 206.77\, m_e$) and with a mean lifetime of $\sim 2.2\mu$s. Proton particle accelerator are commonly used to generate muon beams through the interaction between the proton beam and the carbon nuclei in a thin graphite target. Muon beams suitable for μSR are available at four research facilities around the world: at the Rutherford Appleton Laboratory (ISIS facility) in the UK, at the Paul Scherrer Institut (PSI) in Switzerland, at the J-PARC facility in Japan and at the TRIUMF Centre in Canada.

Intense muon beams can be generated thanks to the decay of charged pions. The pions are created during the collision between the protons and the carbon nuclei. Let's now consider the pions that don't have enough energy to leave the target but instead come at rest close to its surface. The pions decay in muons and neutrinos:

$$\pi^+ \rightarrow \mu^+ + \nu_\mu \tag{2.39}$$

and the out-coming particles have opposite momenta equal to 29.79 MeV/c. To conserve the angular momentum, since the pion is a spinless particle while both the neutrino and the muon have spin 1/2, the neutrino and the muon will have opposite spins. Since all the neutrinos have negative helicity (parity violation in weak interactions) the spin of both the emitted particles will be opposite to their momentum and thus the resulting muon beam is 100% spin polarised.

The produced muons are then implanted into the sample, within a time in the ns range. Once into the specimen the muon stop at energy favorable sites of the lattice where they remain until they decay at time t with a probability $e^{-t/\tau}$ where $\tau \sim 2.2\mu$s in the mean life time of the muon.

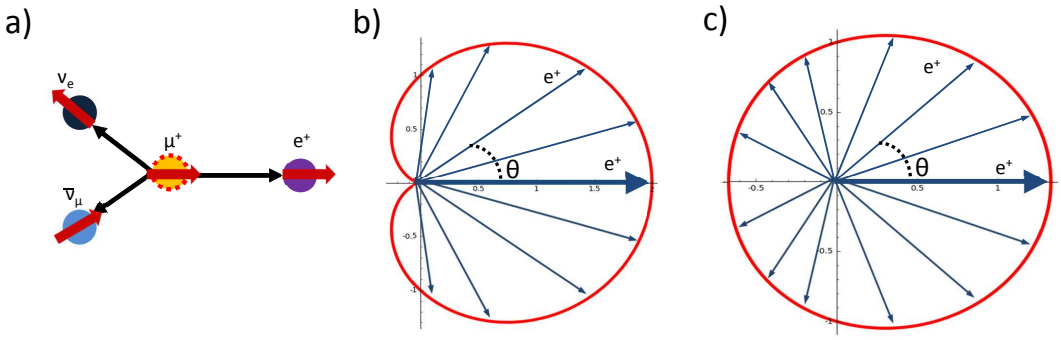

Figure 2.19: a) Sketch of the muon decay process, the spin of the particles is represented by the thick red arrows while the linear momentum by the black arrows. b) Profile of the probability distribution of the emitted muon direction for $E = E_{max}$ c) Same as (b) but this time for the average energy of the muon $(A(E_{average}) = 1/3)$.

Parity violation also allows us to to detect the evolution of the muon spin once it is implanted. The muon decay is a three body process (see Fig. 2.19a):

$$\mu^+ \rightarrow e^+ + \nu_e + \overline{\nu}_\mu \tag{2.40}$$

and the energy and direction of the emitted positron can vary depending on how the momentum is distributed among the three decay products. This reaction is mediated by the weak interaction and like the pion decay it does not conserve the parity. The probability distribution function of the emitted positron is related with its energy and direction through the relation:

$$P(E, \theta) \propto 1 + A(E) \cos\theta, \tag{2.41}$$

where $\theta \in [0, \pi]$ is the emission angle and $A(E)$ is the energy dependent emission asymmetry. The profile of the probability distribution lobe for the maximum positron energy ($E_{max} = 52.83$ MeV, $A(E_{max}) = 1$) is reported in Fig. 2.19b. The average on the whole energy range of $A(E)$ gives rise to an integrated asymmetry of 1/3 and thus $P(\theta) \propto 1 + 1/3 \cos\theta$ (see Fig 2.19c). The positron emission asymmetry is thus correlated with the direction of the muon spin since the emission probability is at its maximum when the muon spin is parallel to the positron momentum.

2.3.2 Basics of a μSR experiment

The time evolution of the muon spin is described by the same Hamiltonian (Eq. 2.6) we already used for the nuclear spins in the previous section, save for the quadrupolar term which is zero since the muon does not have a quadrupole moment. Basically the muon behaves like an implanted "light proton" with a gyromagnetic ratio $\gamma_e \mu / 2\pi = ge/4\pi m_\mu = 135.54$ MHz/T and

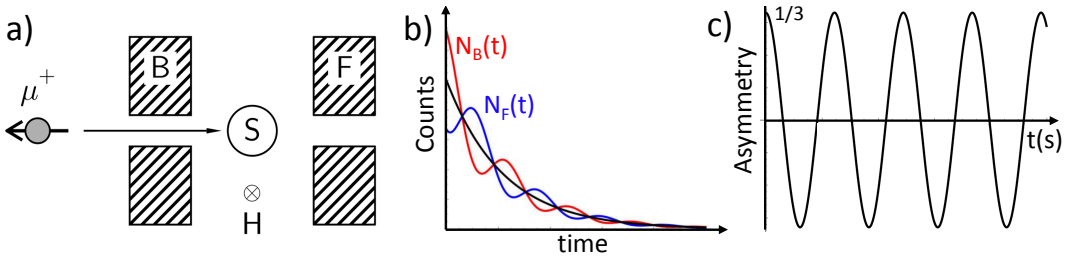

Figure 2.20: a) Sketch of a typical μSR experiment (this panel is adapted from [138]). b) Time dependence of the number of counts in the Forward (blue) and Backward (red) detectors in presence of a static magnetic field perpendicular to the muon beam. The black curve is the total number of muons in the sample at a given time. c) The corresponding evolution of the measured asymmetry.

thus in a magnetic field **B** the muon spin will precess with a Larmor frequency $\omega_\mu = \gamma_\mu \mathbf{B}$. The typical frequencies of μSR lie between those used in NMR and Electron Spin Resonance (ESR). However differently from these resonant techniques, where the actual resonance occurs when the frequency of the external varying electromagnetic field matches the Larmor frequency of the studied particles, in the case of μSR no external radio frequency is needed since it is possible to directly measure the evolution of the muon spins thanks to the asymmetry in the direction of the emitted positron that, as explained in the previous section, follows the direction of the muon spin.

From an experimental point of view the value of the asymmetry at a given time can be easily measured by placing two detectors around the sample, one between the incoming beam and the sample (forward detector, F) and one on the opposite side (backward detector, B). A scheme of this set-up is shown in Fig. 2.20a. If no external magnetic field is present (or if the external field is longitudinal, i.e. parallel to the beam) the B detector will reveal a higher number of events than the F detector in the whole time window. The number of decay events observed in the two detectors decrease exponentially with the law (see Eq. 2.41): $dN(t) = N_0 e^{-t/\tau}(1 + A\cos\theta)\, dn\, d\theta$. The count rates of a real experiment can be found integrating this equation over a finite time bin and over the solid angle covered by the detectors. Both integrations lead to an average and thus to a reduction of the observed asymmetry from the theoretical 1/3. If an external magnetic field perpendicular to the beam direction is turned on (Transverse Field, TF) the muon magnetization will precess and the whole positron emission probability will rotate in the plane, resulting an oscillating positron count in the detectors, as portrayed in Fig. 2.20b.

The muon decay counts are acquired starting from the muon implantation over a few μs time window (usually less than 20μs). A large number (several millions) of muons decays is typically used in order to have a significant statistic. Muons can be implanted either in bunches of hundreds of muons at the pulsed muons source (e.g. ISIS) or one by one at continuous muon sources (e.g. PSI). In this second case the mean time between one muon and

the following one must be much longer than the muon half life in order to have at most one muon in the sample at any given time.

The time evolution of the spin polarization can be obtained by studying the normalized difference of the counts in the two detector for all the time bins:

$$A(t) = \frac{N_B(t) - N_F(t)}{N_B(t) + N_F(t)}. \tag{2.42}$$

In the case of a static transverse field and no intrinsic magnetic fields into the sample the asymmetry will thus oscillate at the Larmor frequency (see Fig. 2.20) while, if the external field is either zero or longitudinal, the asymmetry will be flat and $\sim 1/3$ in ideal conditions. However this value is impossible to reach in actual experiments since not the whole angle is covered by the detectors and also the detector sensitivity is not perfect. It is customary to write the actual experimental asymmetry in the following way:

$$A(t) = \frac{\alpha N_B(t) - N_F(t)}{\alpha N_B(t) + N_F(t)}. \tag{2.43}$$

The parameter α is mainly due to the different geometry of the forward and backward detectors and the exact position of the sample. The easiest way to determine $\alpha = \langle N_F/N_B \rangle$ is to measure the sample in a tenuous transverse magnetic field and then to estimate the offset of the oscillating asymmetry. The obtained value can then be reused for a series of consecutive measurements on the same sample.

In a real system however not only the external fields but also microscopic internal fields, due both to the electron and nuclear moments, are present and also they will influence the time evolution of the asymmetry. The muon thus act as a microscopic magnetic field sensor able to map the local field inside the materials and their time evolution, making it possible to probe the local fields arising from the onset of a magnetic order, the spin dynamics and the field distribution generated by the flux lines in the SC state.

2.3.3 Zero Field (ZF) μSR

A unique feature of μSR is its ability to study the intrinsic magnetism of a material without any external polarizing magnetic field. In general the asymmetry decay in ZF can be written as [173]:

$$\frac{A_{ZF}(t)}{A_0} = G_{ZF}(t) = [1 - V_m(T)]G_{dip}(t) + V_m(T)\left[a^{\perp}(T)F(t)D^{\perp}(t) + a^{\parallel}(T)D^{\parallel}(t)\right], \tag{2.44}$$

where A_0 is an instrument-dependent constant corresponding to the highest asymmetry measurable with the set-up and $G_{dip} \sim \exp(-\sigma^2 t^2/2)$ is the relaxation arising from the nuclear dipolar coupling. Here we assumed for simplicity that only one crystallographically-inequivalent muon stopping site is present. If more muon sites are present, as is the case for example in 1111

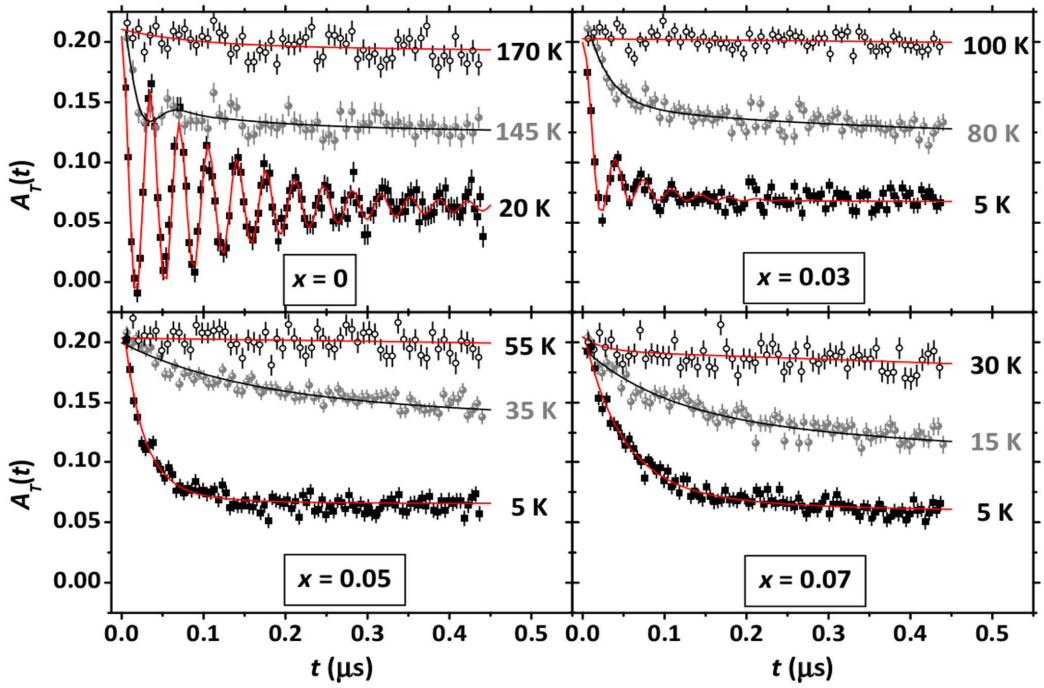

Figure 2.21: ZF-μSR measurement on underdoped $CeFe_{1-x}Co_xAsO$. The increase of the transversal damping with increasing x signals the disordering of the magnetic phase. Figure adapted from [174].

iron based superconductors, additional similar terms must added, one for each site.

For non-magnetic samples (and above T_m in magnetic ones) the magnetic volume fraction V_m is zero and thus only the dipolar coupling of the nuclei contributes to the asymmetry decay. If magnetic transition is present and we assume the presence of a distribution of transition frequencies T_m, as is often the case in real systems, V_m is given by the phenomenological expression:

$$V_m = \mathrm{erfc}\left(\frac{T - T_m}{\sqrt{2}\Delta}\right), \tag{2.45}$$

where $\mathrm{erfc}(x)$ is the error function and Δ is the width of the transition. Below T_m, in the $V_m(T) = 1$ condition, the muon polarization decay is completely determined by the second term of Eq. 2.44. Here $a^{\perp}(T)$ and $a^{\parallel}(T)$ denotes the fractions of all the implanted muons that feel a static field, respectively, in transversal and longitudinal direction with respect to the initial muon polarization. If the sample are powered, as is often the case for μSR experiments, from simple geometrical considerations it can be found that $a^{\perp}(T) = 2/3$ and $a^{\parallel}(T) = 1/3$. $D^{\perp}(t)$ and $D^{\parallel}(t)$ indicates the corresponding damping functions of the two fractions. These to relaxation function very often are a simple exponential damping ($e^{-\lambda_{\perp}t}$ and $e^{-\lambda_{\parallel}t}$). While the field magnitude distribution gives rise to the main component of $D^{\perp}(t)$ it does not contribute to $D^{\parallel}(t)$ since the muons in the longitudinal fraction do not precess. The magnitude

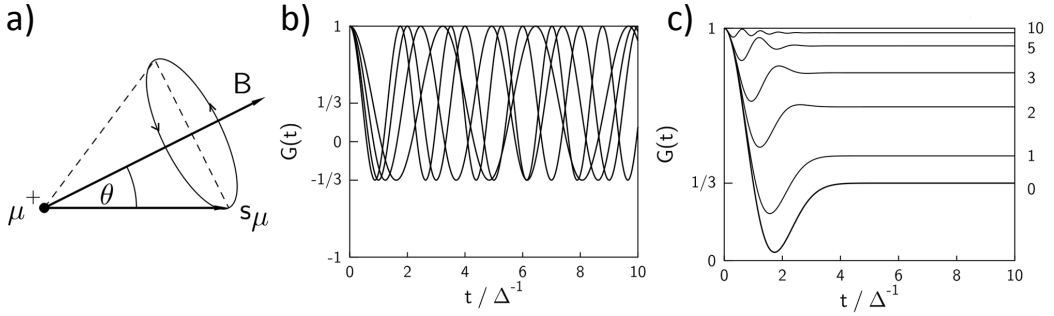

Figure 2.22: a) Sketch the muon spin in an external field **B**. b) Time evolution of the muon polarization for different values of local field. c) The average of the terms in (b) leads to the Kubo-Toyabe relaxation, which is the curve labelled as 0. The other curves represent the asymmetry evolution in presence of an additional external longitudinal field. The time is measured in units of Δ^{-1} and the longitudinal field is in units of Δ/γ_μ Figure adapted from [138].

of $D^{\parallel}(t)$ is usually governed by dynamical T_1 like processes. Finally $F(t)$ is a oscillating term describing the Larmor precession of the transverse polarization around the local field B_μ generated by the magnetic order. Quite often a simple sinusoidal function ($F(t) = \cos(\gamma_\mu B_\mu t)$) is enough to describe the data (see Fig. 2.21).

A very common case encountered in the study of high temperature superconductors and other strongly correlated systems is that of completely disordered local fields. If we neglect the effect of the nuclear dipolar coupling and of the dynamical processes affecting the longitudinal fraction, the muon decay asymmetry is given by the simple formula [138] $G(t) = \cos^2\theta + \sin^2\theta\cos(\gamma_\mu B_\mu t)$, where θ is the angle between the muon spin and the local field (Fig. 2.22a).

If the direction of the local field is completely random, as is the case for a power, the averaging on all the direction gives $G(t) = 1/3 + 2/3\cos(\gamma_\mu B_\mu t)$. In case of a Gaussian distribution of local fields B_μ centred around zero and with width Δ/γ_μ the average over the distribution gives a relaxation of the form:

$$G(t) = \frac{1}{3} + \frac{2}{3}e^{-\Delta^2 t^2/2}(1 - \Delta^2 t^2) \tag{2.46}$$

which is known as the Kubo-Toyabe relaxation function [175] (see Fig. 2.22c).

A qualitative explanation for this peculiar asymmetry decay is presented in Fig. 2.22b which shows the asymmetry evolution for several different local fields. Initially all the curves are very similar but as time goes on the different fields lead to a de-phasing of the components which average out the transverse fraction leaving only the longitudinal one, whose value is one-third.

If an almost uniform static internal field is present into the sample the minute variation from one muon site to the other will result in a progressive dephasing and thus in the damping of the oscillation which is indicated by

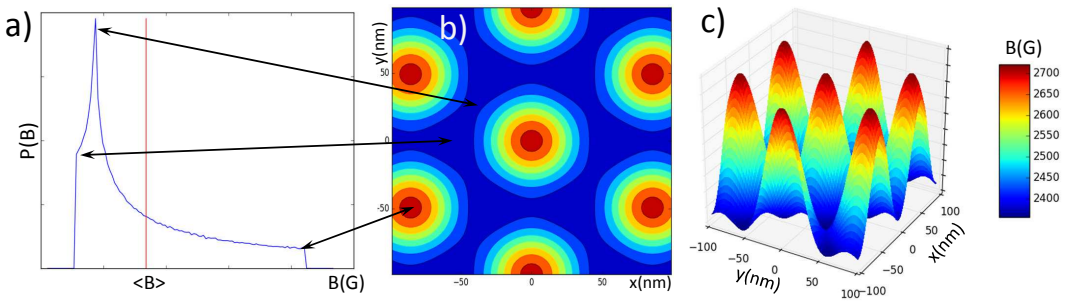

Figure 2.23: a) The numerically calculated field distribution for an hypothetical type II superconductor with λ =60 nm and ξ =20 nm. In the calculation we chose H_0 = 2470 G. b) 2D contour plot of the field intensity, in red the cores of the vortices. The black arrows indicate which parts of the FFI primitive cell give rise to the three singularities of the field distribution. The corresponding 3D plot. The calculation was carried out using the London Model with Gaussian cut off (see [176] for theoretical details). The code was developed in the Python language with the additional Numpy and SAGE packages.

the $D^{\perp}(t)$ in Eq. 2.44, as we explained in the previous paragraph. If the field anisotropy is big the damping can be so fast that no oscillations are observed at all. However such a quick asymmetry decay can also be caused by internal field fluctuations or by the diffusion of the muon. In order to discriminate between the static scenario and the dynamic scenario a longitudinal field (LF) μSR experiment can be carried out. In fact if the external longitudinal field is much bigger than the internal field the transverse components can be neglected (see Fig. 2.22a) and the muons will not precess in their internal field any more. This means that no dephasing will take place and the asymmetry will remain nearly constant at its maximum value. Fig. 2.22c show the recovery of the polarization obtained by increasing the intensity of the longitudinal field. Conversely if the muon relaxation is mainly due to the presence of strong spin fluctuations, as is the case for example in spin glasses, the applied longitudinal field will have a much smaller effect on the relaxation. In general if the dynamics are slow the longitudinal field will have a large effect while if the dynamics are fast the response will be much smaller.

2.3.4 Transverse field (TF) μSR in the superconducting state

Muon Spin Rotation has been widely used to study the superconducting properties of both the cuprates and the iron based superconductors. When type II superconductors ($\lambda > \xi/2$), such as the IBS, are cooled down below T_c in an applied external magnetic field $H_{c1} < H_0 < H_{c2}$ the field anisotropically penetrates inside the material creating a regular triangular lattice of superconducting vortices whose cores remain in the normal state and contain the

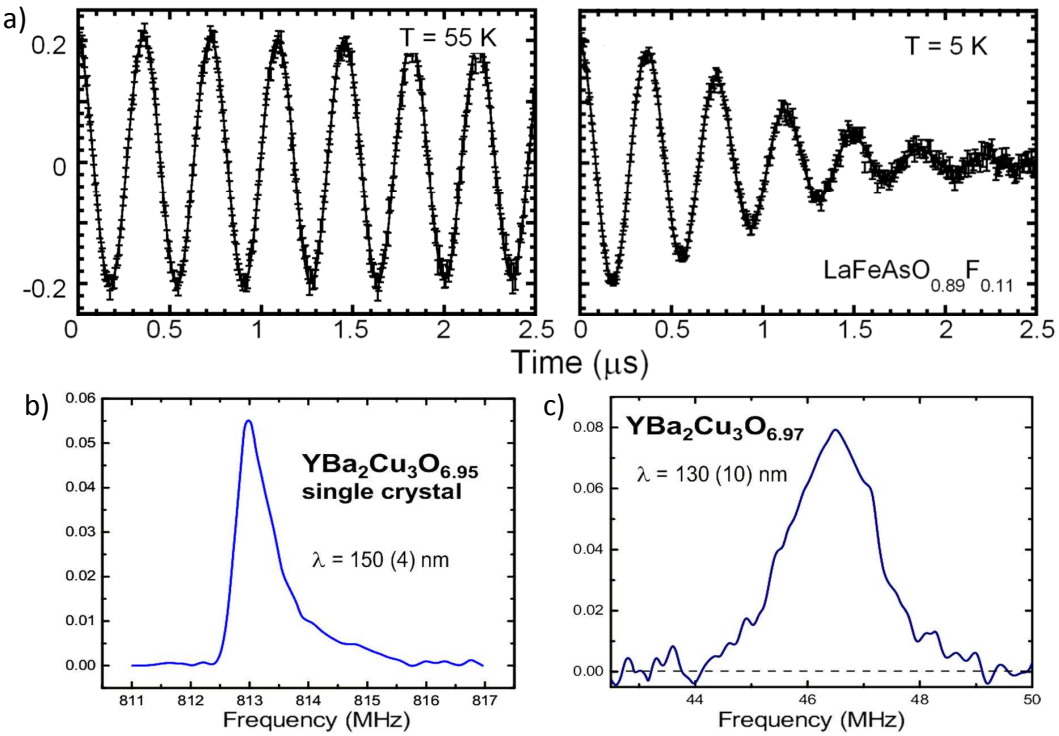

Figure 2.24: Time evolution of the TF-μSR asymmetry for a powder sample of $LaFeAsO_{0.89}F_{0.11}$ at T values above and below $T_c = 28$ K, measured in with $H_0 = 200$ G. Solid curves are best fits to a Gaussian damped precession. Figure adapted from [173]. In d) and e) can be seen, respectively, the TF-μSR spectra for an high quality single crystal and for a powdered sample of YBCO. Figure adapted from [177] and [178].

field lines. Each vortex is associated with exactly one magnetic field flux quantum $\Phi_0 = h/2e \sim 2.06$ Gcm^2. Since the distance between two adjacent vortices ($d \propto \sqrt{H_0}$) is typically much bigger than the lattice step (except for very high values of H_0) and the vortex positions are incommensurate with the lattice, the muons will randomly probe the field distribution generate by the Flux Line Lattice (FLL). The field distribution gives rise to a depolarization of the muon spin which is conveniently observed with a μSR Transverse Field (TF) experiment. The internal field distribution is not symmetric with respect to the value of the applied field [179] as can be easily seen using numerical simulations (see Fig. 2.23), however in real samples and in particular for powdered samples, the presence of vortex pinning centres (e.g. crystal dislocation, vacancies etc) disrupts the uniformity of the FLL thus averaging out the asymmetries of the original field distribution transforming it to a nearly Gaussian distribution centred around the average internal field. (see Fig. 2.24b and 2.24c).

In these conditions the evolution of the asymmetry is often given by the

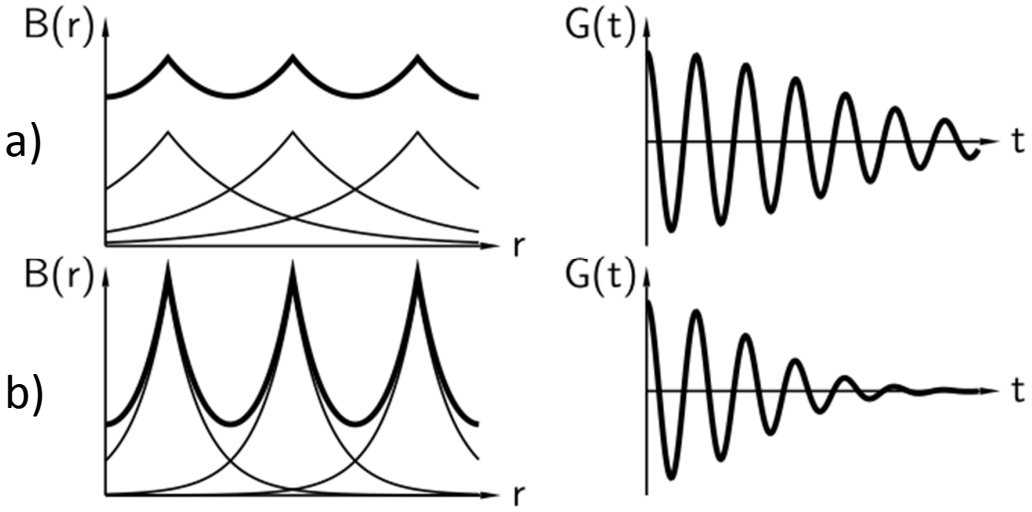

Figure 2.25: Qualitative sketch of the internal field intensity (left) and of the TF-μSR signal (right), for two different values of λ: (a) larger λ and (b) smaller λ. Figure adapted from [138].

function:

$$\frac{A_{TF}(t)}{A_{TF}(0)} = \alpha_{TF} \exp -(\sigma_{SC}^2 + \sigma_N^2)/2 \cos(\gamma_\mu B_\mu t) \tag{2.47}$$

where α_{TF} is the amplitude, σ_N takes into account the weak asymmetry oscillation damping due to the magnetic dipole moment of the nuclei and $\sigma_{SC}/\gamma_\mu = (\overline{B}^2 - B_\mu^2)^{1/2}$ is the width (second moment) of the internal field distribution due to the FLL. The fit of the asymmetry evolution with equation 2.47 is shown in Fig. 2.24a for the iron based superconductor $LaFeAsO_{0.89}F_{0.11}$. As can be seen the internal field distribution gives rise to a polarization damping much faster than that originating from the nuclear dipolar interaction.

It is important to note that the study of the TF-μSR polarization decay can thus be used to determine T_c which in this framework can be easily defined as the temperature at which σ_{SC} appears, or more rigorously it can be extracted by fitting the temperature dependence of $\sigma_{SC}(T)$ with an average field model $\sigma_{SC}(T) = (\sigma_{SC}(0)[1 - (T/T_c)^n]$.

Since increasing the value of the London penetration depth λ the width of the field distribution shrinks (see the sketch in Fig. 2.25) some relation must exist between λ and σ_{SC}. In fact it can be rigorously demonstrated [180] that σ_{SC} is proportional to the inverse of λ^2:

$$\sigma_{SC}[\mu s^{-1}] = \gamma_\mu(\overline{B}^2 - B_\mu^2)^{1/2} = 0.1074 \frac{1}{\lambda[\mu m]^2} . \tag{2.48}$$

The TF-μSR signal can thus be used to directly determine the penetration depth. The λ values measured with μSR are often significantly more accurate

than the ones measured with microwave techniques which are only sensitive to the skin of the superconducting sample.

The measurement of λ and its temperature dependence in HTSC is extremely important since this quantity is a direct measure of the order parameter and thus of the symmetry of the superconducting gap and hence it gives some clue on the pairing mechanism. This type of study first revealed that the symmetry of the superconducting gap in cuprates ($YBa_3Cu_3O_{3.6}$) has a different symmetry (d-wave) with respect to the s-wave symmetry of BCS superconductors.

The penetration depth is connected to the superfluid density by the relation [181]:

$$\frac{1}{\lambda^2} = \frac{4\pi n_s (2e)^2}{m^* c^2} \tag{2.49}$$

where m^* is the effective mass of the Cooper pairs and n_s the density of superconducting carriers (superfluid density). Uemura *et al.* [182] found that in cuprates superconductors a linear relation exists between T_c and the superfluid density. Conversely in the BCS superconductors T_c is independent from n_s. While a satisfying theoretical explanation for this peculiar behaviour, common to all the cuprates families, is still missing, its existence strongly constrains the theories trying to explain superconductivity in these materials.

2.4 μSR studies on Iron Based Superconductors

In the following sections we present a brief review of some of the μSR results on IBS. We will focus on the 1111 and 122 compounds which are the ones more relevant for the experimental section of this thesis.

2.4.1 Zero Field μSR

As thoroughly explained in the previous sections ZF-μSR is an excellent tool for the study of the intrinsic magnetism in the IBS and thus has been widely used to explore their phase diagrams obtained upon changing chemical doping and/or external hydrostatic pressure, in particular in the region at the crossover between magnetism and superconductivity. The study of this region is extremely important since several theoretical models [183, 184] predict that if magnetism and superconductivity coexist then the pairing is unconventional and the $s^{\pm}$ symmetry should be favored.

In order to understand the nature of the coexistence one has to find out the length scale d at which it takes places, in fact the degree of spatial intertwining between the two order parameters can assume very different values depending on the physical phenomenon behind the coexistence. In this framework d can be equivalently defined as the mean distance between two adjacent magnetic domains or between adjacent superconducting domains

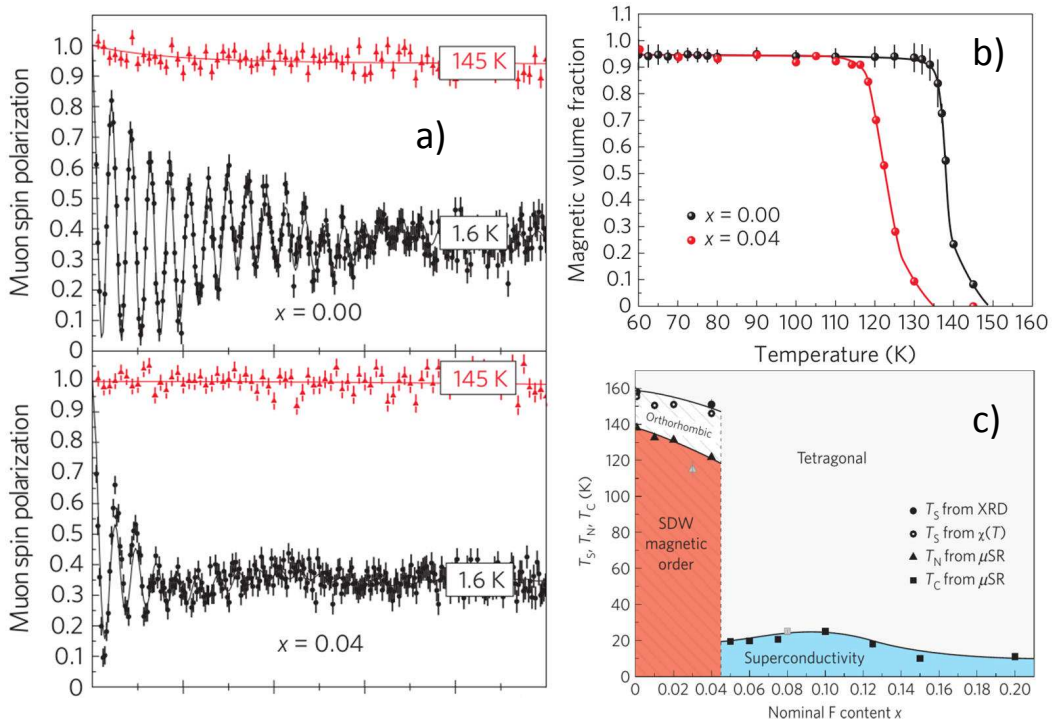

Figure 2.26: ZF-μSR measurement for underdoped (magnetic) $LaFeAsO_{1-x}F_x$ samples. (a) The time dependent evolution fro the undoped and the $x = 0.04$ samples. For both the materials the precession due to the static field generated by the stripe order can clearly be seen. (b) The correspondent values of the magnetic volume V_m, as can be seen despite the increased disorder of the local field which results in a faster damping of the asymmetry in the $x = 0.04$ sample both the composition are still dully magnetic below T_m. c) The phase diagram(see 1.1.1). Figure adapted from [18].

(see Fig. 2.27a). If the value of d is in the 100 nm - 1 μm range the coexistence is macroscopic or mesoscopic. This type of coexistence is not intrinsic of the material but instead the macroscopic phase segregation is promoted by extrinsic factors such as the presence of impurities or the inhomogeneity of the chemical doping. In this case no firm conclusion can be draw on the nature of the pairing or on the gap symmetry since the magnetic and superconducting phases are spatially separated and do not influence each other. The $d \sim$ 1 - 10 nm (*nanoscopic coexistence*) case instead is much closer to the ideal atomic limit at which the two phases coexist at the same position and the two phase strongly influence each other. ZF-μSR is the only technique capable of clearly discriminating the two types of coexistence. In fact while the muons implanted in the magnetic regions obviously sense the internal field those implanted in the superconducting regions are only sensible to the uncompensated magnetic moment domain walls since if the order is antiferromagnetic the total moment of the magnetic regions is zero. In the IBS the minimum distance from the magnetic regions required in order to measure

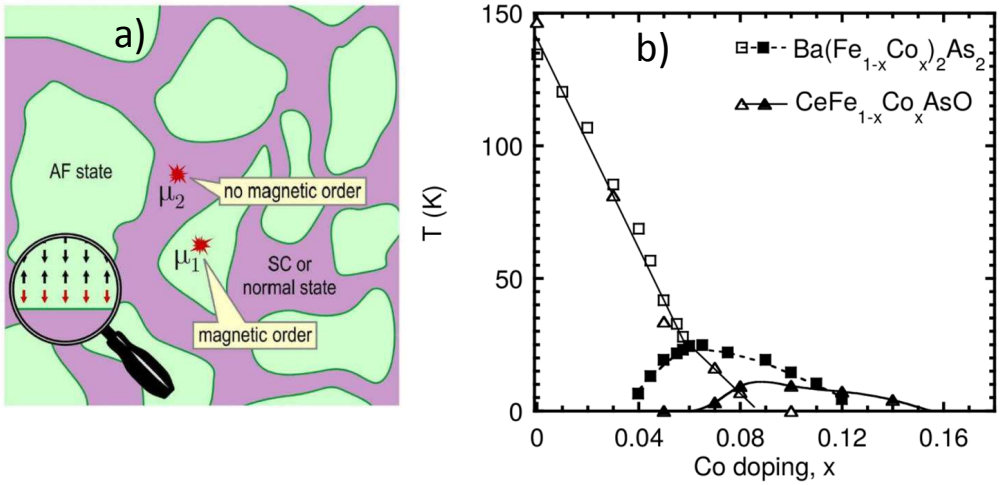

Figure 2.27: a) Sketch of the coexistence of superconducting and magnetic phases. The type of coexistence depends on the distance between magnetic and superconducting domains (Figure adapted from Ref. [185]). b) Comparison between the phase diagrams of $Ba(Fe_{1-x}Co_x)_2As_2$ [174] and of $CeFe_{1-x}Co_xAsO$ [186]. Figure adapted from Ref. [173].

magnetism is $\sim$ 1nm and thus the type of coexistence can be determined by the magnetic volume fraction well below T_m: if $V_m \sim 100\%$ the two phase are nanoscopically intertwined while if $V_m < 100\%$ we have a macroscopic segregation of the phases.

The first systematic ZF-μSR studies where conducted on the compounds belonging to the 1111 family immediately after their discovery. In the 1111 pnictides two muon implantation sites are present and their positions (see Fig. 2.26) have been calculated using DFT [187, 188, 173]. In $LaFeAsO_{1-x}F_x$ the measurements [18] revealed a sharp transition from the magnetic phase to the superconducting phase with even the $x = 0.04$ sample which is very near to the superconducting dome being completely magnetic. The asymmetry oscillations are consistent with the presence of the SDW which is the leitmotiv of the IBS. However the behavior of other electron doped 1111 compounds such as Sm1111 and Ce1111 (see Fig. 2.21 for the asymmetry) turned out to be completely different from that of La111, in fact, as we already pointed out in Section 1.1.1 these compound exhibit a significant region of the phase diagram where magnetism and superconductivity coexist nanoscopically.

A very large region of nanoscopic coexistence has also been observed in the 122 family. In Fig. 2.27b is reported the comparison between the phase digram of Co doped Ba122 and Ce1111. The coexistence region is much bigger in Ba122 than in Ce1111 and is also present in case of hole doping (e.g. K doped Ba122) indicating that this is a very general feature of this family.

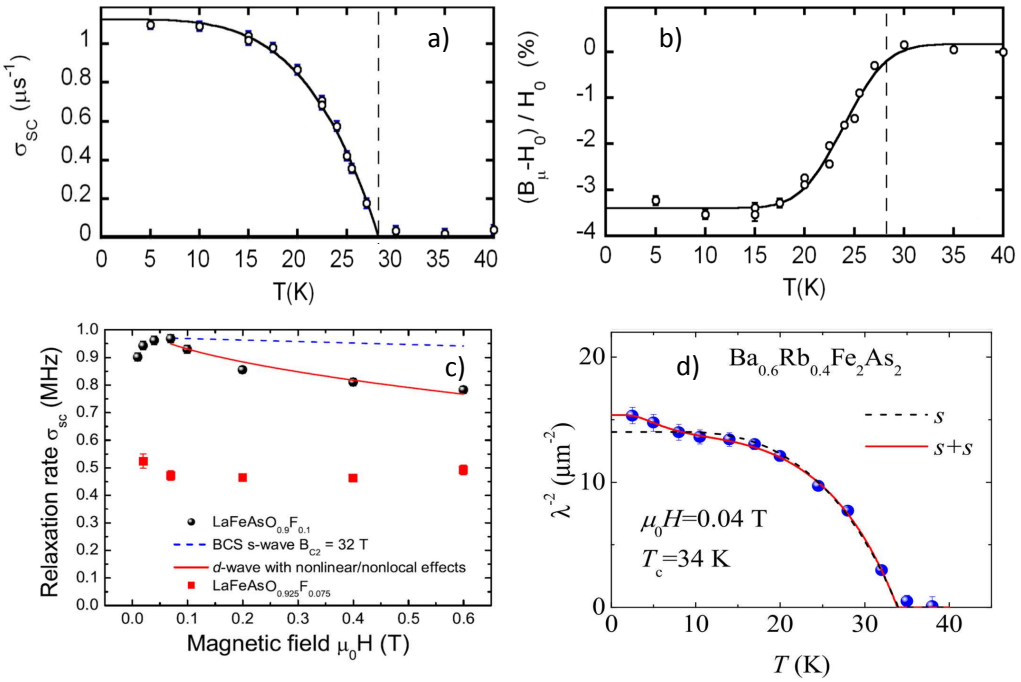

Figure 2.28: a) Temperature evolution of σ_{SC} in $LaFeAsO_{0.89}F_{0.11}$ measured with H_0 = 200G (TF-μSR). The solid line is a fit to the BCS behavior (see text). b) The corresponding evolution of the local field at the muon site. The dashed lines indicate T_c. c) Applied field dependence of $\sigma_{SC}(H_0, T = 1.6K)$. Panels adapted from Ref. [173]. d) $\sigma_{SC}(T)$ in Rb doped Ba122. As can be seen the fit is much more precise using a two gap s-wave model.

2.4.2 Transverse Filed μSR

Transverse field μSR is an excellent tool for the study of the superconducting phase properties, in particular the symmetry of the superconducting gap and the relation between superfluid density and T_c.

As explained in Section 2.3.4 the value of the London penetration depth can be promptly extracted by fitting the TF-μSR asymmetry evolution with Eq. 2.47. Since λ is directly correlated with the SC order parameter, its temperature evolution gives us a direct measurement of the symmetry of the superconducting gap [138, 173]. While this measurement is quite difficult in presence of coexistence between magnetism and superconductivity in non-magnetic samples very precise values of λ can be measured.

The temperature evolution of σ_{SC} in optimally doped La1111 is shown in Fig. 2.28. A very good fit is obtained using the s-wave weak coupling BCS two fluid model [181, 173] $\sigma_{SC}(T) \propto 1/\lambda^2(T) \propto [1 - (T/T_c)^4]$. Also, from the qualitative point of view the flat behavior of σ_{SC} at low temperature is in general a strong indication of a node-less gap. The relative shift of the local field at the muon site (see Fig 2.28b) is due to the diamagnetic shielding generated by superconductivity. A BCS like behavior was also observed in other 1111 [18] and 122 [189] compounds (see Fig.2.28a-d).

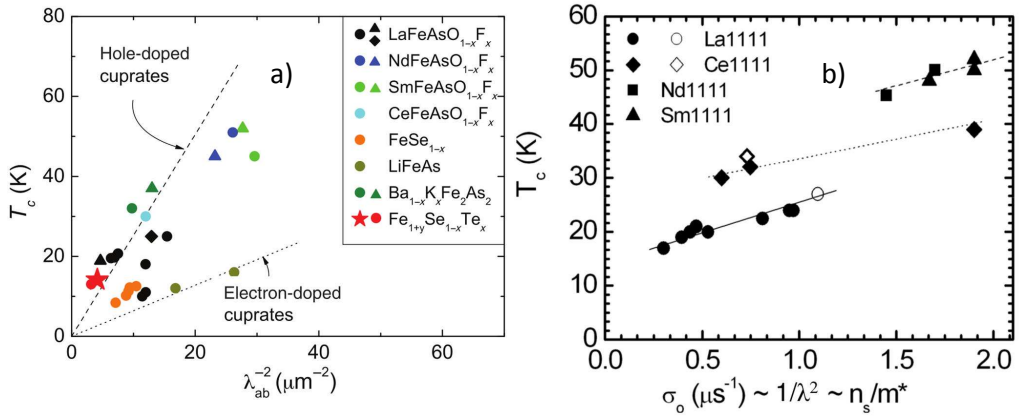

Figure 2.29: a) Uemura plot of several IBS materials. The dashed lines indicates the linear behavior observed in electron and hole doped cuprates. b) Uemura plot for the 1111 family. σ_{SC} was measured at $\sim$ 1.6 K and for the H_0 value ($\sim$ 200 G) corresponding to the σ_{SC} maximum. Figures adapted from [190] and [173], respectively.

Nevertheless the s-wave like picture is in disagreement with the field dependent measurements which show that $\sigma_{SC}(H_0, T \rightarrow 0)$ has a maximum for a magnetic field of $\sim$ 200 G and it decreases for higher fields as is expected in case of nodes in the SC gap. However this effect could also be due to the presence of multiple superconducting gaps as can be expected since in IBS five bands cross the Fermi level (see Fig. 2.28d). It must be remarked that, even if μSR results support a s-wave type gap in IBS, no information can be obtained on the sign of the gap and thus it is not possible, using this technique, to discriminate between the $s^{\pm}$ and s^{++} models.

Differently from the cuprates in IBS no clear linear dependence is found between λ^{-2} and T_c. As it can be seen by looking at the Uemura plots (T_c versus λ^{-2}) in Fig. 2.29a the various families of IBS are quite scattered between the dashed lines indicating the linear behavior of electron and hole doped cuprates. However if we now focus only on the 1111 family (Fig. 2.29b) we see that each subfamily present a linear behavior reminiscent of the one observed in cuprates.

Even if a theoretical explanation of the Uemura plot of IBS is still missing the correlation between λ and n_s strongly depends on the symmetry of the order parameter and thus on the nature of the pair breaking processes. Hence a successful modelling of these materials should be able to qualitatively reproduce the observed behavior for the various IBS families.

Chapter 3

Study of the T_c-charge doping phase diagram of Iron Based Superconductors

Understanding how the properties of iron based superconductors change with charge doping is essential in order to solve the puzzle of high temperature superconductivity in these materials. This Chapter presents a NMR-NQR study of hole and electron doped IBS with the aim of expanding our understanding of both sides of the phase diagram.

The Chapter is divided in three Sections. In the first section we present $1/T_2$ measurements in Rh doped $BaFe_2As_2$ which evidence the presence of unconventional very slow spin fluctuations in the normal phase of this material.

The second section deals with the effect of mechanical uniaxial strain (pressure) on the ^{75}As NMR properties of overdoped $Ba(Fe_{1-x}Rh_x)_2As_2$. These measurements revealed that while T_2 and linewidth are barely affected the spin lattice relaxation rate $1/T_1$ is significantly reduced, suggesting a modification of the low energy dynamics, possibly involving nematic fluctuations.

Finally the third section presents a detailed NQR and NMR study of the electronic properties of $RbFe_2As_2$ and $CsFe_2As_2$. These material can be considered hole doped Ba122 compounds where all the Ba has been substituted with Rb or Cs. Theoretical calculations have shown that the electronic correlations get stronger with hole doping and that these compounds are the IBS closest to a Mott transition, whose properties should be more similar to those of the cuprates. The NQR spectra revealed the presence of a static charge order developing in the normal state of $(Cs,Rb)Fe_2As_2$ akin to the charge order observed in cuprates. This phase had never been observed in IBS material and its presence supports the hypothesis that charge order may play a role in determining the properties of the superconducting state. Furthermore $1/T_1$ measurements in polycrystalline $RbFe_2As_2$ samples revealed a

phase separation between two phases characterized by different excitations at low temperature. This phenomenology could be related to the selective Mott physics predicted to exist in IBS material in presence of strong correlations.

3.1 Study of the low frequency fluctuations in $Ba(Fe_{1-x}Rh_x)_2As_2$

The study of the spin excitations developing in the normal state of High temperature superconductors when the static magnetic state is suppressed by charge doping or by an external pressure is crucial in order to understand if they play a role in the formation of the Cooper pair or if they actually compete with the SC phase.

Nuclear Magnetic Resonance has played an important role in this investigation, first for the cuprates superconductors and then for the IBS. While the tool of choice usually is the spin lattice relaxation rate, which is sensitive to the local field fluctuations perpendicular to the external applied field, in the cuprates several studies [155, 154, 192, 193] have also been conducted by measuring the spin-spin relaxation rate $1/T_2$ which is sensitive to the field fluctuations parallel to the applied field.

They revealed that in these materials the direct $n-n$ coupling is irrelevant [155] and the $1/T_2$ relaxation rate is significantly affected by an indirect dipolar interaction. This indirect coupling involves the electron spins and is related to the non local susceptibility. Takigawa *et al.* [155] showed that in some cuprates such as $YBa_2Cu_3O_{6.63}$ the increase of ^{63}Cu $1/T_2$ upon cooling is due to the presence of antiferromagnetic fluctuations which persist well below the temperatures at which they are weakly coupled with $1/T_1$. Pennington *et al.* [193] found that $1/T_2$ provides useful informations about the q-dependent spin susceptibility, which are complementary to those obtained from $1/T_1$. The spin-spin relaxation rate can also probe the presence of charge ordered phases such as those observed in the cuprates [124, 125, 127, 194]. In particular Wu *et al.* found a very strong increase in $1/T_2$ in correspondence to the phase transition towards the charge ordered phase. In some system this $1/T_2$ upturn is accompanied by a change in the shape of the relaxation, from Gaussian to exponential. The $1/T_2$ rise in correspondence of static charge ordering in cuprates for high magnetic fields has been attributed to the concomitant appearance of very slow spin fluctuation.

In iron based superconductors a complete understanding of the nature of spin fluctuations is still lacking. Recently several NMR and Neutron scattering experiments revealed the possible appearance of a cluster spin glass phase close to the disappearance of the magnetic order upon increasing electron doping. Conversely for lower doping levels a sharp magnetic transition takes place. Even when the spin glass order vanishes, low frequency (MHz

range) spin fluctuations persist and their origin is still far from being clear. While the amplitude of the fluctuations increase moving towards the underdoped regime what happens in the overdoped region of the phase diagram is still unsettled.

In the following a complete $1/T_2$ study of $Ba(Fe_{1-x}Rh_x)_2As_2$ is presented. Previous $1/T_2$ studies in IBS materials (see Chapter 2) revealed a longer than expected T_2 and a marked difference between the T_{2HE} measured with the Hahn echo sequence and the one measured with the CPMG sequence.

Here it is shown that $1/T_2$ is indeed an excellent probe of of the spin fluctuations. The measurements revealed that, quite unexpectedly, the spin dynamics persist well above the optimal doping and well into the overdoped region, at least up to 11% doping. Finally is was found that the vanishing of the superconducting phase in overdoped $Ba(Fe_{1-x}Rh_x)_2As_2$ is accompanied by the fading of the fluctuations, suggesting that the two phenomena could be correlated.

3.1.1 Materials, experimental methods and results

The ^{75}As NMR experiments were performed on $Ba(Fe_{1-x}Rh_x)_2As_2$ single crystals with Rh content and superconducting transition temperature (T_c) of x = 4.1% (T_c = 13.6 K), x = 6.8% (T_c = 22.4 K), x = 9.4% (T_c = 15.1 K), and x = 10.7% (T_c = 12.25 K), respectively. Details on the synthesis of the samples can be found in Chapter 1 and in Ref. [43].

T_c was determined by superconducting quantum interference device (SQUID) magnetometry prior to the NMR experiment and also checked in situ, via the observation of the detuning of the NMR probe.

The magnetic field $\mathbf{H}_0$ was applied along the crystallographic c axis. The x = 6.8%, x = 9.4% and x = 10.7% samples were measured in magnetic fields of 6.4 and 11 T. Furthermore the x = 10.7% sample was also measured for $\mathbf{H}_0$ = 17 T. The magnetic x = 4.1% sample was only measured for $\mathbf{H}_0$ = 6.4 T.

The echo decay time T_2 was measured both with the standard Hanh echo sequence ($\pi_x/2 - \tau - \pi_y$) and with the CPMG sequence ($\pi_x/2 - \tau - \pi_y - \tau - \pi_y \cdots$; see Appendix A.3.1). A $\pi/2$ duration of 3 μs has been chosen in order to irradiate the whole $\frac{1}{2} \rightarrow -\frac{1}{2}$ NMR line. Hereafter $1/T_2$ indicates the decay rate measured with the Hahn echo sequence and $1/T_{2cpmg}$ indicates the one measured with the CPMG sequence.

The spin lattice relaxation time T_1 was measured using the saturation recovery sequence ($\pi/2 - \tau - \pi/2 - \tau_{echo} - \pi$) and fitted with the standard recovery function for the central line of a spin 3/2 nucleus (Eq 2.38) [160]:

$$M_z(t) = M - 0[1 - f(0.1 \cdot e^{-(\tau/T_1)} + 0.9 \cdot e^{-(6\tau/T_1)})] \tag{3.1}$$

Both the relaxation times (T_1 and T_2) are in the 1-100 ms range and thus one can expect a sizeable contribution of T_1 processes to the echo decay (Redfield term, see Section 2.1.5). This is confirmed by the linear dependence,

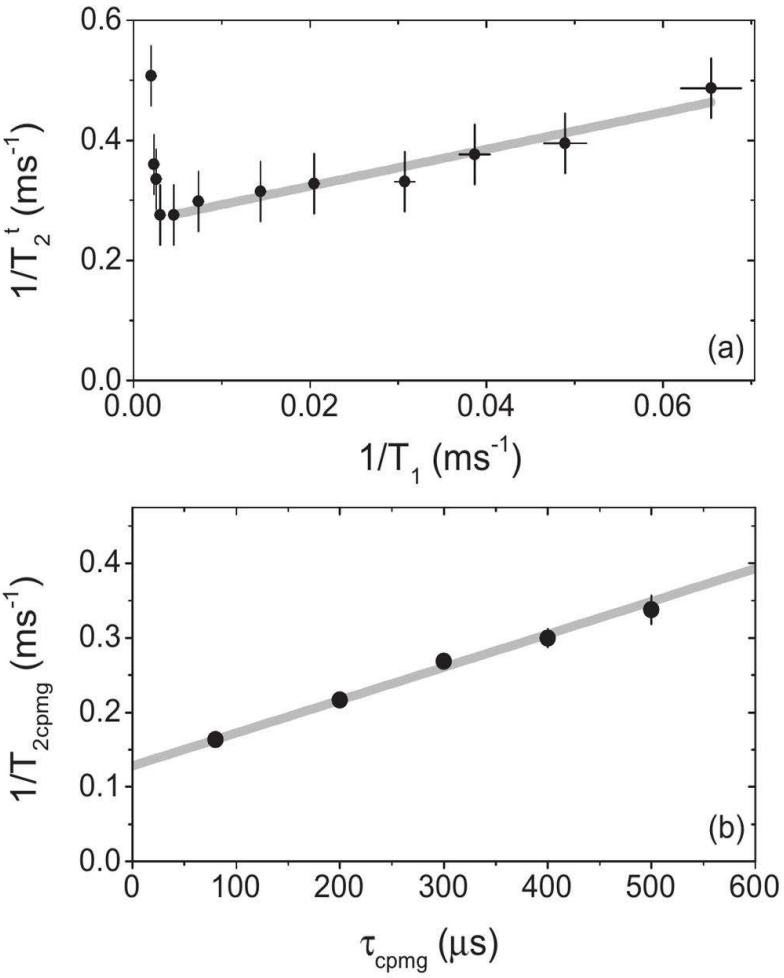

Figure 3.1: a) $1/T_2$ prior to the Redfield correction versus $1/T_1$ in the normal phase of the x = 9.4% sample (H_0 = 6.4 T). The grey line is a linear fit (T > 20 K). b) CPMG measured $1/T_2$ plotted as a function of τ_{cpmg}, for the compound with x = 6.8% (H_0 = 6.4 T; T = 70 K). The grey line is a linear fit to extrapolate $1/T_{2cpmg}$ for τ_{cpmg} = 0.

observed above 20 K, of the raw echo decay rate $1/T_2^t$ on $1/T_1$, where $1/T_2^t$ is defined as the time at which the normalized echo amplitude decays to $1/e$. In this framework the echo intensity versus time can be written as:

$$M_{total}(2\tau) = M(2\tau)\exp\left(-\frac{2\tau}{T_{1R}}\right), \tag{3.2}$$

where $M(2\tau)$ is the T_1 independent echo decay amplitude while the exponential term takes into account the T_1 contribution. In case of an anisotropic spin-lattice relaxation rate, Walstedt and coworkers [154] found that, for the central line of a 3/2 spin nucleus, the effective spin-lattice relaxation rate

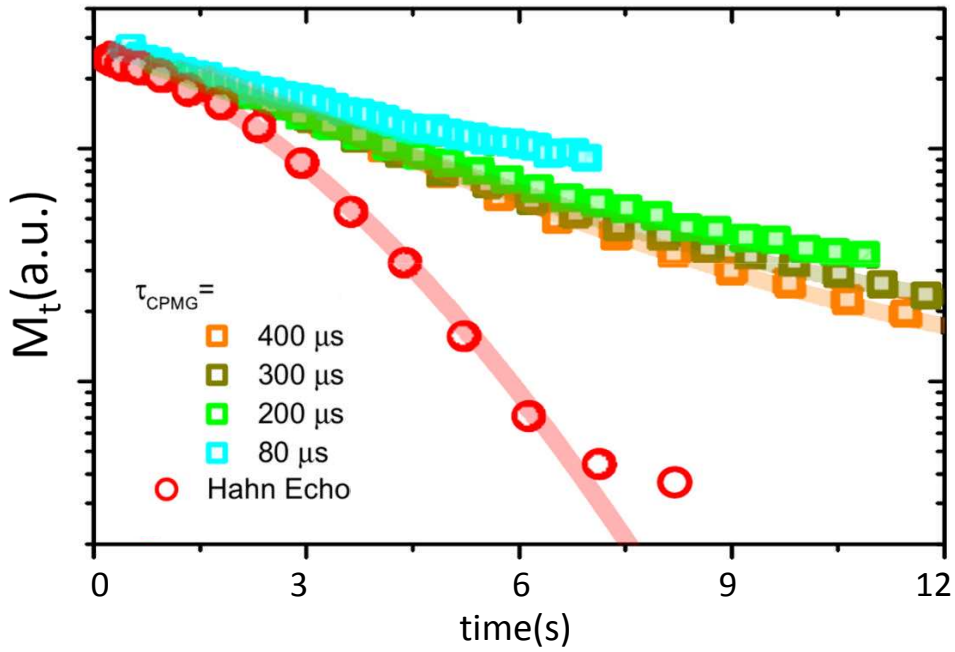

Figure 3.2: Hahn (red circles) and CPMG echo decays, measured on the x = 6.8% compound, at T = 70 K and H = 6.4 T. The delay (τ_{CPMG}) between CPMG echoes is indicated. The solid lines are the fit to a stretched exponential (Eq. 3.4) for the Hahn Echo decay and to a simple exponential for the CPMG decay.

$1/T_{1R}$ to be substituted in Eq. 3.2 is:

$$\frac{1}{T_{1R}^{\parallel}} = \frac{3}{T_1^{\parallel}} + \frac{1}{T_1^{\perp}} \qquad ; \qquad \frac{1}{T_{1R}^{\perp}} = \frac{3}{T_1^{\perp}} + \frac{1}{T_1^{\parallel}}\,, \tag{3.3}$$

where $T_1^{\parallel}$ and $T_1^{\perp}$ denote the spin lattice relaxation rates measured with the static magnetic field parallel and perpendicular to the crystallographic c axis, respectively.

The raw echo amplitude was then divided by $\exp(-\frac{2\tau}{T_{1R}})$ in order to derive $M(2\tau)$. It was found that $M(2\tau)$ deviates from a single exponential decay (see Fig. 3.2) and could be fitted, over the whole temperature range, by a stretched exponential:

$$M(2\tau) = M_0 \exp\left(-\left(\frac{2\tau}{T_2}\right)^{\beta}\right), \tag{3.4}$$

with β the stretching exponent. The stretching coefficient showed a marked temperature dependence as can be seen in Fig. 3.3: at high temperature $\beta \simeq 2$, indicating a Gaussian decay of the spin echo, while it gradually decreases upon lowering the temperature, reaching $\beta \simeq 1$ (simple exponential) close to T_c. This crossover is likely due to the growth of the spin fluctuations which give rise a $e^{-2W_2 t}$ contribution to the echo decay, where $W_2 = \gamma^2 h_z^2 \tau_c$,

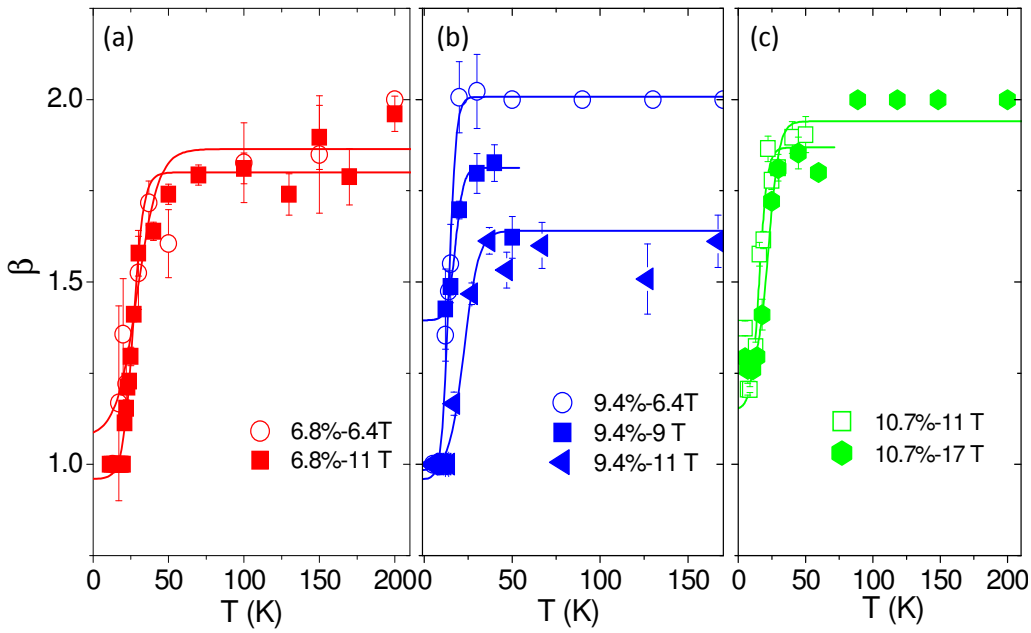

Figure 3.3: Temperature evolution of the stretching exponent β for all the samples and magnetic field. The solid lines are guides to the eye.

as can be derived in the framework of the Redfield theory (see Ref. [136], Cap. 5.12 and Ref. [195]). Some representative results of the Hahn echo decay fits to Eq. 3.4 are reported in Fig. 3.2a-c.

The echo decay time was also measured with the CPMG sequence with τ_{cpmg} ranging between 80 μs and 500 μs. The echo amplitude decays exponentially with time and thus it can be fitted using Eq. 3.4 with $\beta = 1$. The decay rate $1/T_{2cpmg}(\tau_{cpmg})$ is found to increase linearly with τ_{cpmg} as shown in Fig. 3.1b. Hence one can define $1/T_{2cpmg}$, the spin-spin relaxation rate measured with the CPMG sequence, as the limit for $\tau_{cpmg} \to 0$ of $1/T_{2cpmg}(\tau_{cpmg})$.

As can be seen in Figures 3.2 and 3.4d $1/T_2$ is much faster than $1/T_{2cpmg}$. Furthermore also the temperature behaviour of $1/T_2$ differs significantly from the one observed for $1/T_{2cpmg}$.

At high temperature (T > 50 K), the spin-echo decay measured by both methods is temperature independent with $1/T_2 > 1/T_{2cpmg}$. At lower temperatures instead the measurements revealed a strong $1/T_2$ enhancement for all the considered samples and magnetic field intensities, whose onset temperature T^* is always above T_c and can be further shifted upwards by increasing H_0. T^* can be empirically defined as the temperature below which the ratio $T_2(80K)/T_2 > 1$ is true for all the considered temperature values.

This strong echo decay rate enhancement however is not detected by the CPMG sequence as can be seen in Fig. 3.4d.

Since the π pulses of the CPMG sequence were not phase alternated, T_{2cpmg} could be affected by spin-locking effects [196, 197, 198]. This could explain the difference between T_2 and T_{2cpmg} at high temperature where both

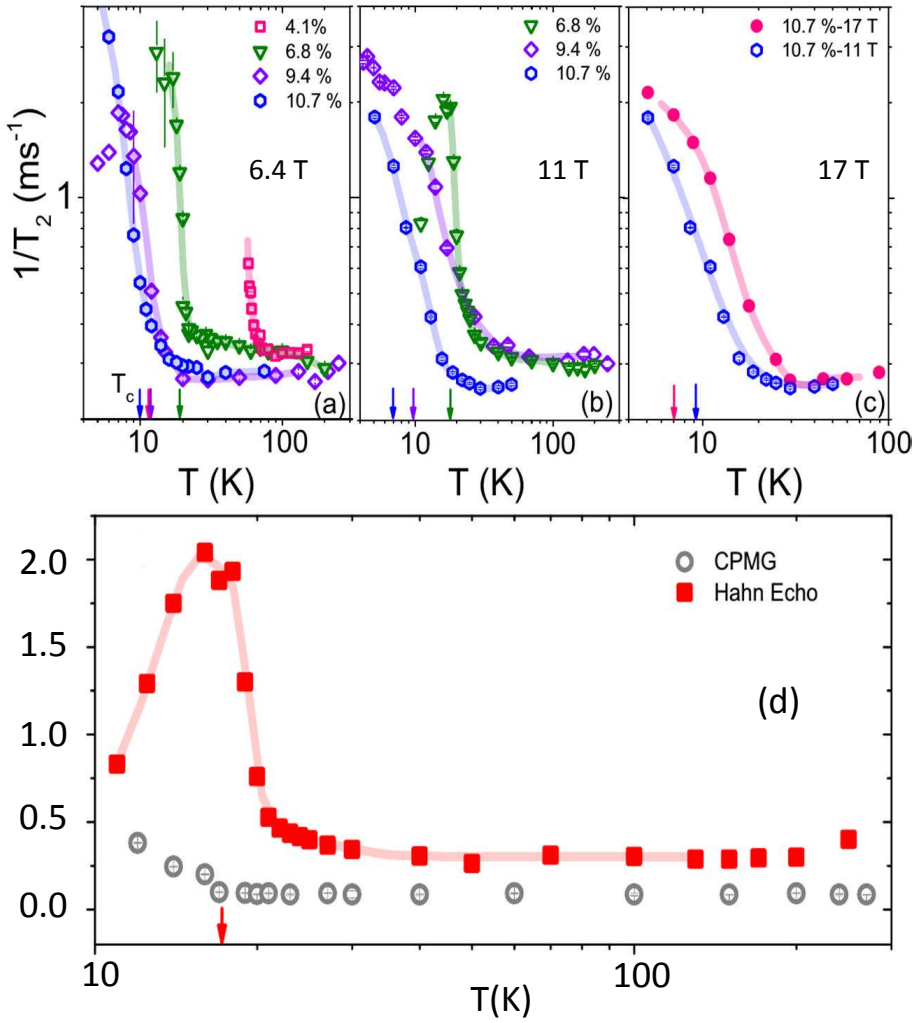

Figure 3.4: a),b) and c): Hahn Echo decay rates as a function of the temperature for different magnetic fields and doping levels. The arrows indicate T_c. d) $1/T_2$ and $1/T_{2cpmg}$ echo decay rates, as a function of the temperature, measured in a magnetic field of 11 T. The red line is a guide for the eye.

the relaxation rates are temperature independent, but this does not affect our conclusions concerning the different temperature dependence observed at low temperature.

It must be noted that at high temperatures $1/T_2 \sim 0.2$ ms^{-1} is well below the values expected from the dipolar interaction between ^{75}As nuclei ($1/T_2 \sim 1.4$ ms^{-1}), in agreement with the previous studies on Co and K doped Ba122 [171, 172].

The study of the spin lattice relaxation time revealed a very regular power law temperature behavior ($1/T_1 \sim BT^b$ where $b \sim 0.5$ is doping dependent) down to 50 K and then the emergence of a bump extending in the 10 - 50 K temperature range (see Fig. 3.6). The origin of this peculiar $1/T_1$ temperature dependence and its link to the enhancement of $1/T_2$ is thoroughly discussed

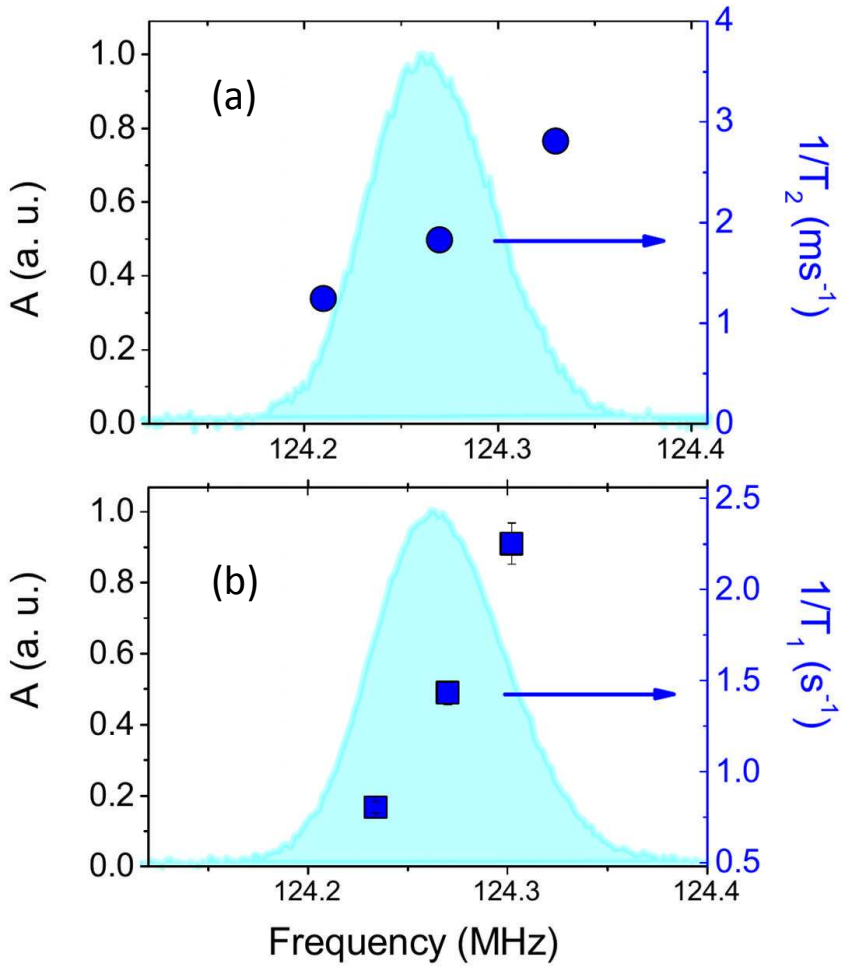

Figure 3.5: $1/T_1$ (a) and $1/T_2$ (b) as a function of frequency measured at H_0 = 17 T and T = 7 K, for the same sample (x=10.7 %). The light blue curve is the spectrum of the central line.

in the next section.

A strong frequency dependence of $1/T_1$ and $1/T_2$ has also been found (see Fig. 3.5). For the overdoped x=10.7 % sample considered in Fig. 3.5 the total variation is $\sim$ 65 %. This spectral anisotropy of the relaxation times indicates that not all the spins are at the same temperature or that a significant spin diffusion process is at work. In the following discussion the relaxation rates are always the ones measured at the centre of the spectrum. In fact, since the pulse length was chosen short enough to irradiate whole the line, they correspond to an average on the relaxation rates spectral distribution. A similar inhomogeneity of $1/T_1$ was also observed in the Co-doped compounds Ba122 [171] suggesting that this could be general feature of the 122 iron based superconductors.

The shape of a typical spectrum is reported in Fig. 3.5(light blue curve). The full width at half maximum ($\Delta\nu$ hereafter) of the ^{75}As central line was derived from the Fast Fourier Transform of half of the echo signal obtained

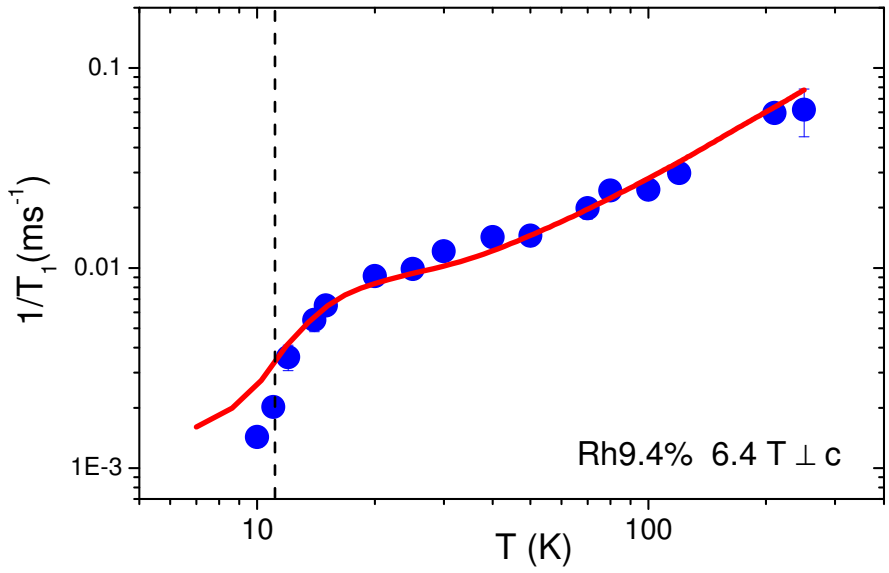

Figure 3.6: Spin-lattice relaxation rate as a function of the temperature for the x = 9.4% sample for $H_0 \perp c$ = 6.4 T. The solid red line is a fit to the BPP law reported in the text. The dashed line indicates T_c.

from a spin-echo pulse sequence. The line width was measured in the 4 - 100 K temperature range, the results for H_0 = 6.4 T can be found in Fig. 3.7. $\Delta\nu$ increase significantly in the underdoped (x = 4.1%) sample in correspondence of the magnetic transition and also in the optimally doped x = 6.8% sample, well above T_c. Its behaviour can be fitted very well using the Curie Weiss law:

$$\Delta\nu = \frac{C}{T+\Theta} + \Delta\nu_0 \ . \tag{3.5}$$

In the overdoped compound instead $\Delta\nu$ remains nearly flat for $T > T_c$ and then increase abruptly well below T_c, probably due to the freezing of the flux lattice lines (see Fig. 3.7). The study of the line width will be greatly expanded in the next chapter where we will present the analysis of the effects of proton irradiation on these compound.

3.1.2 $1/T_2$ vs $1/T_{2cpmg}$

We will first discuss the discrepancy between $1/T_2$ and $1/T_{2cpmg}$. While $1/T_2$ is very effective in refocusing the dephasing of the in-plane nuclear magnetization generated by static field inhomogeneities, the amplitude of the Hahn echo is decreased by dynamics with a fluctuation time scale of the order of the separation between the $\pi/2$ and the π pulses. Conversely the CPMG sequence is very effective is removing the effect of diffusion (see Appendix A.3.1) and the linear increase of $1/T_{2cpmg}(\tau_{cpmg})$ with the delay between the pulses (see Fig. 3.1) observed in Rh doped Ba122 is typical of

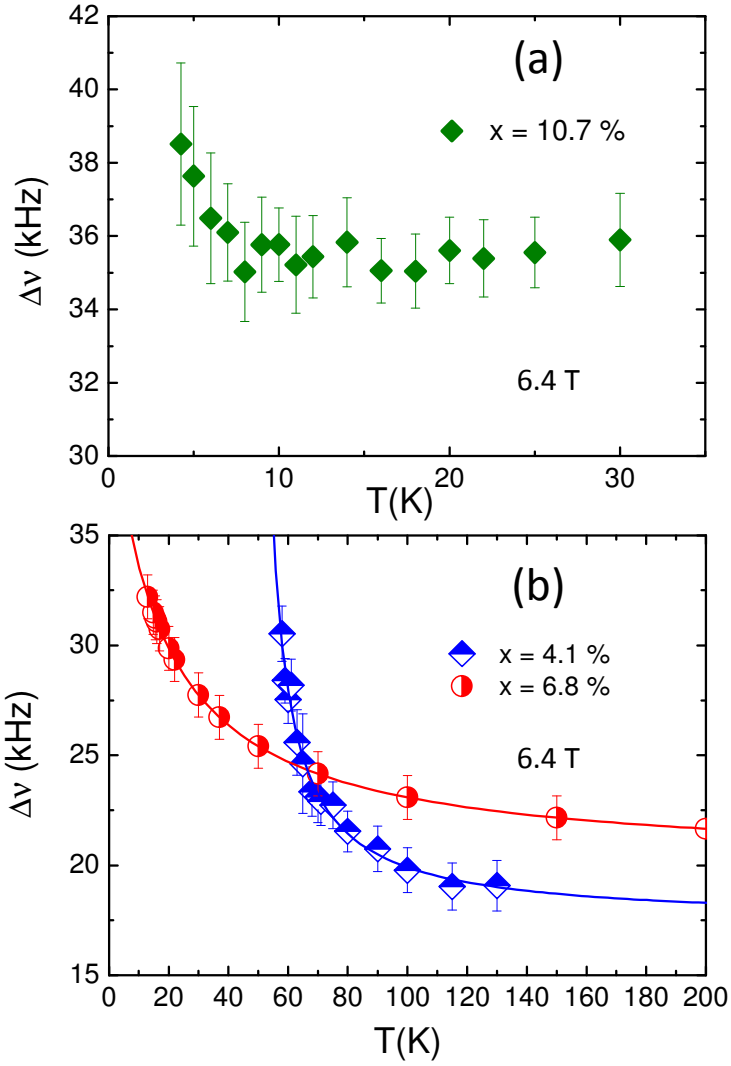

Figure 3.7: Temperature dependence of the line width $\Delta\nu$ for the ^{75}As central line for the x = 10.7% sample (a) and for the x = 6.8% and x = 4.1% samples (b). The magnetic field is $H_0 \parallel c$ = 6.4 T.

systems where a diffusive dynamic takes place. This type of behaviour is extremely common in liquids and has also been observed in solid state systems where restricted electron spin diffusion occurs in a non-uniform magnetic field, as in the case of platinum nanoparticles [199].

Since a physical diffusion of the As nuclei, akin to what often observed in liquids and ionic conductors, is impossible in the IBS materials at low temperatures, another type of mechanism must be at the origin of this dynamic. In the following when referring to spin diffusion we intend a physical process leading to a short-range polarization exchange between electron spins (spin fluctuations).

We assume the existence of an internal field gradient $\nabla\mathbf{B}$ originating from a mismatch $\Delta\chi$ in the magnetic susceptibility. The mismatch can be due to

the presence of Rh impurities or to the domain wall between stripe correlated domains with different orientations. Hence the field gradient can be written as $\nabla\mathbf{B} \sim \Delta\chi\mathbf{H}/2a$ where $\Delta\chi\mathbf{H}$ is the local magnetization and $2a$ defines a typical domain size of the inhomogeneous electronic texture. Since for a diffusion dynamic in a field gradient $\nabla\mathbf{B}$ the longitudinal magnetization $M(2\tau)$ is proportional to the $M_{diff}(2\tau) \sim \exp(-\gamma^2|\nabla B|^2 D(2\tau)^3)$ the Spin Echo sequence is strongly affected by this term while $M_{diff}(2\tau) \sim 1$ for the CPMG sequence with $\tau_{cpmg} \to 0$, in good agreement with the results reported in the previous sections. In this limit in fact $1/T_{2cpmg}$ is no longer affected by the dynamics and only the irreversible decay due to nuclear dipole-dipole interaction between ^{75}As determines the spin-spin relaxation time. The very long $1/T_{2cpmg}$ suggests that not all the As nuclei are contributing to the dipolar field distribution, as one usually expects if the nuclear spin flip-flop mechanism is quenched [136]. The suppression of spin flip-flops typically occurs when the inhomogeneous NMR linewidth is much larger than the dipolar coupling between like-nuclei (^{75}As) as is the case for the studied system. This hypothesis is further supported by the observed distribution of relaxation rates across the NMR line (see Fig. 3.5), which implies a spin-temperature distribution and thus indicates that the electronic system is highly inhomogeneous.

Robertson and Wayne showed that it is possible to describe restricted spin diffusion by an equivalent mechanism of unrestricted diffusion in a periodic field gradient (see Ref. [200, 201]). Here we assume that the internal field inhomogeneity comes from the distribution of hyperfine fields at the ^{75}As sites which also gives rise to the anomalous observed linewidth. In this framework the field gradient probed by the nuclei is given by:

$$\nabla\mathbf{B} = \frac{\pi\Delta\nu}{a\gamma}\,. \tag{3.6}$$

In a realistic scenario we can assume that $2a$ (domain size) is equal to a few lattice step. Under this hypothesis and remembering that for ^{75}As the gyromagnetic ratio $\gamma/2\pi \sim 7.29$ MHz/T we get a magnetic field gradient $\nabla\mathbf{B} \sim 10^8$ G/cm, which correspond to a Larmor frequency difference of ~4kHz for adjacent ^{75}As nuclei. This value is much larger than the ~200 Hz difference predicted by dipolar sums, supporting the observed suppression of the spin flip-flops (see Ref. [202] for a throughout theoretical dissertation of this topic).

In the reasonable assumption that the periodicity of the field gradient is similar to the diffusion length scale, the echo decay rate can be written as [200]:

$$\frac{1}{T_2}(T) = \frac{(\pi a\Delta\nu(H,T))^2}{120D(T)} + \frac{1}{T_{2cpmg}}\,, \tag{3.7}$$

where $D(T)$ indicates the temperature dependent diffusion coefficient which is directly correlated to the characteristic spin diffusion time $\tau_D(T) = a^2/D(T)$. Here we considered $1/T_{2cpmg}$ equal to the relaxation

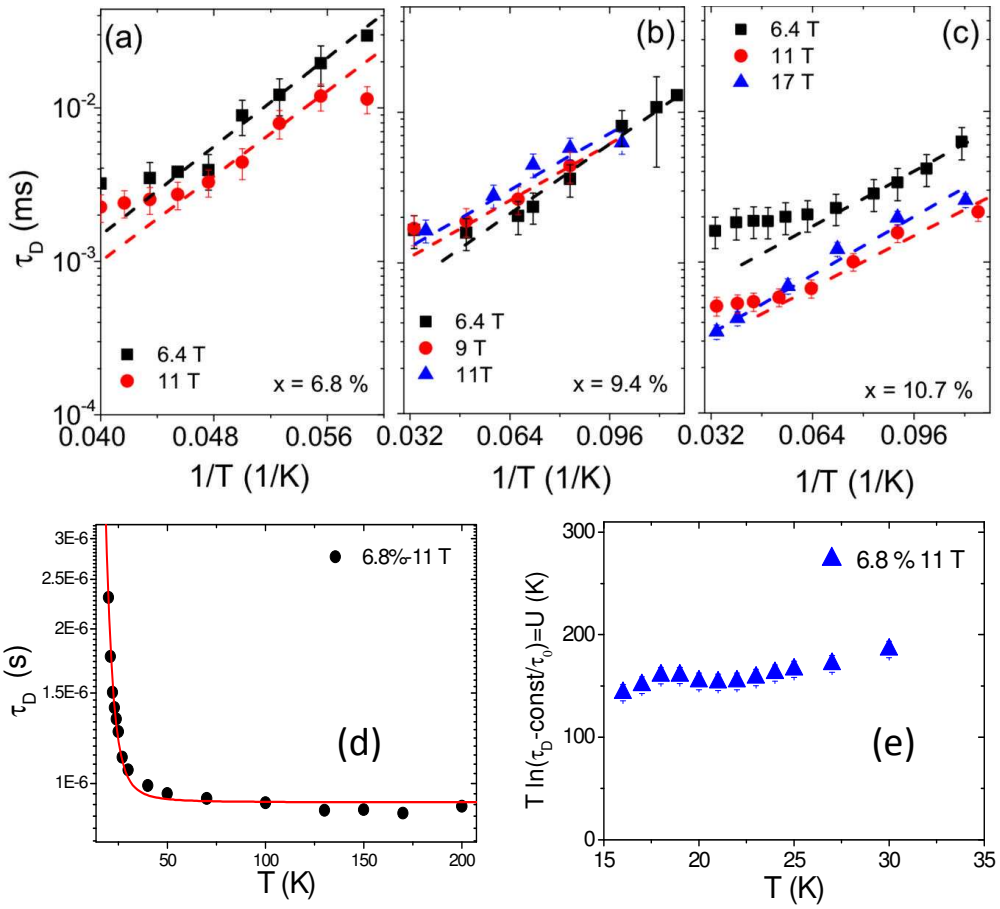

Figure 3.8: (a),(b),(c): Diffusion time τ_D as a function of temperature for all the sample doping levels and magnetic fields. The dashed lines are fits to the Arrhenius law (see text). (d) $\tau_D(T)$ and its Arrhenius fit (solid red line) in the 9.4% sample at 11 T and (e) the respective temperature evolution of the energy barrier derived from Eq. 3.7.

rate without the diffusive dynamics. The temperature dependence of the diffusion time $\tau_D(T)$ can thus be easily obtained by substituting in Eq. 3.7 the measured values of $1/T_2$, $1/T_{2cpmg}$ and $\Delta\nu$. The results can be fitted very well to an Arrhenius law: $\tau_D(T) = \tau_0 e^{U/T}$ with the constant τ_0 in the 1-100 ns range (see Fig. 3.8). As can be seen in Fig. 3.8 $\tau_D(T)$ is nearly independent from the applied field H_0 and hence also the value of the barrier is field independent. The observed filed dependence of $1/T_2$ is thus uncorrelated with τ_D and $1/T_{2cpmg}$ and it is mostly due to the field dependence of $\Delta\nu$. It should be noticed that the duration of τ_D is well into the applicability range of Eq. 3.7 [200].

Remarkably this model also allow us to nicely explain the spin lattice relaxation rate results for $\mathbf{H}_0 \perp c$ which display a low temperature hump. In fact in presence of fluctuating fields associated with the diffusion dynamic it is tempting to fit the T_1 data using the BPP theory presented in

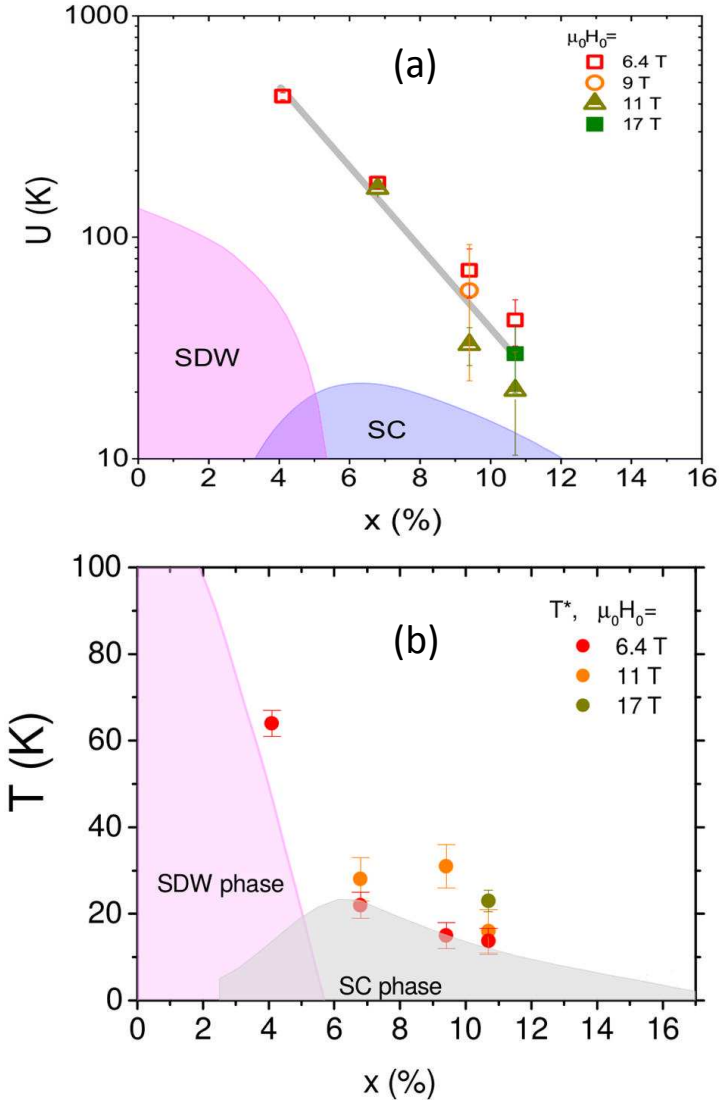

Figure 3.9: Phase diagrams with superimposed the values of U (a) and T^* (b) for all the magnetic field values.

Section 2.1.6.1 with a root mean-squared value of the transverse field of $\langle \Delta h_\perp \rangle = 2\pi\Delta\nu/\gamma$ [136]. Hence we can fit the temperature evolution of $1/T_1$ using the function:

$$\frac{1}{T_1} = A\frac{(2\pi\Delta\nu)^2}{1+(\omega_L\tau_D)^2} + BT^b\,, \tag{3.8}$$

where we took the correlation time for the filed fluctuation τ_c equal to the characteristic diffusion time τ_D. It must be remarked that in agreement with Eq. 3.8 the magnitude of the hump is roughly inversely proportional to the applied field (ω_L^{-1}) and that this feature completely disappears for $H_0 \parallel c$.

In Eq. 3.8 the first term is responsible for the BPP like behavior while the power law in the second term is a modification of the Korringa law for metals due to the presence of correlations ($b \sim 0.5$ for H=6.4 T and x=9.4%). As is

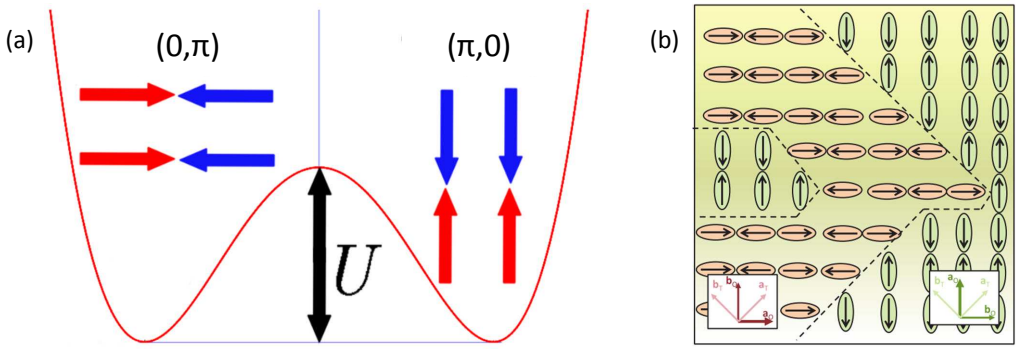

Figure 3.10: a) Sketch of the two nematic degenerate ground state separated by the energy barrier U. (b) Real space sketch of the FeAs plane with $(\pi, 0)$ and $(0, \pi)$ correlated domains. Here the arrows indicates $\mathbf{q}_{max}$ at which we have the maximum of the spin susceptibility $\chi(\mathbf{q})$ and not the static orientation of the Fe momenta below T_m. Panel (b) was adapted from Ref. [195].

shown in Fig. 3.6 the fit calculated using the same parameter obtained from the $1/T_2$ analysis is rather good above T_c, confirming that the model, despite its simplicity is describes very well the physic of in this system. Furthermore the values of the energy barrier ($U \sim 50$ K) obtained from the fit to Eq.3.8 are in good agreement with the ones obtained from the $1/T_2$ measurements.

These results clearly show that the $1/T_2$ rise universally observed above T_c in 122 materials is not due to an increasing amplitude of the spin fluctuations but rather to their slowing down to the MHz range as clearly evidenced by BPP hump in $1/T_1$. This type of slow fluctuations has also been observed [161] in $LaFeAsO_{1-x}F_x$ and thus appear to be a common feature of IBS materials.

Curiously a similar $1/T_2$ increase was also observed in cuprates materials [203] but in that case the spin lattice relaxation rate has a completely different behavior: it is nearly field independent and likely driven by the presence of high frequency correlated dynamics [204, 205, 206]. The $1/T_2$ increase in cuprates was subsequently attributed to the appearance of charge ordering [124].

A possible explanation for the low frequency fluctuations observed in the IBS can be found in the framework of frustrated magnetism. In fact the IBS systems, even in the over-doped regime where correlations are weaker, can be reasonably described by the J_1-J_2 model (see Chapter 1, Sections 1.2.3 and 1.3). In this framework the presence of very slow fluctuations has been predicted [207] and then observed [208] in vanadates, the prototype system of the J_1-J_2 model. These dynamics are associated to the motion of domain walls separating $(\pi, 0)$ and $(0, \pi)$ correlated regions. These two ground state in fact are degenerate and thus slow quantum fluctuations can occur between the two with U being the energy barrier separating the ground states (see Fig. 3.10). Remarkably the domain walls are intrinsic non-equilibrium

systems since, as was shown by Chandra *et al.* [207] they have an excess of free energy that will induce the motion in order to minimize their area.

Interestingly the energy barrier U values decrease while increasing the Rh doping and T^* tracks T_c across whole the phase diagram, suggesting that the fluctuations and superconductivity vanish together.

3.1.3 Conclusions

We presented a spin-spin relaxation rate ($1/T_2$) study of the fluctuations in Rh (electron doped) $Ba(Fe_{1-x}Rh_x)_2As_2$. $1/T_2$ was measured using both the Hahn spin echo and the CPMG sequence techniques. The comparison between the two types of measurements revealed the presence of low-frequency fluctuations in the normal phase of this IBS material extending well into the overdoped region of the phase diagram. The experimental data can be fitted very well in the framework of a simple restricted spin diffusive dynamics model. Remarkably the same model can also explain the temperature dependence of the spin lattice relaxation rate if the parameters derived from the $1/T_2$ analysis are substituted in the standard BPP theory describing the T_1 relaxation in presence of fluctuating fields. These results are consistent with the hypothesis that the IBS materials are characterized by the presence of very slow fluctuations possibly originating from the motions of domain walls separating $(\pi, 0)$ and $(0, \pi)$ correlated regions.

3.2 Effect of uniaxial strain on the low frequency dynamics in $Ba(Fe_{0.932}Rh_{0.068})_2As_2$

Since the low energy fluctuations probed by $1/T_2$ are likely due to nematic fluctuations, it would be unenlightening to study how the relaxation rates vary in presence of uniaxial strain. In this section we present additional ^{75}As NMR results obtained in the optimally doped $Ba(Fe_{1-x}Rh_x)_2As_2$ (x=0.068) sample in presence of uniaxial strain.

Uniaxial strain has been widely [209, 210, 211] employed on Ba122 compounds (single crystal) in order to remove the twinning effect in the orthorhombic state, thus allowing one to study the intrinsic electronic properties of the material, such as the anisotropy of the resistivity in the ab plane.

In particular it was found that, in the strained samples, an in plane resistivity anisotropy arise well above the T-O transition temperature T_O (see Section 1.3). This anisotropy has been attributed to a spin nematic phase breaking the C_4 rotational symmetry and it vanishes with increasing charge doping, in proximity of the maximum of T_c.

Neutron scattering measurements carried out by Lu *et al.* [213] also showed that, for low uniaxial strain-pressure values ($\epsilon =\sim 15$ MPa), the low-energy spin excitations change from fourfold symmetric to twofold symmet-

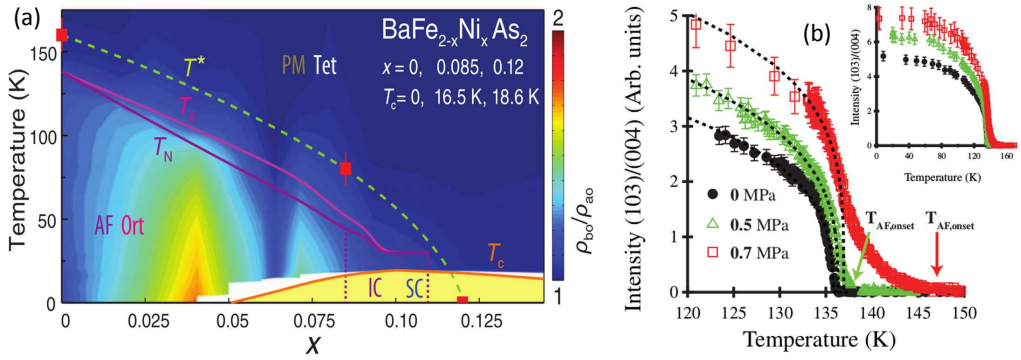

Figure 3.11: a) Electronic phase diagram of $BaFe_{2-x}Ni_xAs_2$ obtained from the resistivity anisotropy ratio ρ_b/ρ_a under uniaxial pressure (see Ref [212]). The temperatures below which the spin excitation anisotropy is detected by neutron scattering are marked as T^*. The T-O transition temperature is indicated by T_s and the magnetic transition temperature by T_m. Figure adapted from [213]. b) Intensity of the AF peak measured with neutron diffraction, plotted as a function of temperature for different pressures applied along the b axis. The inset shows the magnetic phase transition over the entire temperature range. The dashed lines are power-law fits. Figure adapted from [213].

ric at temperatures well above T_O (see Fig. 3.11a) and persist up to the overdoped region of the Ba122 phase diagram.

In underdoped Ba122 it was found that external strain along the a or b axis gives rise to a parallel increase of both of the T-O transition temperature and the magnetic transition temperature [214, 215, 216, 217], with the T_m (T_O) shift being strongly dependent on the strain magnitude (see Fig. 3.11b). This is in contrast with the studies carried out using hydrostatic pressure which revealed that T_m and T_O are suppressed upon increasing the external pressure and eventually superconductivity is recovered even in the undoped compound [218]. The behaviour of T_c as a function of the strain was found to be markedly doping dependent: in P doped $BaFe_2As_2$ T_c decrease with strain in the underdoped samples while it is enhanced by strain in the overdoped ones.

No systematic study about the influence of strain on the spin fluctuations however could be found in the literature. As explained in Section 3.1, ^{75}As $1/T_2$ measurements revealed the presence of very slow spin fluctuations in Rh doped $BaFe_2As_2$ and the onset temperature of the $1/T_2$ rise, signalling the emergence of these dynamics, has been found to be strongly field dependent. Just like the resistivity anisotropy and the twofold spin fluctuation revealed by neutron scattering, these slow fluctuation persist even in the overdoped $x = 0.107$ sample.

In order to understand if the cell structure deformation due to uniaxial strain has some effect on the activation energy of the fluctuations or on their onset temperature we carried out NMR measurements analogous to those reported in Section 3.1 but this time with an uniaxial strain applied to the

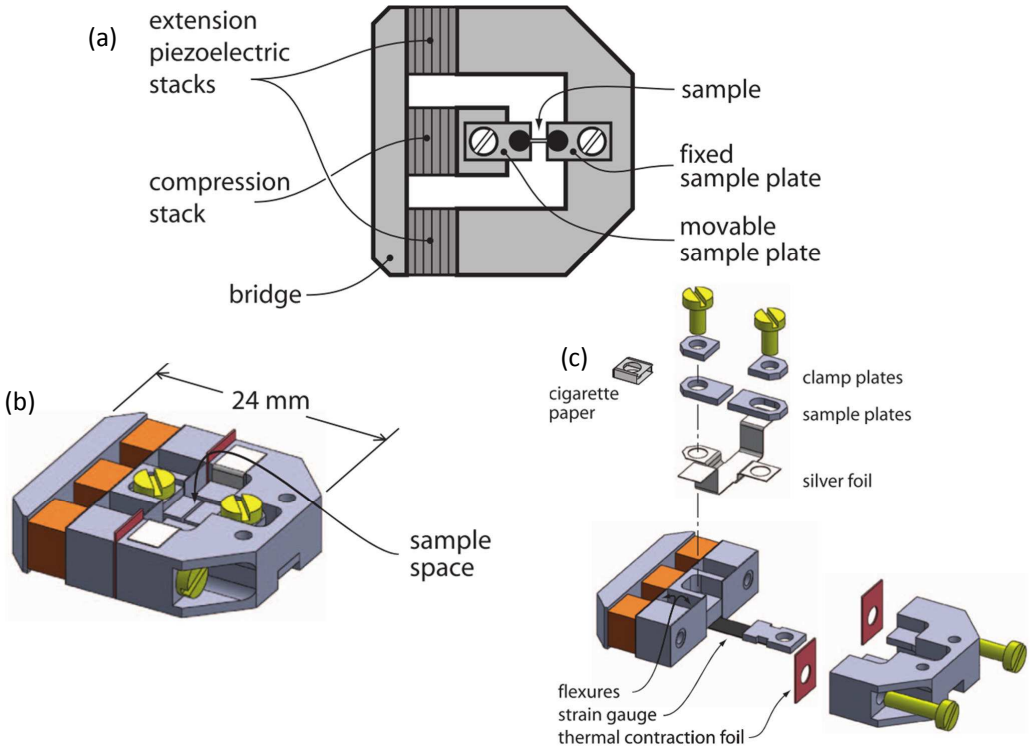

Figure 3.12: (a) Top view scheme of the strain apparatus. (b) and (c) 3D views of the strain apparatus, (b) mounted rig, (c) exploded view. Figure adapted from Ref. [219].

sample. The sample chosen for this study was the $Ba(Fe_{0.932}Rh_{0.068})_2As_2$ single crystal already used for the study reported in Section 3.1.

3.2.1 Experimental Set-Up

All the NMR measurements have been carried out at the IFW institute in Dresden. The uniaxial strain has been applied using a piezoelectric-based apparatus developed by Hicks *et al.* [219] (see Fig. 3.12 and Fig. 3.13). In this set-up the sample is solidly fixed with epoxy between two plates (Fig. 3.12), one of which is fixed while the other can move. The position of the mobile plate with respect to the frame of the strain rig can be adjusted by three piezoelectric stacks which are joined at one end by a bridge. The stacks employed in the strain rig are 18 mm long lead zirconium titanate (PZT) PICMA stacks from Physic Instrumente. At room temperature the working voltage range is -20/+120 V while at low temperatures (< 30 K) a -300/+300 V range is recommended and a maximum ~0.05% stack extension is achievable.

The polarity of the centre piezoelectric stack is opposite to the one of the lateral stacks: a positive voltage applied to the central stack extends the stack and compresses the sample, while a positive voltage on the outer two stacks

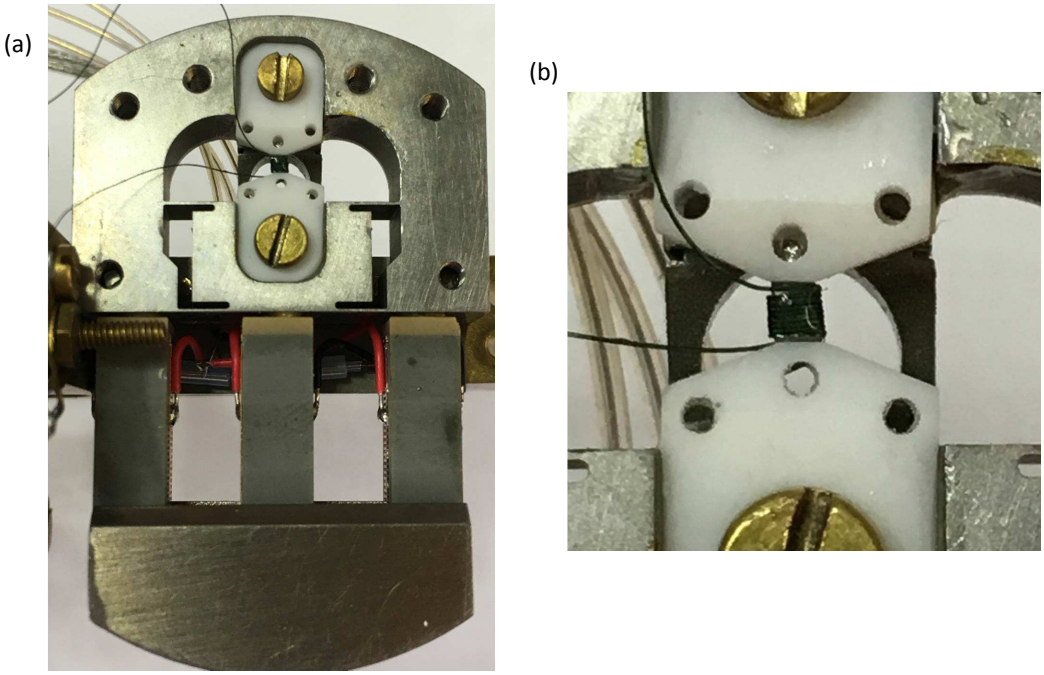

Figure 3.13: (a) Photo of the strain apparatus mounted on the NMR probe. The sample is barely visible inside the dark green coil at the centre of the white alumina mounting plates. (b) Zoom of the NMR coil containing the sample. The gap between the sample plates is 1.5 mm, which corresponds to the section of the sample which is effectively strained (and measured with NMR). The remaining 1.5 mm of the sample length are used to glue the crystal to the plates.

pushes the bridge outwards and tensions the sample. Hence in order to reach the greatest achievable strain a negative voltage can be applied to the centre stack while a positive one is applied to the external stack. However negative voltage results in a slow stack degradation. Hence, in order to extend the life of the stacks, we decided to apply a positive voltage to the external stack in order to strain the sample while the central stack was short circuited. A variable plate capacitor is fitted below the sample space and the direct measurement of its capacity, using an high precision capacitance bridge, allows us to work out the relative displacement of the sample plates.

We indicate the relative sample longitudinal expansion under strain with $\Delta L/L_0$ where L_0 is the length of the sample at 300 K when no strain is applied and ΔL the length variation upon applying a voltage to the stacks.

It should be noted that since the piezoelectric stacks are hysteretic it is not possible to rely on a direct voltage to strain conversion and it is necessary to continuously monitor the capacity in order to have a reliable estimate of $\Delta L/L_0$. Furthermore, at low temperatures the stacks have a very long relaxation time, which means that after the voltage is applied they lengthen nearly immediately to a certain value close to the final one but then they keep getting longer for several hours. This very slow lengthening account

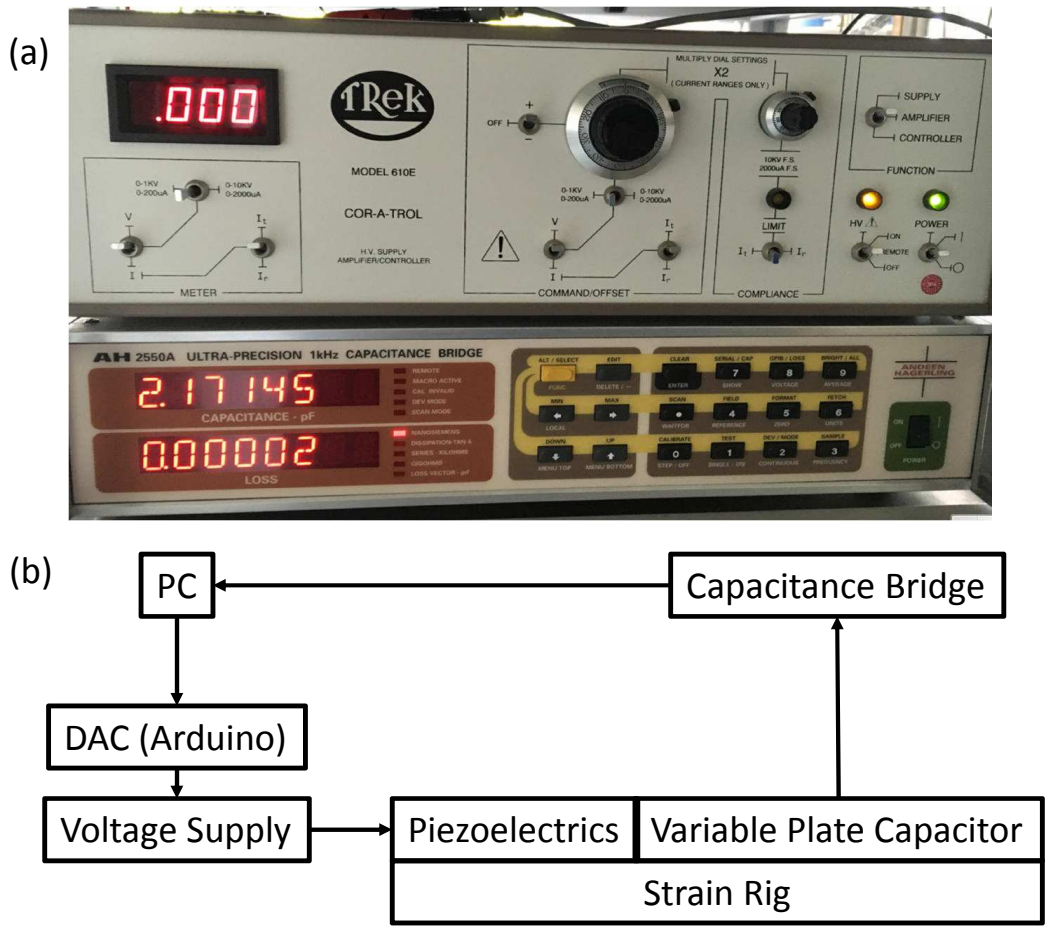

Figure 3.14: (a) Photo of the voltage supply (top) and of the high precision capacitance bridge (bottom) used to control the strain rig. (b) Scheme of the control loop of the strain rig.

for a few percent of the final total length of the stacks and obviously it is an unwanted effect since it would force us to wait a significant amount of time after polarising the piezoelectrics before starting the NMR measurements.

In order to solve these problems and to have a more reproducible and stable sample strain we set up a very simple PC controlled control loop in order to dynamically regulate the voltage applied to the stacks. The scheme of the loop is reported in Fig. 3.14: the capacity of the variable plate capacitor is read by the capacitance bridge and sent to a PC through a serial port, the computer then evaluates the difference between the target capacity and the actual capacity and feeds it to an appropriately tuned PID algorithm which computes a new voltage value which is then sent to the voltage supply (Fig. 3.14,top) as a continuous low voltage generated by a USB connected DAC (Arduino DUE development board, 0-2 V range), amplified by 100, and then applied to the stacks. The control loop allowed us to obtain a very stable strain (target $\Delta L \pm 50$ nm), to completely automate the strain control and implement several safety features. For example the voltage is turned off if

the temperature control is lost (e.g. due to an empty LHe dewar), preventing the sample from breaking.

The $Ba(Fe_{0.932}Rh_{0.068})_2As_2$ 3[100]×1[010]×0.05[001] mm single crystal was inserted in a custom made coil and then mounted on the rig with the strain vector oriented along the [100] (Fe–Fe bond) direction. The sample was clamped between the two alumina support plates and glued to them using Stycast 1266 epoxy. Since alumina is an insulator the metallic $Ba(Fe_{0.932}Rh_{0.068})_2As_2$ sample is electrically separated from the strain rig and thus the NMR signal/noise ratio is improved. Furthermore the alumina thermal expansion is very similar to that of titanium, the metal used for the construction of the rig, making it very good for this application.

We choose, for $T \sim 20$ K, $\Delta L \sim 6$ μm and thus since the strained part of the sample is 1.5 mm long, $\Delta L/L_0 \sim 0.25\%$. Since the piezoelectric stacks are hysteretic the applied voltage was different from one temperature cycle to the other, but always larger than 100 V.

In order to correctly calculate the strain on the sample however we also have to take into account that the PZT piezos, differently from most the other materials significantly lengthens (0.1%) along the poling direction upon cooling. While the geometry of the cell (parallel piezos mounted to the same bridge) cancel out most of this effect a still significant ∼3.5 μm expansion of the sample gap was measured upon cooling down to 20 K. Furthermore the $Ba(Fe_{0.932}Rh_{0.068})_2As_2$ sample should contract by ∼0.15% (ΔL ∼2.25 μm) upon cooling which should also be added to the other two terms for a total contraction of ∼12 μm ($\Delta L/L_0$ ∼0.8%) which is a very significant lengthening. The total applied force can be calculated using the relation:

$$F = EA\frac{\Delta L}{L_0} \tag{3.9}$$

where F is the force, E ∼55 GPa [220] the young modulus and $A \sim 5{\times}10^{-8}m^2$ the area of the sample section [219]. From Eq. 3.9 we find that F ∼20 N and the uniaxial stress is S ∼0.44 GPa, pretty large when compared to the stress-pressure commonly used to detwin the $BaFe_2As_2$ samples (∼10 MPa).

3.2.2 ^{75}As NMR measurements

The strain rig was screwed at the bottom of a standard NMR probe and the measurements carried out in the 20-35 K temperature range. Measurements in the proximity of T_c (∼ 21 K) were very difficult due to the enhanced screening (skin effect) and to the very high quality factor Q of the tank circuit used. Q was so high that near T_c even a tiny 0.05 K temperature variation was enough to move the resonance of the tank circuit away from the Larmor frequency. Degrading the quality factor of the circuit, for example mounting a small resistor (∼2 Ω) in series with the coil, was not feasible since the signal to noise ratio was already very low. The low signal to noise ratio is

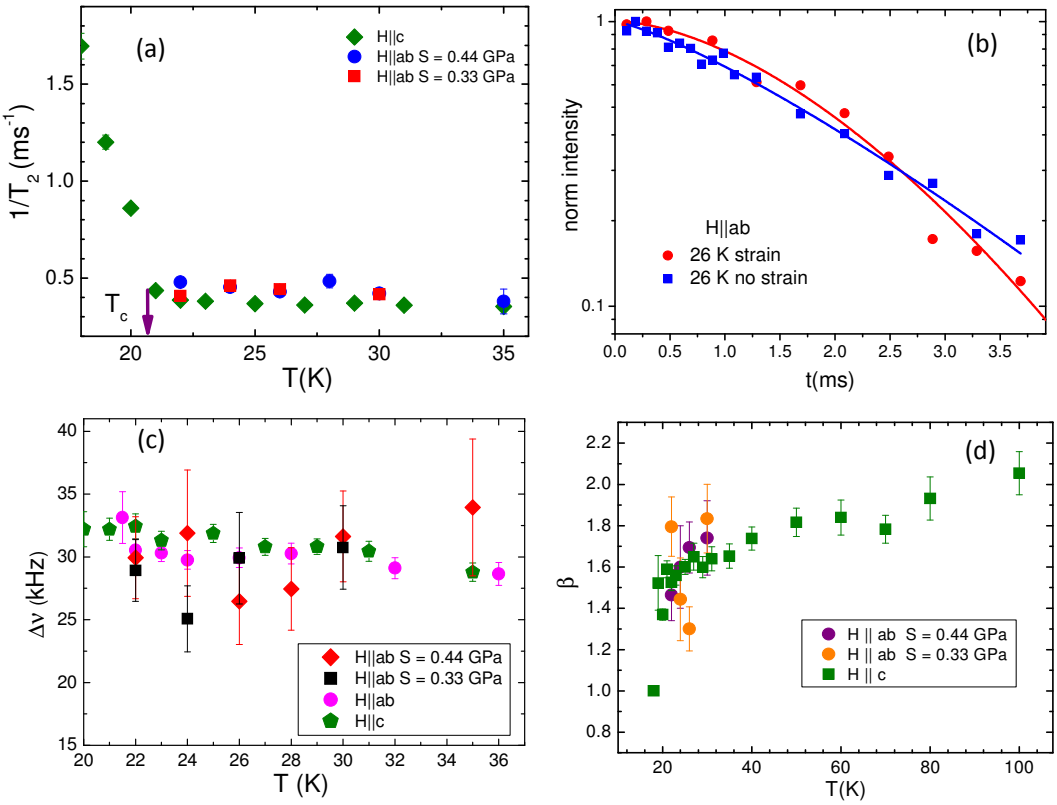

Figure 3.15: (a) $1/T_2$ temperature evolution for different stress values. (b) Comparison of the echo intensity decay with and without uniaxial strain. (c) Temperature evolution of the ^{75}As line width. (d) Temperature evolution of the stretching coefficient β (see Eq. 3.4).

mainly due to the noise caused by the piezoelectrics voltage supply and is not affected by the control loop electronics.

It should be noted that surprisingly T_c, estimated from the detuning temperature of the tank circuit, is barely affected by the strain: for $S \sim 0.44$ GPa we detected a very small ~ 1 K T_c drop.

All the NMR measurements were carried out and analysed using the same methods explained in Section 3.1.

The temperature evolution of ^{75}As $1/T_2$ and line width is reported in Fig. 3.15. As can be seen these properties are strain independent in the whole considered temperature range. However, unluckily, it was impossible to measure $1/T_2$ under strain in correspondence of T^* due to its proximity with T_c for $H = 7$ T and thus no definitive conclusion can be draw on the effect of the strain on the very low frequency fluctuations giving rise to the $1/T_2$ upsurge in $Ba(Fe_{1-x}Rh_x)_2As_2$. Future experiment with a modified set-up or with in an higher magnetic field to decouple T^* from T_c may clarify this point.

Differently from the $1/T_2$ case a very strong effect originating from the

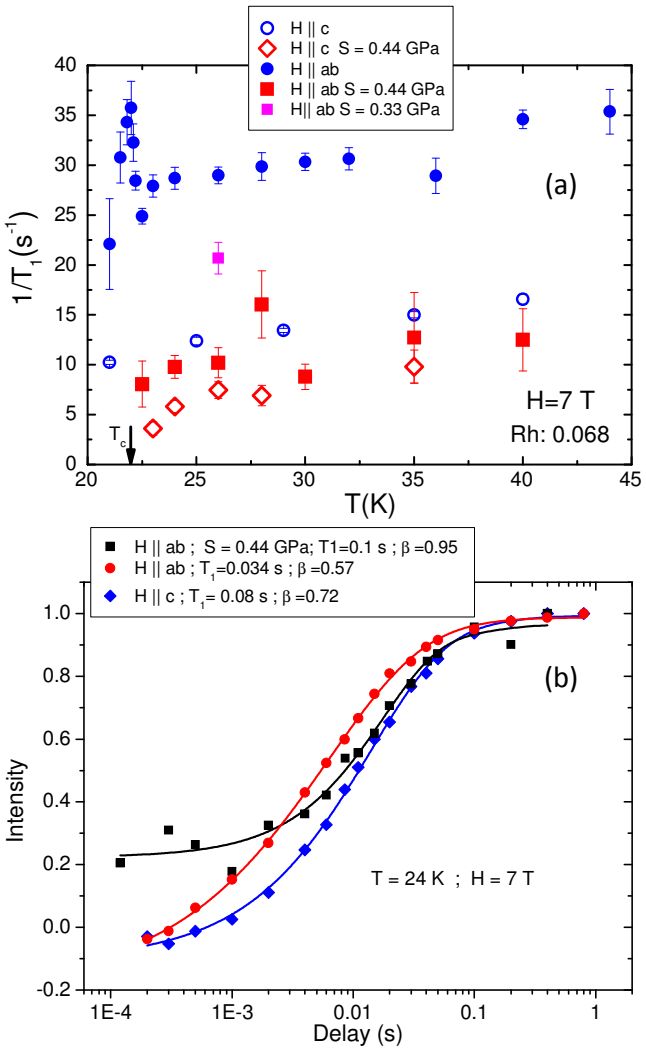

Figure 3.16: (a) ^{75}As $1/T_1$ temperature evolution for different stress values and field orientations. (b) Comparison of the transverse magnetization recoveries with and without uniaxial strain.

applied longitudinal stress was observed in the ^{75}As $1/T_1$ temperature dependence.

In the unstrained sample a significant $1/T_1$ anisotropy with respect to the direction of the applied field had already been observed in previous works [113] and ascribed to the suppression of the slow fluctuations, also responsible for the $1/T_2$ rise. The sharp peak emerging in $1/T_1$ for $T < T_c$ (see Fig. 3.16a) is probably associated with the motion of the flux lattice lines (see Ref. [221]).

As it can be seen in Fig. 3.16a in the strained sample we observed a marked, nearly temperature independent, reduction of $1/T_1$. The effect is particularly significant for H parallel to the ab plane with $1/T_1$ decreasing from ~30 s^{-1} to ~10 s^{-1}. It should also be noted that remarkably the $1/T_1$

anisotropy is nearly completely suppressed by the strain.

Furthermore also the stretching exponent of the recovery curve increases from ~ 0.6 to ~ 1 upon straining the sample, indicating that the T_1 distribution is removed by the stress, leading to a single exponential recovery law.

These findings suggest that the uniaxial strain is capable of suppressing the inhomogeneous spin fluctuations present in the 122 compounds, which, in the non strained sample, are responsible both for the T_1 anisotropy [113] and for the stretched exponential magnetization recovery law [195]. It should however be noted that part of the observed effect could be due to a modification of the quadrupolar relaxation rate induced by the modification of the lattice geometry in presence of uniaxial strain. However this term is usually much smaller than the magnetic relaxation component in IBS materials (see Section 3.3).

3.2.3 Conclusions

We carried out an ^{75}As NMR study of optimally doped $Ba(Fe_{0.932}Rh_{0.068})_2As_2$ in presence of uniaxial strain. The measurements were carried out with the sample mounted on a custom made piezoelectric based strain apparatus which allowed us to apply a significant uniaxial stress (up to 0.44 GPa) along the [100] direction of a $Ba(Fe_{0.932}Rh_{0.068})_2As_2$ single crystal.

Surprisingly T_c was found to be only weakly affected by the strain ($\Delta T_c \sim 1$ K for $S \simeq 0.44$ GPa).

While the $1/T_2$ results were inconclusive since it was not possible to carry out measurements in the temperature range (< 20 K) in which the $1/T_2$ upsurge was observed in the unstrained samples, the $1/T_1$ measurements revealed a significant $1/T_1$ decrease in the 20 K - 35 K temperature range. The effect is particularly strong for $H \parallel ab$ and results in the nearly complete disappearance of the $1/T_1$ anisotropy present in the unstrained sample.

This result suggest that the spin fluctuations revealed by NMR [195, 113] are suppressed by the uniaxial stress but other experiments are needed in order to shed new light on the $1/T_2$ behaviour and on the relation between these low frequency fluctuations, strain and chemical doping. In fact, quite interestingly, the results described here are in disagreement with the measurements carried out in strained undoped $BaFe_2As_2$ by Kissikov *et al.* [222, 223] who observed an increase of $1/T_1$ for $H \parallel ab$ in the orthorhombic phase developing just above T_n, suggesting that in the sample without Rh the uniaxial strain may instead enhance the nematic fluctuations.

3.3 Charge order and low temperature phase separation in (Rb,Cs)Fe_2As_2

The IBS have several astonishing similarities with the cuprates superconductors as we have thoroughly described in Chapter 1. However, while the

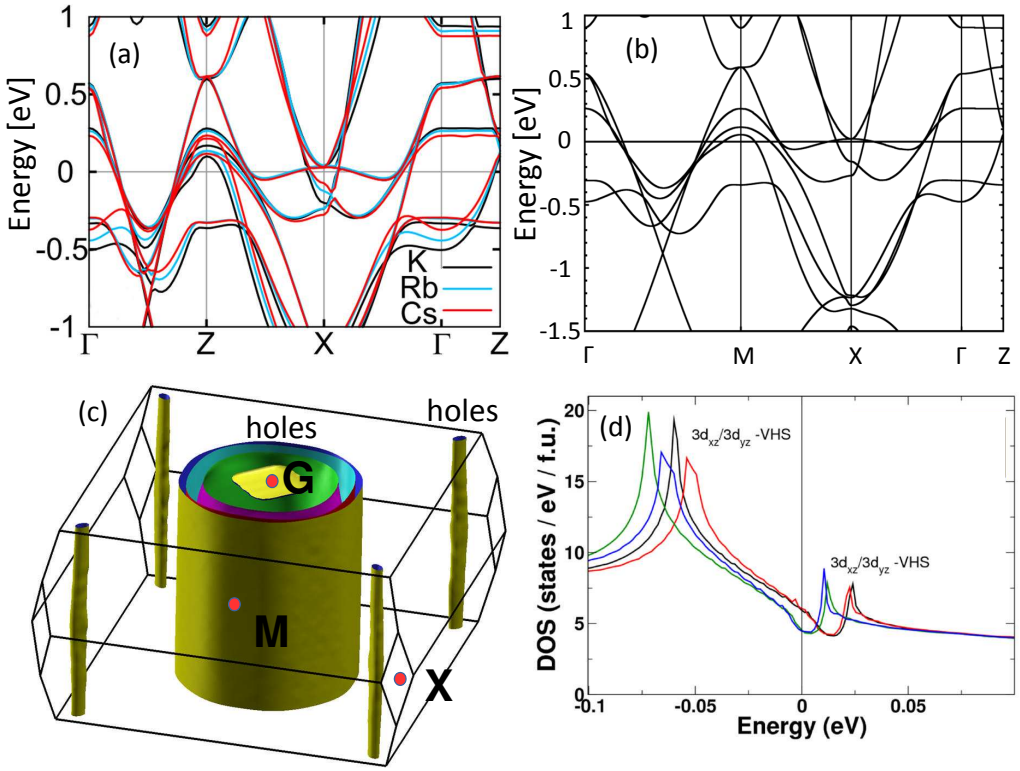

Figure 3.17: a) Band structure of AFe_2As_2 reported in Ref [224] (calculated with GGA-PBE, WIEN2K). (b) $RbFe_2As_2$ band plot calculated by us using the Elk package (FP-LAPW, GGA-PBE) and the corresponding Fermi surface (c). (d) The Van Hove singularity (VHS) in the DOS at $\sim$ + 10-25 meV calculated in Ref. [225]. The VHS is independent from the details of the calculation: GGA/LDA(black/green) with or without spin orbit (red/blue)), however it is only visiblke if the k-mesh is very dense ($> 50^3$).

undoped cuprates are Mott insulators at half band filling, where the large Coulomb interaction U overcomes the transfer integral t and gives rise to an insulating antiferromagnetic ground state, the undoped IBS are not Mott insulators but strongly correlated metals well above half band filling.

In cuprates the electronic correlations remain very strong upon charge doping well into the superconducting state, giving rise to a very complex phase diagram at low hole doping levels characterized by the onset of a charge density wave (CDW) coexisting with superconductivity up into the overdoped region [128].

In IBS it is possible to approach the half band filled condition (5 3d electrons per Fe atom) by doping with holes. Hence the study of the hole doped region of the phase diagram is very interesting since these compounds are those whose ground state is more similar to that of the cuprates and thus could share some of their characteristic macroscopic properties, such as the presence of charge density wave.

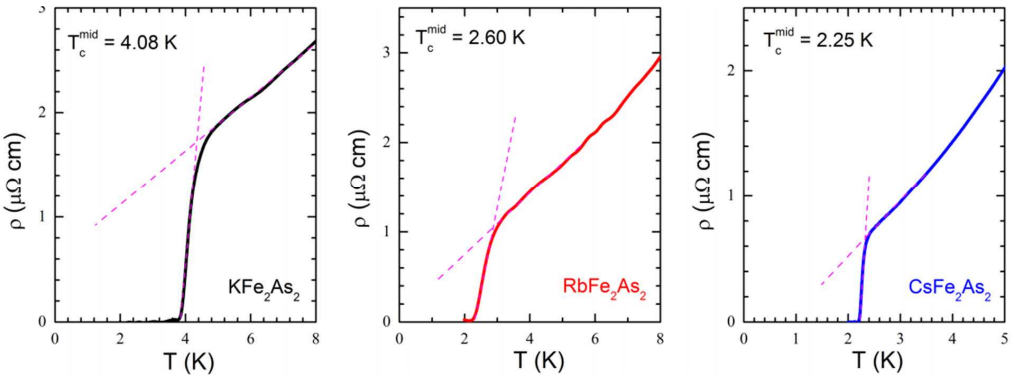

Figure 3.18: Temperature dependence of the resistivity in AFe_2As_2. T_c was defined as the mid-point temperature of the superconducting transition. Figure adapted from Ref. [133].

In this Section we present an extensive NQR and NMR study of $RbFe_2As_2$ and $CsFe_2As_2$. AFe_2As_2 compounds, where A=K, Rb, Cs, can be considered hole doped $BaFe_2As_2$ where all the Ba^{2+} has been substituted by an alkali metal A^{1+}. This doping level correspond to one hole per formula unit, resulting in N = 5.5 ($3d$) electrons per Fe atoms [226] to be compared with N = 6 electrons per Fe in undoped $BaFe_2As_2$.

As we already throughly explained in Chapter 1 (Fig. 1.11) hole doping gives rise to an expansion of the hole pocket at the center of the Brillouin zone while the electron sheets at the corners vanish since the relevant bands are shifted above the Fermi energy and are replaced by thin quasi-cylindrical hole pockets [225, 227, 224]. The Fermi surface and the band plots are reported again in Fig. 3.17 for the convenience of the reader. The density of states relative to the $3d$ orbitals, calculated using DFT-GGA [225], reveals a weak Van Hove singularity just above E_f due to the proximity of the electron pockets to the Fermi surface (see Fig. 3.17d). Thus the proximity to the disappearance of the electron pockets may have a significant influence on the macroscopic properties of this system. For a complete review of the DFT calculations see Ref. [225].

The AFe_2As_2compounds are superconductors and their transition temperatures were found to be (see Fig. 3.18): T_c = 4.08 K for KFe_2As_2, T_c = 2.6 K for $RbFe_2As_2$ and T_c = 2.25 K for $CsFe_2As_2$ [133]. Superconductivity in these materials is unconventional like in the other Fe based superconducting materials [226, 133, 229]. Specific heat measurements near T_c (see Fig. 3.19a) revealed that the C/T temperature dependence deviates from the behaviour expected for a single s-wave gap [228], indicating that the gap is anisotropic or that more than one gap exists, akin to the two band superconductivity observed in MgB_2.

Specific heat measurements revealed that in KFe_2As_2 the Sommerfield coefficient is more than ten times larger than in $BaFe_2As_2$ and it can be further enhanced by increasing the radius of the alkali metal substituting K with Rb

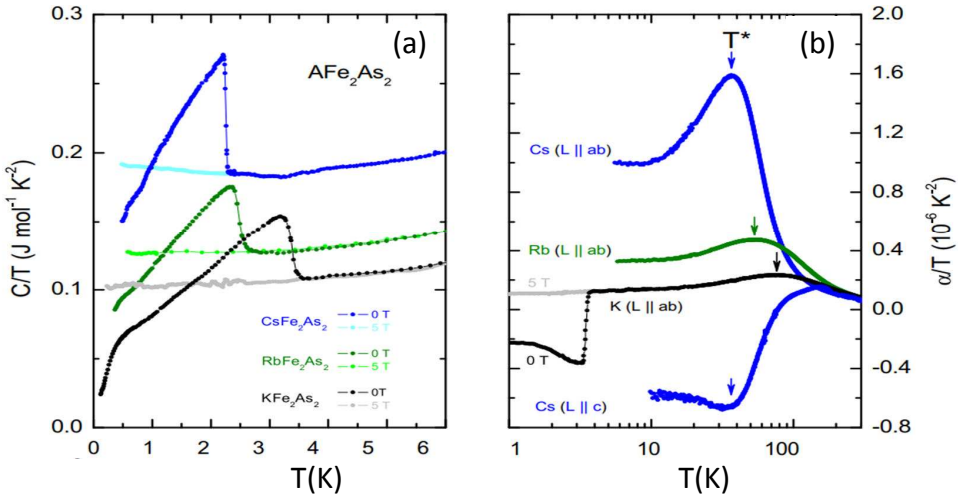

Figure 3.19: a) Temperature dependence of the specific heat in AFe_2As_2 near T_c. b) Temperature dependence of the uniaxial thermal expansion. The arrows indicate the coherence temperature. Figure adapted from [228].

or Cs [228]. This behaviour indicates an increase of the effective mass and of the electronic correlations with hole doping.

The expansion coefficient temperature dependence displays the presence of a well defined maximum between 50 K and 100 K depending from the alkali metal [228](see Fig. 3.19). The presence of this peak was attributed to the enhanced correlations leading to a coherence-incoherence crossover at a critical temperature T^* akin to what has also been observed in heavy fermions compounds where conduction electrons screen the local moments via the Kondo interaction leading to coherent heavy quasiparticles at low temperature [228, 133, 135]. This finding is also supported by the behaviour of the magnetic susceptibility which can be described by a Curie-Weiss relation for $T >> T^*$ while it flattens for $T << T^*$ [228, 230].

A similar phenomenology was also observed by Wu *et al.* using ^{75}As NMR (H_0 = 12 T) knight shift and $1/T_1$ measurement, whose behaviour was also initially ascribed to the coherent-incoherent crossover [133, 229] (see Fig. 3.20).

The increase of the correlation is in good agreement with the theoretical studies carried out using the Spin Slave method (DFT+SSMF) [232, 231, 228]. In this theoretical framework it has been shown that if the electronic correlations in $(Cs,Rb)Fe_2As_2$ are sizeable, namely U/t is of the order of the unity, Hund coupling may promote the single electron occupancy of the Fe $3d$ orbitals and decouple interband charge correlations leading to a orbital selective Mott transition. Accordingly while the electrons of a given band localize the electrons of other bands remain delocalized, leading to a metallic behaviour and eventually to superconductivity.

This prediction can explain the experimental discrepancies in the mass enhancement derived with different techniques [120] (see Fig 3.21). In fact,

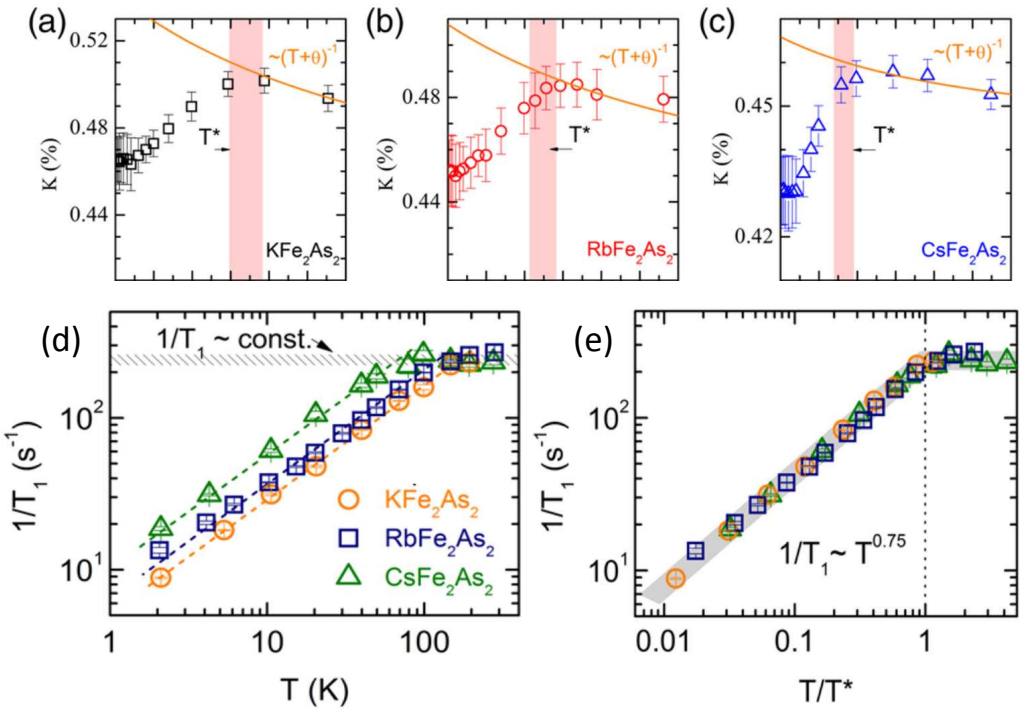

Figure 3.20: (a), (b), (c) Knight shift ($K(T)$) in AFe_2As_2, T^* is defined as the temperature at which K deviates from the Curie Weiss behaviour. (d) The $1/T_1$ behaviour. The temperature at which $1/T_1$ is not constant any more is very close to T^*. (e) $1/T_1$ versus T/T^* clearly shows the universality of this behaviour in AFe_2As_2. Figure adapted from Ref. [133].

while specific heat (Fig. 3.21, top) measures the "average" effective mass on the whole BZ thus confirming the correlations enhancement induced by hole doping, optical techniques are k dependent and thus are capable of investigating single sheets of the FS. These measurements revealed a sizeable spread in the effective mass values, suggesting an orbital dependent behaviour.

3.3.1 Sample preparation and characterization

We measured polycrystalline and single crystals $RbFe_2As_2$ samples and a single crystal $CsFe_2As_2$ sample (see Ref. [233]).

The polycrystalline samples were synthesized by M. Babij and Z. Bukowski at the Institute of Low Temperature and Structure Research in Wroclaw (Poland) using a two step method. RbAs and Fe_2As precursors powders were first prepared from stoichiometric amounts of rubidium, arsenic and iron. The components were then mixed and heated in evacuated and sealed silica tubes at 350 C° and at 800 C°, respectively. Then the two precursors were mixed together in a molar ratio 1:1, pressed into pellets and placed in an alumina crucible and sealed in an evacuated silica ampoule.

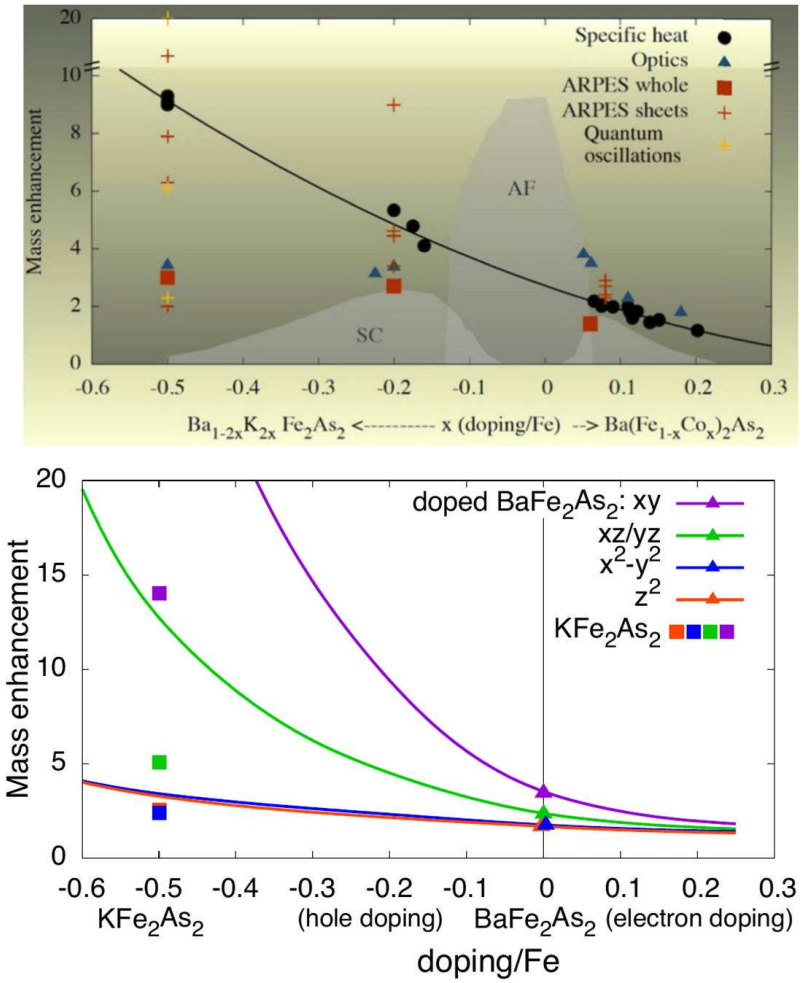

Figure 3.21: Top: Experimental mass enhancement for doped $BaFe_2As_2$ and KFe_2As_2. Bottom: Theoretical SSMF calculations. The different colours indicate electrons of different orbital character. Figure adapted from Refs. [231, 120].

The sample was annealed at 650 C° for three days, ground and annealed for another three days at the same temperature.

The quality of the samples was checked with X-Ray diffraction and AC susceptibility. The X-Ray data confirmed that the geometry of the cell is tetragonal $I4/mmm$ ($ThCr_2Si_2$) with a = 3.871 Å and c = 14.464 Å in very good agreement with literature [234]. The AC susceptibility measurements were performed on heating with an ac field of 10 Oe at 1111 Hz. The onset of diamagnetic shielding due to superconductivity has been detected at T_c = 2.7 K (see Fig. 3.22 bottom panel). The NQR/NMR measurements where performed using ~ 400 mg of powdered polycrystalline sample sealed in a Ar filled (0.2 bar) quartz tube in order to prevent deterioration.

The single crystal $RbFe_2As_2$ and $CsFe_2As_2$ samples instead were grown at the IFW (Dresden) using an alkali metal rich self-flux technique similar to that described in Chapter 1. The X-Ray and SQUID characterization revealed

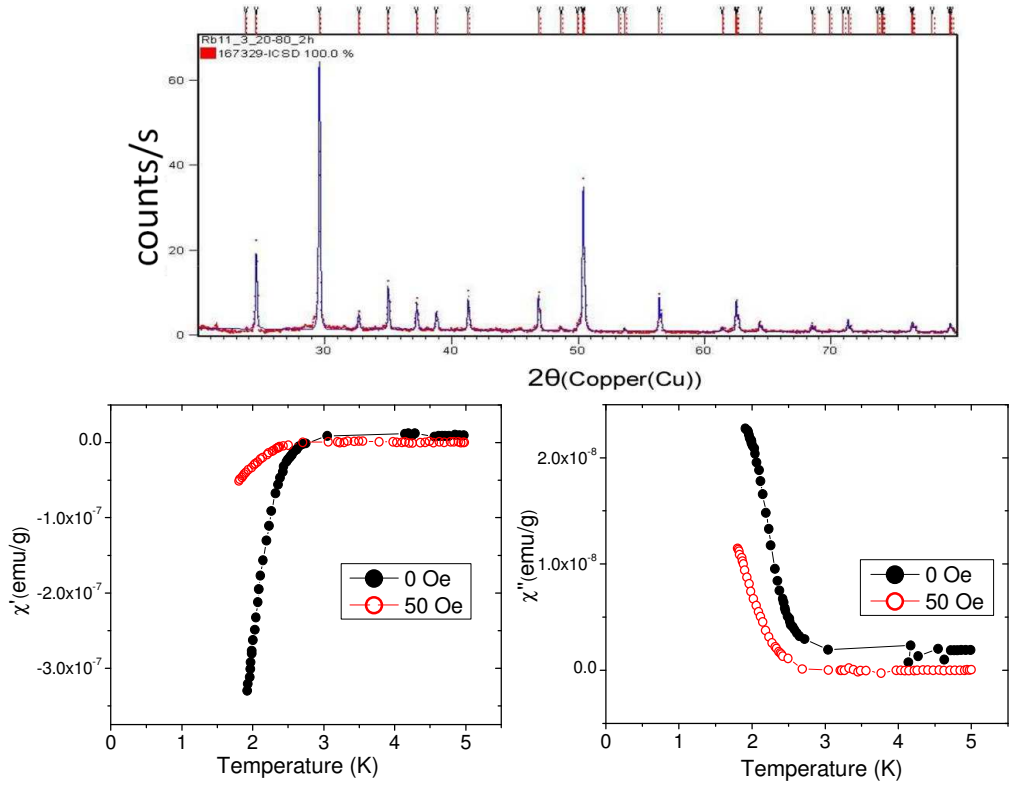

Figure 3.22: Top: X-Ray diffraction pattern of the polycrystalline $RbFe_2As_2$ sample measured at room temperature. Bottom: Temperature dependence of the real $(\chi'(T))$ and imaginary part $(\chi''(T))$ of the ac susceptibility close to T_c in $RbFe_2As_2$ in zero field and for a static external magnetic field of 50 Oe.

that the sample are nearly identical to the polycrystalline ones.

3.3.2 ^{75}As and ^{87}Rb NQR spectra in polycrystalline $RbFe_2As_2$

First of all we shall discuss the appearance of a charge order in the FeAs planes of $RbFe_2As_2$ revealed by the measurement of the ^{75}As and ^{87}Rb NQR spectra in the polycrystalline sample.

The NQR spectra allow us to directly measure the distribution of the electron density. In fact (see Section 2.1.2.3) the NQR frequency

$$\nu_Q = \frac{eQV_{ZZ}}{2h}\left(1+\frac{\eta^2}{3}\right)^{1/2} \quad \text{for} \quad I = 3/2 \tag{3.10}$$

is directly proportional to the electric field gradient (EFG) at the nuclear site. Since, in (Cs,Rb)Fe_2As_2 and also in the other IBS, the EFG has a cylindrical symmetry, then $\eta = 0$.

The NQR spectrum probes the EFG generated by the surrounding charge distribution $n(r)$ and since the EFG is proportional to $\partial^3 n(r)/\partial r^3$ even a

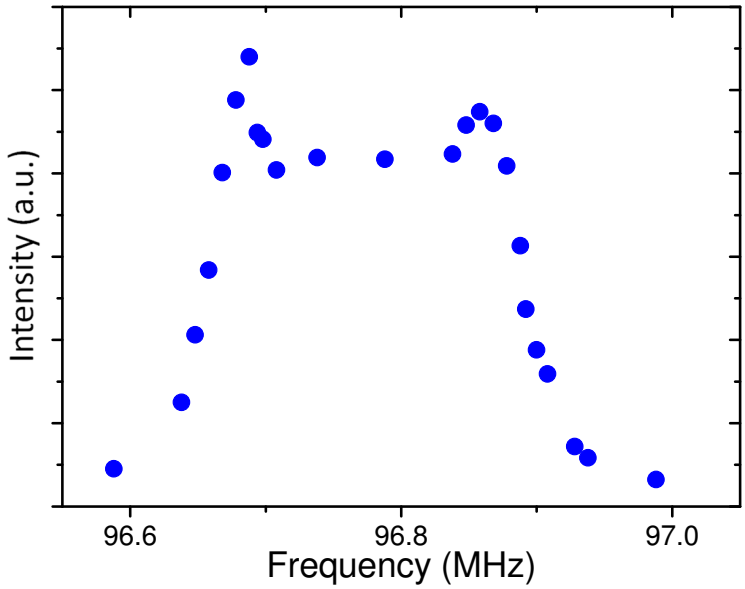

Figure 3.23: ^{87}Rb NMR powder spectrum in $RbFe_2As_2$ for the central $(1/2 \rightarrow -1/2)$ line measured for T=20 K and H_0 = 7 T.

minute variation in $n(r)$ can give rise to a strong effect on the NQR line. Hence measuring the width of the NQR spectrum is often useful in order to determine the quality of a specimen due to the intrinsic sensitivity of the technique to the presence of impurities. Furthermore since ν_Q depend so strongly on the electron density even relatively similar compounds usually have extremely different ν_Q and thus NQR is a phase selective technique. Furthermore ZF-μSR revealed that no magnetic phases is present in the $RbFe_2As_2$ sample, in excellent agreement with the narrow ^{87,85}Rb NQR lines.

Remarkably $RbFe_2As_2$ contains three NQR active nuclei: ^{75}As (I=3/2), ^{87}Rb (I=3/2) and ^{85}Rb (I=5/2). While the ^{75}As NQR frequency ν_Q = 14.6 MHz was already known (see Wu *et al.* [133], sup. material) we directly determined ^{87}Rb ν_Q = 6.2 MHz by measuring the NMR powder spectrum of the ^{87}Rb central line in a 7 T magnetic field by recording the intensity of the echo measured after a $\pi/2 - \tau - \pi$ (τ = 40μs, π = 14μs) echo sequence as a function of the irradiation frequency (see Fig 3.23). We than derived ν_Q from the width of the central line powder spectrum using Eq. 2.19.

We also calculated *ab initio* the values of the EFG at the ion sites, and thus the values of ν_Q for ^{87,85}Rb and ^{75}As, by using the density functional theory (DFT). The calculations have been carried out using the full-potential linearised augmented plane-wave method as implemented in the Elk package [235]. We choose the generalized gradient approximation of Perdew, Burke, and Ernzerhof (GGA-PBE) [236]. The atomic positions used in the calculation are those obtained from room temperature x-ray diffraction. The

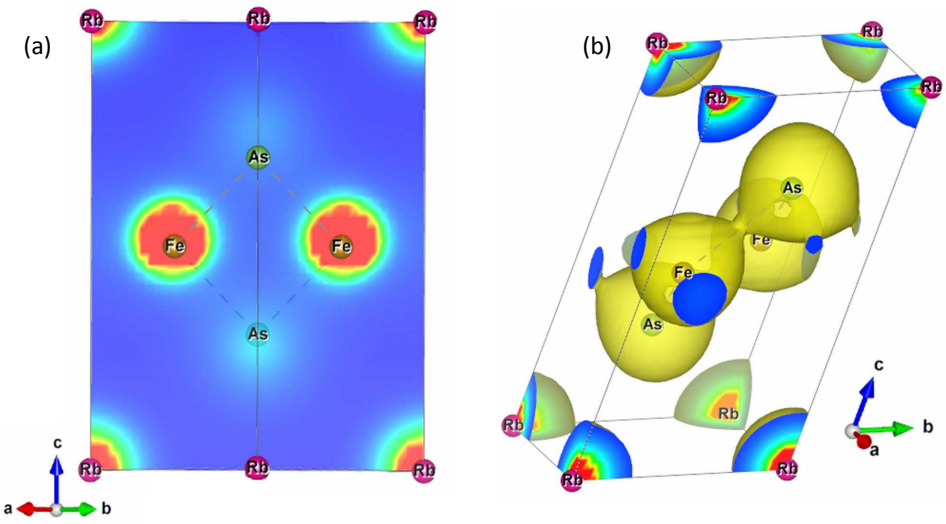

Figure 3.24: (a) 2D projection along the diagonal of the primitive cell and (b) 3D $RbFe_2As_2$ electronic density plot obtained from DFT calculations (see text). The isosurface in (b) correspond to $n(\mathbf{r}) = 0.07\ e/a_0^3$ in atomic units. The *ab initio* calculation confirms that the wave function are localized on the atom sites.

electric field gradient (EFG) tensor components V_{ij}^{α} have been derived directly from the ground state electronic density $n(\mathbf{r})$ (see Fig. 3.24) by solving the Poisson equation ($\nabla^2\varphi = \rho$) to determine the electrostatic potential φ and subsequently we calculated V_{ij}^{α} from

$$V_{ij}^{\alpha} = \left.\frac{\partial^2\varphi}{\partial\mathbf{r}_i\partial\mathbf{r}_j}\right|_{\mathbf{r}_\alpha}, \tag{3.11}$$

where α runs over the nuclei at $\mathbf{r}_\alpha$. Since the EFG tensor is extremely sensitive to the charge distribution a very well converged basis is essential to obtain the correct EFG tensor components. We used muffin tin radii of 2.6 a_0 for Rb and 2.4 a_0 for Fe and As with $R_{min}^{MT} \times max(||k||) = 9$, where R_{min}^{MT} is the smallest muffin tin radius inside the MT spheres and $||k||$ the length of the reciprocal space vectors. We choose 9 for the cut off of the angular quantum number in the lattice harmonics expansion inside the MTs. Reciprocal space was sampled with the Monkhorst-Pack [237] scheme on a $24 \times 24 \times 24$ grid. The smearing is 270 meV with the Methfessel-Paxton [238] scheme. Convergence of the EFG components with respect to all these parameters has been carefully checked.

The obtained values, $(^{75}\nu_Q)_{\mathrm{DFT}}$ = 14.12 MHz and $(^{87}\nu_Q)_{\mathrm{DFT}}$ = 6.7 MHz are in good agreement with the experimental values $(^{75}\nu_Q)_{\mathrm{exp}}$ =14.6 MHz and $(^{87}\nu_Q)_{\mathrm{exp}}$ = 6.2 MHz and the discrepancy represents an estimate of the accuracy of the DFT calculation which is known not to properly account for the electronic correlations. The rather good agreement with the experimental values however shows that, even for this correlated IBS, DFT is still able to provide a fair description of the system as far as it remains a normal metal.

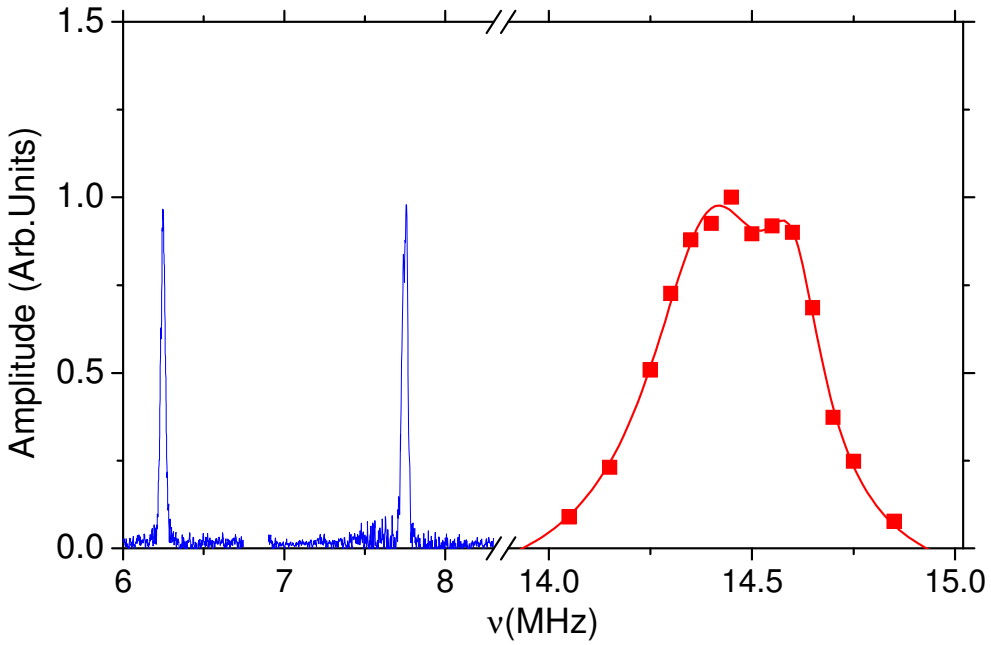

Figure 3.25: The whole NQR spectrum of $RbFe_2As_2$. The three lines are associated with the $m_I = \pm 3/2 \rightarrow \pm 1/2$ transition for ^{75}As and ^{87}Rb and with the $m_I = \pm 5/2 \rightarrow \pm 3/2$ transition for ^{85}Rb ($I = 5/2$), is shown for $T = 4.2$ K. The intensity of the three spectra has been corrected for better visualisation so that all three spectra have the same height.

3.3.2.1 ^{75}As NQR spectra of polycrystalline $RbFe_2As_2$

Above 140 K the ^{75}As NQR spectrum (see Fig. 3.25) is centered around 14.6 MHz, with a linewidth of about 170 KHz, while the ^{87}Rb NQR spectrum is centered around 6.2 MHz with a width of about 20 kHz. The ^{85}Rb ($\pm 3/2 \rightarrow \pm 5/2$) line is nearly identical and is centred around 7.75 MHz (see Fig. 3.25). While the narrow ^{87,85}Rb NQR spectra were obtained from the Fourier transform of half of the echo signal the spectrum of the broader ^{75}As line was derived from the frequency dependence of the spin echo intensity. At a few temperatures the ^{75}As NQR spectra was also obtained by taking the envelope of the Fourier transforms of half of the echo recorded at different frequencies and they were found to be identical to those obtained using the echo intensity method. The narrow NQR Rb spectra (Fig. 3.25) confirm the good quality of our sample.

However things get really interesting while cooling down below 140 K. The ^{75}As spectrum is observed to progressively broaden with decreasing temperature, below 50 K the presence of two separated humps nearly symmetrically shifted can be clearly observed and if temperature is lowered further no other significant modification of the spectrum takes place (see Fig. 3.27 and 3.26).

The presence of two peaks in the NQR spectrum is a common feature of the 1111 family compounds [166, 239] in presence of electron doping (see

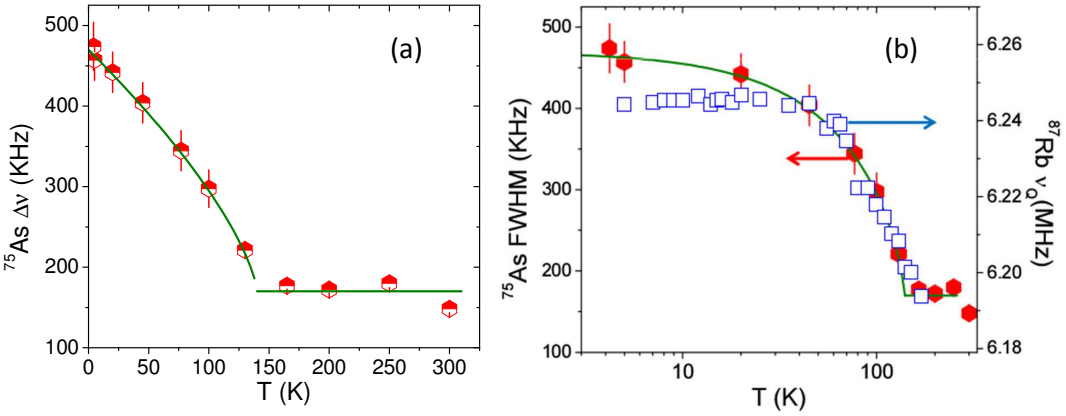

Figure 3.26: (a) Temperature dependence of the full width at half intensity (FWHM) of ^{75}As NQR spectra The green solid line is a phenomenological fit to $\Delta\nu_Q = 300(1-(T/T_0))^{\beta} + 170$ KHz, with T_0=140 K and $\beta \sim 0.7$. (b) Blue squares (right scale): the temperature dependence of ^{87}Rb ν_Q. Red octagons, (left scale) ^{75}As FWHM, the two temperature dependences are shown together for comparison.

Section 2.2.1) and it has been associated with a nanoscopic phase separation in regions characterized by different electron doping levels. However for the 1111 compounds the spectrum is not symmetric, as it is instead the case for $RbFe_2As_2$, and it is nearly temperature independent from very low temperatures (4.2 K) up to 650 K (see Fig. 3.28). Furthermore in $RbFe_2As_2$ no doping is present and thus this type of phase separation is not expected a priori.

A similar temperature dependent behaviour of the ^{75}As NMR satellite lines spectra was instead observed in KFe_2As_2 under pressure [240] (2.42 GPa) in a $H_0 = 10.6$ T magnetic field, which, however, disappear in zero field (NQR).

The behaviour of the ^{75}As NQR spectrum in $RbFe_2As_2$ strongly resembles the one expected in presence of a charge density wave order (CDW) [241, 242, 243] which causes a periodic modulation of electronic density and thus of the EFG, giving rise to two symmetrically shifted peaks in the NQR spectrum for several types of possible CDW geometries [243]. This type of NQR spectra could also be associated with the emergence of an orbital order [244] but from NQR spectra alone it is not straightforward to discriminate among the two scenarios.

However it is clear that we are detecting a phase transition, at $T=T_0$, to a low temperature phase characterized by a spatial modulation of the EFG, even if we are unable to precisely determine the step of the modulation. Accordingly the temperature dependence of the ^{75}As line width ($\Delta\nu_Q$) can be fitted with the phenomenological behaviour $\propto (1-T/T_0)^{\beta}$ expected for an order parameter in correspondence of a phase transition.

The presence of a phase transition is also evident in the temperature evolution of the ^{87}Rb NQR frequency which abruptly increases at T_0 mimicking

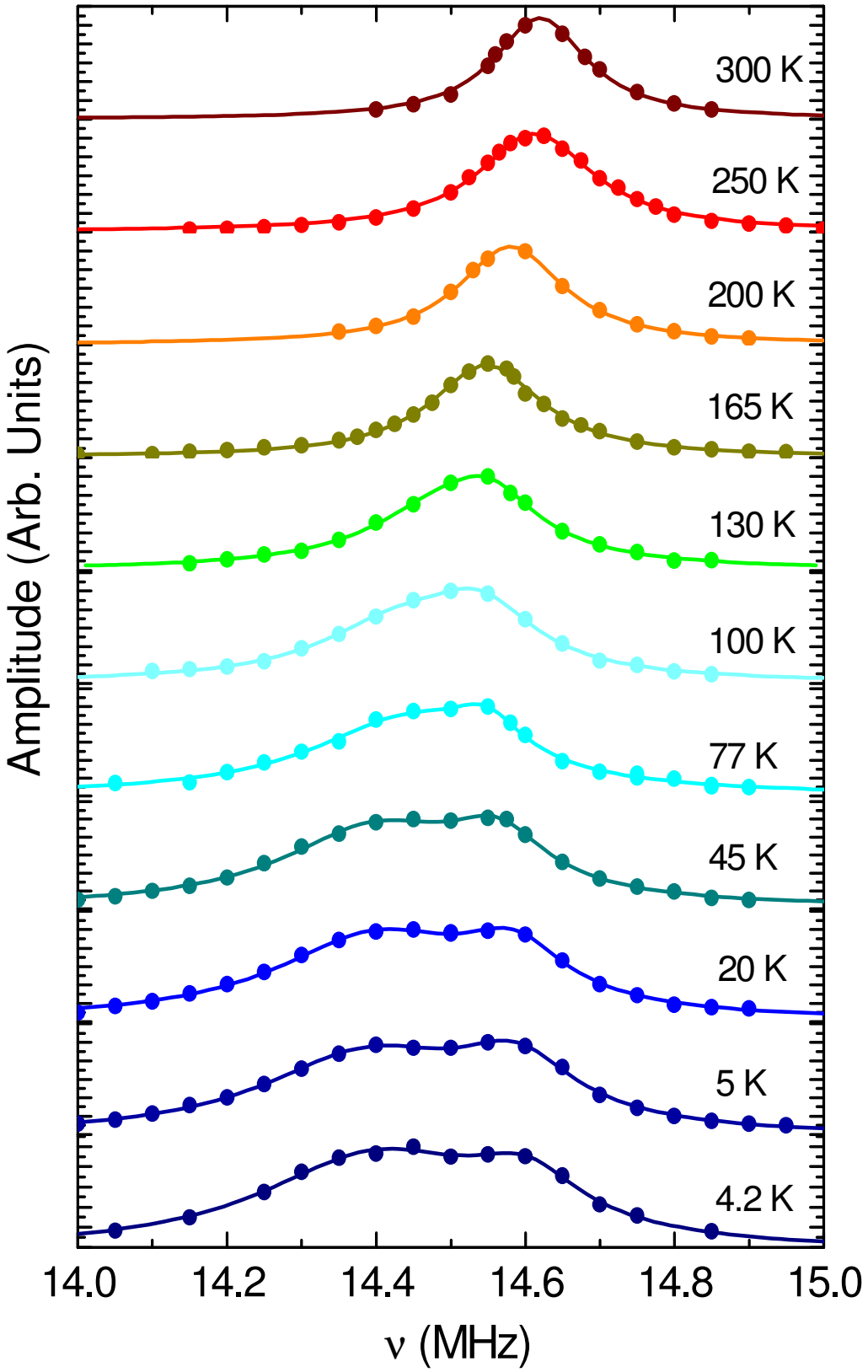

Figure 3.27: The ^{75}As NQR spectrum in polycrystalline $RbFe_2As_2$ is reported at different temperatures between 5 K and 300 K. The solid lines are best fits with one or two (for T $<$ 130 K) Lorentzian.

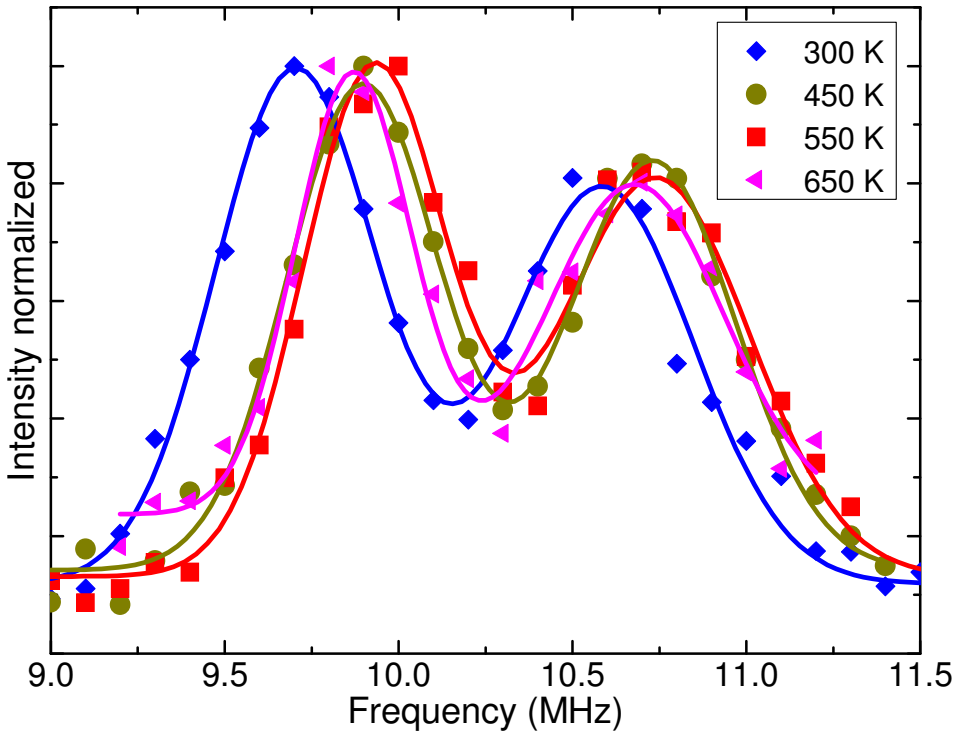

Figure 3.28: The spectrum of underdoped $LaFeAsO_{1-x}F_x$ ($x = 4.5\%$) measured at different temperatures higher than 300 K. A custom high temperature NQR set-up with self tuning capabilities (see Appendix B) was used to carry out these measurements. The low temperatures spectra are nearly identical (Fig. 2.15) indicating that if the shape of the spectrum is due to a CDW order the transition temperature is high (> 650 K). The solid lines are fits carried out using two Gaussians.

the ^{75}As $\Delta\nu_Q$ behaviour (Fig. 3.26). Differently from ^{75}As however the ^{87}Rb $\Delta\nu_Q$ remains basically unchanged indicating that the electronic density modulation is in the FeAs layer (far away from Rb) and that the modulation of the EFG at ^{75}As nuclei should occur over very few lattice steps, otherwise one should expect a splitting also of the narrow ^{87}Rb NQR spectrum.

In this framework the small shift of the Rb ν_Q is probably due to a tiny modification of the lattice constants and/or of the electronic density in proximity of the Rb atoms as a consequence of the emergence of the charge order in the FeAs plane.

These results strongly indicate that akin to cuprates, a static charge order develops in the normal state of IBS when the electronic correlations are sizeable and thus they may play a significant role in determining the superconducting state properties.

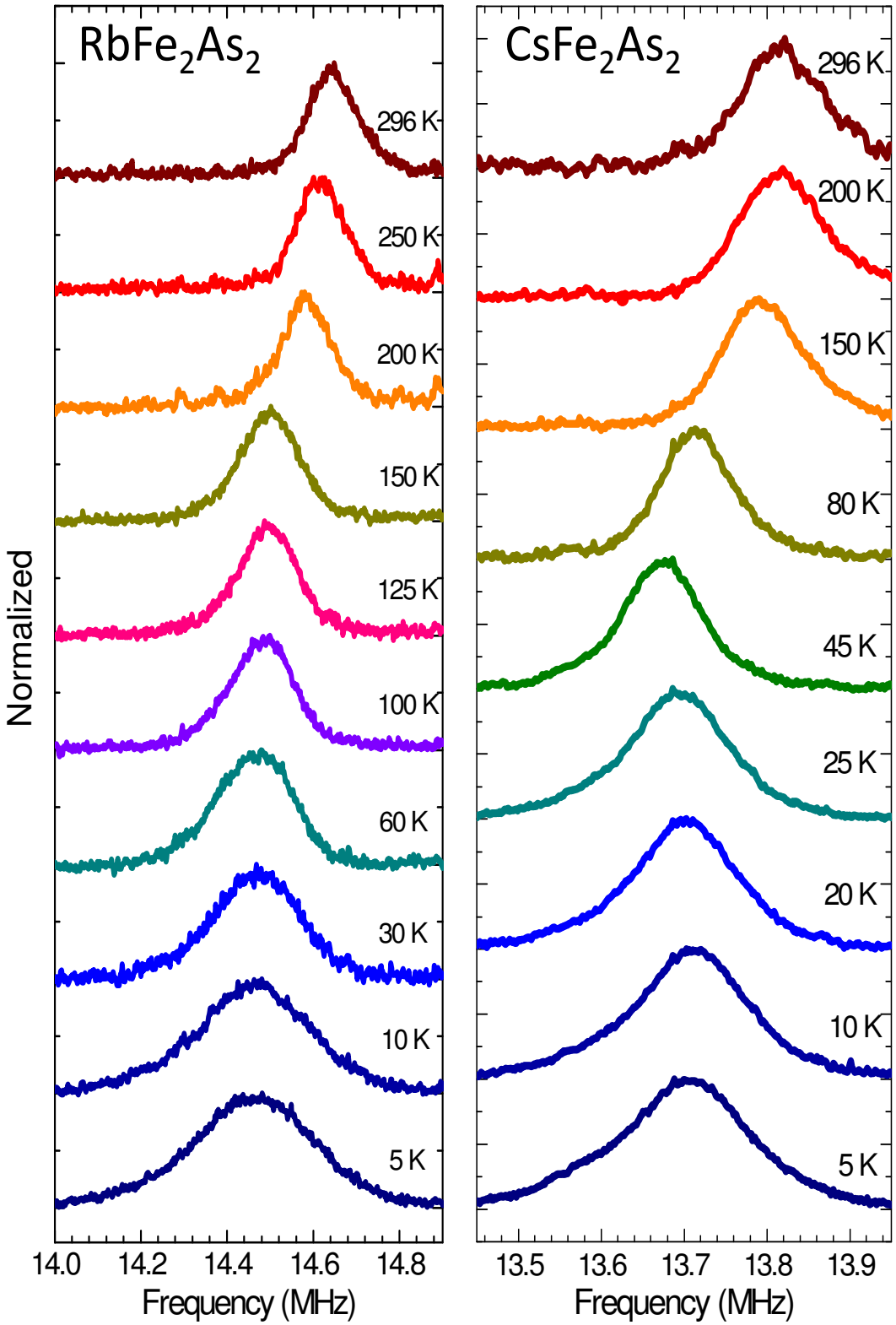

Figure 3.29: The ^{75}As NQR spectra of $RbFe_2As_2$ (left) and $CsFe_2As_2$ (right) measured at different temperatures with the Fourier Transform envelope method. The spectra temperature dependence is clearly reminiscent of that observed in the polycrystalline $RbFe_2As_2$ sample.

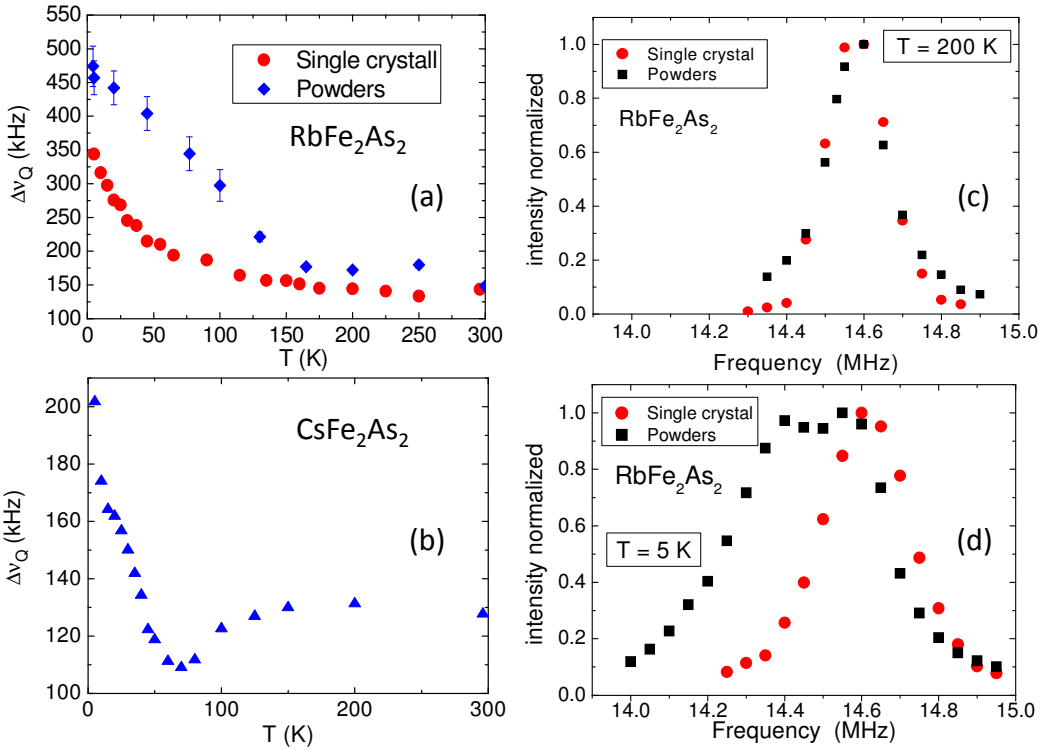

Figure 3.30: (a) and (b): Temperature dependence of ^{75}As $\Delta\nu_Q$ measured in single crystal $RbFe_2As_2$ and $CsFe_2As_2$, respectively. In (a) the results for the polycrystalline sample are also shown for comparison. (b) and (b): comparison of the ^{75}As NQR spectra of single-crystal and polycrystalline $RbFe_2As_2$, measured with the echo intensity method at 5 K and 200 K.

3.3.2.2 ^{75}As NQR spectra of single crystal $RbFe_2As_2$ and $CsFe_2As_2$

In order to verify that the charge order is really an intrinsic property of these material we also measured the ^{75}As NQR spectra of a $RbFe_2As_2$ single crystal and of the related $CsFe_2As_2$ compound. $RbFe_2As_2$ and $CsFe_2As_2$ differ only for the size of the alkali metal that results in a different chemical pressure, giving rise to an enhancement of the Sommerfeld coefficient in $CsFe_2As_2$. However most of their properties (T_c, spin susceptibility (Knight shift), ^{75}As $1/T_1$) are rather similar suggesting that the charge order could also be present in $CsFe_2As_2$ [133, 133].

For the single crystal $CsFe_2As_2$ sample T_c = 2.3 K and ^{75}As $\nu_Q(300\,K) \simeq$ 13.82 MHz while for $RbFe_2As_2$ $T_c \sim$ 2.7 K and ^{75}As $\nu_Q(300\,K) \simeq$ 14.6 MHz, identical to those measured in polycrystalline $RbFe_2As_2$ sample. The resulting spectra and line width temperature dependences are reported in Fig. 3.29 and Fig. 3.30, respectively.

Very interestingly the temperature evolution of single crystal $RbFe_2As_2$ spectra is significantly different from that of the powdered polycrystalline sample: while at high temperatures (e.g. 200 K see Fig. 3.30c) the spectra are very similar, below T_0 in single crystal $RbFe_2As_2$ $\Delta\nu_Q$ does not increase

as fast as in the powder sample and it does not saturate at low temperatures (see Fig. 3.30a). It should however be noticed that for both the samples the spectrum begins to broaden at the same temperature $T_0 \sim 140$ K, suggesting that the transition temperature remains unchanged. The different growth rate of $\Delta\nu_Q$ is possibly related to the presence of defects pinning the charge density wave. In fact we can only observe the CDW order when it is nearly static on the time scale of the NQR spectrum measurements, which is typically in the $\sim$100 μs range. However charge fluctuations (dynamic CDW), akin to that observed in cuprates using x-ray scattering [127], could possibly persist at much higher temperatures. The larger number of crystal defects (e.g. dislocations) present in the polycrystalline sample could thus pin the charge fluctuations slowing them down significantly faster than in the single crystal sample, giving rise to the faster $\Delta\nu_Q$ increase. Since the line width is smaller for the single crystal sample the two humps characterizing the NQR spectrum of polycrystalline $RbFe_2As_2$ cannot be clearly resolved in the single crystal one (see Fig. 3.29 and Fig. 3.30c).

The temperature evolution of the $CsFe_2As_2$ NQR spectrum is also similar to that observed in $RbFe_2As_2$ but the $\Delta\nu_Q$ increase takes place at much lower temperature indicating a lower T_0 with respect to $RbFe_2As_2$ ($T_0 \sim 60$ K, see Fig. 3.30b).

3.3.3 $1/T_1$ and low temperature phase separation in polycrystalline $RbFe_2As_2$

Now we discuss the temperature dependence of the low-energy dynamics probed ^{75}As and ^{87}Rb $1/T_1$ in the polycrystalline $RbFe_2As_2$ sample. The spin-lattice relaxation rate was determined from the recovery of the transverse nuclear magnetization after saturation recovery pulse sequence (see Section 2.1.6.2).

3.3.3.1 ^{75}As NQR $1/T_1$ in polycrystalline $RbFe_2As_2$

For ^{75}As $1/T_1$ the recovery has been fitted using the standard formula for the NQR $\pm 1/2 \rightarrow \pm 3/2$ line of a $I = 3/2$ nucleus in presence of a magnetic relaxation mechanism [160]:

$$M(\tau) = M_0\left(1 - fe^{-3\tau/T_1}\right) , \tag{3.12}$$

where M_0 is the equilibrium magnetization and f takes into account the non zero signal at $t = 0$ due to imperfect saturation. The results for ^{75}As are reported in Fig. 3.31.

Above 20 K, for $T < 140$ K $1/T_1$ increases with a power law $1/T_1 = aT^b$, with $b = 0.79 \pm 0.01$ for ^{75}As, and flattens around ~ 140 K (see Fig.3.31a), in very good agreement with the $1/T_1$ results reported by Wu et al.[133] from ^{75}As NMR. It should be noticed that the temperature at which $1/T_1$

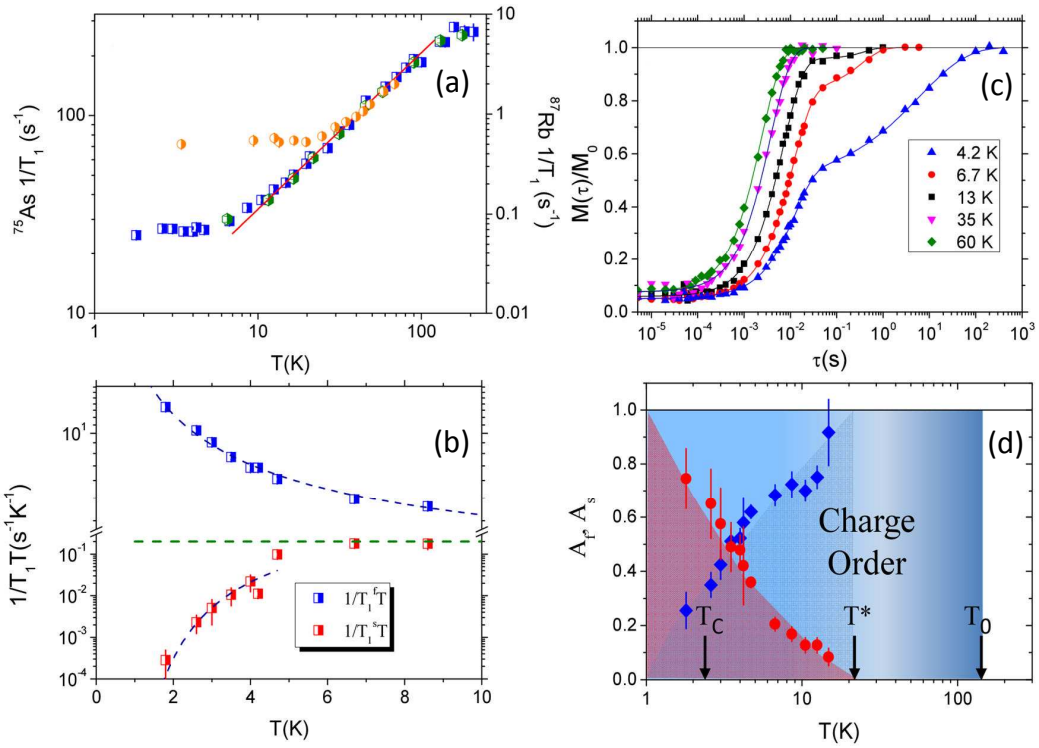

Figure 3.31: (a) $RbFe_2As_2$ ^{75}As NQR (blue: high frequency hump, green low frequency hump) and ^{87}Rb NMR (H_0 = 7 T) $1/T_1(T)$ (orange). (b) ^{75}As NQR $(T_1T)^{-1}$: fast (blue) and slow (red) components. The uncertainty on the experimental points is comparable to the size of the symbols. (c) Magnetization recovery curves (saturation recovery sequence) measured at different temperatures. (d) temperature evolutions of the weights of the slow (A_s: red) and of the fast (A_f: blue) relaxation components.

flattens is very close to the temperature $T_0 \sim 140$K at which we observed the broadening of the ^{75}As NQR spectrum signalling the onset of the charge order (see Fig. 3.27 and Fig. 3.26). This strongly suggest that the power law $1/T_1$ temperature dependence is related to the onset of the charge order. A similar power law $1/T_1$ behaviour, also with an exponent close to 0.7, was observed in heavy fermion compounds (e.g. $CeCu_{5.9}Au_{0.1}$ [245]) with AF spin correlations close to a quantum critical point (QCP).

Below 20 K (T^* hereafter) we observed instead a rather interesting behaviour: the single exponential recovery law of Eq. 3.12 is not able to fit the magnetization recovery any more and we observe, by lowering temperature, the gradual appearance of a second component characterized by much longer relaxation times (see Fig. 3.31c). The recovery was thus fit to:

$$M(\tau) = M_0\left[1 - f\left(A_f e^{-3\tau/T_1^f} + A_s e^{(-3\tau/T_1^s)^\beta}\right)\right] , \qquad (3.13)$$

where A_f and A_s are, respectively, the fraction of fast relaxing and slow

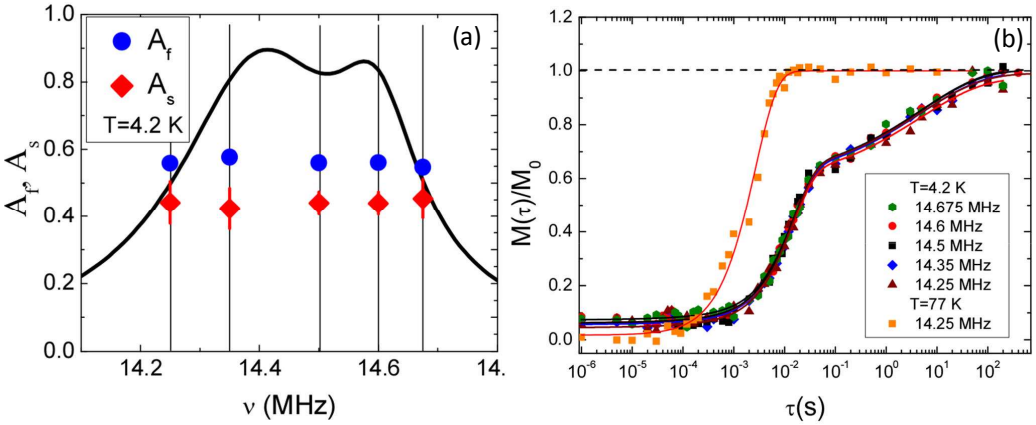

Figure 3.32: (a) Frequency dependence of the weights of the fast (blue circles) and slow (red diamonds) ^{75}As $1/T_1$ components, the solid black line is the $RbFe_2As_2$ ^{75}As NQR spectrum. (b) Recovery of ^{75}As NQR magnetization after a saturation pulse sequence for different irradiation frequencies across the NQR spectrum, at $T = 4.2$ K. The single exponential recovery law for $T = 77$ K is reported up to times longer than $10^3 T_1$. The solid lines are best fits according to Eq. .

relaxing nuclei and and $0.8 \geq \beta \geq 0.3$ a stretching exponent characterizing the slowly relaxing component.

As the temperature is lowered one observes a progressive increase of A_s with respect to A_f and at the lowest temperature ($T = 1.7$ K), about 80% of the nuclei are characterized by the slow relaxation (Fig.3.31c-d).

Even if we could not completely rule out the quadrupolar origin of one this relaxation components this scenario is extremely unlikely since no significant quadrupolar relaxation was observed by comparing the NQR spin lattice relaxation rates of the two Rb isotopes (see Section 3.3.3.3 for further details).

In order to check a possible dependence of the spin lattice relaxation rate from the irradiated portion of the NQR spectrum, ^{75}As $1/T_1$ was measured both on the high frequency and on the low-frequency shoulder of the NQR spectrum and it was found to be the same (Fig.3.31a and Fig 3.32) over a broad temperature range. Moreover, at $T = 4.2$ K we carefully checked the frequency dependence of T_1^f, T_1^s, A_f and A_s and found that neither the two relaxation rates nor their amplitude vary across the spectrum (see Fig. 3.32).

This implies that nuclei resonating at different frequencies probe the same dynamics, which suggest that the charge modulation induced by the charge order has a nanoscopic periodicity [166]. We also measured the ^{75}As NQR $1/T_2$ and verified that, once the Redfield correction is applied (see Section 3.1.1), $1/T_2$ is temperature independent with a value of $1/T_2 \sim 1.7\text{ms}^{-1}$. This means that the efficiency of the spin-spin relaxation in establishing a common spin temperature does not vary with temperature. Hence, since T_2 is constant, the slow T_1 cannot be present at high temperature, hidden by a

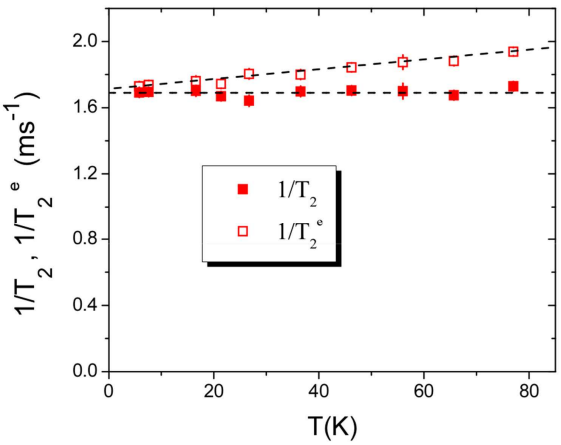

Figure 3.33: Temperature dependence of ^{75}As NQR $1/T_2^e$ (open squares) before Redfield correction and $1/T_2$ (closed squares), after Redfield correction, for $RbFe_2As_2$. The dashed lines are guide to the eye.

faster T_2 homogenizing the spin temperature (and thus T_1) across the spectrum. Thus the appearance of a different relaxation rates below T^* arise from a phase separation causing a slight change in the average electronic charge distribution (no effect on the NQR spectra) but a marked differentiation in the low-energy excitations, which is detectable at low temperature.

The behaviour of the fast component ($1/T_1^f$) and of the slow ($1/T_1^s$) component is completely different below T^*. $1/T_1^f$ deviates from the power law behaviour and progressively flattens as the temperature is lowered. The same behaviour is detected for ^{87}Rb NMR $1/T_1$, although the flattening appears to start at a higher temperature, suggesting that T^* might be field dependent (see Fig. 3.31). Conversely $1/T_1^s$ gets progressively longer as the temperature is lowered and follows an activated behaviour, with an energy barrier $E_g = 17 \pm 0.9$ K (see Fig. 3.31b).

The behaviour of $1/T_1^f$ is characteristic of a system approaching a QCP where localization occurs. In fact, from Moriya self-consistent renormalization (SCR) approach for a quasi-2D system with AF correlations, one should have $1/T_1 = T\chi(Q)$ [246, 247, 164, 248] with $\chi(Q)$ the static susceptibility at the AF wave-vector. In the proximity of the QCP $\chi(Q) \sim \ln(1/T)/T$, leading to a weak logarithmic divergence of $1/T_1 \sim \ln(1/T)$ for $T \to 0$, while at higher temperature $\chi(Q)$ should show a Curie-Weiss behaviour, yielding a nearly flat $1/T_1$, as we do observe in $RbFe_2As_2$ (see Fig. 3.31b). Conversely the slow component $1/T_1^sT$, which at temperature below 5 K is the dominant $1/T_1$ component (see Fig. 3.31d), display an opposite temperature behavior decreasing upon cooling and at $T_c \sim 2.7$ K the corresponding fraction is around $A_s \sim 0.65$. Upon further decreasing the temperature the volume fraction of the heavy electron phase vanishes while the one of the metallic phase grows to $A_s \sim 1$. Since the system is metallic at low temperatures the deviation of $1/T_1^sT$ from the constant Korringa law behaviour could be related with

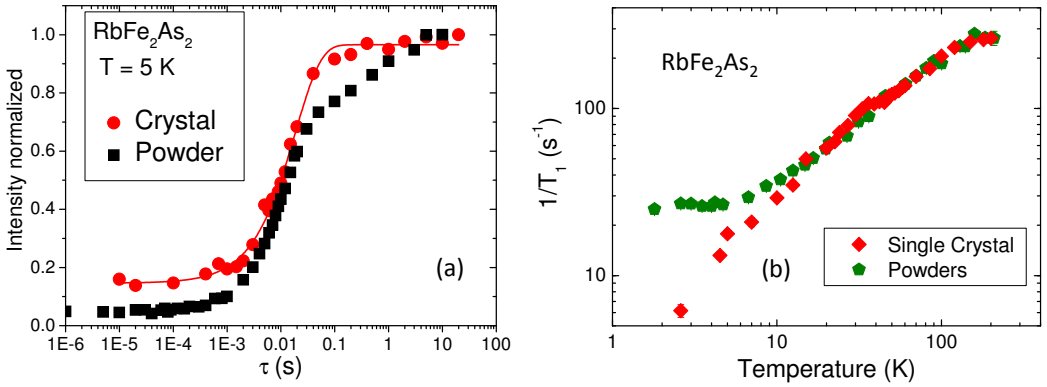

Figure 3.34: (a) Recovery of ^{75}As (NQR) in polycrystalline (black) and single crystal (red) $RbFe_2As_2$. The solid red line is a fit to a single component Eq. 3.12. Clearly no second T_1 component is present in the single crystal magnetization recovery. See also Fig. 3.32 for low temperature recoveries in polycrystalline sample. (b) Temperature evolution of NQR ^{75}As $1/T_1$ in n polycrystalline (green) and single crystal (red) $RbFe_2As_2$. No deviation from the power law behavior is present in the single crystal sample.

the opening of a pseudo-gap akin to what has been observed in underdoped cuprates [249, 250, 251] and theoretically predicted for systems analogous to hole doped IBS [252].

The charge order may promote this phase separation into metallic and nearly insulating regions, which could result from the theoretically predicted orbital selective behaviour [120, 232].

3.3.3.2 ^{75}As NQR $1/T_1$ in single crystal $RbFe_2As_2$

We also carried out the same ^{75}As NQR $1/T_1$ measurements on a $RbFe_2As_2$ single crystal sample in order to check if the amount of disorder has some influence also on the spin-lattice relaxation rate behaviour. In fact single crystal IBS samples are typically much cleaner than polycrystalline powdered samples.

Quite interestingly we found that in this sample the power low $1/T_1$ decrease persist down to 1.6 K and that there is no evidence of the emergence of a second $1/T_1$ component (see Fig. 3.34).

It should be noticed that in a previous ^{75}As $H_0 = 12$ T NMR study carried out on single crystal (Cs,Rb)Fe_2As_2, Wu *et al.* [133] did not observe a clear separation of the recovery in two components as we do in polycrystalline sample but they did observe deviations from the single exponential recovery below 20 K which, however, were fitted with a stretched exponential law that could yield an average $1/T_1$ value between $1/T_1^s$ and $1/T_1^f$. Conversely, in good agreement with our single crystal measurements, they didn't observe any deviation from a single component recovery in their low temperature NQR $CsFe_2As_2$ data (see Sup. Material of Ref. [133]).

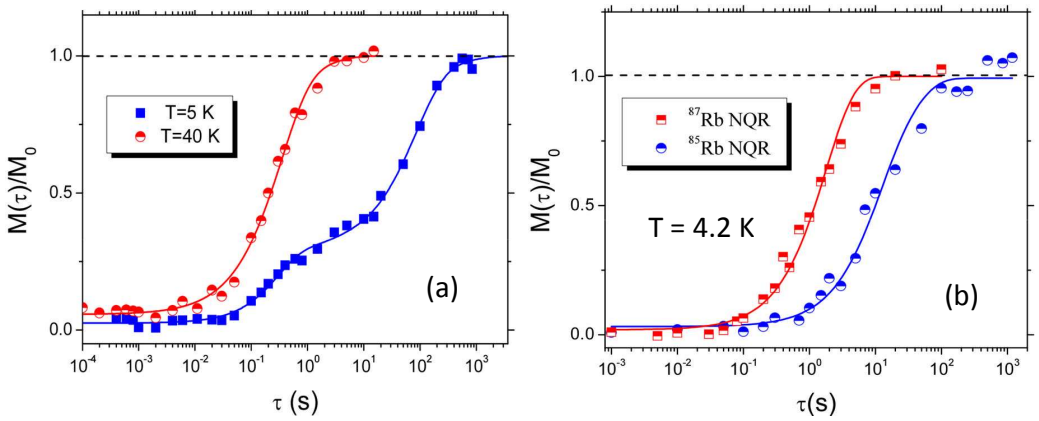

Figure 3.35: (a) Recovery of ^{87}Rb NMR magnetization, $1/2 \rightarrow -1/2$ transition $\theta = 90°$ peak, $T = 40$ K (red circles) and $T = 5$ K (blue squares). The solid lines are fit to Eq. 3.1 with two components. (b) Recovery of ^{87}Rb (red squares) and of ^{85}Rb (blue circles), $\pm 5/2 \rightarrow \pm 3/2$ transition, $T = 4.2$ K. The solid lines are the best fits according to Eq. 3.12 and 3.14.

These observations suggest that the emergence of the low temperature phase separation giving rise to two $1/T_1$ components could indeed be induced by the presence of defects and/or by an external strong magnetic field which may induce the complete freezing of the charge order, similarly to what has been observed in cuprates superconductors with NMR measurements [124], where high magnetic fields induce a static charge order.

3.3.3.3 ^{87,85}Rb NMR $1/T_1$ in polycrystalline $RbFe_2As_2$

^{87,85}Rb NMR $1/T_1$ was measured, for the polycrystalline sample ($H = 7$ T) by irradiating the high frequency shoulder of the powder spectrum of the central line (see Fig. 3.23) corresponding to grains with the c-axes perpendicular to H_0 ($\theta = 90°$). The recovery of the transverse magnetization was fit according to the usual spin 3/2 relaxation (Eq. 3.1 [160]). In analogy with the ^{75}As measurements the magnetization recovery displays two components appearing at low temperature ($T < 25$ K, see Fig. 3.35 and 3.31).

We then carried out the NQR spin lattice relaxation measurements both for ^{87}Rb ($\nu_Q = 6.2$ MHz) and ^{85}Rb ($\pm 3/2 \rightarrow \pm 5/2$ line, $\nu_Q = 7.75$ MHz). In the NQR measurements we only measured the temperature dependence of the fast component since the much weaker signal in zero field and the very long relaxation times of the slow component make the measurement of $1/T_1^s$ impractical.

The recovery of nuclear magnetization was fit according to the recovery laws expected for a magnetic relaxation mechanism which is given by Eq. 3.12 [253, 160] for ^{87}Rb ($I = 3/2$) and

$$M(\tau) = M_0\left(1 - f(0.427e^{-3\tau/T_1} + 0.573e^{-10\tau/T_1})\right) , \qquad (3.14)$$

for ^{85}Rb ($I = 5/2$). The ratio between the $1/T_1$ of the two nuclei for the fast relaxing component was measured at a few selected temperatures between 4 and 25 K and we found that $^{87}(1/T_1)/^{85}(1/T_1) \simeq 12\pm1$ in good agreement with the ratio between the square of the gyromagnetic ratios of the two nuclei $(^{87}\gamma/^{85}\gamma)^2 = 11.485$, confirming the adequacy of the magnetic relaxation recovery laws we used to estimate $1/T_1$ and the fact that the relaxation is driven by electron spin fluctuations. Notice that if the relaxation was dominated by EFG fluctuations induced by CDW amplitude and phase modes [243], $1/T_1$ should scale with the square of the nuclear electric quadrupole moment and one should have $^{87}(1/T_1)/^{85}(1/T_1) = 0.226$, a value roughly 50 times smaller than the experimental one.

3.3.4 ZF-μSR study of polycrystalline $RbFe_2As_2$

The presence of static charge order should also be observable with other experimental techniques, such as electron microscopy, elastic and inelastic x-ray scattering and muon spin rotation.

Although μSR (see Section 2.3 for a description of the technique) is usually used as a local magnetic probe it can also be sensitive to the presence of a CDW phase, either because the charge order gives rise to a modulation of the paramagnetic shift or because it causes a shift of the muon implantation site owing to the modification of the local charge distribution, resulting in a different muon spin polarization relaxation rate originating from the magnetic dipole moments of the surrounding nuclei.

We carried out ZF-μSR relaxation measurements in order to look for this effect in polycrystalline $RbFe_2As_2$. Since the modification of the asymmetry decay rate in the charge ordered phase with respect to the "normal" phase was projected to be small it is necessary to measure the asymmetry evolution in a fairly long time window ($> 15\mu$s). Hence the measurements were carried out using the EMU instrument at the ISIS pulsed beam μSR facility, which is very suited to study very long asymmetry relaxations thanks to its very high muon count rate (~ 50 MEv/h, MEv: millions of events). Since $RbFe_2As_2$ is very sensitive to oxygen, in order to prevent sample degradation the $RbFe_2As_2$ powder was sealed in a custom built, air tight, aluminium μSR cell fitted with a thin Mylar window to let the muons beam impinge onto the sample.

The ZF asymmetry evolution can be fitted at all temperatures using a simple stretched exponential function:

$$A(t) = A(0)\exp[(-\lambda t)^{\beta}] + B \tag{3.15}$$

where $A(0) \sim 0.1$ is the total initial asymmetry due to the muons implanted into the sample, β is the stretching coefficient and $B \sim 0.11$ is the temperature independent background which is mainly due to the muons implanted into the sample cell. No missing muon fraction or fast asymmetry decay

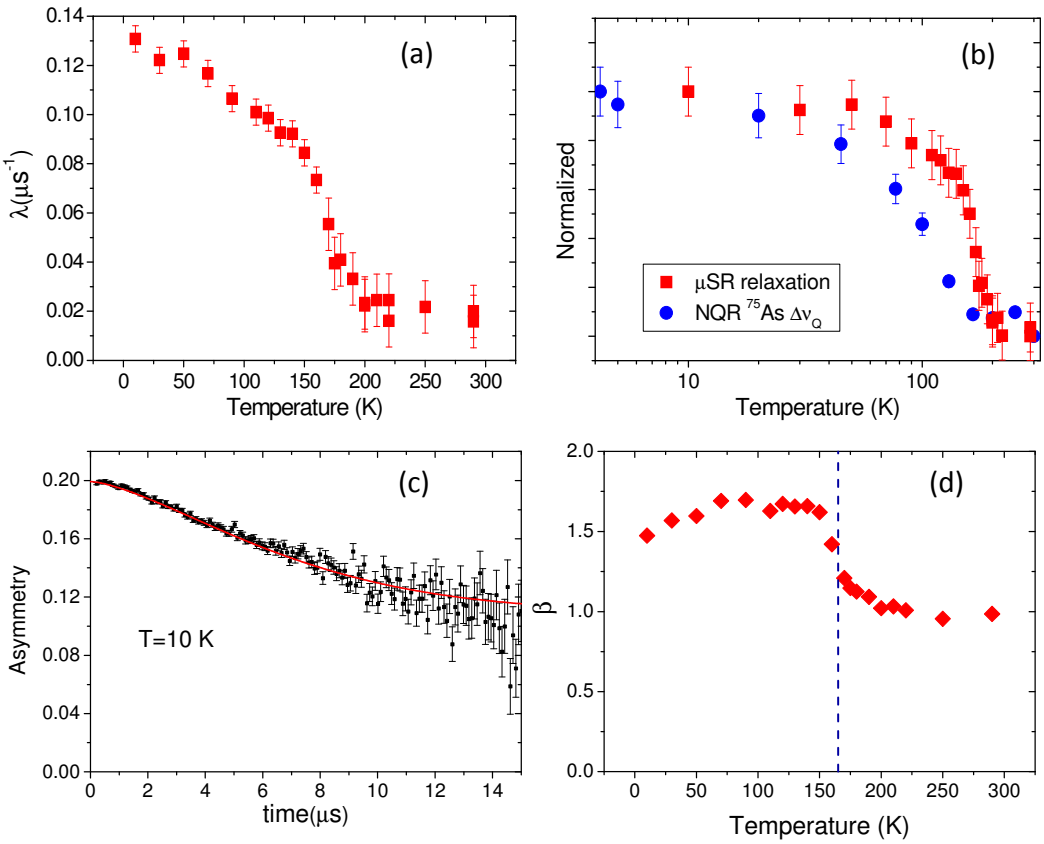

Figure 3.36: (a) ZF-μSR asymmetry relaxation rate λ temperature dependence in polycrystalline $RbFe_2As_2$. (b) Comparison of $\lambda(T)$ with $\Delta\nu_Q(T)$. The two temperature dependences have been normalized to the maximum value. (c) The asymmetry decay in the 1-15μs time window measured at T=10 K. The solid red line is a fit to a stretched exopnential decay function (see Eq. 3.15). (d) Temperature evolution of the stretching coefficient β. The dashed line indicates the temperature of the β jump. (Eq. 3.15).

was observed by lowering temperature, ruling out the presence of spurious magnetic phases in the polycrystalline $RbFe_2As_2$ sample.

The temperature evolution both of λ and β clearly show a marked change for $T \sim T_0$ (see Fig. 3.36). In particular λ begins to increase just above T_0 while β display a pretty sharp transition from $\beta = 1$ (simple exponential) to $\beta \sim 1.65$ indicating a distribution of relaxation decays below T_0. The abrupt relaxation rate increase is particularly significant since it could be due to the shift of the muon implantation site in correspondence with the emerging CDW. The β jump may indicate the distribution of relaxation rates, and thus of muon sites, developing in correspondence of the charge density modulation or alternatively the emergence of second muon site related with the charge order.

3.3.5 Conclusions

We conducted an extensive NQR, NMR and μSR study of hole doped (Cs,Rb)Fe_2As_2 122 iron based superconductors. These compounds are the 122 IBS closest to half band filling and thus to the Mott transition also charactering the cuprates HTSC.

The temperature evolution of the ^{75}As NQR spectra strongly suggest the emergence of a charge order developing below T_0 in both the studied compounds (T_0 ~140 K in $RbFe_2As_2$ and T_0 ~60 K in $CsFe_2As_2$). In single crystal $RbFe_2As_2$ the broadening of the NQR spectrum due to the charge modulation is much less marked, suggesting that the greater disorder typically present in polycrystalline IBS samples could play a role in slowing down the charge fluctuations.

^{75}As NQR and ^{85,87}Rb $1/T_1$ (NQR and NMR) temperature dependences also show a marked behaviour shift in correspondence of T_0 which is probably related with the emergence of the charge ordered phase. Even more interestingly in polycrystalline $RbFe_2As_2$, when the charge order is frozen (T<20 K), we observe a local electronic separation in two phases characterized by different excitations which could possibly be explained in terms of the orbital selective behaviour theoretically predicted for these compounds [120].

Finally also the ZF-μSR relaxation rate displays a marked increase which is possibly related to the shift of the muon site due to the emergence of the charge order in the FeAs plane. Notably also the muon polarization decay function abruptly changes shape at T_0, evolving from a simple exponential decay into a stretched exponential with stretching coefficient $\beta \sim 1.65$. This effect could be caused by the appearance of a distribution of relaxation rates in correspondence of the charge density modulation.

In the light of these results we can conclude that charge order appears to be a common feature in the phase diagrams of cuprates and iron-based high T_c superconductors and thus it may play an important role in determining the superconducting state properties.

Chapter 4

Effects of impurities in electron doped Iron Based Superconductors

The introduction of impurities in superconducting materials is a well known method to test their stability for future technological applications as well as to shed new light on their intrinsic microscopic properties, such as the symmetry of the superconducting gap. In cuprates superconductors, for example, the introduction of nonmagnetic Zn impurities results in a decrease of T_c consistent with the theoretical prediction for a d-wave superconductor [254].

In iron-based superconductors several studies on the effect of impurities have been carried out and it has soon emerged that the behaviour may vary a lot depending on the family considered and the type of the implanted impurities. For the $Ln1111$ (Ln = La, Ce, Nd, Sm) family materials it was found that the introduction of Zn, Co, Ni [255, 256, 257] and Ru [258, 259] impurities leads to a very low initial T_c suppression rate ($|dT_c/dx|_{x\to 0}$), significantly smaller than the one expected in systems with an $s^{\pm}$ symmetry of the superconducting gap. Conversely the introduction of magnetic Mn impurities leads to an abrupt decrease of T_c, both in $LaFeAsO_{1-x}F_x$ [255, 248] and in $Ba_{0.5}K_{0.5}(Fe_{1-x}Mn_xAs)_2$ [260, 261] which was initially attributed to the suppression of stripe magnetic fluctuation from the localized magnetic moment introduced by Mn impurities [255, 248]. However Hammerath *et al.* [262] also showed that in correspondence of the complete suppression of superconductivity, in $LaFe_{1-x}Mn_xAsO_{0.89}F_{0.11}$ (y = 0.2%), a magnetic phase arise.

In the first section of this chapter we will greatly expand this study of the effect of Mn impurities in $LaFe_{1-y}Mn_yAsO_{1-x}F_x$ and $Y_{0.2}La_{0.8}Fe_{1-x}Mn_xAsO_{1-y}F_y$, demonstrating that the magnetic order emerging for $y > 0.2$ is still the same stripe magnetism present in the undoped LaFeAsO parent compound and that a tiny amount ($y \sim 0.2\%$) of Mn doping actually induce an exceptionally strong localization effect which compensates the electron doping induced by F for oxygen substitutions

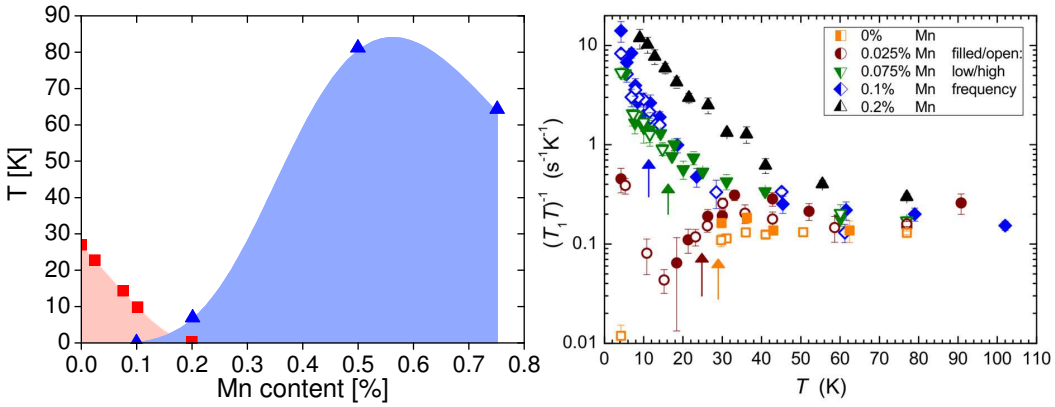

Figure 4.1: spin-lattice relaxation rate divided by temperature ^{75}As $1/T_1$ for $LaFe_{1-x}Mn_xAsO_{0.89}F_{0.11}$ with $y = 0\,\%$ up to $y = 0.2\,\%$. $1/T_1$ was measured at the low and high frequency peak of the double-peaked ^{75}As NQR spectra. The arrows denote the superconducting transition temperatures for $x = 0\,\%$ (orange, $T_c = 29\,\mathrm{K}$) up to $x = 0.1\,\%$ (blue, $T_c = 11.5\,\mathrm{K}$) Figure adapted from [248].

($x \sim 11\%$) thus recovering a ground state very similar to that of the parent compound (magnetic and orthorhombic).

In the second section instead will focus on the effect of proton irradiation in Rh doped $BaFe_2As_2$. It will be shown that the defects induced by irradiation have a significant influence on the low frequency fluctuation revealed by $1/T_2$, in good agreement with the hypothesis that they originate from the motion of the domain walls separating the regions dominated by either $(0,\pi)$ or $(\pi,0)$ correlations. Furthermore we found that the presence of the defects gives rise to a significant broadening of the ^{75}As NMR spectrum. The effect is stronger in the optimally doped sample where the Curie Weiss temperature dependence of the line width suggests the onset of ferromagnetic correlations coexisting with superconductivity at the nanoscale. This section is intended as an extension of Sections 3.1 and 3.2.

4.1 The poisoning effect of Mn doping in F-doped 1111 compounds

In the $Ln1111$ (Ln: lanthanide ion) family Mn doping ($LnFe_{1-y}Mn_yAsO_{1-x}F_x$) gives rise to a very fast decrease of T_c, and just $x = 0.2\%$ Mn content is enough to totally suppress superconductivity in the optimally fluorine doped $LaFe_{1-x}Mn_xAsO_{0.89}F_{0.11}$ compound [255, 256, 248]. This behaviour is completely different from what observed upon introducing other types of impurities (e.g. Ru [258, 259]) which often require very large concentrations in order to destroy the superconducting state (e.g. $\sim 60\%$ Ru doping in $LaFeAsO_{1-x}F_x$).

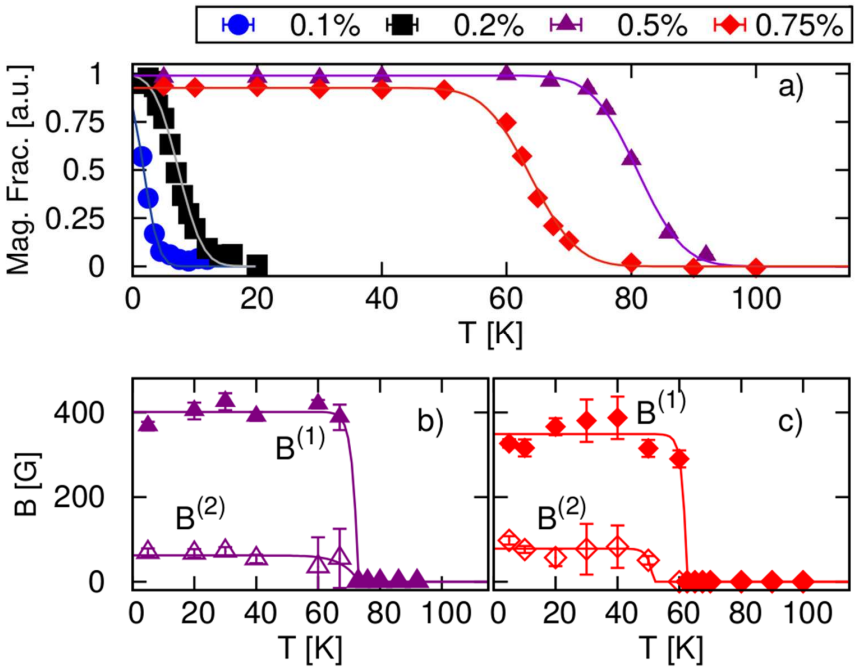

Figure 4.2: (a) Powdered $LaFe_{1-x}Mn_xAsO_{0.89}F_{0.11}$ ZF-μSR Magnetic volume fraction (see Section 2.3). (b) and (c) Temperature dependence of the local magnetic fields at the two La1111 muon sites (filled and empty symbols) for $x = 0.5\%$ and 0.75%. The lines are guides to the eye. Figure adapted from [248].

Remarkably the strength of the effect strongly depends on the *Ln* ion, in fact in optimally F-doped Sm1111 T_c vanishes for a Mn content around 8%, more than an order of magnitude larger than the critical Mn content $x_c = 0.2\%$ observed in $LaFe_{1-x}Mn_xAsO_{0.89}F_{0.11}$. The different behaviour of Sm1111 and La1111 against Mn impurities suggests that by decreasing the lanthanide ion size T_c decreases more slowly with the Mn doping and that the system is driven away from the magnetic transition.

Hammerath *et al.* [248] carried out an extensive μSR and ^{75}As NQR study of $LaFe_{1-x}Mn_xAsO_{0.89}F_{0.11}$for several Mn doping levels. Their ZF μSR results revealed that a magnetic phase appears when superconductivity is destroyed for $x > x_c$ (see the phase diagram in Fig. 4.1). A careful analysis of the muon polarization decay indicates [248] that magnetism is intrinsic to the FeAs plane and thus it is not simply due to the diluted magnetic Mn impurities. The internal field measured by μSR in $LaFe_{1-x}Mn_xAsO_{0.89}F_{0.11}$ (x =0.5%) is $\sim$ 400 G (see Fig. 4.2), much smaller than the $\sim$ 1600 G field measured at the muon site in undoped LaFeAsO [18] (see Fig. 4.2).

The nature of the magnetic ground-state developing at high Mn is not easy to determine. In $Ba_{0.5}K_{0.5}(Fe_{1-x}Mn_xAs)_2$ superconductors neutron scattering measurements suggested that Mn doping modifies the magnetic wavevector from the $(\pi, 0); (0, \pi)$ order of the parent compound ($BaFe_2As_2$) to the (π, π) Néel magnetic order [263]. However for $LaFe_{1-x}Mn_xAsO_{0.89}F_{0.11}$ the

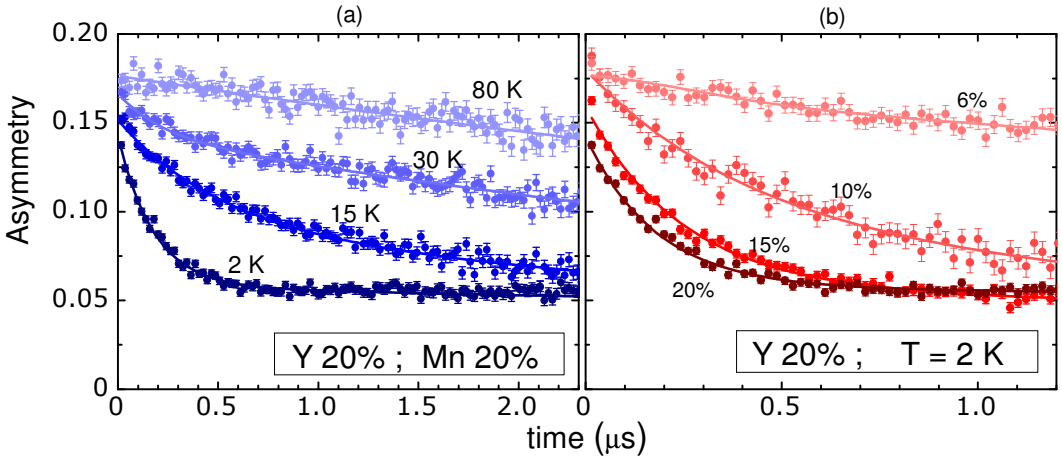

Figure 4.3: (a) Zero field μSR signal for the $La_{0.8}Y_{0.2}Fe_{1-x}Mn_xAsO_{0.89}F_{0.11}$ sample with x = 20%, measured at different temperatures. (b) ZF μSR signal for LaY20 samples with Mn doping x = 6%,10%,15% and 20%, at T = 2 K. Solid lines in (a) and (b) represent the best fits to Eq. 4.1 (see also Section 2.3.3).

significant disorder induced by fluorine doping and the necessity of a large quantity of sample with a small and very precise Mn content (x~ 0.5%) make the neutron scattering measurements more challenging.

NQR ^{75}As $1/T_1$ measurements evidenced that the spin fluctuations slow down with increasing Mn content giving rise to an enhancement of ^{75}As $(T_1T)^{-1}$. The $(T_1T)^{-1}$ temperature dependence can be fitted using the Moriya's SCR theory for weakly itinerant systems near a quantum critical point (QCP). This indicates that the spin fluctuations are of 2D antiferromagnetic character and that the transition from superconductivity to magnetism take place in correspondence of a QCP [248].

In order to better investigate the nature of the T_c suppression by Mn impurities in $Ln1111$ compounds we carried out similar ZF-μSR measurements on $Y_{0.2}La_{0.8}Fe_{1-x}Mn_xAsO_{0.89}F_{0.11}$ [264] and $SmFe_{1-x}Mn_xAsO_{0.88}F_{0.12}$ [265] which, together with SQUID magnetometry and TF-μSR (see Section 2.3), allowed us to plot the Mn dependent phase diagram of these compounds. Furthermore we also measured the ZF-NMR spectrum of the magnetic $LaFe_{1-x}Mn_xAsO_{0.89}F_{0.11}$ (x=0.5%) compound from which we were able to directly determine that the magnetic order is stripe and not Neel as in the 122 family. We also measured ^{19}F $1/T_1$ both in $LaFe_{1-x}Mn_xAsO_{0.89}F_{0.11}$ and in $Y_{0.2}La_{0.8}Fe_{1-x}Mn_xAsO_{0.89}F_{0.11}$ which revealed [266] the presence of low-frequency fluctuations analogous to those present in other IBS compounds [195] (see Section 3.1).

4.1.1 ZF-μSR measurements and phase diagrams

The ZF-μSR measurements have been carried out at the Paul Sherrer Institut (PSI) with the Dolly instrument both on $SmFe_{1-x}Mn_xAsO_{0.88}F_{0.12}$ (SmMn

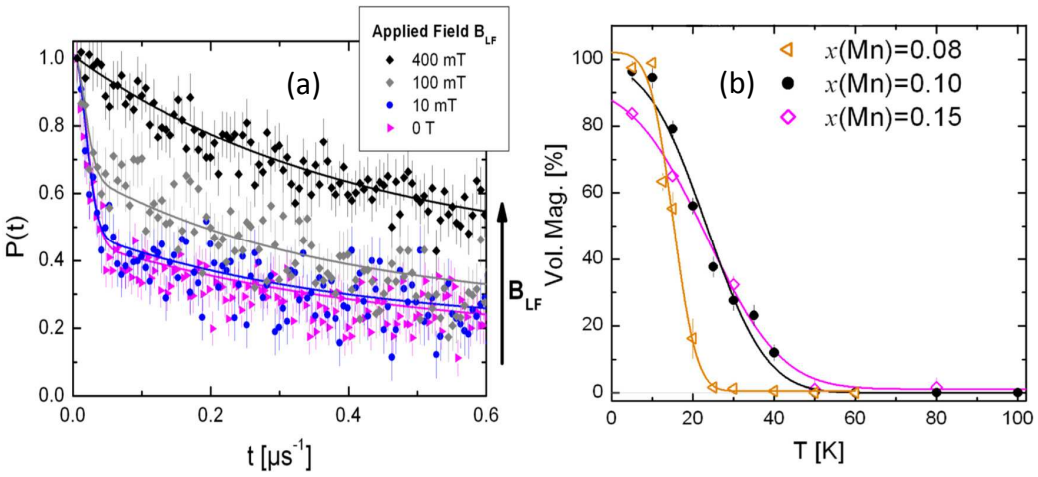

Figure 4.4: (a) LF-μSR polarization evolution measured at T=5 K in the $SmFe_{1-x}Mn_xAsO_{0.88}F_{0.12}$ x=0.10 sample. (b) Temperature dependence of the magnetic volume fractions for the $SmFe_{1-x}Mn_xAsO_{0.88}F_{0.12}$ x=0.08, 0.10, 0.15 samples

hereafter) and $La_{1-y}Y_yFe_{1-x}Mn_xAsO_{0.89}F_{0.11}$ polycrystalline samples.

Two series of polycrystalline $La_{1-y}Y_yFe_{1-x}Mn_xAsO_{0.89}F_{0.11}$ samples have been studied: the first one with fixed y = 20% yttrium content (LaY20 hereafter) and nominal Mn contents ranging from x = 0% to 20%, while the second one was prepared with fixed x = 0.5% Mn content and y = 0.5%, 1%, 5%, 10%, 20%, 23% yttrium contents (LaYMn05 hereafter).

For further details about the experimental technique see Section 2.3.3. Figure 4.3a shows the typical time dependence of the ZF μSR asymmetry at different temperatures for the samples that display a magnetic order below T_m while in Fig. 4.3b the evolution of the T=2 K asymmetry upon increasing Mn doping is reported. The time evolution of the muon asymmetry could be fit with the standard function (see Section 2.3.3):

$$A(t) = A_0 \left[f_{\parallel} e^{-\lambda_{\parallel} t} + f_{\perp} G(t, B_\mu) \right] , \tag{4.1}$$

where A_0 is the initial μSR asymmetry, while $f_{\parallel}$ and $f_{\perp}$ are the longitudinal ($\mathbf{B}_\mu \parallel \mathbf{S}_\mu$) and transverse ($\mathbf{B}_\mu \perp \mathbf{S}_\mu$) fractions of the asymmetry, respectively. The function $G(t, B_\mu)$ determines the time dependence of the transverse component, whereas the longitudinal one decays exponentially with a decay rate $\lambda_{\parallel}$. In our case we found that both in SmMn1111 and YLa1111 $G(t, B_\mu) = \exp(-\lambda_{\perp} t)$.

At high temperature ($T > 30$ K) the samples of the LaY20 and LaYMn05 series are in the paramagnetic regime and the muon asymmetry can be fit by setting $f_{\perp}$=0, with decay rates $\lambda_{\parallel} \sim 0.09\ \mu s^{-1}$. Upon decreasing the temperature a fast decaying component $f_{\perp}$ emerges in LaY20 samples with $x \geq 10\%$, evidencing the presence of overdamped oscillations in the muon asymmetry. An analogous trend was also observed in the SmMn samples

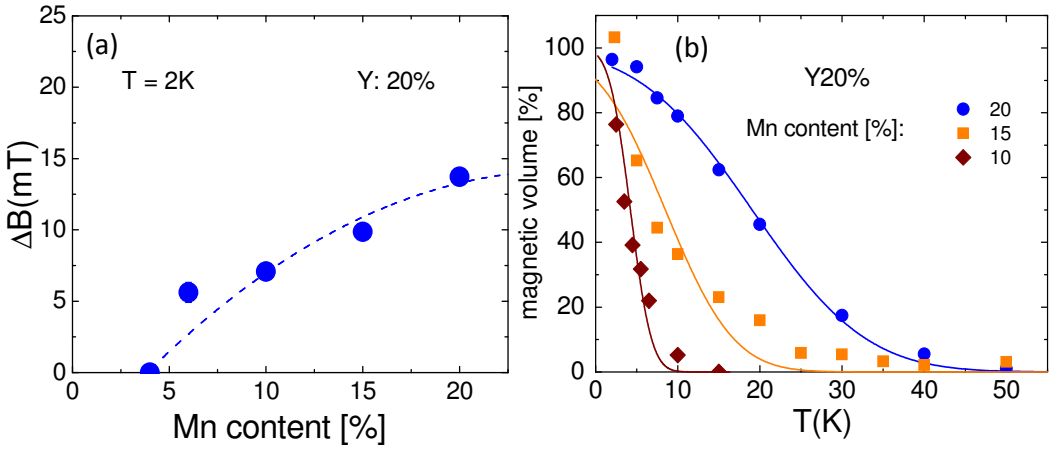

Figure 4.5: The values of ΔB at 2 K, for all the samples showing a magnetic order (see Fig. 7), obtained from the fit of the muon asymmetry to Eq. 4.1. The dashed line is a guide to the eye. (b) The magnetic volume fraction temperature dependence is shown for $y = 20\%$ and $x = 10\%$, 15% and 20%. The solid lines are best fits to Eq. 4.3.

for $x > 2\%$ while no traces of magnetism ($f_\perp > 0$) have been detected in LaYMn05 down to 2 K.

A similar behaviour has been observed for samples close to the boundary between magnetism and superconductivity [173, 174] and reflects the presence of a significant distribution of local magnetic fields, typically observed when a short range AF magnetic order develops [173]. The sample magnetic volume fraction V_m, namely the fraction of the sample volume where the muons sense the magnetic order, can be derived from $f_\parallel$, in fact, from simple geometric arguments (see Section 2.3.3) in a polycrystalline sample with a 100% magnetic volume fraction, $f_\parallel = 1/3$. Then V_m can be determined by:

$$V_m(T) = 3/2(1 - f_\parallel(T)) \ . \tag{4.2}$$

The temperature dependence of V_m (Fig. 4.5b and 4.4b) indicates that the full magnetic volume condition is reached only at low temperatures for all the magnetic samples: LaY20 with $x \geq 10\%$ and SmMn with $x \geq 3\%$.

The width of the internal field distribution ΔB_μ can be roughly estimated as $\Delta B_\mu = \lambda_\perp/\gamma_\mu$. The values of ΔB_μ obtained from the fit of the data with Eq. 4.1 (~10 mT) are shown in Fig 4.5a. In SmMn instead the typical value of ΔB_μ is 50 mT (see Fig. 4.8).

The static character of the magnetism developing at $T < T_m$ has been confirmed by LF μSR experiment which have shown that a field of about 100 mT is enough to completely recover the initial muon asymmetry at 2 K in LaY20 while a ~400 mT field is needed in SmMn (see Fig. 4.4a), as expected for the larger value of ΔB_μ.

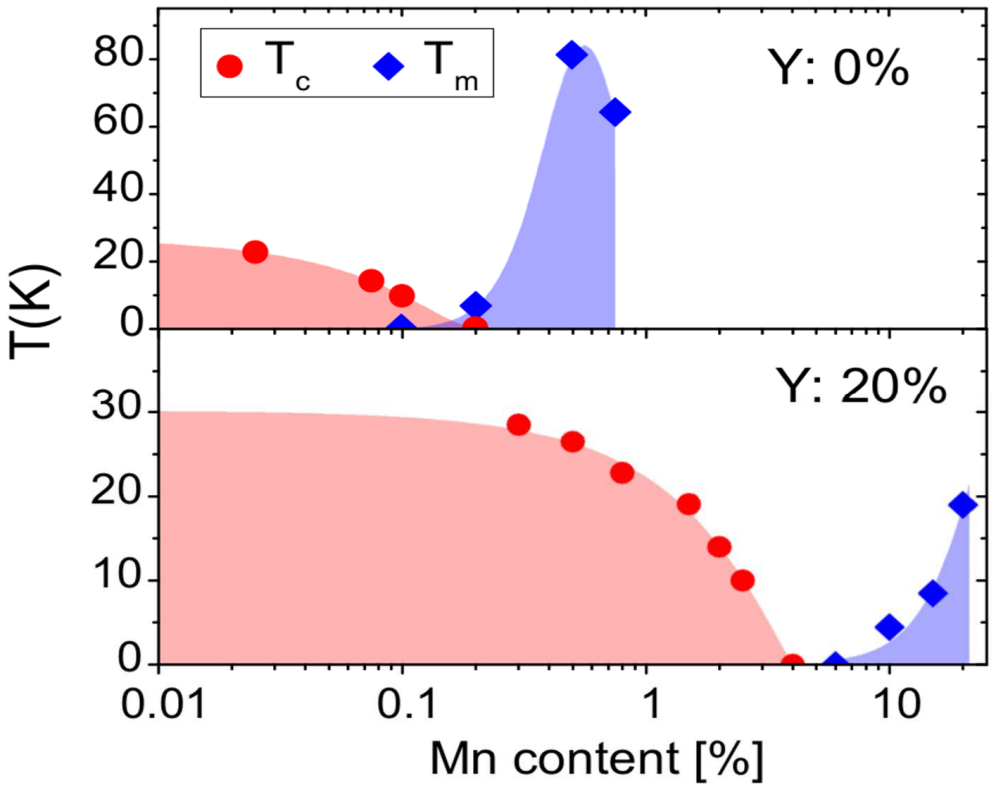

Figure 4.6: Phase diagram of $LaFe_{1-x}Mn_xAsO_{0.89}F_{0.11}$ (LaY0, top) and of $La_{0.8}Y_{0.2}Fe_{1-x}Mn_xAsO_{0.89}F_{0.11}$ (LaY20, bottom). The red and blue shaded areas are the superconductive and the magnetic phases, respectively.

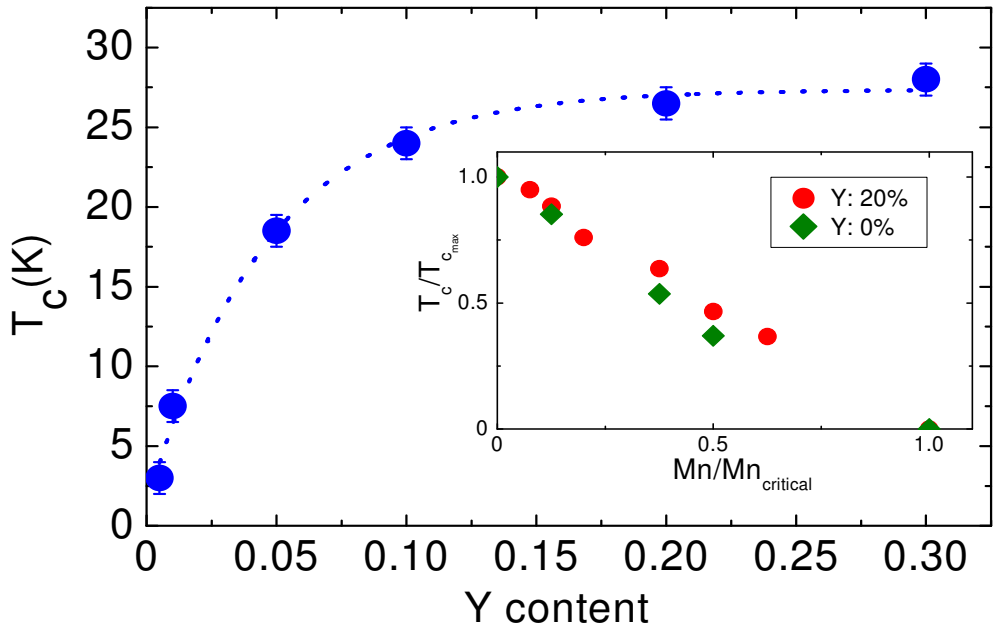

Figure 4.7: Critical temperatures for the LaYMn05 samples. The dashed line is a guide to the eye. Inset: $T_c(x)/T_c(x = 0)$ versus the Mn content normalized by the critical Mn doping causing the vanishing of T_c.

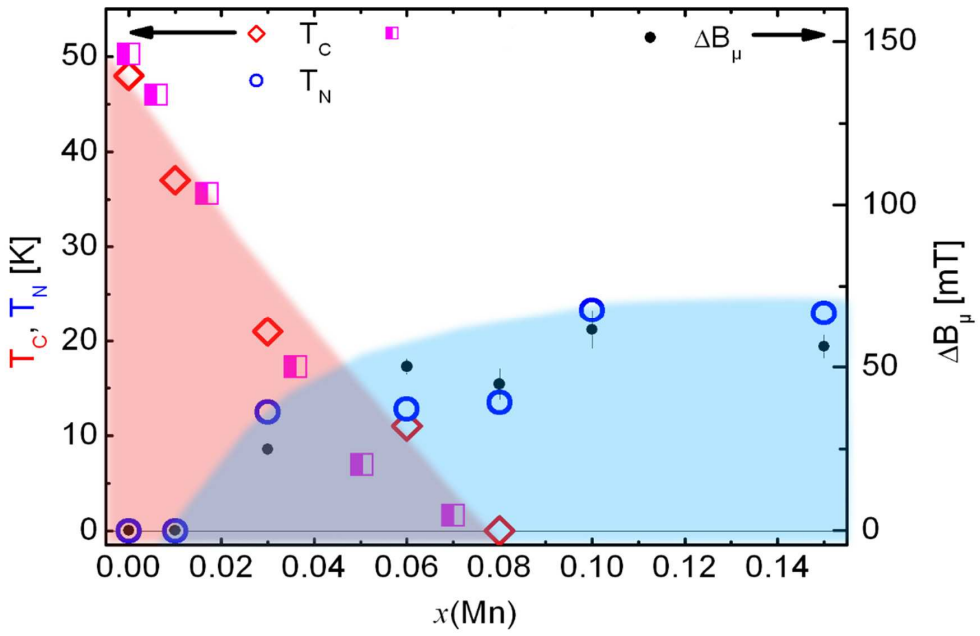

Figure 4.8: Magnetic ordering T_N (•) and critical superconducting temperature T_c (◇) vs Mn content x in the $SmFe_{1-x}Mn_xAsO_{0.88}F_{0.12}$ samples. The internal field widths ΔB_μ (•) are also reported (right scale). The magenta squares represent the results from theoretical calculations carried out by Gastiasoro *et al.* [267] (see Section 4.1.2.2).

The magnetic ordering temperature can be estimated by fitting $V_m(T)$ to the error function

$$V_m(T) = \frac{1}{2}\left(1 - \mathrm{erf}\left(\frac{T - T_m}{\sqrt{2}\Delta T_m}\right)\right) \tag{4.3}$$

which assumes the presence of a Gaussian distribution of local transition temperatures centered around the average value T_m. The value of T_m and T_c as a function of Mn, measured from ZF-μSR and SQUID magnetometry, are reported in the phase diagrams presented in Figs. 4.6, 4.7 and 4.8 (T_c data come from SQUID and TF-μSR).

These measurements show that the substitution of La with Y causes a sizable increase of the critical Mn threshold x_c required to suppress superconductivity, with an increase from 0.2% to 4% on raising the Y content from 0 to 20%. This x_c boost is comparable to that first observed by Sato *et al.* [255] when a smaller lanthanide substitutes La (x_c ~4% for Nd and x_c ~8% for Sm, see Fig. 4.8)

The results on LaY20, where La is partially substituted by the smaller but non-magnetic Y ion, clearly evidence that the electronic properties of $LaFeAsO_{0.89}F_{0.11}$ are significantly affected by the chemical pressure induced by the different radii of the lanthanide ions on the FeAs planes. The effect of the chemical pressure is further evidenced in Fig. 4.7 showing T_c as a function

of the La/Y substitution in $La_{1-y}Y_yFe_{0.995}Mn_{0.005}AsO_{0.89}F_{0.11}$. Superconductivity, suppressed by just x_c = 0.2% Mn doping for the Y free compound, is gradually restored by increasing the Y content, which correspond to increasing the chemical pressure.

Differently from the $LaFe_{1-x}Mn_xAsO_{0.89}F_{0.11}$ case (LaY0 hereafter) where T_c drops very fast and the disappearance of T_c corresponds to the rise of magnetism [248], for LaY20 a crossover region where both T_c and T_m are zero is observed for 4% $< x <$ 6% where the samples are neither magnetic nor superconductive. This suggests that chemical pressure is driving the system away from the QCP also revealed by NQR ^{75}As $1/T_1$.

4.1.2 The nature of the $LaFe_{1-y}Mn_yAsO_{0.89}F_{0.11}$ magnetism revealed by ZF-NMR and NQR

In order to understand the mechanism responsible for the T_c suppression it is essential to figure out what is the nature of the magnetic order developing at Mn contents larger than x_c. In fact the critical Mn concentration in $LaFe_{1-x}Mn_xAsO_{0.89}F_{0.11}$ x_c = 0.2% is so low that no significant Mn induced hole doping is possible and also Mn impurities are too few to completely curb superconductivity by acting as magnetic scattering centres [248]. On the other hand the shift of the magnetic ordering wave vector from $(\pi, 0); (0, \pi)$ to (π, π) observed in 122 compounds [263] suggests that the magnetic Mn impurities may suppress the stripe type fluctuation which are thought to be an essential ingredient for the appearance of the superconducting state (see Section 1.3). Furthermore recent theoretical calculations by Giovannetti *et al.* [49] showed that also the orthomagnetic order, characterized by a $\pi/2$ rotation of the adjacent spins, could be present in LaFeAsO related compounds.

A powerful approach to understand the type of magnetic order present in the Mn doped *Ln*1111 compounds is the measurement of the ZF-NMR spectra. As extensively explained in Section 2.2 this method was also used to probe the magnetic order in underdoped LaFeAsO and $BaFe_2As_2$. In fact with this technique we directly probe the internal field generated by the ordered Fe/Mn moments on the ^{75}As nuclei.

However, in order to correctly interpret the experimental ZF-NMR data, it is useful to first simulate the internal field expected at the ^{75}As site for different types of magnetic order and for several Mn concentrations.

4.1.2.1 Internal field calculations and Mössbauer

Both the long range dipolar interaction and the short range transferred hyperfine interaction between the As nucleus and magnetic moments on the four nearest neighbor Fe ions have been considered in the calculations. The

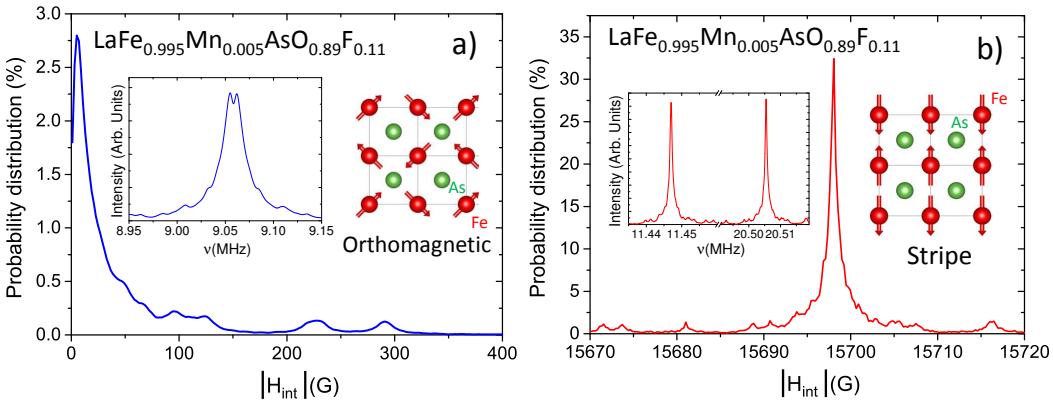

Figure 4.9: Simulated (see text) distribution of internal fields on the As site (main panels) and simulated ^{75}As ZF-NMR spectra (left insets) of $LaFe_{0.995}Mn_{0.005}AsO_{0.89}F_{0.11}$ in case of orthomagnetic order (a) and stripe order (b). In this simulation Mn impurities takes part to the magnetic ordering so their moments have the same orientation of the magnetic moment of the substituted Fe ion, pictorially shown in the right insets. The effect of the Mn moments can be directly seen in the orthomagnetic order simulated spectrum and gives rise to the small splitting of the NQR-ZFNMR line.

internal field can be written as the sum of the contributions from each one of the Fe sites:

$$\mathbf{H}_{\text{int}} = \sum_i \mathbf{A}_i \cdot \mathbf{m}_i \tag{4.4}$$

where $\mathbf{m}_i$ is the ordered electron moment at the i-th Fe site and $\mathbf{A}_i$ is the nuclear-electron hyperfine coupling tensor between the As nucleus and i-th Fe site. We considered only the contributions due to the Fe sites in the same plane of the As nucleus since the contribution to the internal field from the other Fe-As layers is vanishingly small due to the r^{-3} scaling of the dipolar coupling (see Section 2.1.2.2). The diagonal components of the symmetric transferred hyperfine interaction tensor for the four nearest neighbour Fe sites (Fig. 4.9, insets) was derived from ^{75}As Knight shift measurements while two of the three off diagonal components can be derived from the strength of the internal field in the stripe order configuration, as reported in Ref. [66]. Since we are only interested in understanding which types of order give rise to spectra in qualitative agreement with the measured ones, we used the values of the transferred hyperfine tensor components reported in Ref. [268] and chose $m_{Fe} = 0.36\ \mu_B$ for the Fe magnetic moment and $m_{Mn} = 4\ \mu_B$ for the Mn magnetic moment. The third off-diagonal component of the transferred hyperfine coupling is relevant only in case of Néel order and was chosen equal to the stripe one. The distribution of the internal fields for each type of magnetic order was calculated by randomly substituting Mn (for $x = 0.5$ %) on the Fe site in a 24×24 size mesh and repeating the calculation 10^5 times. The spectra were then obtained by diagonalizing the Zeeman-Quadrupole

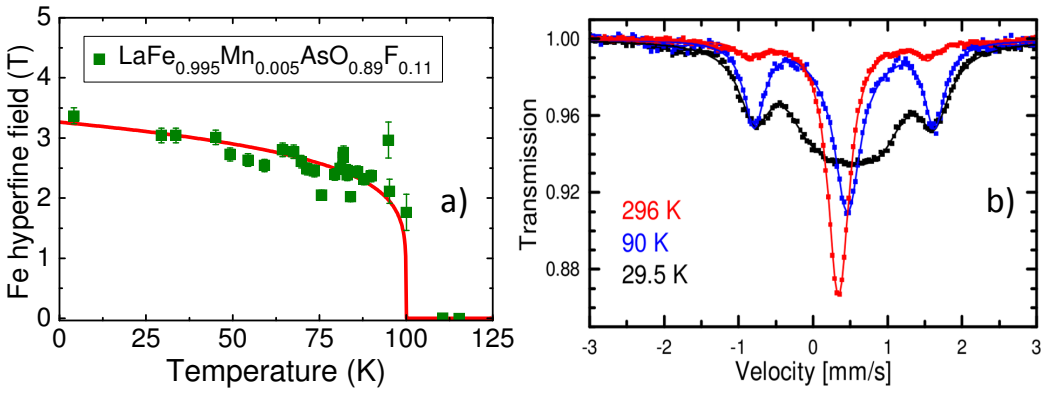

Figure 4.10: (a) Temperature dependence of the hyperfine magnetic field, B_h, for $x = 0.5$ % as derived from Mössbauerspectra. The red solid line tracking the order parameter is a phenomenological fit of B_h with $B_h = 3.3(1-(T/T_m))^{\beta}$ where $T_m = 100$ K and $\beta = 0.17$.(b) Mössbauer spectra for the $x = 0.5\%$ compound at a few selected temperatures both above and below T_m. Measurements carried out by P. Materne, H.-H. Klauss at the Dresden TU.

Hamiltonian:

$$\mathcal{H} = \mathcal{H}_{\text{Zeeman}} + \mathcal{H}_Q = -\gamma\hbar \mathbf{H}_{\text{int}} \cdot \mathbf{I} + \frac{eQV_{ZZ}}{12}[3I_z^2 - I^2 + \eta(I_x^2 - I_y^2)] \qquad (4.5)$$

for each value of the magnetic field and applying magnetic dipole selection rules. The results for orthomagnetic (see [49]) and stripe order are reported in Fig. 4.9.

For the orthomagnetic order we found $H_{\text{int}} \sim 0$ while for the usual stripe order instead we found a $\sim$ 1.6 T field from which we obtained a simulated ZF-NMR spectrum (inset of Fig. 4.9b) analogous to that observed in LaFeAsO [68] (see Fig. 2.13b).

In case of Néel order instead the internal field is found to be $H_{\text{int}} > 1$ T. However in this magnetic structure the field is parallel to a and the splitting between the ZF-NMR lines is half of the one observed for the stripe order.

Another possible type of magnetic structure is the spin-charge order [49] which should give rise to two inequivalent iron sites. However this is in contrast with the Mössbauer measurements (see Fig. 4.10) which reveal only one iron site and so it was discarded a priori. TheMössbauer measurements also confirmed that the EFG asymmetry η is zero, as expected due to the tetragonal unit cell of LaFeAsO, and thus all the calculations have been carried out with $\eta = 0$.

4.1.2.2 ZF-NMR measurements

In order to carry out the NMR experiments the polycrystalline samples were crushed to a fine powder to improve radio frequency penetration. Since ^{75}As

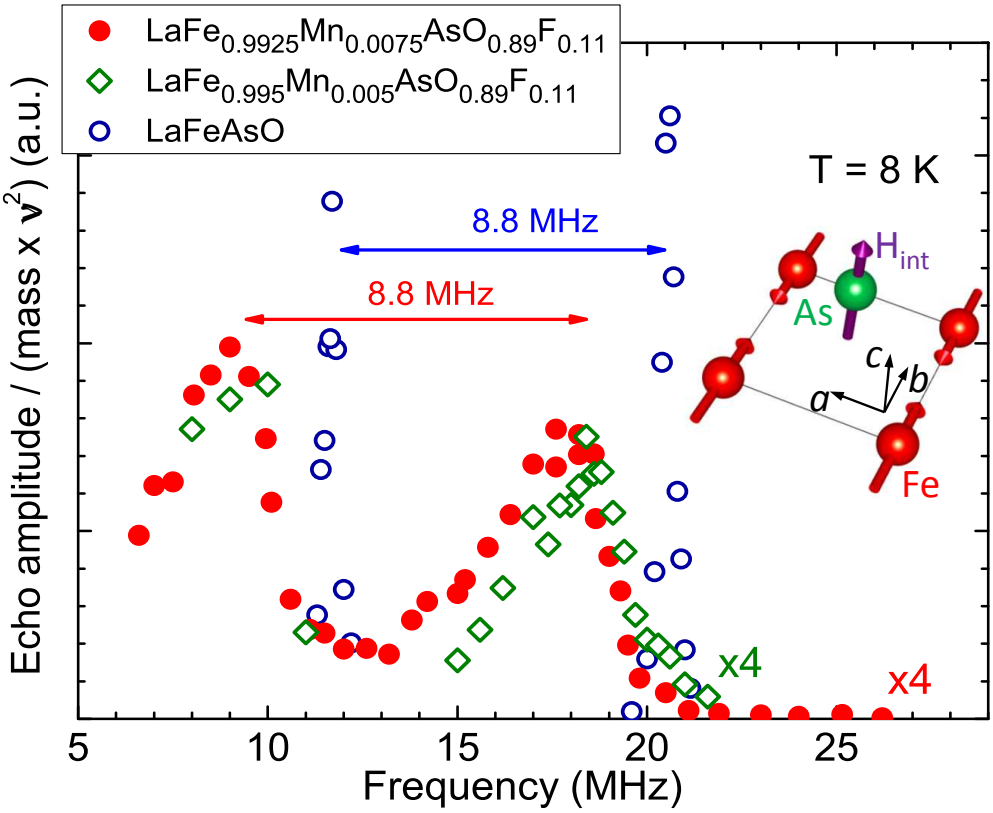

Figure 4.11: Comparison of the ^{75}As Zero-Field NMR spectra between the LaFeAsO parent compound and $LaFe_{1-x}Mn_xAsO_{0.89}F_{0.11}$ for x = 0.5 % (green) and 0.75 % (red). For clarity the intensity of the spectra for the Mn-substituted compounds are multiplied by 4. Inset: sketch of the magnetic unit cell for the stripe order (the red arrows represent the Fe magnetic moments directions while the magenta arrow corresponds to the orientation of the internal field at the As site)

is a spin I = 3/2 nucleus, above T_m, the NQR spectrum is characterized by a single line at a frequency given by Eq. 2.16:

$$\nu_Q = \frac{eQV_{ZZ}}{2h}\left(1+\frac{\eta^2}{3}\right)^{1/2} \tag{4.6}$$

with Q the electric quadrupole moment of the ^{75}As nucleus, V_{ZZ} the main component of the electric field gradient (EFG) tensor at the As site generated by the surrounding charge distribution and η its asymmetry. Since LaFeAsO is tetragonal $\eta = 0$ and c is the quantization axis. The broadening of the line is mainly due to the disorder present in the system since the EFG strongly depends on the local charge distribution.

Below T_m however, in case of a stripe magnetic order, an internal field $H_{int} \parallel c$ is present at the As nuclei and we can perform standard NMR experiments with the only difference that the magnetic field is not provided by an

external magnet but by the magnetic ordering of the Fe moments (ZF-NMR). Even if below T_m the unit cell could become orthorhombic the asymmetry η is still small ($\eta \sim 0.15$) as reported in Ref. [108] and confirmed by the Mössbauer measurements.

The ^{75}As NQR and ZF-NMR spectra of the $LaFe_{1-x}Mn_xAsO_{0.89}F_{0.11}$ samples (x=0.5%, x=0.75%) were derived by recording the integral of the echo signal after a $\pi/2 - \tau_e - \pi$ pulse sequence as a function of the irradiation frequency. All the ZF-NMR spectra were measured with exactly the same set-up and coil filling factor in order to compare the relative intensity of the lines.

The ^{75}As ZF-NMR spectra have been measured in the 6-26 MHz range for T=8 K. In these samples $T_m \sim 80$ K for x=0.5% and $T_m \sim 65$ K for x=0.75%.

Both the spectra of the LaFeAsO parent compound and of the x=0.75% sample are characterized by two peaks above 5 MHz (see Fig. 4.11), which in the latter compound are rigidly shifted to lower frequencies and broadened. The peaks are associated with the $m_I = 1/2 \rightarrow m_I = -1/2$ and $m_I = -1/2 \rightarrow m_I = -3/2$ transitions, with m_I the component of the nuclear spin I along the quantization axis, which in the case of the stripe order, as it is the case for LaFeAsO, is along the c axis. The frequency shift between the two peaks is thus given by the nuclear quadrupole frequency determined by the local charge distribution, which at 8 K is $\nu_Q = 8.8$ MHz both for LaFeAsO and for the $x = 0.5\%$ and 0.75% samples.

The only magnetic structure compatible with the observed experimental results is the (π,0) or (0,π) stripe ordering as can be seen comparing the measured spectrum with the simulated ones reported in Section 4.1.2.1. In addition, one must notice that the linewidth induced by the magnetic disorder is three orders of magnitude smaller than the measured one. This prediction is in good agreement with the observation that no significant change is induced in the line width by increasing the Mn content from 0.5% to 0.75%. Conversely, as it can be seen in the NQR spectra (see Fig. 4.14) fluorine doping has a strong effect on the line width. This implies that the line broadening of $LaFe_{1-x}Mn_xAsO_{0.89}F_{0.11}$ (x=0.5% and 0.75%) with respect to LaFeAsO is mostly due to the disorder induced by F doping and possibly by the magnetic disorder related to the formation of (0,π) and (π,0) magnetic domains that get pinned by the Mn impurities. Furthermore some additional internal field disorder is also generated by the structural discorded due to the F doping, in fact it was also observed in the ZF-μSR measurements carried in underdoped $LaFeAsO_{1-x}F_x$ [18].

It must be noted that however we cannot completely rule out the presence of an incommensurate magnetic order with magnetic wave vector very close to the stripe one. In fact the incommensurability leads to a broadening of the ZF-NMR line, which, in this case, would be impossible to observe since it can be much smaller than the line broadening due to fluorine doping.

The position of the low-frequency peak (ν_c), associated with the $1/2 \rightarrow -1/2$ transition, is determined by the magnitude of the hyperfine field at ^{75}As, and one can write that $\nu_c = (\gamma/2\pi)|\mathcal{A}\langle\vec{S}\rangle|$, with γ the ^{75}As

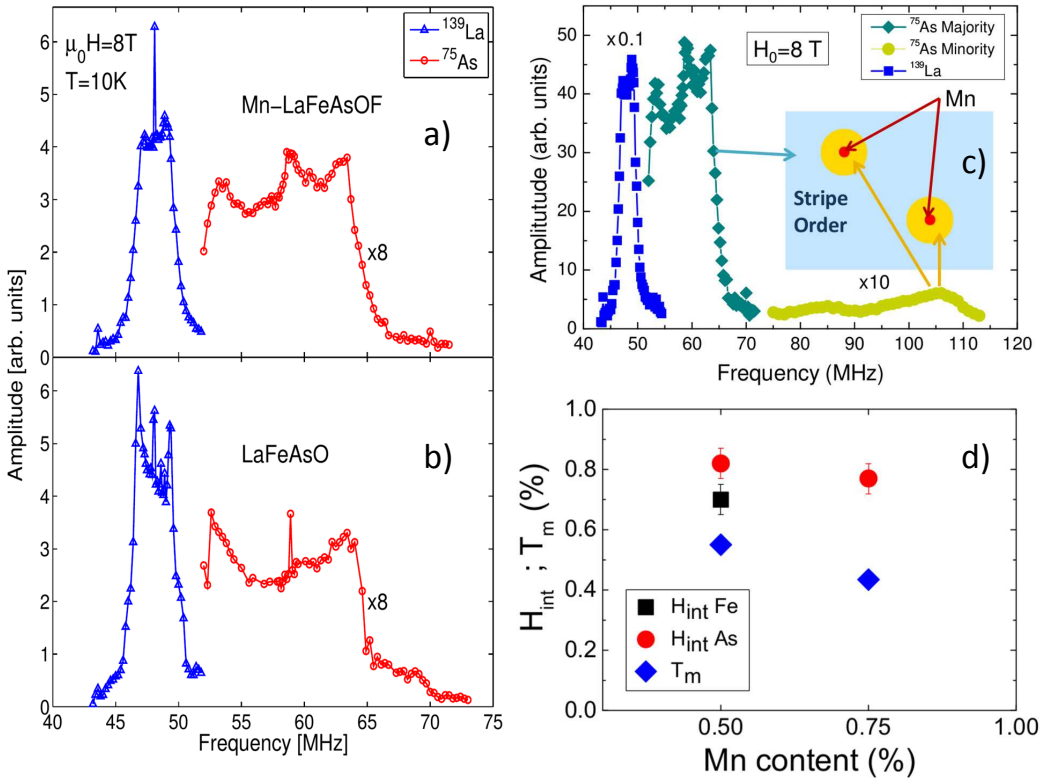

Figure 4.12: a): ^{75}As (majority signal) and ^{139}La NMR spectra of $LaFe_{1-x}Mn_xAsO_{0.89}F_{0.11}$x=0.5% at T = 10 K and $\mu_0 H_0$ = 8 T. b): ^{75}As and ^{139}La spectra of LaFeAsO at the same temperature and applied field. c): Same as (a) but also including the high frequency minority signal (enhanced 10x for readability). Inset: pictorial representation of the Fe layer with Mn impurities. d) Intensities of the hyperfine magnetic fields at the As (H_{int} As) and Fe (H_{int} Fe) (8 K) and T_m in $LaFe_{1-x}Mn_xAsO_{0.89}F_{0.11}$ (x = 0.5% and x = 0.75%) normalized to those measured in undoped LaFeAsO. The reference values measured in LaFeAso are: T_m = 145 K, H_{int} As =1.6 T and H_{int} Fe=5 T.

gyromagnetic ratio, $\mathcal{A}$ the total hyperfine coupling tensor and $\langle \vec{S} \rangle$ the average electron spin, corresponding to the magnetic phase order parameter. Accordingly, the low-frequency shift of the two peaks in the sample with x = 0.75 % would indicate a reduction of the order parameter to about 80% of the value found for LaFeAsO. The sample with x = 0.5 % displays a very similar behavior with a moderate increase in the low-temperature order parameter, which is probably related to its slightly higher magnetic transition temperature (T_m) [248].

The temperature dependence of Mössbauer spectra for the x = 0.5 % sample (Fig. 4.10a) shows that in the low temperature limit the internal field at the Fe site is of about 3.5 T, i.e. the magnitude of the order parameter is reduced to about 70% of the value found in pure LaFeAsO [269, 270, 79], in qualitative agreement with what we derived above from ZF-NMR.

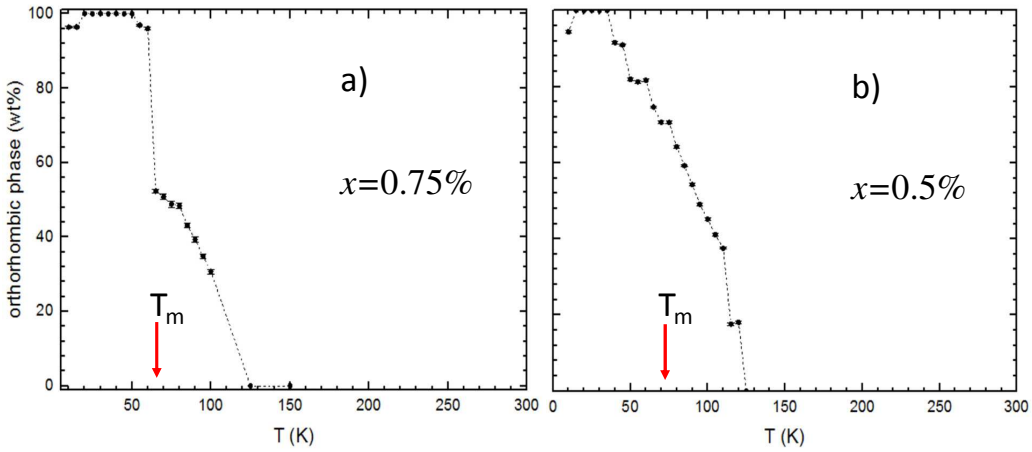

Figure 4.13: The orthorhombic volume fraction temperature dependence measured through X-Ray diffraction in $LaFe_{1-x}Mn_xAsO_{0.89}F_{0.11}$ (x=0.5%).

We have performed a quantitative estimate of the amount of nuclei contributing to the x = 0.75 % sample ZF-NMR spectrum in Fig. 4.11 by comparing its integrated intensity with that of the LaFeAsO sample, where 100 % of the sample is in the stripe collinear phase. We found that 95 ± 5 % of the x = 0.75% sample is in the stripe order.

In order to further check if there is a small (≤ 5 %) fraction of ^{75}As nuclei that we are missing, ^{75}As NMR measurements in a 8 T magnetic field have been carried out. In Fig. 4.12c the powder NMR spectrum displays a large fraction of nuclei with a spectrum broadened by the internal field developing in the stripe phase (cyan diamonds) as well as a small fraction of about 3±1 % of ^{75}As nuclei with a significant NMR shift towards higher frequencies (yellow circles). These latter nuclei are likely the ones close to Mn impurities where a large hyperfine field is expected. For x = 0.5% there are 2% of As nuclei which are nearest neighbors of a Mn impurities, a value very similar to the one we found.

Hence, the introduction of Mn suppresses superconductivity and leads to the recovery of the stripe magnetic order found in the parent LaFeAsO compound, as also confirmed by the powder NMR spectrum (Fig. 4.12a,b) which is strikingly similar to that of LaFeAsO.

4.1.2.3 NQR measurements

Further insights on the nature of the magnetic ground state developing below 100 K in Mn doped $LaFeAsO_{0.89}F_{0.11}$ (x>0.2%) can be grasped by studying the temperature dependence of the ^{75}As NQR frequency. ν_Q (Fig. 4.15 shows a jump on passing from just above T_m (^{75}As NQR) to below T_m (^{75}As ZF-NMR) which is very similar to the one detected [108] in LaFeAsO. This abrupt change in ν_Q is associated with the orthorhombic distortion.

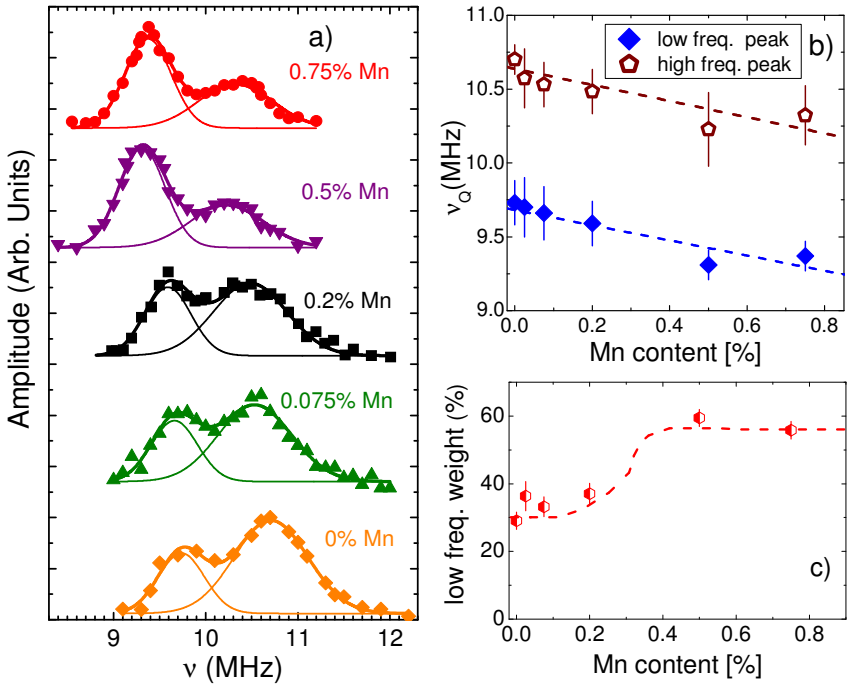

Figure 4.14: a) ^{75}As NQR spectra of $LaFe_{1-x}Mn_xAsO_{0.89}F_{0.11}$ for different Mn contents, measured at $T = 77$ K for $x \leq 0.2$ % and $T = 100$ K (above T_m) for $x > 0.2$ %. The solid lines are fits to a sum of two Gaussian functions. b) Frequency of the low (blue diamonds) and high energy (red pentagons) peaks as a function of Mn content. The dashed lines are a guide to the eye. c) Weight of the low frequency peak as a function of Mn content, the dashed line is a guide to the eye.

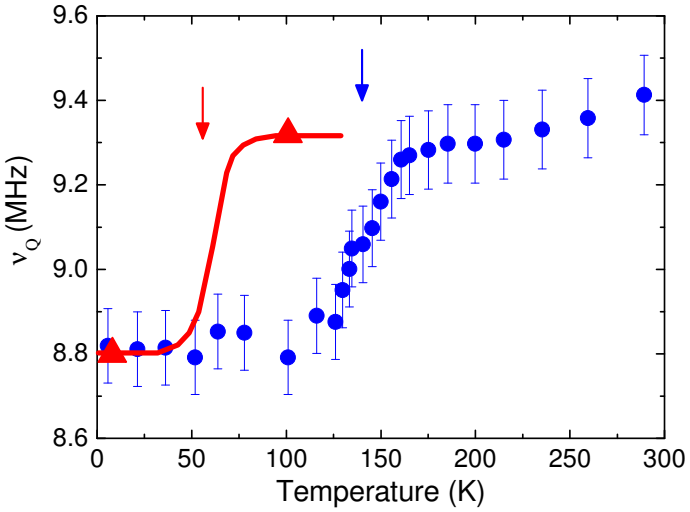

Figure 4.15: Quadrupolar frequency, ν_Q, as a function of temperature for the LaFeAsO (blue circles, data from Ref.[108]) and $LaFe_{1-x}Mn_xAsO_{0.89}F_{0.11}$ with $x = 0.75$ % (red triangles). For the latter the point above T_m is taken as the frequency of the low-frequency peak of Fig. 4.14a. The arrows indicate the magnetic transitions, while the red solid line is a guide to the eye.

Therefore, the observation of a similar change in ν_Q for the $x = 0.5-0.75\%$ compound indicates that when the stripe magnetic order is recovered by Mn doping the tetragonal - orthorhombic (T-O) structural transition is also recovered, confirming that this transition is closely related to the onset of large stripe magnetic correlations (see Section 1.3). Recently we also carried out high resolution X-Ray diffraction measurements at the ESRF synchrotron in Grenoble which also confirmed the presence of a T-O distortion for the samples with x>0.5% with $T_{ortho}>T_m$ (Fig. 4.13).

Another relevant aspect emerge from the study of the Mn content dependence of the ^{75}As NQR spectra. As can be seen in Fig. 4.14, the spectra, measured at $T = 77$ K for $x \leq 0.2\%$ and at $T = 100$ K (above T_m) for $x > 0.2\%$, display a clear shift towards lower frequency with increasing Mn content (see Fig. 4.14b) and a rapid change in the intensity of the low-frequency peak for $x>0.2$ %. It is worth to note that for $x>0.2$ % the frequency of the dominant low frequency peak perfectly matches that of the paramagnetic phase of LaFeAsO (see Fig. 4.15 and 4.14b), indicating a similar electronic ground state. According to Lang et al. [166, 168], the low and high-frequency NQR peaks should be associated with nanoscopically segregated regions with different electron doping levels (see Section 2.2.1). In particular, the low-frequency peak should be associated with a lower electronic concentration of weakly itinerant electrons. Hence, the increase in the magnitude of the low-frequency peak above $x = 0.2$ % indicates a tendency towards electron localization. This finding is also corroborated by the rapid increase of the electric resistivity as a function of Mn content previously observed [255, 271] across the metal-insulator crossover taking place around $x = 0.2\%$. A similar rise in resistivity was also observed [272] in $LaFeAsO_{1-x}F_x$ with decreasing F content.

4.1.2.4 Theoretical model

In order to clarify from a theoretical point of view the origin of the dramatic effect of Mn doping in $LaFeAsO_{0.89}F_{0.11}$, M. N. Gastiasoro carried out real space calculations using a realistic five band Hamiltonian [267, 46].

This model of $LaFe_{1-x}Mn_xAsO_{0.89}F_{0.11}$ includes both a realistic (five-orbital) model of the kinetic energy

$$\mathcal{H}_0 = \sum_{\mathbf{ij},\mu\nu,\sigma} t_{\mathbf{ij}}^{\mu\nu} \hat{c}^{\dagger}_{\mathbf{i}\mu\sigma} \hat{c}_{\mathbf{j}\nu\sigma} - \mu_0 \sum_{\mathbf{i}\mu\sigma} \hat{n}_{\mathbf{i}\mu\sigma}, \tag{4.7}$$

with tight-binding parameters determined in Ref. [273], and electronic interactions given by the multi-orbital Hubbard Hamiltonian

$$\begin{aligned} \mathcal{H}_{int} = U \sum_{\mathbf{i},\mu} \hat{n}_{\mathbf{i}\mu\uparrow} \hat{n}_{\mathbf{i}\mu\downarrow} + (U' - \frac{J}{2}) \sum_{\mathbf{i},\mu<\nu,\sigma\sigma'} \hat{n}_{\mathbf{i}\mu\sigma} \hat{n}_{\mathbf{i}\nu\sigma'} \\ - 2J \sum_{\mathbf{i},\mu<\nu} \vec{S}_{\mathbf{i}\mu} \cdot \vec{S}_{\mathbf{i}\nu} + J' \sum_{\mathbf{i},\mu<\nu,\sigma} \hat{c}^{\dagger}_{\mathbf{i}\mu\sigma} \hat{c}^{\dagger}_{\mathbf{i}\mu\bar{\sigma}} \hat{c}_{\mathbf{i}\nu\bar{\sigma}} \hat{c}_{\mathbf{i}\nu\sigma}, \end{aligned} \tag{4.8}$$

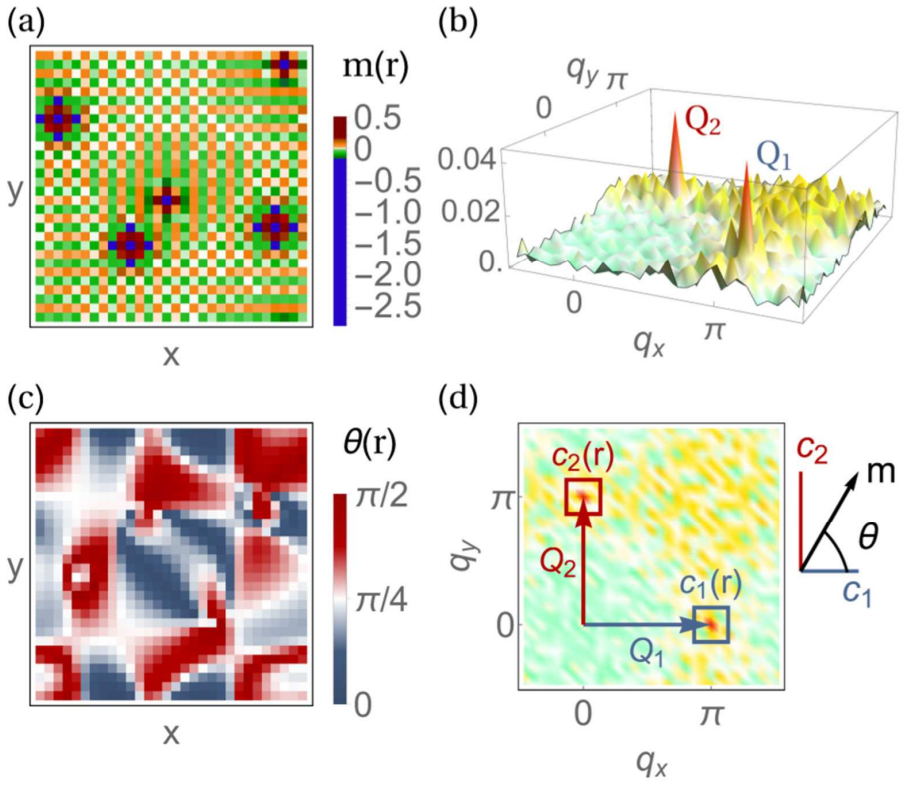

Figure 4.16: (a) Induced magnetic order $m(r)$ for 0.55% Mn moments and (b) its Fourier transform $|m(q)|$. (c) Local phase map $\theta(r) = \arctan(|c_1(r)|/|c_2(r)|)$ showing the ordering vectors on the lattice: $\theta = 0$ and $\pi/2$ for single-Q Q_1 (blue) and Q_2 (red) domains respectively, and $\theta = \pi/4$ for double-Q regions (white). The coefficient associated with Q_1 (Q_2), $c_l(r) = \sum_n c_n \exp[i(q_n - Q_l)r]$, was calculated by a filtered Fourier transform with the $\{q_n\}$ wave vectors contained inside the blue and red squares shown in panel (d). The inset illustrates the definition of the local phase $\theta(r)$.

Here μ, ν are orbital indexes, $\mathbf{i}$ denotes lattice sites, and σ is the spin. The interaction includes intraorbital (interorbital) repulsion U (U'), the Hund's coupling J, and the pair hopping energy J'. We assume $U' = U - 2J$, $J' = J$, and choose $J = U/4$. Superconductivity is included by a BCS-like term

$$\mathcal{H}_{BCS} = -\sum_{\mathbf{i}\neq\mathbf{j},\mu\nu} [\Delta^{\mu\nu}_{\mathbf{ij}} \hat{c}^{\dagger}_{\mathbf{i}\mu\uparrow} \hat{c}^{\dagger}_{\mathbf{j}\nu\downarrow} + \text{H.c.}], \tag{4.9}$$

with $\Delta^{\mu\nu}_{\mathbf{ij}} = \sum_{\alpha\beta} \Gamma^{\beta\nu}_{\mu\alpha}(\mathbf{r_{ij}}) \langle \hat{c}_{\mathbf{j}\beta\downarrow} \hat{c}_{\mathbf{i}\alpha\uparrow} \rangle$ the superconducting order parameter, and $\Gamma^{\beta\nu}_{\mu\alpha}(\mathbf{r_{ij}})$ denoting the effective pairing strength between sites (orbitals) $\mathbf{i}$ and $\mathbf{j}$ (μ, ν, α and β). In agreement with a general $s^{\pm}$ pairing state, the next-nearest neighbor (NNN) intra-orbital pairing was included, $\Gamma_{\mu} \equiv \Gamma^{\mu\mu}_{\mu\mu}(\mathbf{r_{nnn}})$. Magnetic disorder modeling the Mn moments is included by $\mathcal{H}_{imp} = I \sum_{\{\mathbf{i}^*\}\mu\sigma} \sigma S_{\mu} c^{\dagger}_{\mathbf{i}^*\mu\sigma} c_{\mathbf{i}^*\mu\sigma}$, where S_{μ} is magnetic moment in orbital μ

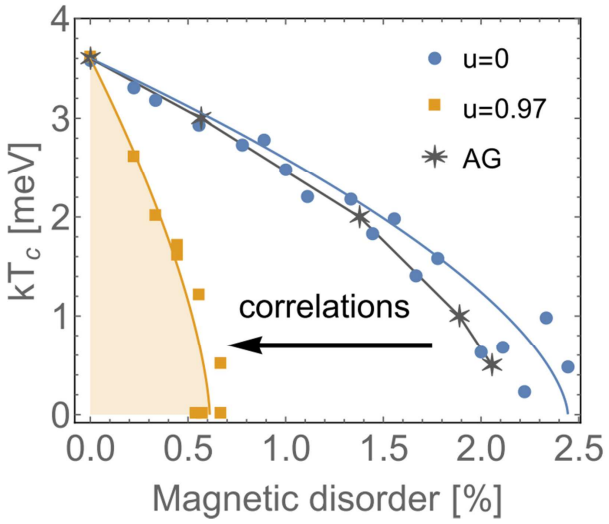

Figure 4.17: Superconducting critical temperature T_c as a function of magnetic impurity concentration for strong ($u = 0.97$) and weak correlations ($u = 0$). In the weak correlation case the value of T_c is in good agreement with the prediction from the Abrikosov-Gorkov theory [276]. Figure adapted from [267].

at the disorder sites given by the set $\{\mathbf{i}^*\}$ coupled to the spin density of the itinerant electrons.

In Ref. [267] it was already demonstrated that in this framework the enhanced spin correlations developing around Mn severely speed up the reduction of T_c driven by the magnetic disorder, and may quench the entire superconducting phase already at Mn concentrations below 1%. The Mn moments, while substituting random Fe positions, orient their moments favourably to generate a long-range ordered SDW phase which minimizes the total free energy of systems at the brink of a SDW instability [274, 275].

The total magnetization for a collection of 0.55% Mn ions randomly placed in the square Fe lattice is shown in Fig. 4.16. This concentration of Mn is able to fully suppress T_c and spin polarize all Fe sites (which were all non-magnetic without Mn impurity ions). The Mn-induced magnetic order existing in the inter-impurity regions is long-ranged as reproduced by the sharp peaks in Fig. 4.16b, which are absent in the Mn free compound. A small fraction of the sites, roughly corresponding to the Mn sites and to their nearest-neighbors (amounting to $\sim 5\%$ of the lattice) exhibits a significantly larger moment, in overall agreement with the above discussion of the ^{75}As NMR data (see Fig. 4.12c).

The magnetic order generated by Mn doping is efficiently stabilized due to correlation-enhanced RKKY exchange couplings between neighboring Mn ions. The structure of the induced order is thus dictated by the susceptibility of the bulk itinerant system which, in the present case, is peaked at $Q_1 = (\pi, 0)$ and $Q_2 = (0, \pi)$ regions. In Fig. 4.16c we provide a real-space map of the dominant momentum structure by utilizing a filtered Fourier transform

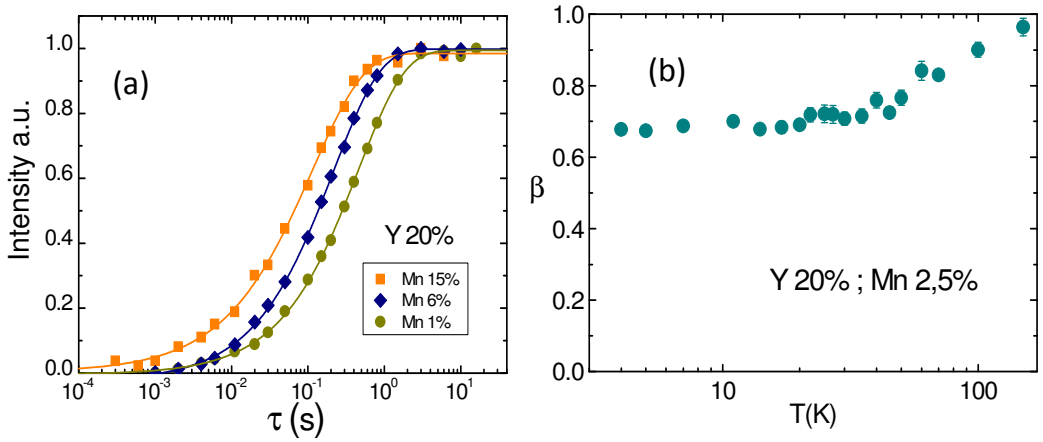

Figure 4.18: a) ^{19}F nuclear magnetization recovery for several LaY20 samples at 22K, around the $1/T_1$ peak, for different values of x (see legend). The solid lines are fits to Eq. 4.10. b) Temperature dependence of the stretching exponent β used to fit the longitudinal nuclear magnetization recovery for $x = 2.5\%$ in $Y_{0.2}La_{0.8}Fe_{1-x}Mn_xAsO_{0.89}F_{0.11}$.

illustrated in Fig. 4.16d. As can be seen, the system breaks up into regions of single-Q domains, i.e. either Q_1 or Q_2 dominated regions. This is consistent with the presence of a (reduced) orthorhombic transition associated with the Mn-induced magnetic order, as found by ^{75}As NQR.

Notably the model is also able to qualitatively explain the reduced Mn effect in the $Y_{0.2}La_{0.8}Fe_{1-x}Mn_xAsO_{0.89}F_{0.11}$and $SmFe_{1-x}Mn_xAsO_{0.88}F_{0.12}$samples where the chemical pressure is higher. It fact it has been shown that in this framework chemical pressure reduce the electronic correlations leading to an increase of x_c (see Fig. 4.17).

Finally it should be remarked that the results clearly show that there is a critical concentration of Mn above which the system leaves the SC phase and is back to the stripe phase which also characterize the undoped LaFeAsO. The critical concentration inferred from the calculation is in good agreement with the experimental one. While the mean distance between Mn impurities is obviously an important parameter it should be remarked that the recovery of magnetism is a collective and non-local effect so the number of Mn ions is a particular region of the system (e.g. magnetic domains) is not so important.

4.1.3 Low frequency fluctuations in $LaFe_{1-x}Mn_xAsO_{0.89}F_{0.11}$ and $Y_{0.2}La_{0.8}Fe_{1-x}Mn_xAsO_{0.89}F_{0.11}$

Further insights on the effect of Mn in LaY0 and LaY20 can be derived from the analysis of the ^{19}F NMR spin-lattice relaxation rate. Y for La substitution allows to vary the chemical pressure without introducing paramagnetic lanthanide ions (e.g. Sm) which would significantly affect ^{19}F NMR $1/T_1$ [277].

^{19}F NMR measurements were performed at low magnetic fields, $H \leq 1.5$ Tesla. The spin-lattice relaxation rate was estimated by following the recovery of nuclear magnetization $M_z(\tau)$ after a saturation recovery sequence. Since ^{19}F is a spin 1/2 nucleus the recovery (see Fig) was fit according to simple exponential function:

$$M_z(\tau) = M_0[1 - f\, e^{-(\tau/T_1)^{\beta}}]\,, \tag{4.10}$$

where all the symbols have the usual meaning.

The stretching exponent β was found to be 1 for $T > 80$ K and decreased to about 0.5 at low temperature (see Fig. 4.18). This behaviour indicates the presence of a distribution of spin lattice relaxation times which is a common feature of disordered systems [195] and in our case it is probably due to the different inequivalent impurity configurations resulting from Y and Mn doping. In fact, the low temperature values of β get smaller on increasing the Mn content, namely the number of impurities.

The temperature dependence of $1/T_1$ in LaY0 and LaY20, for Mn contents ranging from $x = 0\%$ up to $x = 20\%$, is shown in Fig. 4.19 and Fig. 4.20, respectively. While at high temperature $1/T_1$ displays a linear Korringa behavior typical of weakly correlated metals, below 80K the spin lattice relaxation rate progressively increases upon cooling, giving rise to a broad peak around 25 K. It is remarked that this increase starts well above T_c and well above T_m for the magnetically ordered samples.

Insights on the nature of the peak can be gained by observing its evolution upon changing the magnitude of the external magnetic field H_0. Measurements in a lower field of 0.75 T (see Fig. 4.21) revealed that while at high temperature $1/T_1$ is only weakly field dependent, the magnitude of the peak at ~25 K is significantly enhanced, which is exactly the behaviour expected for slow dynamics with a characteristic frequency in the MHz range, close to the Larmor frequency ω_0 (BPP law, see Section 2.1.6.1).

The introduction of increasing Mn contents gives rise to a progressive enhancement of the peak magnitude, suggesting that the presence of paramagnetic impurities strengthens the low-frequency dynamics already present in the pure compound (see Fig. 4.20).

This peak should not be ascribed to the slowing down of the critical fluctuations on approaching T_m, which are present only in the magnetic samples and give rise to a steeper increase in $1/T_1$ only at lower temperatures. In fact behavior of $1/T_1$ in LaY20 below 25 K depends on the Mn doping level: in samples with Mn doping below 10% the spin lattice relaxation rate decreases with lowering temperature, while for samples with higher Mn doping we observed a steep increase of $1/T_1$ with a divergence at temperatures approaching the magnetic transition temperature determined by μSR (see Fig. 4.20). This behavior is associated with the critical divergence of the spin correlation length on approaching the magnetic transition, which yields a power law divergence of $1/T_1 \propto (T - T_m)^{-\alpha}$.

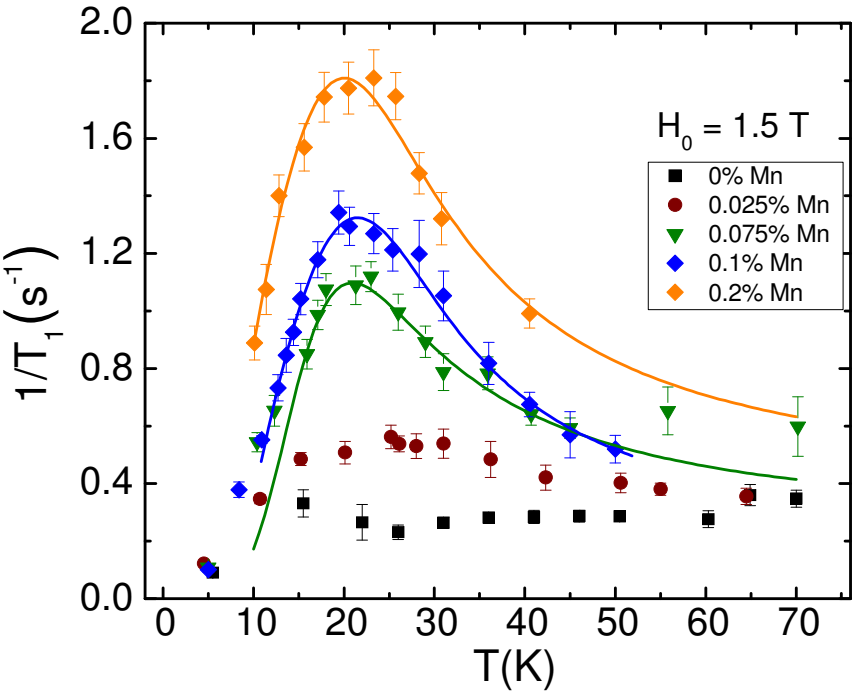

Figure 4.19: Temperature dependence of ^{19}F NMR $1/T_1$ for $LaFe_{1-x}Mn_xAsO_{0.89}F_{0.11}$with x up to 0.2%. The solid lines are fits to Eq. 4.12.

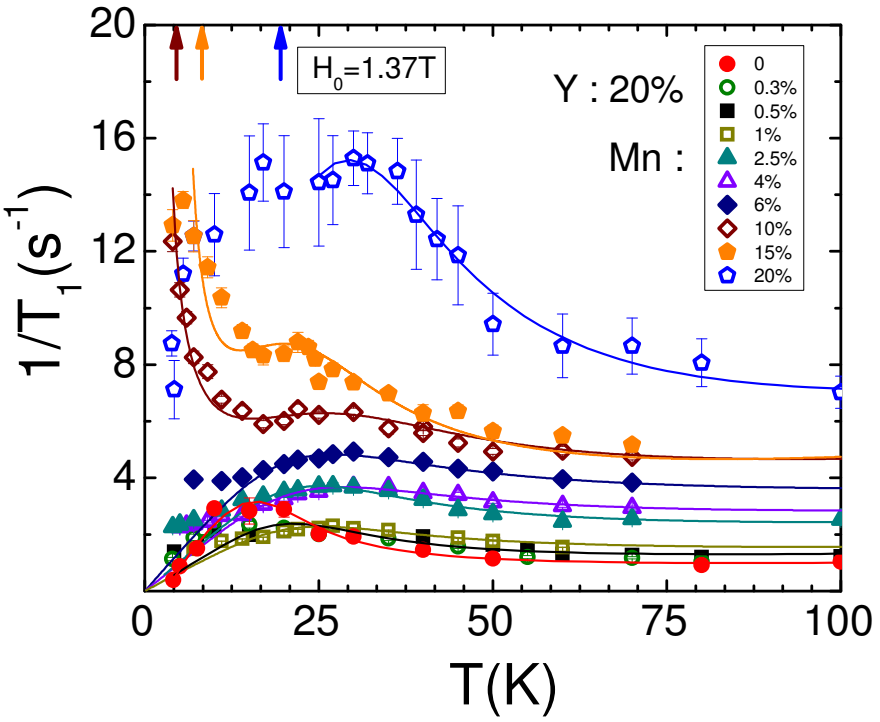

Figure 4.20: Temperature dependence of ^{19}F NMR $1/T_1$ for $La_{0.8}Y_{0.2}Fe_{1-x}Mn_xAsO_{0.89}F_{0.11}$ for Mn doping levels up to x =20%. The solid lines are fits to Eq. 4.12.

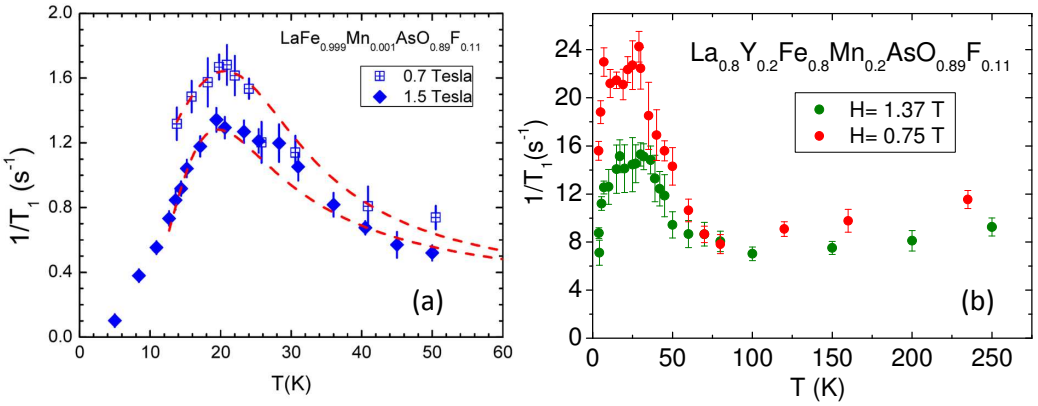

Figure 4.21: (a) ^{19}F NMR $1/T_1$ temperature dependence in the $x = 0.1\%$ LaY0 sample (x =0.1%) at two different magnetic fields: 0.7 and 1.5 Tesla. Dashed lines are fits according to Eq. 4.12. (b) The same as (a) but for a LaY20 sample (x =20%).

In order to fit the ^{19}F $1/T_1$ temperature dependence we adopted the BPP law, (Section 2.1.6.1) as suggested by the field dependence of the peak. This approach is often suited to describe $1/T_1$ in presence of hyperfine field $\vec{h}(t)$ fluctuations approaching the Larmor frequency ω_0, namely in the MHz range.

In this framework the spin lattice relaxation rate takes the form (see Section 2.1.6.1):

$$\frac{1}{T_1} = \gamma^2 \langle h_\perp^2 \rangle \frac{\tau_c(T)}{1 + \omega_0^2 \tau_c(T)^2} \,, \tag{4.11}$$

where $\tau_c(T)$ is described by a thermally activated law $\tau_c(T) = \tau_0 \exp(E_a/T)$, where E_a is the energy barrier and τ_0 the correlation time at infinite temperature. However, monodispersive fluctuations cannot explain the broad peaks observed in Mn doped compounds.

A much better result can be obtained by considering a distribution of energy barriers, and thus of correlation times, associated with the irregular distribution of Mn impurities. For simplicity, the energy barrier distribution was taken as squared, centered around E_a and with a width Δ. Accordingly Eq. 4.11 takes the form [279]:

$$\begin{aligned} \frac{1}{T_1} = \frac{\gamma^2 < h_\perp^2 > T}{2\omega_0 \Delta} \Big[& \arctan\left(\omega_0 \tau_0 e^{(<E_a>+\Delta)/T}\right) \\ & - \arctan\left(\omega_0 \tau_0 e^{(<E_a>-\Delta)/T}\right) \Big] + cT \end{aligned} \tag{4.12}$$

where a linear Korringa-like term cT was added to account for the high temperature behaviour. Eq. 4.12 was used to fit the $1/T_1$ data for all samples of the LaY0 series and the sample of the LaY20 series with Mn contents lower than 8%, while for samples with higher Mn doping a term proportional to $(T - T_m)^{-\alpha}$ was added to take account the divergence of $1/T_1$ at the magnetic phase transition (see Fig. 4.20). The critical exponent was found to be

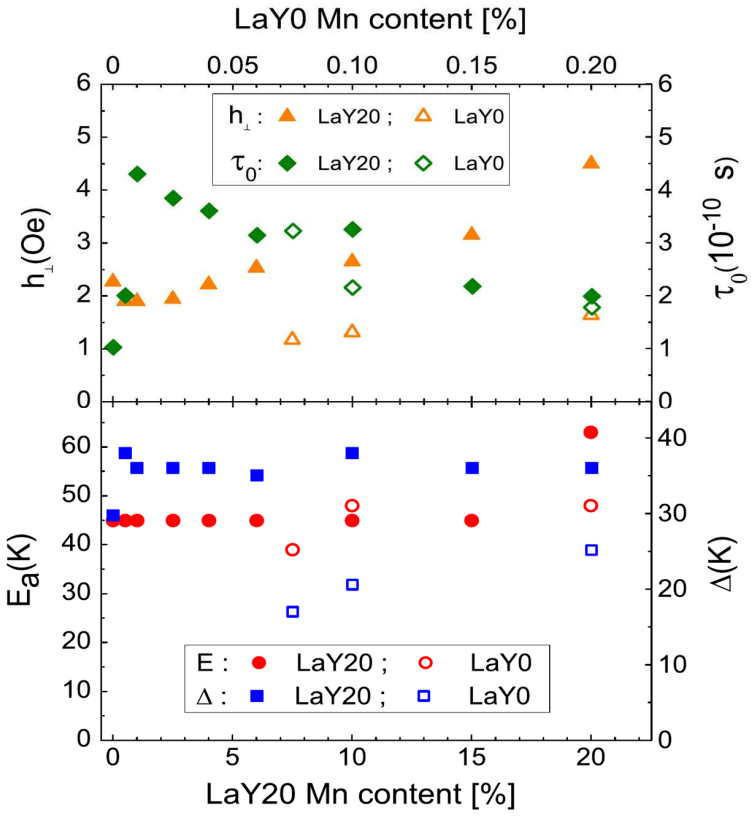

Figure 4.22: Parameters extracted from the fit of $1/T_1$ to Eq. 6 as a function of the Mn content for the LaY20 series (filled symbols, bottom horizontal axes) and for the LaY0 series (open symbols, top horizontal axes). Top panel: mean value of the local fluctuating magnetic field $h_\perp$ (left) and correlation time τ_0 (right). Bottom panel: energy barrier E_a (left) and width of the energy barrier distribution Δ (right).

$\alpha \simeq 1$ both for $x = 10\%$ and for $x = 15\%$. Since in quasi-2D antiferromagnets $1/T_1 \sim \xi^z$ [280], with $\xi \propto (T - T_m)^{-\nu}$ the spin correlation length and z and ν scaling exponents close to the unity [281], the value derived for α appears to be quite reasonable. For the LaY20 sample with Mn content $x = 20\%$ the divergence due to magnetic ordering and the broad BPP peak overlap making it impossible to obtain a reliable fit on the whole temperature range, so only the high temperature data were fitted with Eq. 4.12.

The values of the fit parameters for both the series is reported in Fig. 4.22. As can be seen, in the LaY20 series, the mean value of the energy barrier E_a is nearly constant as a function of Mn and the variation of the correlation time τ_0 of the spin fluctuations is small, in the range of 0.1-0.4 ns. In the LaY0 series Δ increases with x suggesting that the Mn leads to a distribution of activation energies which reflects a strong inhomogeneous electronic environment, even at very small Mn doping levels. Conversely for the LaY20 system this distribution is nearly constant and probably dominated by the

disorder induced by the large amount of Y introduced in the system.

The most significant change is the increase in the amplitude of the local fluctuating field $(< h_{\perp}^2 >)^{1/2}$ with x, which indicates that the strength of the local spin susceptibility in the FeAs plane becomes progressively enhanced by Mn doping.

4.1.3.1 ^{19}FNMR line width

Further indications of the enhancement of the local spin susceptibility is provided by the analysis of the temperature dependence of the ^{19}F NMR line width (see Fig. 4.23), which is directly related to the amplitude of the staggered magnetization developing around the impurity.

$\Delta\nu$ was derived from the Fast Fourier Transform of half of the echo signal after a Hahn spin-echo pulse sequence. As it can be seen in Fig. 4.23b by increasing the Mn content a marked increase of $\Delta\nu$ is observed. The data reported were fitted with a Curie-Weiss law:

$$\Delta\nu = (\Delta\nu)_0 + \frac{C}{T+\Theta} \ . \tag{4.13}$$

The temperature independent term $\Delta\nu_0 \sim 14$ kHz estimated from the fit of the data up to $T = 300$ K, is in very good agreement with the value 13.5 kHz estimated for the nuclear dipole-dipole interaction derived from lattice sums (method of moments, see [137]). About 80% of the second moment is due to F-La nuclear dipole interaction and about 19.5% to F-F interaction, while only a minor contribution arises from F-As interactions.

This term practically does not change by increasing the Mn doping since the lattice parameters vary by less than 1.2% between $x = 0$ and $x = 20\%$ and the dipolar contribution of ^{55}Mn nuclei for $x = 20\%$ would cause a change by less than 1% in the linewidth. The results of the fits in LaY20 are summarized in Table. 4.1. Both the Curie constant and the Curie-Weiss temperature increase as a function of Mn, indicating that the insertion of Mn strengthens the spin correlations.

We also observed, comparing the ^{19}F $\Delta\nu$ for LaY0 and LaY20 with similar Mn doping, that the linewidth is unambiguously larger in the sample without

Table 4.1: Curie constant C and Curie-Weiss temperature θ obtained from the analysis of the temperature evolution of the ^{19}F NMR line width $\Delta\nu$ shown in Fig. 4.23b for $La_{0.8}Y_{0.2}Fe_{1-x}Mn_xAsO_{0.89}F_{0.11}$.

Mn (%)	C (kHz·K)	θ (K)
1	300 ± 30	4 ± 1
4	490 ± 20	11 ± 1
15	870 ± 20	16 ± 1

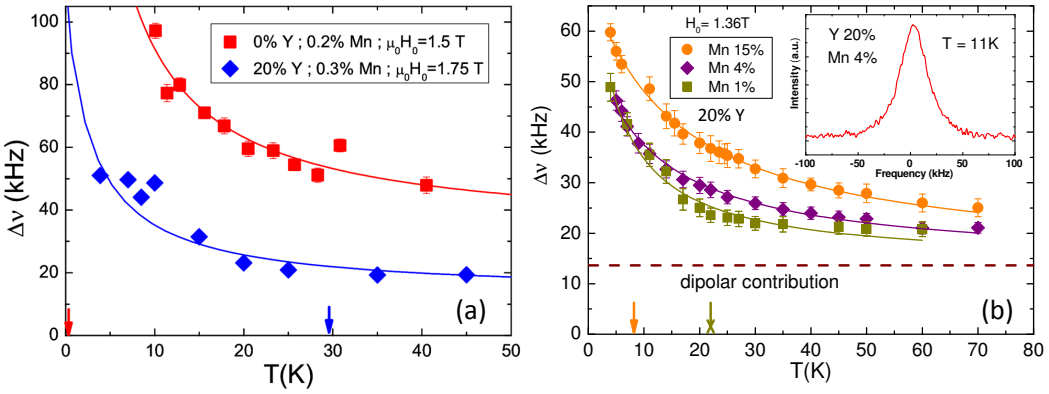

Figure 4.23: a) ^{19}F NMR line full width at half maximum $\Delta\nu$ in the x = 0.2% LaY20 sample (blue diamonds) and in the LaY0 x = 0.3% sample (red squares). Solid lines are best fits according to a Curie-Weiss law (see text), while the arrows indicate the T_c of the two samples. b) ^{19}F NMR full width at half intensity for three representative samples of the LaY20 series. Solid lines are best fits according to a Curie-Weiss law while the arrows indicate T_c of the x=1% sample (green arrow) and T_m of the x=15% sample (orange arrow). Inset: a typical 19 F NMR spectrum (x=4%, y =20%, T =11 K).

Y, as it can be seen in Fig 4.23a. The fits clearly show that C increases by a factor 3 and that Θ increases from about 3 K to 11 K between the x = 0.3% LaY20 sample and that the x = 0.2% LaY0 sample. This indicates that, the staggered magnetization regions are much larger around the Mn impurities in LaY0 confirming that this compound is much closer than LaY20 to the QCP and the spin correlations are so strong that, owing to the enhanced spin susceptibility at $Q = (\pi, 0)$, the effect of a tiny amount of impurities extends over many lattice sites, giving rise to a sizable RKKY coupling among them which abruptly destroy superconductivity and restore the stripe magnetic order (see Section 4.1.2.2).

4.1.4 Conclusions

We presented a comprehensive study on the effect of Mn doped $Ln1111$ compounds. We discovered that the very fast T_c suppression observed in $LaFe_{1-x}Mn_xAsO_{0.89}F_{0.11}$ upon Mn doping is concomitant to the reappearance of the static stripe (π,0);(0,π) magnetic order present in undoped LaFeAsO. Together with stripe magnetism also the tetragonal to orthorhombic structural transition is recovered. The electronic ground state observed in the magnetic $LaFe_{1-x}Mn_xAsO_{0.89}F_{0.11}$ through ^{75}As NQR spectra is also strikingly similar to that of the undoped compound. These observation strongly indicates that a huge localization effect is induced by tiny amounts ($\sim$ 0.5%) of Mn impurities in optimally electron doped $LaFeAsO_{0.89}F_{0.11}$ which is able to completely overcome the effect of the 11% F doping thus restoring the localized ground state of the undoped compound. We observed that a realistic

five band Hubbard model [267] is able to nicely explain all our experimental findings.

Furthermore we observed that the localization effect is much less pronounced in $Y_{0.2}La_{0.8}Fe_{1-x}Mn_xAsO_{0.89}F_{0.11}$, demonstrating that the chemical pressure generated by the smaller Y atoms significantly reduce the Mn induced localization effect, in good agreement with the theoretical model. Hence the $Ln1111$ compounds can be considered as a formidable example of how the electronic properties of strongly correlated systems can be significantly affected by fine-tuning the correlation strength with impurities and chemical pressure.

We also carried out a ^{19}F $1/T_1$ study of the slow spin fluctuations present in these compounds. Our results clearly indicate that these dynamics seem to be intrinsic to the system since they are detected also for the compound without manganese. Furthermore the related activation energies E_a and correlation time τ_0 are almost insensitive to the Mn content indicating that the low-frequency dynamics is nearly unaltered when approaching the disruption of superconductivity. This observation suggests that they are not correlated with the appearance of the superconducting state.

While the origin of the low-energy fluctuations giving rise to the peak in ^{19}F NMR $1/T_1$ is not yet clear similar features in the $1/T_1$ vs T behaviour have also been detected in other optimally electron-doped iron-based superconductors such as Rh doped Ba122 (see Sections 3.1 and 4.2) and have been tentatively associated with nematic fluctuations [195] or with the motion of domain walls separating nematic phases (see Section 3.1). In this scenario the energy barrier E_a may be related to the one separating the degenerate nematic phases and the enhancement of the low-frequency dynamics could be associated with the pinning of these fluctuations by impurities.

4.2 Effect of proton irradiation in Rh doped $BaFe_2As_2$

Chemical substitution is the most common approach used to introduce impurities in strongly correlated electron systems in order to probe their local response function. However, this method often gives rise to structural distortions, unwanted inhomogeneity and to charge doping. Accordingly, in order to study the effect of the bare impurities the right dopant must be carefully chosen and the options are often very limited. Thus irradiation with energetic particles, electrons and ions, may represent a powerful alternative to chemical substitutions.

The most common applications of particle irradiation in iron based superconductors are the study of how the defects pin the Abrikosov vortices and the study of the effects of nonmagnetic defects, such as those created by irradiation, on the superconducting transition temperature.

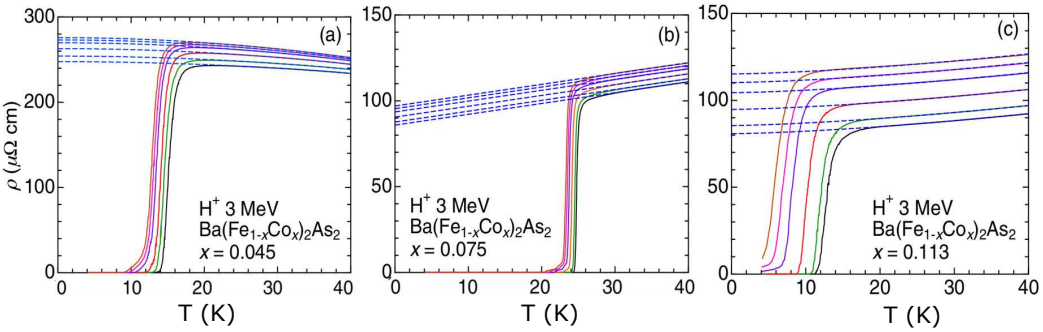

Figure 4.24: Temperature dependence of the resistivity for $Ba(Fe_{1-x}Co_x)_2As_2$ with x=0.045, x=0.075, x=0.075, measured in function of proton irradiation (3 MeV protons). The fluences are 0, 0.1, 0.5, 0.8, 1.0, and 1.2×10^{16} cm^{-2} from the lowest curve. The dased lines are continuations of the $\rho(T)$ trends measured above T_c. Figure adapted from [286].

Heavy ions irradiation (e.g. with Au and Pb) typically introduce anisotropic columnar defects, which are effective in pinning the flux lines [282, 283] but due to their size (they can span the whole sample) an their shape they are not well suited to study the microscopic properties.

On the other hand, low mass and low energy ions, such as protons, α particles or electrons, give rise to uniformly distributed point like defects, originating from the displacement of single atoms, whose density can be precisely controlled. In the cuprates the decrease of the superconducting transition temperature T_c with the radiation fluence ϕ was found to strongly depend on the ion type, on its energy and on the total dose [284]. Remarkably, in $YBa_2Cu_3O_{7-\delta}$ and $Tl_2Ba_2CuO_{6+x}$, it was found [285] that the defects introduced by electron irradiation play a role analogous to nonmagnetic Zn impurities and the magnitude of the T_c suppression rate, $dT_c/d\phi$, is consistent with the theoretical prediction for a d-wave superconductor [254].

In the IBS several irradiation studies have already been conducted with heavy [287, 288, 289, 290, 291, 292, 283, 293] ions, light ions [286, 294, 290, 292, 295] and electrons [296, 297, 298, 299, 300, 301]. Notably all the studies have been carried out on compounds belonging to the 122 families which can be easily grown as sizeable single crystal suited for irradiation.

It has been found that the $(dT_c/d\phi)$ is much smaller than expected in $s^{\pm}$ superconductors [60, 110], where interband scattering by nonmagnetic impurities should cause a marked T_c suppression [73]. For example in Fig. 4.24 the evolution of resistivity with increasing fluences and Co doping in $BaFe_2As_2$ is shown. As it can be seen the T_c decrease in the underdoped (Fig. 4.24a) and optimally doped (Fig. 4.24b) sample is very small and it becomes more significant only for the overdoped (x=0.113, Fig. 4.24c) sample [286].

Interestingly, this result is consistent with the reduced T_c suppression rate in $Ba(Fe_{1-x}Co_x)_2As_2$ and $LaFeAsO_{1-x}F_x$ with nonmagnetic Zn doping [302,

303, 75, 76].

However this is not necessarily an indication of a gap symmetry different from $s^{\pm}$, in fact the defects weaken both superconductivity (SC) and the spin density wave (SDW) order which is competing with the superconductivity in the underdoped part of the phase diagram[73]. Hence, while $dT_c/d\phi$ strongly depends on the system parameters in the underdoped regime, it is found always to increase significantly on moving to the overdoped regime. This phenomenology is observed both for proton irradiation and nonmagnetic Zn doping (see Fig. 4.24 [286]).

While considerable attention has been addressed to the superconducting phase no studies can be found in literature about the evolution of the normal state properties, except for the residual resistivity which is usually measured in order to estimate the radiation damage. In particular no attention has been devoted to the effect of radiation on the spin and nematic correlations. In the following we present a detailed ^{75}As NMR study of the effect on proton irradiation on the normal state properties of Rh doped $BaFe_2As_2$ which partially fill this gap.

4.2.1 Sample preparation and characterization

The ^{75}As NMR experiments have been carried out on the same samples also used for the T_2 reported in Section 3.1. The sample compositions we chose for irradiation are x=0.068 and x=0.107. After SQUID and resistivity measurements, a few crystal belonging to these batches were irradiated with 5.5 MeV protons at the CN Van de Graaff accelerator of INFN-LNL (Istituto Nazionale di Fisica Nucleare - Laboratori Nazionali di Legnaro, Italy), with a fluence of 3.2×10^{16} cm^{-2} by the group of G. Ghigo and L. Gozzelino [304]. Contacts to the samples remained intact during irradiation, thus eliminating uncertainty of geometric factor determination and enabling quantitative comparison of resistivity measurements. To minimize the heating of the crystals under irradiation the proton flux was always limited to 10^{12} cm^{-2} s^{-1}.

The irradiation with 5.5 MeV protons produces random point defects and some defect nanoclusters, due to elastic scattering of protons against the target nuclei [295, 286, 294]. The thickness of the crystals was much smaller

Table 4.2: Summary of the average displacements per atom (dpa) and distance between defects as a function of the proton irradiation fluences.

ϕ (cm^{-2})	dpa	Inter-defect distance (nm)
2×10^{16}	5.1×10^{-4}	3.5
3.2×10^{16}	8.2×10^{-4}	3
4×10^{16}	1×10^{-3}	2.8
6.4×10^{16}	1.6×10^{-3}	2.4

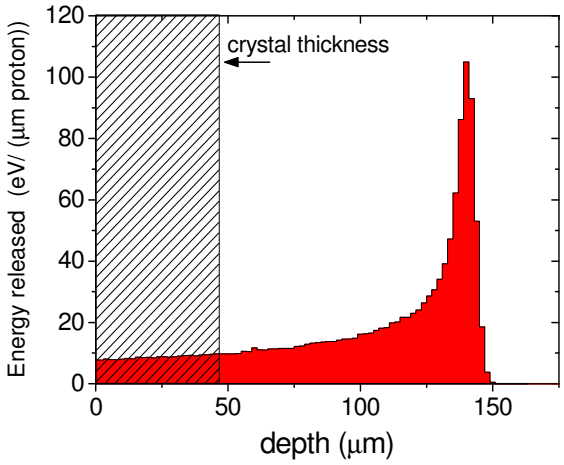

Figure 4.25: Distribution of the proton energy loss in the superconducting crystals (less than 50 μm thick) as a function of depth. The thickness of the thickest irradiated sample is about 45 μm, as evidenced in the picture. Therefore, the energy release can be considered homogeneous throughout the crystals, as well as the distribution of defects.

than the proton implantation depth. This ensured a homogeneous defect distribution in the superconductor (see Fig. 4.25). Radiation penetration and energy deposition was calculated using SRIM code [305]. In Table 4.2 the average displacement damage (dpa: displacements per atom, the probability of a given atom of being displaced at a given fluence) and the inferred average distance between proton-induced point defects are reported as a function of the irradiation fluence. This approach does not give a direct evaluation of which atoms (Fe, Ba, or/and As) atoms are displaced in the irradiation process. In fact in SRIM code the sample is amorphous and just the stoichiometric abundance of the target atoms is taken into account, namely it is implicitly assumed that 20% of displacements involve Ba, 37.3% Fe, 40% As and 2.7% Rh, which means that the defects mainly affect the superconducting layer.

Electrical resistivity measurements were carried out at the Ames Laboratories using the four-probes technique on cleaved samples with typical dimensions 2×0.5×0.05 mm^3, with the long dimension corresponding to [100] crystallographic direction. Low resistance contacts to the samples were made by soldering 50 μm Ag wires using Sn. Measurements were made on 6 samples of x=0.068 and 7 samples of x=0.107. In both cases resistivity of the samples at room temperature $\rho(300K)$ was 230±30 $\mu\Omega$cm (see Fig. 4.26), consistent with the results obtained in Co doped $BaFe_2As_2$, with a Co concentration similar to the Rh concentration [306].

After irradiation the samples were again characterized with resistivity measurements to check the reduction of T_c. Fig. 4.27 shows temperature dependent resistivity of the samples with x=0.068 (left panel) and x=0.107 (right panel) before and after irradiation. Sample x=0.068 was subject to

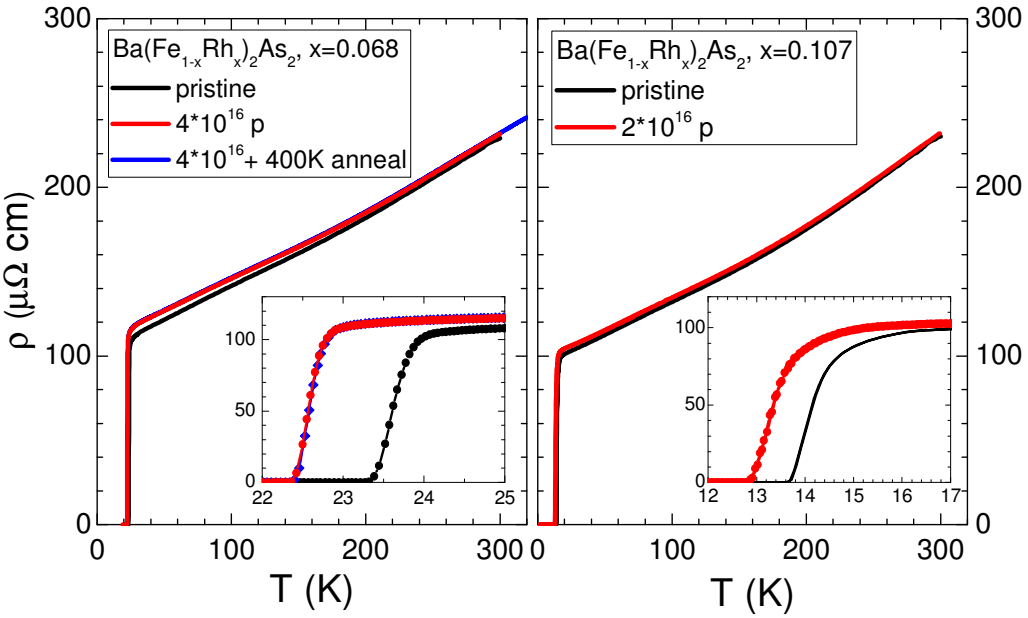

Figure 4.26: Temperature-dependent electrical resistivity $\rho(T)$ of optimally doped x=0.068 (left panel) and overdoped x=0.107 (right panel) samples of $Ba(Fe_{1-x}Rh_x)_2As_2$. Insets zoom into superconducting transition range. Black lines show $\rho(T)$ for samples in the pristine state, red lines show the data for the same samples after proton irradiation. Blue line in left panel shows $\rho(T)$ of the same sample after annealing at 400 K, revealing permanent character of proton irradiation damage, in contrast to damage by electron irradiation [297]. Note non-parallel shift of the $\rho(T)$ curves after irradiation, revealing Matthiessen rule violation.

a fluence up to 4×10^{16} cm^{-2}, which resulted in approximately 1 K decrease of T_c from 23.3 K to 22.3 K as determined by zero resistance criterion. Resistivity above the transition increased from 106 to 115 $\mu\Omega$cm. To check the stability of radiation damage, one sample of x=0.068 was heated up to 400 K. This protocol is known to show significant T_c restoration and residual resistivity decrease in electron irradiated samples [297], none of which is observed for proton irradiation. Due to a two times smaller irradiation fluence, 2×10^{16} cm^{-2}, T_c suppression in samples of x=0.107 is somewhat smaller, $\Delta T_c \approx$0.8 K, from 13.7 to 12.9 K. Resistivity increase is also notably smaller, $\Delta\rho \approx 3$ $\mu\Omega$cm.

For both $Ba(Fe_{1-x}Rh_x)_2As_2$ compositions (x=0.068 and X=0.107) the resistivity increase after irradiation is not a rigid offset as one would expect from the Matthiessen rule. The shift becomes notably larger at low temperatures, in line with observations on hole-doped $Ba_{1-x}K_xFe_2As_2$ [299]. In Fig. 4.27 we report the effect of irradiation on T_c as a function of the residual resistivity change with respect to pristine sample which is a good indicator of the induced radiation damage. For reference we also reported the data for

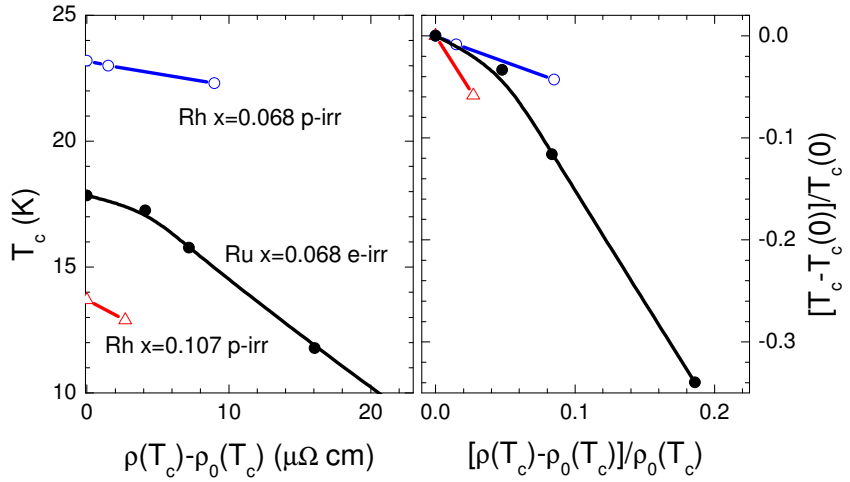

Figure 4.27: (Left panel) The superconducting transition temperature T_c as a function of change in sample resistivity $\rho(T_c)$ for samples of $Ba(Fe_{1-x}Rh_x)_2As_2$ with optimal doping x=0.068 (blue curve, open circles) and x=0.107 (red curve, open up-triangles). For reference we show data for iso-electron substituted $Ba(Fe_{1-x}Ru_x)_2As_2$ at optimal doping x=0.24, subjected to low-temperature 2.5 MeV electron irradiation, Ref. [297]. Right panel shows same data plotted as a change in T_c and resistivity $\rho(T_c)$ normalized by their values in pristine samples $T_c(0)$ and $\rho_0(T_c)$.

iso-electron substituted $Ba(Fe_{1-x}Ru_x)_2As_2$ at optimal doping x= 0.24, irradiated with 2.5 MeV electrons [297]. For low fluence values the rates of T_c variation are comparable in both cases, with some differences which can be ascribed to the variation of response due to the different doping level, rather than to the amount of disorder. This suggests that irradiations with protons and electrons of some MeV energy provide a similar kind of defects, even if only the defects produced by protons are really permanent while those created by electron irradiation vanish annealing the sample at 400 K.

The T_c shift resulting from proton induced defects was also measured with SQUID magnetometry and *in situ* during the ^{75}As NMR experiments by checking the detuning temperature of the probe tank circuit. The Zero Field Cooling (ZFC) SQUID magnetisation curves are reported in Fig. 4.28. The sharper superconducting transition in the irradiated x=0.107 sample is probably due to the lower magnetic field at which the pristine sample (see Fig. 4.28b) was measured, which results in an lower magnetic field penetration (fluxons).

The decrease of T_c after irradiation (ϕ =3.2×10^{16} cm^{-2}) was found to be small both for the x = 0.068 (from 23.3 K before irradiation to ~22 K afterwards) and for the x = 0.107 (from ~13.3 K to ~12.5 K). The samples were then irradiated again to increase the total fluence to ϕ =6.4×10^{16} cm^{-2} and the SQUID and NMR measurements were then repeated.

The second irradiation lowered T_c to 21.3 K for x = 0.068 and to 12 K for x = 0.107. Hence, the T_c decrease rate is $dT_c/d\phi \simeq 0.3 \times 10^{-16}$ K·cm^2 for

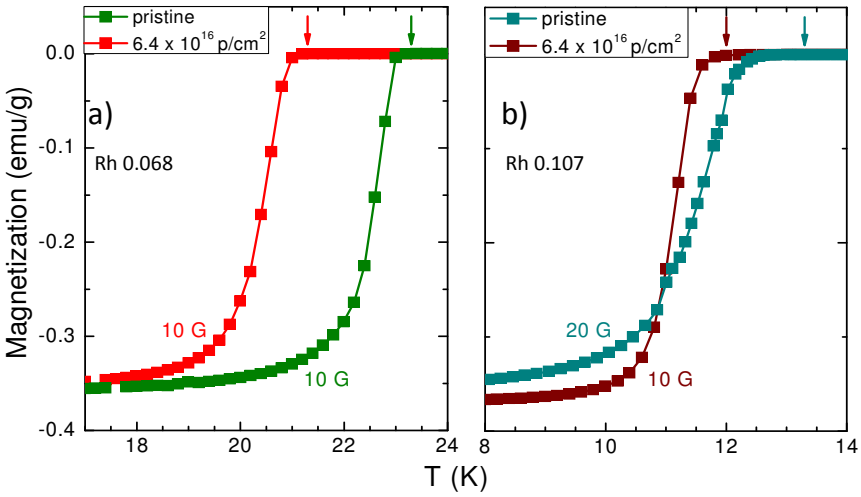

Figure 4.28: a) and b): Zero Field Cooling SQUID magnetization measurements for the x =0.068 sample (a) and x = 0.107 sample (b) carried out before and after irradiation. The arrows indicate T_c as determined by the onset of diamagnetism. The magnetic field value used for the measurements is 10 G for the x=0.068 sample and for the irradiated x=0.107 sample while it is 20 G for the pristine x=0.107 sample.

the optimally doped sample (x = 0.068) and about 0.2 $\times 10^{-16}$ K·cm^2 for the overdoped one (x = 0.107).

The values of $dT_c/d\phi$ are lower than those observed in $Ba(Fe_{1-x}Co_x)_2As_2$ and $Ba_{1-x}K_xFe_2As_2$ irradiated with 3 MeV protons [286, 294]. This effect was expected since the non-ionizing energy loss, which drives the number of defects produced per incoming proton, decreases if the energy of the incoming proton is increased [284]. This means that, somewhat counterintuitively, the effectiveness of protons in damaging the lattice decreases by increasing their energy.

4.2.2 Effect of proton irradiation on ^{75}As NMR $1/T_2$ and spectral width

4.2.2.1 ^{75}As NMR Line Width

For each sample doping and dose value we measured the temperature dependence of the ^{75}As NMR linewidth, of the spin-lattice relaxation rate ($1/T_1$) and of the spin-spin relaxation rate ($1/T_2$). The magnetic field $\mathbf{H}_0$ = 7 T was applied along the crystallographic c axis unless otherwise specified.

The full width at half maximum ($\Delta\nu$ hereafter) of the ^{75}As central line was derived from the Fast Fourier Transform of half the echo signal after a Hahn echo sequence ($\pi/2 - \tau - \pi$, with a $\pi/2$ length of = 2.5μs). The results for the optimally doped sample are shown in Fig. 4.29 and those for the overdoped crystal can be found in Fig. 4.30.

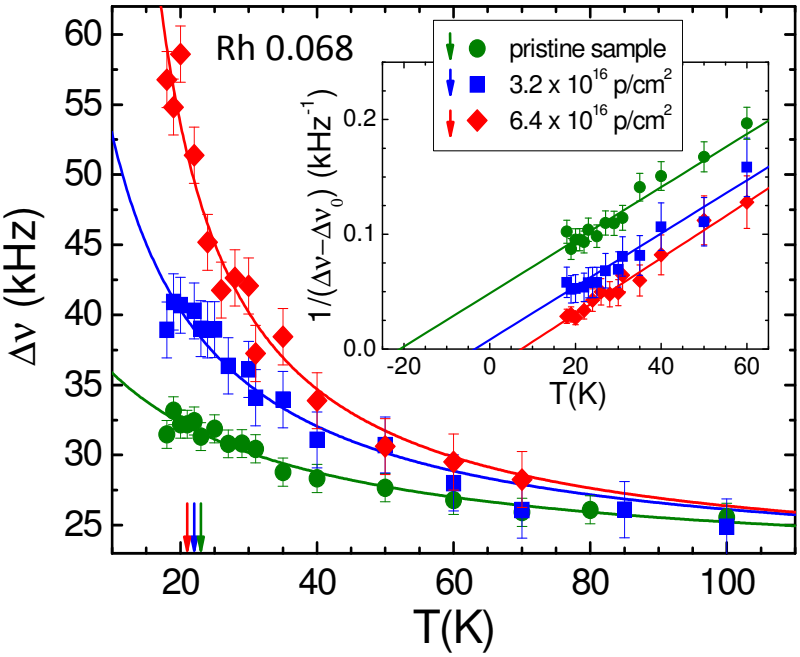

Figure 4.29: Temperature dependence of the Full Width at Half Maximum $\Delta\nu$ for the ^{75}As central line in the x = 0.068 sample. The solid lines are fits to a Curie-Weiss law (see text). Inset: Inverse of the temperature dependent component of the line width. The intercepts of the linear fits with the x axis correspond to $-\theta$ (see text). The arrows indicate T_c for each radiation dose.

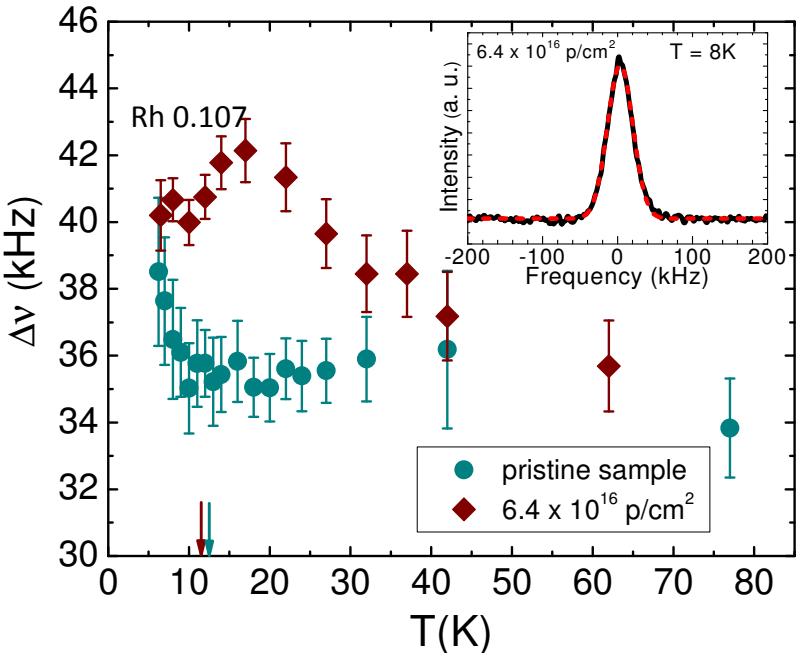

Figure 4.30: Temperature dependence of the linewidth (FWHM) for the ^{75}As central line in the x =0.107 sample. In the inset a low temperature ^{75}As NMR spectrum is shown, the dashed line is a fit to a gaussian function. The arrows indicate T_c for each radiation dose.

In the x=0.068 sample the linewidth increases significantly upon cooling, for all the fluences. Conversely, for x=0.107, $\Delta\nu$ remains nearly flat down to T_c in the non-irradiated sample while it slowly increases, reaching a maximum around 20 K, in the irradiated one.

For the $x = 0.068$ compound it is possible to fit the line width temperature dependence with a Curie Weiss law:

$$\Delta\nu = \Delta\nu_0 + \frac{C}{T+\theta} \tag{4.14}$$

where $\Delta\nu_0$ is a temperature independent component, C is the Curie constant and θ the Curie-Weiss temperature. The fit parameters are summarized in Table. 4.3.

The Curie-Weiss behavior of the linewidth and the observation that, for T< 50 K, $\Delta\nu$ decreases upon decreasing the magnetic field intensity indicate that the low temperature broadening is associated with the modulation of the local magnetic field at the nuclei induced by the electron spin texture (magnetic broadening) and hence it is not a quadrupolar broadening.

The high temperature line width, $\Delta\nu_0 \simeq 21.5$ kHz, is due to the sum of nuclear dipolar line broadening, of the quadrupolar broadening and possibly of the magnetic broadening ($\Delta\nu_{magnetic} \propto M(T, H_0) \propto \chi(T)H_0$). From dipolar sums it can be found that the nuclear dipolar contribution is actually very small (< 2 kHz) [172, 113]. The quadrupolar broadening should be zero for $H \parallel c$, however a small sample misalignment by an angle ϑ may lead to some broadening of the central ^{75}As NMR line, which can be estimated from Eq. 2.19 by taking its Taylor expansion:

$$\Delta\nu_{0_Q} \sim \frac{3\nu_Q\Delta\nu_Q}{\nu_L}\vartheta^2, \tag{4.15}$$

where ν_Q is the splitting between the central line ($\frac{1}{2} \rightarrow -\frac{1}{2}$) and the satellite line ($\frac{1}{2} \rightarrow \frac{3}{2}$), $\Delta\nu_Q$ the width of the satellite and $\nu_L = \gamma H_0/2\pi$ the Larmor frequency.

In the $x = 0.068$ sample $\nu_Q \sim 2.3$ MHz and $\Delta\nu_Q \sim 1$ MHz. The width of the satellite lines is mainly due to the EFG inhomogeneity originating from Rh

Table 4.3: Curie constant C and Curie-Weiss temperature θ obtained from the analysis of the temperature evolution of the ^{75}As NMR central line width $\Delta\nu$ shown in Fig. 4.29 for $Ba(Fe_{0.932}Rh_{0.068})_2As_2$. The temperature independent term $\Delta\nu_0$ is equal to 21.5 kHz.

ϕ (cm^{-2})	C (kHz·K)	θ (K)
0	420 ± 40	20 ± 4
3.2×10^{16}	460 ± 50	5 ± 3
6.4×10^{16}	440 ± 40	−6.5 ± 1.5

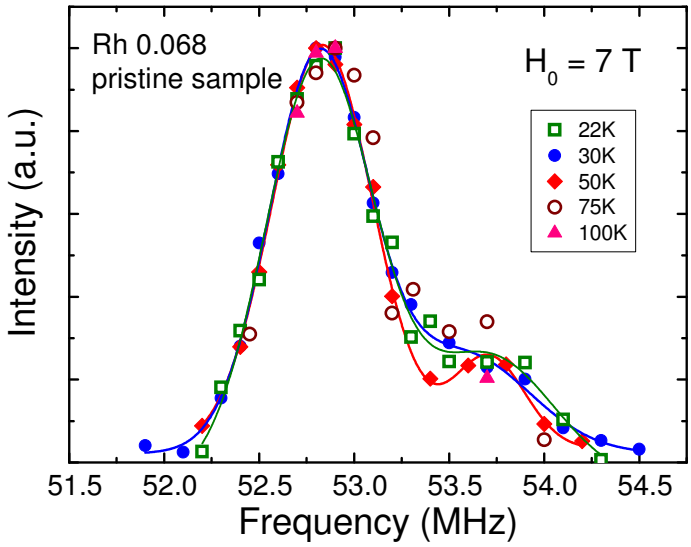

Figure 4.31: Spectra of the high frequency satellite line of $Ba(Fe_{0.932}Rh_{0.068})_2As_2$ for various temperatures. The intensity is the integral of the spin echo and the solid lines are fits to a double Gaussian. The amplitude of the low frequency peak is three times that of the high frequency peak. The high frequency peak is thus the signal from ^{75}As nuclei near neighbours of Rh in the $x = 0.068$ sample, which are roughly 1/4 of the total [307].

doping. The spectrum of the $Ba(Fe_{0.932}Rh_{0.068})_2As_2$ high frequency satellite line is reported in Fig. 4.31. The high frequency hump corresponds to the signal from the ^{75}As near neighbours of Rh, in fact the intensity of the hump is roughly 1/4 of the total [307], just like the As near neighbours to a Rh atom in the optimally doped sample. Now, if one considers a misalignment $\vartheta < 10^\circ$, than the quadrupolar broadening is $\sim \Delta\nu_{0_Q} \leq 10$ kHz, still much smaller than $\Delta\nu_0$. It is then likely that the temperature independent magnetic broadening has to be associated with the T-independent component of the electron spin susceptibility, similarly to what reported by Mukhopadhyay et al. [172] for Ba_{1-x} $K_xFe_2As_2$.

The Curie-Weiss $\Delta\nu$ behaviour indicates the presence of spin correlations and has often been observed in cuprates in presence of defects [308]. In fact, the impurities induce a local spin polarization $\langle S_z \rangle$ on the conduction electrons which leads to a spatially varying spin polarization $s(\mathbf{r}) = \chi(\mathbf{r})\langle S_z \rangle$. The resulting NMR spectrum is the histogram of the spin polarization probed by the nuclei and the line width at a given temperature depends on the temperature evolution of $\chi(\mathbf{r})$. Accordingly, $\Delta\nu$ follows the susceptibility of the local moments which can be described by a Curie-Weiss law [308].

The small low temperature line broadening already present in the pristine $x = 0.068$ sample is likely due to the presence of defects related to Rh doping. For this composition in fact the spin correlation are still strong and thus some line broadening due to intrinsic defects is not unexpected.

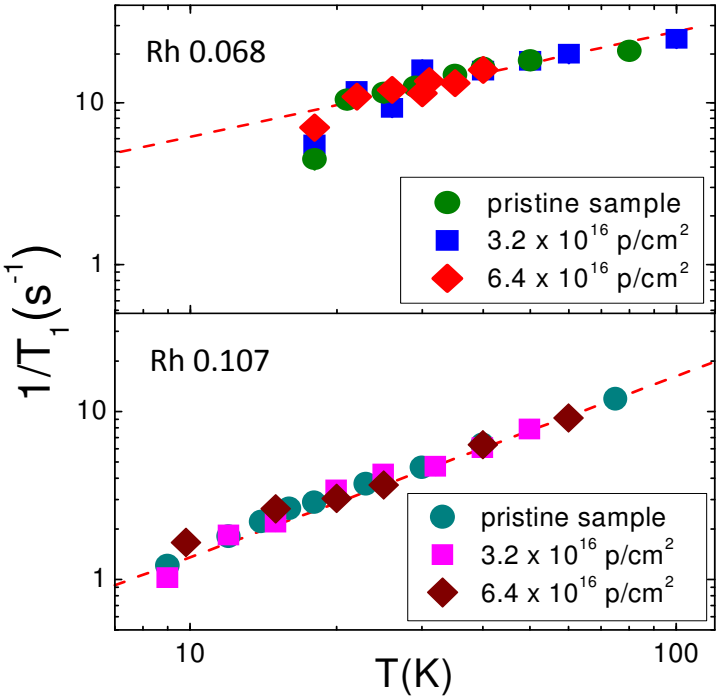

Figure 4.32: Temperature dependence of the ^{75}As $1/T_1$ measured with H $\parallel c$ for the $x = 0.068$ (top) and $x = 0.107$ (bottom) samples. The red dashed lines are guides to the eye.

Remarkably, for $\phi = 6.4 \times 10^{16}$ cm^{-2}, the Curie-Weiss temperature becomes negative, signalling the shift of the correlations from antiferromagnetic to ferromagnetic. Ferromagnetic correlations were detected in other compounds of the 122 family, in particular in the non-superconducting $Ba(Fe_{1-x}Mn_x)_2As_2$ [309] and, with a much lower θ, in the superconducting $Ba(Fe_{1-x}Co_x)_2As_2$ and $BaFe_2(As_{1-x}P_x)_2$ [310] after the introduction of Mn impurities. However the rise of magnetism upon ion irradiation was observed in several other materials [311] and the Ba122 family is quite unstable towards the emergence of impurity driven static magnetism [172, 312]. Also in the cuprates a very similar behaviour is sometimes observed (e.g. in YBCO) upon Zn doping [308]. Hence, the observation that the nonmagnetic defects introduced by irradiation lead to enhanced spin correlations and to a broadening of the NMR lines is not too surprising.

Finally, in the overdoped compound, the behaviour of the linewidth is utterly different from that of the optimally doped (see Fig. 4.30). The pristine sample displays a flat $\Delta\nu(T)$ down to 9 K and then a rapid increase, likely due to the freezing of the vortex motions [171, 113]. In the irradiated sample ($\phi = 6.4 \times 10^{16}$ cm^{-2}) $\Delta\nu$ reaches a maximum around 18 K and then decreases slightly at lower temperatures. Interestingly the temperature at which the line width of the irradiated sample starts to decrease is close to the temperature T* at which the spin-spin relaxation rate begins to rise and the echo decay becomes a single exponential. This suggests that the

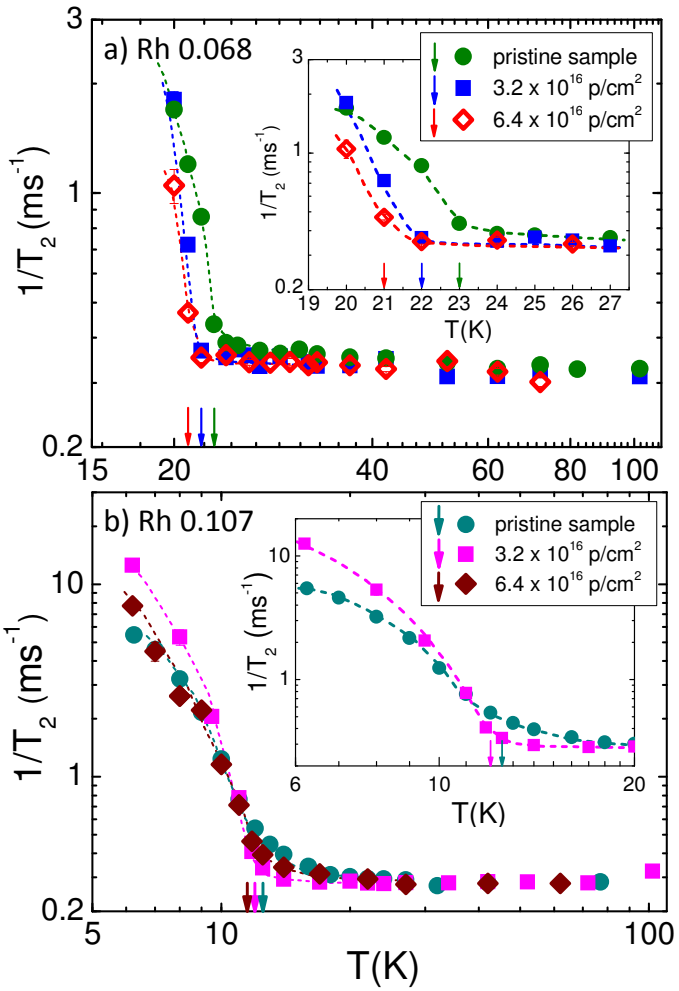

Figure 4.33: Temperature. dependence of the ^{75}As $1/T_2$ relaxation rate of the $x = 0.068$ (top) and $x = 0.107$ (bottom) samples for different values of fluence (see legend). In the insets the low temperature data are shown in greater detail. The arrows indicate T_c for each radiation dose and Rh doping level. The dashed lines are guides to the eye.

low frequency spin fluctuations, which are responsible for the $1/T_2$ enhancement, partially average out the static frequency distribution probed by the ^{75}As nuclei.

4.2.2.2 $1/T_2$ and low frequency fluctuations

We will now discuss the effect of irradiation on the $1/T_2$ relaxation rates. ^{75}As $1/T_2$ and $1/T_1$ were measured using the same method already discussed in Section 3.1. The temperature dependence of the spin lattice relaxation is reported in Fig. 4.32 and it is completely irradiation independent. The temperature dependence of the Redfield corrected $1/T_2$ is shown in Fig. 4.32.

While at temperatures much higher than T_c the spin echo decay rate is

flat for both compounds and for all the fluences, a sharp rise in $1/T_2$ was observed just above T_c. This is the same effect already widely discussed in Section 3.1 and thus here we just extend the analysis presented there to the case of the irradiated samples.

In the pristine sample (x = 0.068) $T^* \sim T_c$ = 23 K while for the irradiated one ($\phi = 3.2 \times 10^{16}$ cm^{-2}) T^* decrease slightly, following T_c ($T^* \sim$ 22 K). In the overdoped compound (x = 0.107) the effect of irradiation on T^* is much bigger: in the irradiated (3.2×10^{16} cm^{-2}) sample T^* = 12.5 K while the pristine sample value is T^* = 18 K. Hence in the overdoped compounds the T^* shift upon irradiation ($\Delta T^* \sim$ 6 K) is much bigger than the T_c shift ($\Delta T_c \sim$ 1 K).

In order to discuss the data in a more quantitative way we carried out the same analysis described in Section 3.1. We fitted the $1/T_2$ data using Eq. 3.7 in the 20 - 26 K temperature range for x=0.068 and in the 7 K - 30 K range for x=0.107. In the pristine samples we found that, for x=0.068, the activation energy is $U \simeq 200 \pm 30$ K while in the overdoped x =0.107 sample $U \simeq 40 \pm 20$ K (see Fig. 3.9).

In the irradiated samples U increases markedly in the x=0.068 compound ($U \sim 500 \pm 100$ K for $\phi = 3.2 \times 10^{16}$ cm^{-2}) while it remains basically unchanged in the overdoped sample. Unfortunately, the quality of the fit decreases with increasing dose, pointing out that possibly the dynamics can no longer be described by a single activation barrier and that a distribution of energy barriers should be considered. This fact is particularly evident in the overdoped sample where the increase of $1/T_2$ becomes significantly sharper and T^* decrease by $\sim$ 6 K (see Fig. 4.33).

The substantial enhancement of the activation energy suggests that the presence of the defects slows down the fluctuations between the $(0, \pi)$ and $(\pi,0)$ ground states. It should be remarked that such an effect has also been detected in the prototypes ($Li_2V_{1-x}OTi_xSiO_4$) of the J_1-J_2 model on a square lattice (see Sections 1.2.3 and 1.3) doped with nonmagnetic impurities [313].

4.2.3 Conclusions

We have shown that proton irradiation (5.5 MeV) in Rh doped $BaFe_2As_2$ results in a very weak T_c suppression, in good agreement with previous experiments carried out in other 122 compounds. This finding confirms the imperviousness of iron based superconductivity to the presence of non-magnetic defects, in disagreement with what initially expected for $s^{\pm}$ superconductors.

Remarkably the measurements of the ^{75}As NMR spectra revealed that the defects introduced by proton irradiation induce ferromagnetic correlations in the optimally electron doped x=0.068 compound, which have never been observed in Ba122 compounds in absence of magnetic impurities (e.g. Mn [309]). This effect is totally absent in the overdoped sample which has a ground state much nearer to that of an uncorrelated metal.

Finally the analysis of the spin echo decay rate ($1/T_2$) show that the low-frequency fluctuations, already observed in several IBS families, are damped by the irradiation induced defects, consistently with the hypothesis that they could be associated with the presence of nematic fluctuations between $(0,\pi)$ and (π,0) nematic phases being pinned by the implanted impurities.

Summarizing Remarks and Future Perspectives

In this thesis we have addressed several interesting phenomena taking place in iron based superconductors (IBS) using local techniques: Nuclear Magnetic Resonance (NMR), Nuclear Quadrupole Resonance (NQR) and Muon Spin Rotation (μSR).

The main topics have been:

- The study of the low frequency fluctuations revealed by NMR relaxation both in the 1111 and 122 families of IBS.
- The study of the effect of impurities, Mn doping in *Ln*1111 material and proton irradiation induced defects in $Ba(Fe_{1-x}Rh_x)_2As_2$, both on the macroscopic quantities (e.g. T_c, T_m) and on the low frequency fluctuations.
- The study of the static magnetic and charge orders and their evolution upon chemical and impurity doping.

For the convenience of the reader we present here a brief summary of the main results obtained in each of studied families of compounds, highlighting their relevance in this research field and outlining possible future extension of these studies.

***Ln*1111 Compounds** We carried out an extensive study of the effect of Mn impurity doping in *Ln*1111 (*Ln*: lanthanide ion) family (see Section 4.1). It was found that Mn is a poison for superconductivity in all of these material but the strength of this poisoning effect is strongly dependent on the radius of the *Ln* ion and thus on the chemical pressure (Section 4.1.1). In fact while a tiny 0.2% Mn content is enough to destroy the superconducting state in optimally F-doped $LaFe_{1-x}Mn_xAsO_{0.89}F_{0.11}$ a much larger amount of Mn is needed to reach the same effect in $SmFe_{1-x}Mn_xAsO_{0.88}F_{0.12}$. This

effect is even more visible in $La_{1-y}Y_yFe_{1-x}Mn_xAsO_{0.89}F_{0.11}$ where the chemical pressure and the critical amount of Mn needed to suppress T_c can be continuously tuned by increasing the Yttrium content.

Zero Field NMR measurements (Section 4.1.2) allowed us to determine that the magnetic state developing in correspondence of the T_c suppression in the same stripe magnetic state present in undoped LaFeAsO. NQR measurements also revealed that the T-O transition is also recovered and that the electronic ground state of Mn doped $LaFe_{1-x}Mn_xAsO_{0.89}F_{0.11}$is very similar to that of LaFeAsO, indicating that in this system Mn doping (0.5%) gives rise to a huge localization effect which is able to completely compensate the effects of 11% fluorine (electron) doping. Thus *Ln*1111 is an example of a strongly correlated system whose electronic property can be significantly modified by fine-tuning the correlation strength with impurities and chemical pressure. These results are also very important because they indicate Mn is not directly hindering the pairing mechanism but instead it is driving the system towards a QCP.

Furthermore ^{19}F NMR studies revealed that in this compound the strength of the low frequency spin fluctuations is strongly affected by Mn doping which suggest that those dynamics, widely observed in IBS, are not correlated with the appearance of superconductivity (Section 4.1.3).

Rh doped $BaFe_2As_2$ We carried out a throughout ^{75}As NMR study of $Ba(Fe_{1-x}Rh_x)_2As_2$ as function of the external field, uniaxial strain, and of the proton irradiation fluence.

The $1/T_2$ experimental results revealed the onset of very low frequency fluctuation emerging in the normal state below a characteristic temperature T^*. In particular it was found that T^* is enhanced by the magnetic field and that the fluctuations persist into the overdoped region of the phase diagram. Furthermore the same dynamic was also observed to be present in the T_1 data and we were able to fit both $1/T_2$ and $1/T_1$ relaxation rates temperature dependences using the same model. These fluctuation have been proposed to originate from the motion of the domain walls separating nematic correlated phases [195, 314] (Section 3.1).

It was also observed (Section 4.2) that the defects induced by proton irradiation significantly affect the $1/T_2$ temperature dependence, particularly in the overdoped region of the phase diagram, in good agreement with the hypothesis that the fluctuations are pinned by the presence of the irradiation induced defects. Furthermore, in the optimally doped sample, a sizeable broadening of the NMR spectra was observed at low temperatures. The Curie Weiss temperature dependence of the line width change sign upon increasing the fluence, suggesting the onset of ferromagnetic correlations coexisting with superconductivity at the nanoscale.

Finally we studied the evolution of the relaxation rate in presence of uniaxial strain (Section 3.2) in the optimally doped sample. The results revealed

that $1/T_1$ is strongly reduced in the strained sample and its anisotropy between $H \parallel c$ and $H \parallel ab$ diminishes significantly. These observation strongly suggest that the low frequency fluctuation are suppressed in presence of uniaxial strain, possibly due to the breaking of the symmetry between the two in plane crystal directions. Future experiments are needed in order to thoroughly clarify the relation between these fluctuations, uniaxial strain and chemical doping. In particular it would be interesting to check if uniaxial pressure and strain give rise to the same effect and how chemical doping is related with the strain induced suppression rate of the spin fluctuations.

(Cs,Rb)Fe_2As_2 An extensive ^{75}As NQR study of (Cs,Rb)Fe_2As_2 has been presented in Section 3.3. The study of the temperature evolution of the NQR spectrum of these material revealed the presence of a static charge ordered phase emerging at low temperatures in both the compounds.

While a similar phenomenology had been observed before in KFe_2As_2 high pressure NMR spectra, this is the first direct evidence that a charge order is present in the iron pnictides at ambient pressure, and thus that it is not an exclusive feature of the cuprates phase diagram.

We also carried out $^{(87,85)}$Rb NMR-NQR and μSR measurements whose result can also be nicely explained by the emergence of the charge order.

Future X-Ray, neutron scattering and NMR studies are needed in order to better understand the nature of the charge order and to find out the region of the 122 phase diagram where this ordered phase is present. This could gives us a much better understanding of the relation between charge order and superconductivity in High Temperature Superconductors.

Appendices

Appendix A

Miscellaneous NMR concepts and methods

A.1 The rotating frame

It is often very useful, in particular when dealing with pulse NMR experiments, to study the motion of the magnetization not in the fixed laboratory frame but in a coordinate system that rotates around $\mathbf{H}_0 \parallel z$ at the Larmor frequency $\omega_0 = \omega\mathbf{H}_0$. This coordinate system is called the rotating frame.

Starting from Eq 2.21 we will now describe the motion of the magnetization in a frame x', y', $z' = z$ rotating at an angular velocity $\boldsymbol{\omega}$ with respect to the laboratory frame x, y, z, with ($\mathbf{H}_0 \parallel \hat{z}$). For a generic vector $\mathbf{A}$, $\frac{d\mathbf{A}}{dt} = \frac{\partial \mathbf{A}}{\partial t} + \boldsymbol{\omega} \times \mathbf{A}$, where $\frac{d\mathbf{A}}{dt}$ is the total time derivative in the stationary frame and $\frac{\partial \mathbf{A}}{\partial t}$ is the derivative in the rotating frame. Thus the equation of motion of the magnetization will become:

$$\frac{\partial \mathbf{M}}{\partial t} = \gamma\, \mathbf{M} \times \left(\mathbf{H}_0 + \frac{\boldsymbol{\omega}}{\gamma} \right) . \tag{A.1}$$

This equation has the same form of Eq. 2.21 where $\mathbf{H}_0$ has been substituted with an effective field $\mathbf{H}_0 + \boldsymbol{\omega}/\gamma$. If $\boldsymbol{\omega} = -\gamma\mathbf{H}_0$ than in the rotating frame $\partial\mathbf{M}/\partial t = 0$, which means that $\mathbf{M}$ is stationary in the rotating frame if the rotation frequency of the frame is equal to ω_L. Now we add a rotating field $\mathbf{H}_1$. In the laboratory frame x, y, z we have that $\mathbf{H}_1 \equiv (\mathbf{H}_1 \cos\omega t, \mathbf{H}_1 \sin\omega t, 0)$. In a frame rotating with the same frequency of $\mathbf{H}_1$ instead we have that $\mathbf{H}_1$ will be stationary and we assume $\mathbf{H}_1 \parallel x'$. We also have that $\boldsymbol{\omega} \parallel \mathbf{H}_0$ and it has the same or the opposite orientation of $\mathbf{H}_0$ depending if the rotation is clockwise or anticlockwise. Since in the laboratory frame $\frac{d\mathbf{M}}{dt} = \gamma\, \mathbf{M} \times (\mathbf{H}_0 + \mathbf{H}_1)$, from Eq. A.1 we deduce that in the rotating frame:

$$\frac{\partial \mathbf{M}}{\partial t} = \gamma\, \mathbf{M} \times \left(\mathbf{H}_0 + \frac{\boldsymbol{\omega}}{\gamma} + \mathbf{H}_1 \right) = \gamma \mathbf{M} \times \mathbf{H}_{eff} . \tag{A.2}$$

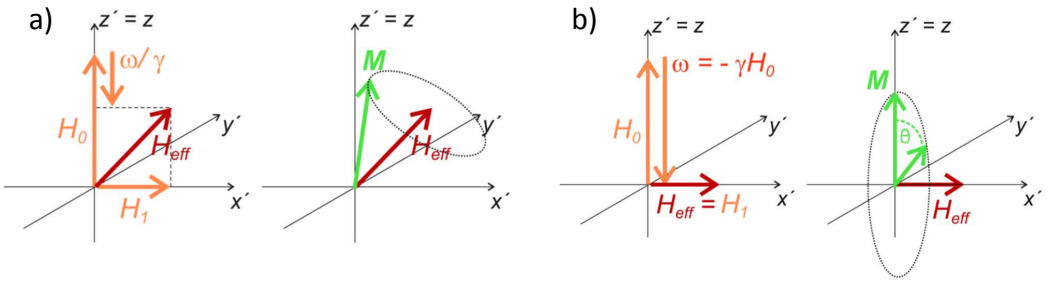

Figure A.1: a) sketch of the fields and the precession of the magnetization around $\mathbf{H}_{eff}$. b) the magnetization rotating around $\mathbf{H}_1$ in the resonance condition. Figure adapted from Ref. [143].

Since $\omega_1 = -\gamma H_1$ and $\omega_0 = -\gamma H_0$ the angle θ between $\mathbf{H}_{eff}$ and $\mathbf{H}_0$ is given by (see Fig A.1):

$$\tan\theta = \frac{|\mathbf{H}_1|}{|\mathbf{H}_0 + \boldsymbol{\omega}/\gamma|} = \frac{\omega_1}{\omega_0 - \omega} \ . \tag{A.3}$$

If H_1 is small with respect to H_0, as is the case for an NMR experiment, θ remains extremely small unless $\omega \sim \omega_0$. So the effect of $\mathbf{H}_1$ is negligible until its frequency does not match the Larmor frequency $-\gamma H_1$. This is called the resonance condition.

When the resonance condition is satisfied the fictitious magnetic field completely cancels out $\mathbf{H}_0$ (see Fig. A.1) and the magnetization will precess around $\mathbf{H}_1 \parallel x$. Thus in presence of a $\mathbf{H}_1$ field rotating at the Larmor frequency and applied for a time interval τ, the magnetization in the rotating frame will be tilted by an angle:

$$\theta = -\gamma H_1 \tau \ . \tag{A.4}$$

The values of $\mathbf{H}_1$ varies from ~0.1 mG for some high resolution continuous wave NMR set-up to ~100 G for pulse NMR experiments.

A.2 Bloch equations in presence of a rotating field

In presence of a rotating magnetic field $\mathbf{H}_1$ perpendicular to the external static field the resulting total magnetic field is given by (in the laboratory frame):

$$\mathbf{H}(t) = H_1(\hat{x}\cos\omega t - \hat{y}\sin\omega t) + H_0\hat{z} \ . \tag{A.5}$$

where $\hat{y}, \hat{y}$ and $\hat{y}$ are unit vectors along the axes. The rotation is chosen clockwise, $\omega > 0$. Substituting $\mathbf{H}(t)$ in the Bloch equations (Eq. 2.22, 2.23) and expanding the rotor one immediately gets:

$$\frac{dM_x}{dt} = \omega_0 M_y + \omega_1 M_z \sin\omega t - \frac{M_x}{T_2} \ . \tag{A.6}$$

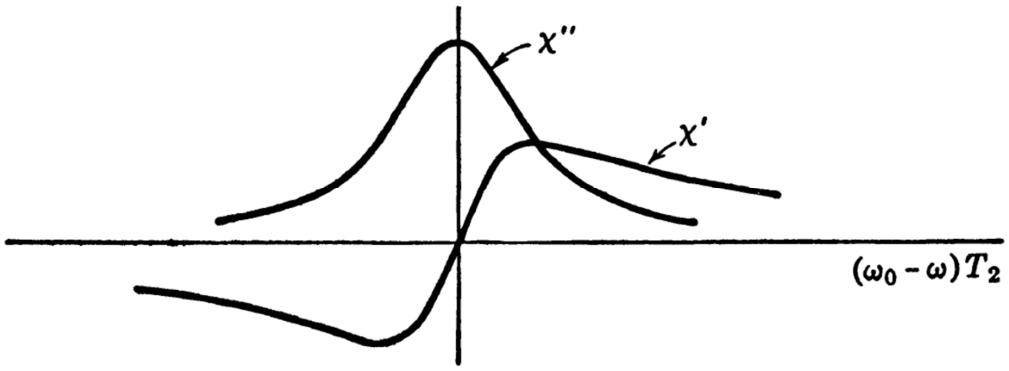

Figure A.2: Sketch of χ' and χ'' derived from the Bloch equations plotted versus $(\omega_0 - \omega)T_2$. Figure adapted from [136].

$$\frac{dM_y}{dt} = -\omega_0 M_x + \omega_1 M_z \cos\,\omega t - \frac{M_y}{T_2}\ . \tag{A.7}$$

$$\frac{dM_z}{dt} = -\omega_1 (M_x \sin\omega t + M_y \cos\omega t) + \frac{M_0 - M_z}{T_1}\ . \tag{A.8}$$

where $\omega_0 = \gamma H_0$ and $\omega_1 = \gamma H_1$. If $\mathbf{H}_1$ is small the transverse magnetization component will also be small when compared with M_z and the two terms $\omega_1 M_x$ and $\omega_1 M_y$ can be safely neglected. The condition of "small H_1" can be written in a more quantitative way as (see Ref. [137, 136, 315]):

$$\gamma^2 H_1^2 T_1 T_2 \ll 1\ . \tag{A.9}$$

With this condition on $\mathbf{H}_1$ from equation A.8 follows that $dM_z/dt = 0$. In this framework the general solutions for Eq. A.6 and A.7 are given by:

$$M_x = m\cos(\,\omega t + \phi) \qquad M_y = -m\sin(\,\omega t + \phi)\,, \tag{A.10}$$

where ϕ is the angle by which $\mathbf{M}$ leads $\mathbf{H}$. Substituting in the Bloch equations and differentiating we find [316]:

$$m = \frac{\gamma M_0 T_2 H_1}{[1 + (\omega_0 - \omega)^2\, T_2\,^2]^{1/2}}\ , \tag{A.11}$$

and for the angle ϕ:

$$\cos\phi = \frac{(\omega_0 - \omega)}{[1 + (\omega_0 - \omega)^2 T_2^2]} \qquad \sin\phi = -\frac{1}{[1 + (\omega_0 - \omega)^2 T_2^2]}, \tag{A.12}$$

We can write the transverse magnetization as $\mathbf{m}(t) = M_x(t)\hat{x} + M_y(t)\hat{y}$, than from Eq. A.10 we get:

$$\mathbf{m}(t) = m[\hat{x}(\cos\omega t\cos\phi - \sin\omega t\sin\phi) - \hat{y}(\sin\omega t\cos\phi + \cos\omega t\sin\phi)] \tag{A.13}$$

Now we call $\mathbf{m}'$ the component of $\mathbf{m}(t)$ which has the same phase of the rotating field while $\mathbf{m}''$ will denote the component in quadrature. From Eq. A.13:

$$\mathbf{m}'(t) = m\ \cos\phi\ (\hat{x}\cos\omega t - \hat{y}\sin\omega t) \qquad \mathbf{m}''(t) = -m\sin\phi\ (\hat{x}\sin\omega t + \hat{y}\cos\omega t)\,, \tag{A.14}$$

The in phase and out of phase susceptibility ($\chi(\omega) = \chi'(\omega) + i\chi''(\omega)$ in complex notation) are given by:

$$\chi'(\omega) = \frac{m\cos\phi}{H_1} \qquad \chi''(\omega) = -\frac{m\sin\phi}{H_1}\,, \tag{A.15}$$

The real part χ' represent the energy dispersion while the imaginary part χ'' represent absorption. Substituting m, $\cos\phi$, and $\sin\phi$ we arrive to:

$$\chi'(\omega) = \chi_0 \cdot \frac{\omega_0(\omega_0-\omega){T_2}^2}{1+(\omega_0-\omega)^2{T_2}^2}\,, \qquad \chi''(\omega) = \chi_0 \cdot \frac{\omega_0{T_2}^2}{1+(\omega_0-\omega)^2{T_2}^2}\,. \tag{A.16}$$

When the resonance condition is satisfied we get:

$$\chi'(\omega) = 0\,; \qquad \chi''(\omega) = \chi_0 \cdot \omega_0 T_2 = \chi_0 \frac{\omega_0}{(\Delta\omega)_{1/2}}\,. \tag{A.17}$$

where $\Delta\omega_{1/2}$ is the full width at half maximum of the absorption. A sketch of χ' and χ'' is shown in Fig. A.2. Since usually the line width $\Delta\omega_{1/2} \ll \omega_0$ than χ'' at resonance will be much larger than the static susceptibility.

A.3 Supplementary NMR Sequences

A.3.1 The Carr-Purcell Sequence

The Hahn echo technique is limited in its range of applicability because when a dynamic is present, such as a diffusion process, the nuclei can change their precession frequency by drifting into a different location, where the local field has a different value. In fact the precise refocusing of the magnetic moments takes place only if each nucleus remain in a constant magnetic field for all the measurement time 2τ. This problem is particularly severe in liquids where the diffusion process are usually strong but spin diffusion phenomena can also be present in solid as we will show in the next Chapter.

In presence of a spin diffusion in a magnetic field gradient $\partial H/\partial z$ it can be shown that [136]:

$$M(2\tau) = M(0)\exp(-2\tau/T_2)\exp\left[-\left(\frac{\gamma\partial H}{\partial z}\right)^2\frac{2}{3}D\tau^3\right]\,. \tag{A.18}$$

where D is the diffusion constant in the static field gradient. It must be noted that Eq. A.18 holds in the hypothesis that the field, though inhomogeneous,

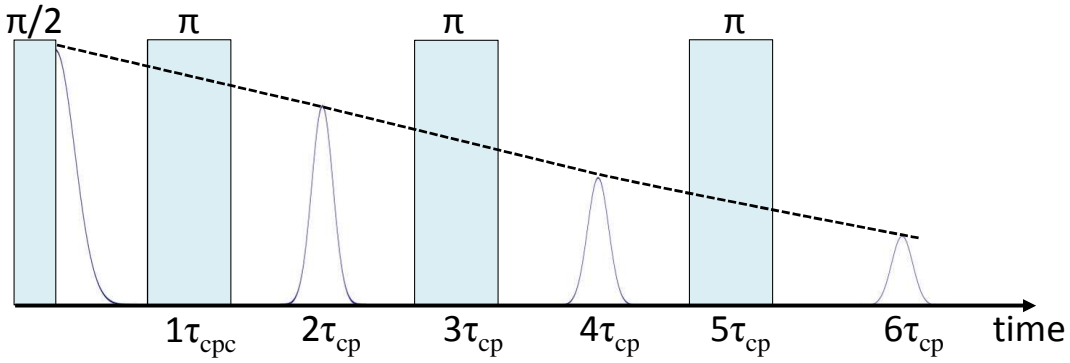

Figure A.3: Scheme of a Carr-Purcell-Meiboom-Gill sequence. The dotted line is the envelope of the CPMG echoes.

has an axial symmetry which means that at any point one can write the field as:

$$H(x, y, z) = H_0 + z\frac{\partial H}{\partial z} \ . \tag{A.19}$$

From equation A.18 follows that, depending on the values of the coefficients, the second exponential term can greatly affect the T_2 value measured using the Hahn echo method. Carr and Purcell (CP) developed a new sequence in order to measure T_2 which greatly mitigates the effect of diffusion term.

This sequence consist in a $\pi/2$ pulse followed by a $\tau_{CP} - \pi - 2\tau_{CP} - \pi - 2\tau_{CP} \cdots$ pulse train (see Fig. A.3). The pulses are applied along x'. The sequence causes a series of echoes at 2τ,4τ, 6τ $8\tau \cdots$, in fact the subsequent π pulses continuously refocus the magnetization.

The CP sequence has two main advantages on the simple Hahn echo sequence:

1) Using this sequence for measuring T_2 requires much less time than making lots of Hahn echoes. In fact after every single echo one as to wait for the magnetization to come back at the equilibrium condition $M \parallel z$, but this may require a lot of time if T_1 is long (several seconds).

2) The effect of diffusion may be nearly completely eliminated if one choose τ_{CP} short enough because the diffusion processes do not have time to take place.

The most precise way for measuring T_2 is to perform various CP measurements with smaller and smaller τ_{CP} and than extrapolating the limit of $T_2(\tau_{CP})$ for $\tau_{CP} \to 0$.

Despite its usefulness this sequence has an important drawback: if T_2 is long lots of $\pi/2$ pulses will be required and any error, however small, on the length of the pulses will sum up giving rise to an incomplete rephasing of the spins and thus to a measured T_2 shorter than the real one. Meiboom and Gill improved the sequence by choosing y' as the direction of the π pulses. This trick removes the summation of the phase errors and also results in the

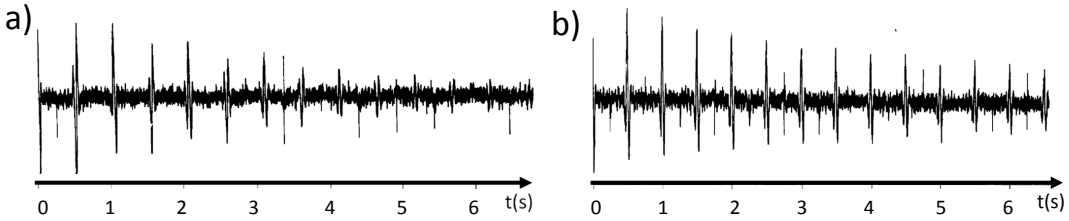

Figure A.4: a) Carr Purcell sequence (^{13}C in $CH_4\,^{13}COOH$). b) The result of the CPMG sequence in the same compound. Note that in b) the echoes have the same sign and persist for a much longer time. Figure adapted from [145].

spins always refocusing along $+y$ generating a positive echo [145] and thus removing the alternating ± sign of the echoes characterizing the original CP sequence. The typical result of the two sequences is shown in Fig. A.4.

A.3.2 The inversion recovery sequence

The inversion recovery sequence has a different preparation phase with respect to the saturation recovery. It consists of a π pulse followed by a normal Hahn spin echo pulse sequence after a variable delay time. The π pulse flips the nuclear magnetization in the $-z$ direction. The magnetization begins to relax back to its equilibrium value during the free evolution time. The following Hahn echo is proportional to $M_z(\tau_1)$. The sequence and a typical recovery curve are sketched in Fig. A.5.

A.4 The Hyperfine Hamiltonian components and the Knight shift

In Section 2.1.2.2 we wrote the hyperfine Hamiltonian as:

$$\mathcal{H}_{n-e} = \gamma_n \gamma_e \hbar^2 \mathbf{I} \cdot \left[\overbrace{\left(3\frac{(\mathbf{S}\cdot\mathbf{r})\mathbf{r}}{r^5} - \frac{\mathbf{S}}{r^3} \right)}^{K_{dip}} + \overbrace{\frac{8\pi}{3}\mathbf{S}\delta(\mathbf{r})}^{K_{contact}} + \overbrace{\frac{\mathbf{L}}{r^3}}^{K_{orb}} \right]. \tag{A.20}$$

We will now give some more detail on the various terms of the Hamiltonian and explain how the values of the components of the hyperfine tensor A_{hyp} can be derived from a NMR line shift measurement.

A.4.1 The orbital shift

The last term of the hyperfine Hamiltonian (Eq. A.20) represents the orbital interaction between the nuclear spin $\mathbf{I}$ and the angular momentum $\mathbf{L}$ of the

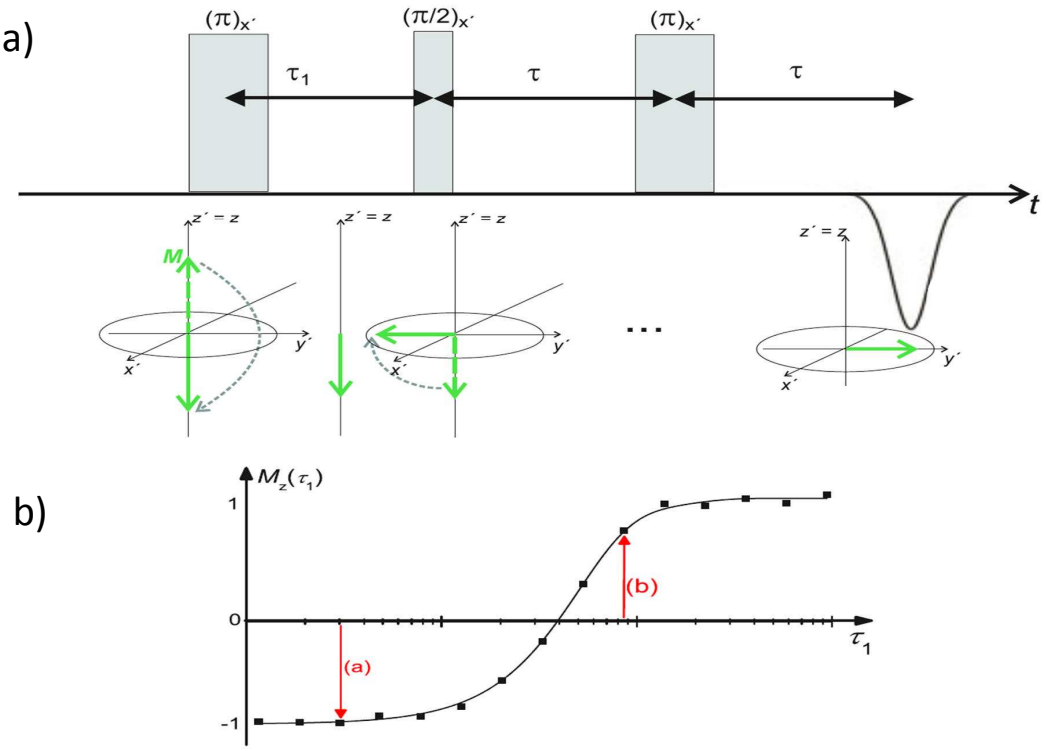

Figure A.5: a) Sketch of the inversion recovery sequence for to different durations of the evolution time τ_1. b) The integral of the measured spin echo. The sign of the signal changes from negative to positive as τ_1 increases and the magnetizations recovers along $+z$. Figure adapted from [143].

electron. This term is zero for transition metals where the orbital angular momentum is quenched. An externally applied magnetic field can however partially reconstruct an orbital moment by mixing the ground state with low lying excited states (see Ref. [148]). This effect is the so called Van Vleck paramagnetism. The resulting shift [152] is temperature independent since the Van Vleck susceptibility χ_{VV} does not change with temperature.

A.4.2 The spin shift

The first two terms in Eq. A.20 ($K_s = K_{dip} + K_{contact}$) are responsible for the component of the shift due to the interaction of the nuclear moments with the electron spins. The first component, K_{dip}, describes the dipolar interaction between the spins. This term is different from zero for the unpaired electron spins of the p, d and f orbitals while it vanish for the s orbital for symmetry reasons. The shift is proportional to $1 - 3\cos^2\theta$ were θ is the angle between the magnetic field $\mathbf{H}_0$ and the lobe of the wave function (see Fig. A.6).

The second term, $K_{contact}$, is a Fermi contact term that is non-zero only if the wave function of the electron is $\Psi(0) \neq 0$ and thus it is necessar-

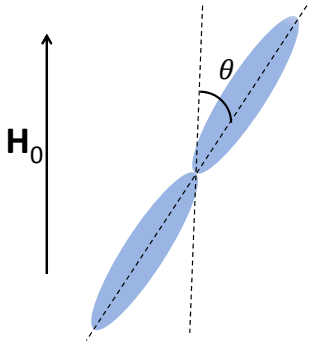

Figure A.6: Sketch of a p-orbital in the external magnetic field $\mathbf{H}_0$.

ily an isotropic contribute which does not depend on the orientation of the field. The orbitals contributing to $K_{contact}$ are the s-electron but a non negligible fraction of $K_{contact}$ is often transferred from the neighboring atomic sites through orbital hybridization.

A.4.3 NMR Knight shift and hyperfine tensor

In order to evaluate the complete hyperfine tensor in solids a very precise first principle calculation of the band structure is usually needed. However from the experimental point of view the components of A_{hyp} can be easily extracted from the NMR measurements. In fact the resonance frequency depends on the local field probed by the nucleus:

$$\omega_{res} = \gamma_n \langle \mathbf{H}^z_{loc} \rangle = \gamma_n (\mathbf{H}_0 + \langle \mathbf{H}^z_{el} \rangle) = \gamma_n (\mathbf{H}_0 + A_{hyp} \langle \mathbf{S}^z \rangle) \,, \tag{A.21}$$

In this framework the Knight Shift is usually defined as:

$$K = \frac{\omega_{res} - \gamma_n \mathbf{H}_0}{\gamma_n \mathbf{H}_0} = \frac{\langle \mathbf{H}^z_{el} \rangle}{\mathbf{H}_0} = \frac{A_{hyp} \langle \mathbf{S}^z \rangle}{\mathbf{H}_0} \,. \tag{A.22}$$

Since the molar static spin susceptibility is given by:

$$\chi_{mol} = \frac{g \mu_B N_A \langle \mathbf{S}^z \rangle}{\mathbf{H}_0} \,, \tag{A.23}$$

combining Eq. A.22 and A.23 one immediately arrives to:

$$K^{\alpha\beta}_{spin} = \frac{A^{\alpha\beta}_{hyp}}{g \mu_B N_A} \chi^{\alpha\beta}_{mol} \,, \tag{A.24}$$

where again $\alpha\beta = x, y, z$. $K^{\alpha\beta}_{spin}$ is often written as:

$$K^{\alpha\beta}_{spin} = A^{\alpha\beta}_{hyp} \; \chi^{\alpha\beta} \,, \tag{A.25}$$

where all the factors are considered dimensionless.

A.5 Derivation of the T_1 dependence on spin system susceptibility

In order to work out a theoretical expression for T_1 one should consider the population of all the nuclear magnetic energy levels E_m and the possible transitions between these levels. The transition probabilities will be defined in terms of the of matrix elements of the interaction Hamiltonian. Let's start by writing down the time dependence of the normalized population N_m of a nuclear magnetic energy level E_m:

$$\frac{dN_m}{dt} = \sum_{n \neq m}^{N} (N_n W_{nm} - N_m W_{mn}) \,, \tag{A.26}$$

where $m = 1, 2, ..., N = 2I + 1$, N_m is the population of the m-th level and W_{mn} are the transition probabilities. The NMR signal will be proportional to the time evolution of the population imbalance. For a $I = 1/2$ nucleus the magnetization recovery is shown to be given by [136, 317]:

$$y(t) = \frac{M_z(\infty) - M_z(t)}{M_z(\infty)} = \exp(-t/T_1) \,, \tag{A.27}$$

where $M_z(\infty)$ is the equilibrium magnetization and

$$\frac{1}{T_1} = 2W_{\pm} \,. \tag{A.28}$$

For a nucleus with $I \neq 1/2$ the general solution is given by the sum [160]:

$$y(t) = \sum_j c_j \exp(-\alpha_j t/T_1) \,. \tag{A.29}$$

where the c_j and α_j coefficients are function of I and of the interaction mechanisms. The general form of the transition probabilities W_{mn} can be derived using the Fermi Golden Rule:

$$W_{mm'} = \frac{2\pi}{\hbar} \sum_{ff'} P_f |\langle fm|\mathcal{H}'|f'm'\rangle|^2 \delta(E_f + E_m - E_{f'} - E_{m'}) \,. \tag{A.30}$$

where P_f is the probability of occupancy of the f state, $\mathcal{H}'$ is the perturbing Hamiltonian and $|fm\rangle$, $|f'm'\rangle$ are respectively the initial and final states. If the spin lattice relaxation is dominated by magnetic fluctuations from equation A.30 it is possible to derive the more usable expression:

$$W_{mm'} = \frac{1}{\hbar} \int e^{-i\omega_{mm'}\tau} \langle \mathcal{H}'_{mm'}(0) \mathcal{H}'_{mm'}(\tau) \rangle d\tau \propto J(\omega) \,. \tag{A.31}$$

where $J(\omega)$ is the spectral density of the fluctuating field which usually has a Lorentzian shape and $\langle \mathcal{H}'_{mm'}(0) \mathcal{H}'_{mm'}(\tau) \rangle$ is the so called auto-correlation function G.

In case of a completely magnetic relaxation the interaction Hamiltonian will have the form:

$$\mathcal{H}' = -\hbar\gamma \mathbf{I} \cdot \mathbf{h}(t) \ . \tag{A.32}$$

where $\mathbf{h}(t)$ is the fluctuating magnetic field. From here it is relatively straightforward to work out the explicit form of the correlation function:

$$G_{\alpha\alpha}(\tau) = \langle h_\alpha(t) h_\alpha(t+\tau) \rangle \tag{A.33}$$

and after a few calculations one arrives to the formula (see [136]):

$$\frac{1}{T_1} = \frac{\gamma^2}{2} \int e^{i\omega_0 t} \langle h_x(t) h_x(0) + h_y(t) h_y(0) \rangle dt = \frac{\gamma^2}{2} \int e^{i\omega_0 t} \langle h_+(t) h_-(0) \rangle dt \propto J(\omega_0) \ , \tag{A.34}$$

where $J(\omega_0)$ if the Fourier Transform of the correlation function at the Larmor frequency and $h_\pm = h_x + i h_y$ (rising-lowering operators).

This expression implies that $1/T_1$ depends from the transverse components of the fluctuating magnetic field and is proportional to the spectral density of the fluctuations at the Larmor frequency.

A very useful expression of $1/T_1$ can be derived remembering that the local field can be written as:

$$\mathbf{h}(t) = \sum_i A_{hyp_i} \cdot \mathbf{S}_i \tag{A.35}$$

where A_{hyp} is the hyperfine tensor coupling the nuclear spins with the electronic spins $\mathbf{S}_i$ and the sum is on all the lattice sites. The spin components can be rewritten as:

$$\mathbf{S}_i = \frac{1}{\sqrt{N}} \sum_{\mathbf{q} \in BZ} e^{i\mathbf{q}\cdot\mathbf{r}_i} \mathbf{S}_\mathbf{q}(t) \ , \tag{A.36}$$

where the sum is over all the reciprocal lattice vectors in the first Brillouin zone. The correlation function can be rewritten using Eq. A.36 and Eq. A.35 (for detailed calculation see [136, 318]). At this point after introducing the dynamical structure factor,

$$S^{\alpha\alpha}(\mathbf{q}, \omega_0) = \int e^{i\omega_0 t} \langle S^\alpha_\mathbf{q}(t) S^\alpha_{-\mathbf{q}}(0) \rangle dt \ , \tag{A.37}$$

the analytic expression of $1/T1$ can be written in the more compact and familiar form:

$$\frac{1}{T_1} = \frac{\gamma^2}{2} \sum_{\mathbf{q} \in BZ} |\mathbf{A}_q|^2 S^{\alpha\alpha}(\mathbf{q}, \omega_0) \ , \tag{A.38}$$

At this point we can apply the fluctuation dissipation theorem:

$$S^{\alpha\alpha}(\mathbf{q}, \omega) = \frac{2k_B T}{\omega} \chi''(\mathbf{q}, \omega) \ , \tag{A.39}$$

from which follows that in correlated metals [319]:

$$\frac{1}{T_1} = \frac{2\gamma^2 k_B T}{g^2 \mu_B^2 \omega_0} \sum_{\mathbf{q} \in BZ} |\mathbf{A}_q|^2 \chi''(\mathbf{q}, \omega_0) \ , \tag{A.40}$$

Appendix B

NMR experimental set up

B.1 The NMR spectrometer

The spectrometer used for the experiments described in this thesis is a commercial Fourier Transform NMR, Apollo Tecmag Spectrometer. The building blocks on an NMR spectrometer are shown in figure B.1.

The beating heart of an NMR spectrometer is the Synthesizer, which generates the radio frequency signal. The chosen frequency can be setted by the user through the spectrometer software interface installed on the PC. The PC is connected to the spectrometer either through a standard USB cable or through a dedicated PCI board. The rf signal can be shaped into pulses of different lengths. The phase modulator then mixes the signal to four possible carriers with a phase difference of 0° , 90° , 180° , 270° from the reference signal from the synthesizer. Particular phase cycling sequences are a very useful method for getting rid of the spurious ringing.

The signal coming out from the phase modulator is then amplified, typically to several hundred volts, and sent it to the duplexer. The duplexer is a simple circuit that allows the high power pulse signal to reach the coil but prevents it from reaching the sensitive readout electronics of the spectrometer. After the end of the pulse instead it allows the weak NMR signal to reach the readout electronics without being dispersed along the high power pulse transmission line (a scheme of a duplexer is shown in Fig. B.2).

The rf pulse, after exiting the duplexer, finally reaches the NMR probe, which is inside a strong magnetic field (usually $\mathbf{H}_0$ >1 T). The probe is nothing more than an home-made LC circuit. The sample is inserted in the inductance of the LC circuit. The coil must have a very high filling factor, which means that the sample must occupy more or less all the available space inside the coil. However one also has to choose the number of turns that maximize the quality factor Q:

$$Q = \frac{\omega L}{R}\,, \tag{B.1}$$

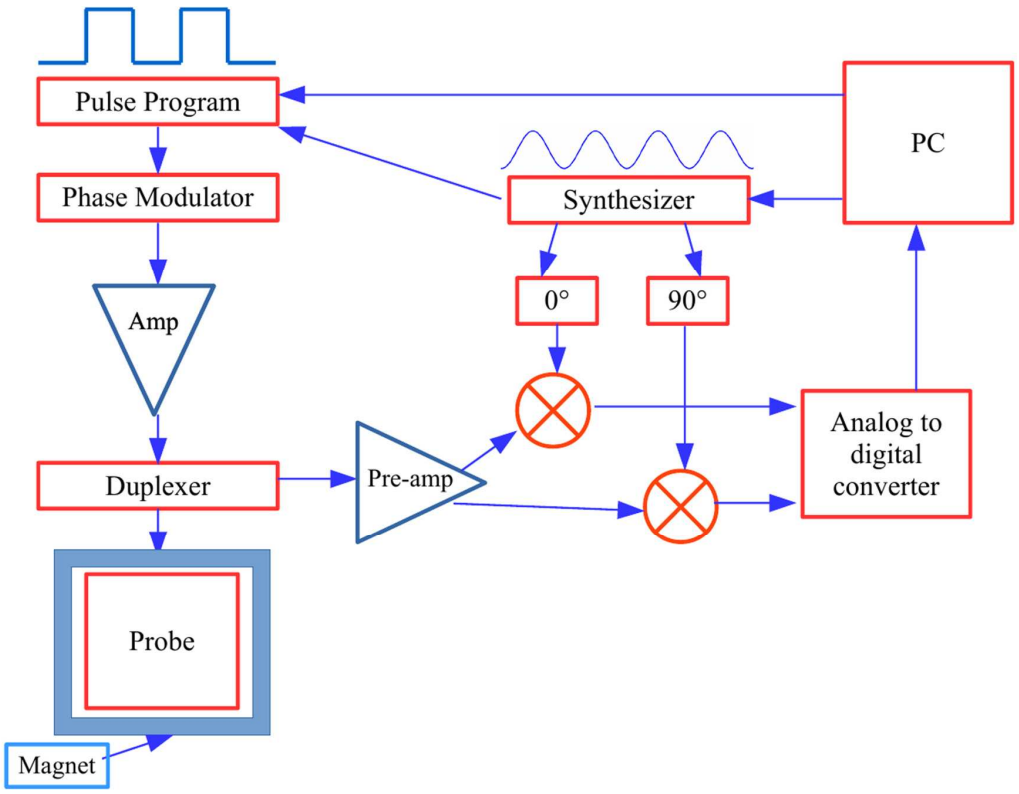

Figure B.1: Scheme of a NMR spectrometer.

where L is the inductance and R is the combined resistance of all the elements of the circuit. A good combination of high filling factor and high quality factor allows one to maximize the NMR signal of a given sample. The pick up coil is sometimes immersed in a bi-component epoxy resin, which enhance the mechanic stability and minimize the spurious ringing effect.

The maximum power transmittance to the sample is provided by the impedance matching of the LC circuit (50 Ω) at the Larmor frequency [147]. If this condition is not satisfied a significant portion of the pulse signal will be reflected back to the amplifier and will not reach the sample coil. This happens because since the impedance of the spectrometer electronics is 50 Ω, if the RLC circuit does not have the same impedance it will behave as a mirror for the radio waves.

The tuning and matching of the probe is adjusted through a set of variable capacitors that can be mounted either at the tip of the probe or as a part of the transmission line. In order to check the quality of the tuning a Morris Instruments SWR meter device was used.

Mounting the capacitors in the transmission line induces higher rf losses and a lower Q factor. On the other hand if the capacitors are mounted on the tip of the probe (close to the coil) while Q is significantly better, for superconducting samples, the enhanced Q makes the circuit so sensitive that

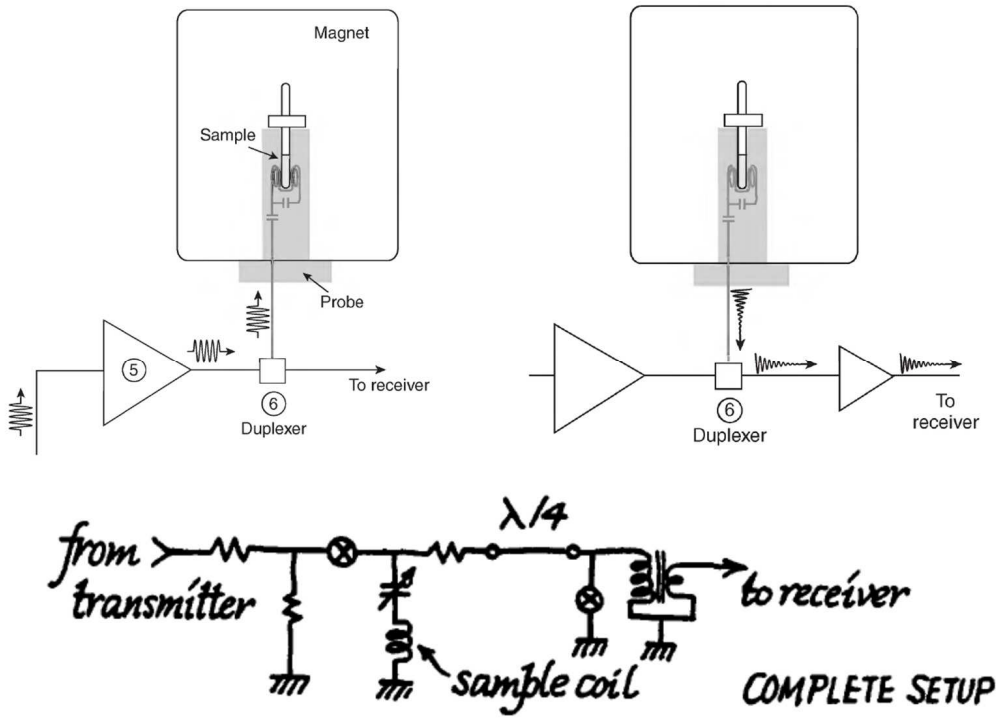

Figure B.2: Top: duplexer with rf pulse on (left), duplexer with rf pulse off (right). Adapted from [146] Bottom: the duplexer electrical circuit scheme. Adapted from [147].

the superconductivity may affect the circuit inductance so enough to shift the resonance away from the Larmor frequency (see Section 3.2).

The receiver section of the spectrometer is composed by two main elements: the mixer and the ADC converter. In the mixer the signal is split and mixed with the two reference signals from the synthesizer, one in phase with the original rf signal and one with a 90° phase difference. This allows one to extract the dissipative part (out of phase) and the dispersive part of the signal. The two components of the signal are then converted to a digital signal using a two channel ADC. The digital signal is subsequently delivered to the PC where the analysis takes place.

B.1.1 Auto-tuning setup

In order to automate the boring procedure of changing the tuning and matching of the NMR probe while measuring very wide NMR-NQR spectra we devised a very simple auto-tuning setup. The scheme of the set-up is shown in Fig. B.3.

The core of the auto-tuning apparatus is a USB VNA board (miniVNA Tiny board from Mini Radio Solutions) which measure the SWR frequency dependence of the NMR tank circuit thus determining both the position of the LC circuit resonance and the quality of the matching.

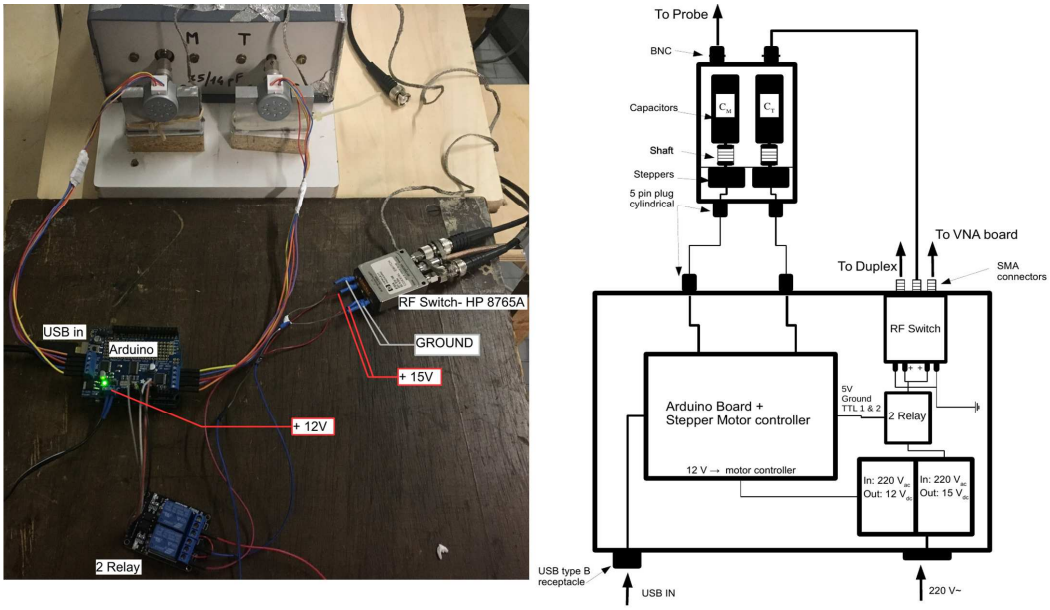

Figure B.3: Left: photo of the first working version of the auto-tuning set-up. Right: scheme of the auto-tuning set-up

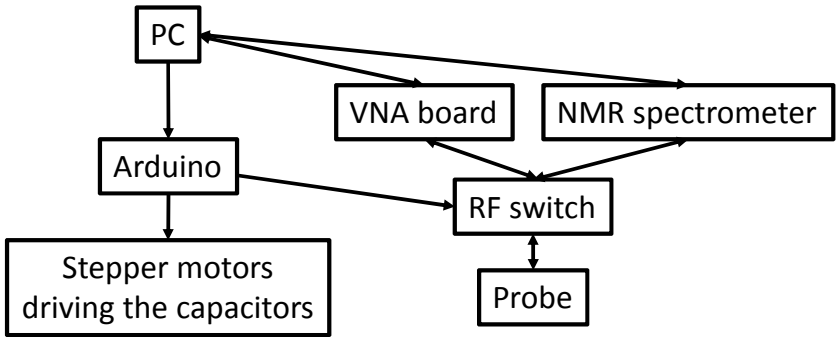

Figure B.4: Block diagram of the autotuning set-up.

A Python script running on a PC controls both the spectrometer and the tuning setup. Before starting a measurement the PC activates an RF switch controlled by an Arduino board. The switch disconnects the NMR spectrometer from the probe and connects the VNA board. At this point the VNA measures the frequency response of the probe. The results are then sent to the PC which determines the error in tuning and matching and feeds them to a control loop algorithm which drives (thanks to the Arduino UNO board) the two stepper motors connected to the variable matching and tuning capacitors. The control loop (measure resonance position → adjust variable capacitors) is repeated until the probe LC circuit is tuned and matched at the correct frequency. The switch is then activated again to reconnect the spectrometer and the measurement is carried out.

This whole process is repeated for the desired number of frequency steps,

until the whole NMR spectrum is acquired.

This customized set-up allowed us to measure very broad NMR-NQR spectra with very weak signals, such as the high temperature (650 K) NQR measurements of fluorine doped LaFeAsO(see Fig. 3.28).

B.1.2 Magnets

The magnets are obviously an essential component of an NMR set-up. In this thesis we have used both electromagnets (e.g. for fluorine NMR measurements in $Ln1111$) and superconducting magnets.

In the case of electromagnets, magnetic fields up to nearly 2 T can be generated. The ferromagnetic core, thanks to the high magnetic permeability of the ferromagnetic materials, gives rise a significant enhancement of the field generated by the coils. In order to dissipate the great amount of heat produced by the strong current circulating in the coils a water-based cooling systems is typically used.

Superconducting magnets nowadays are much more common in NMR set-ups. Superconductors in fact are capable of supporting very large electric currents without any external supply and are also extremely stable allowing one to obtain much higher and more uniform fields than those typically achievable with electromagnets.

The windings of the superconducting coils are usually made from an alloy of niobium and titanium, however for the higher field magnets ($\mathbf{H}_0$ >15 T) a niobium tin-alloy is often used. The extremely thin superconducting wires are embedded in a copper matrix in order to obtain better mechanical properties and to create a low resistivity escape path for the current in case of a magnet quench. The superconducting coil is immersed in a liquid helium bath. The helium is itself insulated by a large reservoir of liquid nitrogen (T=77K). The two baths are separated from each other and from the outside by evacuated jackets.

In order to inject a current in the superconducting coil a persistent switcher is commonly used. This type of switch is comprised of a short section of superconducting wire, connected across the output terminals of a current generator, and of an heater used to drive the wire into the normal state. When the heater is turned on the section of the superconducting coil becomes resistive and the circuit behaves in a ohmic way, so a current of the chosen intensity can be circulated into the coil. Once the correct current value is reached the heater is switched off, the wire becomes superconducting again and the current will continue to circulate in the magnet for an indefinite amount of time.

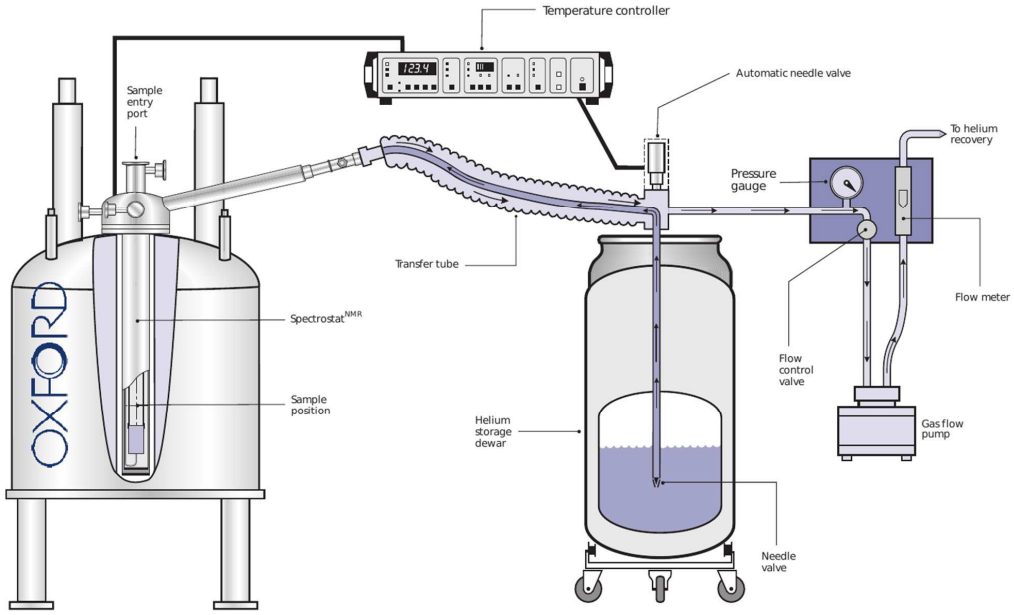

Figure B.5: Scheme of a dynamic flow cryostat in operation.

B.2 Cryogenics and temperature control

Cryogenics is an important part of an NMR experiment, since many of the studied effects take place at very low temperature.

Most of the measurements have been carried out using a dynamic helium flow cryostat. In this type of set-up (see Fig. B.5) liquid helium is transferred from the dewar to the cryostat, through a vacuum insulated transfer line and the He flow directly cools the sample. A very similar apparatus is the static flow cryostat. Its working principle is identical to that of the dynamic flow cryostat the only difference being that the sample is inserted into a GHe filled chamber which than is cooled down by the helium flow from the dewar. In these cryostat the temperature is controlled both by changing the He flow through a needle valve and by heating the sample space through a electrical heater connected to a PID temperature controller

For the very low temperature measurements a bath cryostat has been used. In this type of cryostat the sample is inserted directly in the helium bath and the temperature is controlled changing the pressure of the bath with a powerful pump.

Sometimes it is also useful to carry out NMR-NQR measurements at high temperature (see Fig 3.28). In this case a custom built water cooled furnace has been used. In this set up a continuous water flow keeps the external jacket of the furnace cold while a powerful electrical heater warms up the sample space up to 650 K. Since standard industrial oven controllers often produce a significant high frequency noise which is detrimental for NMR-NQR measurements of very weak signals a custom PC controlled PID loop has been devised. In this set up the thermocouple from the oven is read using a

digital voltmeter and the current is controlled through a GPIB connected high precision DC power supply which regulates the gate current of the TRIAC circuit feeding the high voltage AC current to the oven's heater.

Bibliography

[1] J. G. Bednorz and K. A. Müller, Z. Phys. B **64**, 189 (1986).

[2] Y. Kamihara, T. Watanabe, M. Hirano, and H. Hosono, J. Am. Chem. Soc.**130**, 3296-3297 (2008).

[3] Shimizu, K., T. Kimura, S. Furomoto, K. Takeda, K. Kontani, Y. Onuki, and K. Amaya, 2001, Nature **412**, 316-318 (19 July 2001).

[4] H. Kamerlingh Onnes, Commun. Phys. Lab. Univ. Leiden **12**, 120 (1911).

[5] W. A. Little and R. D. Parks Phys. Rev. Lett. **9**, 9 (1962).

[6] L. C. Hebel and C. P. Slichter Phys. Rev. **107**, 901 (1957).

[7] N. W. Ashcroft, Phys. Rev. Lett. **21**, 1748 (1968).

[8] W. L. McMillan Phys. Rev. **167**, 331 (1968).

[9] A. P. Drozdov, M. I. Eremets, I. A. Troyan, V. Ksenofontov and S. I. Shylin, Nature **525**, 73-76 (2015).

[10] Pia Jensen Ray. Masters thesis, "Structural investigation of $La_{2-x}Sr_xCuO_{4+y}$ - Following staging as a function of temperature". Tech. rep. Copenhagen, Denmark: Niels Bohr Institute, Faculty of Science, University of Copenhagen (2015).

[11] F. Steglich, J. Aarts, C. D. Bredl, W. Lieke, D. Meschede, W. Franz, and H. Schäfer, Phys. Rev. Lett. **43**, 1892 (1979).

[12] S. S. P. Parkin et al, J. Phys. C: Solid State Phys. **14** 5305 (1981).

[13] K. Ishida, Y. Nakai and H. Hosono, J. Phys. Soc. Jpn. **78**, 062001 (2009).

[14] Johnpierre Paglione and Richard L. Greene, Nature Physics **6**, 645–658 (2010).

[15] H. Okada, K. Igawa, H. Takahashi et al., J. Phys. Soc. Jpn. **77**, 113712 (2008).

[16] X. F. Lu, N. Z. Wang, H. Wu, Y. P. Wu, D. Zhao, X. Z. Zeng, X. G. Luo, T. Wu, W. Bao, G. H. Zhang, F. Q. Huang, Q. Z. Huang and X. H. Chen, Nature Materials **14**, 325-329 (2015).

[17] Y. L. Sun, H. Jiang, H. F. Zhai, J. K. Bao, W. H. Jiao, Q. Tao, C. Y. Shen, Y. W. Zeng, Z. A. Xu, and G. H. Cao, J. Am. Chem. Soc., **134** (31), pp 12893–12896 (2012).

[18] H. Luetkens, H.H. Klauss, M. Kraken et al., Nat. Mater. **8**, 305–309 (2009).

[19] A.J. Drew, C. Niedermayer, P.J. Baker et al., Nat. Mater. **8**, 310–314 (2009).

[20] S. Limura, S. Mutuishi, H. Sato et al., Nat. Commun. **3**, 943 (2013).

[21] C. Wang, Y.K. Li, Z.W. Zhu et al., Phys. Rev. B **79**, 054521 (2009).

[22] Iimura S, Matuishi S, Sato H, Hanna T, Muraba Y, Kim S W, Kim J E, Takata M and Hosono, Nat. Commun. **3** 943 (2012).

[23] H. Kito, H. Eisaki, and A. Iyo: J. Phys. Soc. Jpn. **77** (2008) 063707.

[24] J.-H. Chu, J.G. Analytis, C. Kucharczyk, I.R. Fisher, Phys. Rev. B **79** (2009) 014506.

[25] M. Rotter, M. Pangerl, M. Tegel, D. Johrendt, Angew. Chem. Int. Ed. **47** (2008) 7949.

[26] S. Jiang, H. Xing, G. Xuan, C. Wang, Z. Ren, C. Feng, J. Dai, Z. Xu and G. Cao, Journal of Physics: Condensed Matter, **21**, Number 38.

[27] M. Rotter, M. Tegel, D. Johrendt, I. Schellenberg, W.Hermes, and R.Pottgen, Phys. Rev. B **78**, 020503(R) (2008).

[28] L. Z. Deng, B. Lv, K. Zhao, F. Y. Wei, Y. Y. Xue, Z. Wu, and C. W. Chu, Phys. Rev.B, **93** (2016) 054513.

[29] K. Kudo, K. Iba, M. Takasuga, Y. Kitahama, J.-i. Matsumura, M. Danura, Y. Nogami, M. Nohara, Scientific Reports **3**, 1478 (2013).

[30] X. C. Wang, Q. Liu, Y. Lv, W. Gao, L. X. Yang, R. C. Yu, F. Y. Li, and C.Jin, Solid. State. Comm. **148**, 538 (2008).

[31] J.J. Tapp, Z. Tang, B. Lv et al., Phys. Rev. B **78**, 060505(R) (2008).

[32] A.F. Wang, J.J. Lin, P. Cheng et al., Phys. Rev. B **88**, 094516 (2013).

[33] Z.R. Ye, Y. Zhang, M. Xu et al., arXiv:1303.0682 (2013).

[34] S. Oh, A. M. Mounce, Jeongseop A. Lee, W. P. Halperin, C. L. Zhang, S. Carr, Pengcheng Dai, A. P. Reyes, and P. L. Kuhns, Phys. Rev. B **88**, 134518 (2013).

[35] S. Medvedev, T.M. McQueen, I.A. Troyan et al., Nat. Mater. **8**, 630–633 (2009).

[36] T.J. Liu, J. Hu, B. Qian et al., Nat. Mater. **9**, 716 (2010).

[37] Y. Mizuguchi, Y. Takano, J. Phys. Soc. Jpn. **79**, 102001 (2010).

[38] Fong-Chi Hsu et al. (2008) PNAS **105** (38): 14262–14264.

[39] Kuo-Wei Yeh et al, EPL **84** 37002 (2008).

[40] Jian-Feng Ge, Zhi-Long Liu, Canhua Liu, Chun-Lei Gao, Dong Qian, Qi-Kun Xue, Ying Liu, Jin-Feng Jia, Nature Materials **14**, 285–289 (2015).

[41] B. C. Chang et al. EPL, **84** (2008) 67014.

[42] X. Zhu, H. Yang, L. Fang, G. Mu, H.H. Wen, Superconductor Science and Technology **21**, 105001 (2008).

[43] N. Ni, M. E. Tillman, J.-Q. Yan, A. Kracher, S. T. Hannahs, S. L. Bu'ko, and P. C. Canfield, Phys. Rev. B **78**, 214515 (2008).

[44] Peter D. Johnson, Guangyong Xu, Wei-Guo Yin, *Iron-Based Superconductivity*, Springer International Publishing (2015).

[45] X.F. Wang, T. Wu, G. Wu et al., Phys. Rev. Lett. **102**, 117005 (2008).

[46] M. Moroni, P. Carretta, G. Allodi, R. De Renzi, M. N. Gastiasoro, B. M. Andersen, P. Materne, H.-H. Klauss, Y. Kobayashi, M. Sato, and S. Sanna, Phys. Rev. B **95**, 180501(R) (2017).

[47] M. I. Aroyo and H. Wondratschek, Z. Kristallogr. **210**, 243 (1995).

[48] D. C. Johnston, J. Adv. Phys. **59**, 803-1061 (2010).

[49] Gianluca Giovannetti, Carmine Ortix, Martijn Marsman, Massimo Capone, Jeroen van den Brink and José Lorenzana, Nature Communications **2**, 398 (2011).

[50] D. J. Singh and M.-H. Du Phys. Rev. Lett. **100**, 237003 (2008).

[51] G.A. Sawatzky, I.S. Elfimov, J. van den Brink, and J. Zaanen, Europhys. Lett. **86**, 17006 (2009).

[52] M. Berciu, I. Elfimov, and G.A. Sawatzky, Phys. Rev. B **79**, 214507 (2009).

[53] E. Razzoli, C. E. Matt, M. Kobayashi, X.-P. Wang, V. N. Strocov, A. van Roekeghem, S. Biermann, N. C. Plumb, M. Radovic, T. Schmitt, C. Capan, Z. Fisk, P. Richard, H. Ding, P. Aebi, J. Mesot, and M. Shi, Phys. Rev. B **91**, 214502 (2015).

[54] C. Liu, G. D. Samolyuk, Y. Lee, N. Ni, T. Kondo, A.F. Santander-Syro, S. L. Bud'ko, J. L. McChesney, E. Rotenberg, T. Valla, A. V. Fedorov, P. C. Canfield, B. N. Harmon, and A. Kaminski, Phys. Rev. Lett. **101**, 177005 (2008).

[55] Chul-Ho Lee, Akira Iyo, Hiroshi Eisaki, Hijiri Kito, Maria Teresa Fernandez-Diaz, Toshimitsu Ito, Kunihiro Kihou, Hirofumi Matsuhata, Markus Braden, Kazuyoshi Yamada, J. Phys. Soc. Jpn **77**, 083704 (2008).

[56] I. M. Lifshitz and M. I. Kaganov, Usp. Fiz. Nauk **78**, 411-461 (1962).

[57] N. Qureshi, Y. Drees, J. Werner, S. Wurmehl, C. Hess, R. Klingeler, B. Büchner, M. T. Fernández-Díaz, and M. Braden, Phys. Rev. B **82**, 184521 (2010).

[58] C. Lester, Jiun-Haw Chu, J. G. Analytis, T. G. Perring, I. R. Fisher, and S. M. Hayden, Phys. Rev. B. **81**, 064505 (2010).

[59] K. Kuroki, S. Onari, R. Arita, H. Usui, Y. Tanaka, H. Kontani, H. Aoki, Phys. Rev. Lett. **101**, 087004 (2008) .

[60] I.I. Mazin, D.J. Singh, M.D. Johannes, M.H. Du, Phys. Rev. Lett. **101**, 057003 (2008).

[61] K. H. J. Buschow and F. R. de Boer, *Physics of magnetism and magnetic materials*, Kluwer Academic Publishers, NY (2004).

[62] T. Yildirim, Phys. Rev. Lett.**101**, 057010.

[63] H. Ding, P. Richard, K. Nakayama, K. Sugawara, T. Arakane, Y. Sekiba, A. Takayama, S. Souma, T. Sato, T. Takahashi, Z. Wang, X. Dai, Z. Fang, G. F. Chen, J. L. Luo, and N. L. Wang, Europhys. Lett. **83**, 47001 (2008).

[64] Y. Zhang, L.X. Yang, M. Xu, Z.R. Ye, F. Chen, C. He, H.C. Xu, J. Jiang, B.P. Xie, J.J. Ying, X.F. Wang, X.H. Chen, J.P. Hu, M. Matsunami, S. Kimura, D.L. Feng, Nat. Mater.**10**, 273–277 (2011).

[65] S. Tan, Y. Zhang, M. Xia, Z. Ye, F. Chen, X. Xie, R. Peng, D. Xu, Q. Fan, H. Xu, J. Jiang, T. Zhang, X. Lai, T. Xiang, J. Hu, B. Xie, D. Feng, Nat. Mater. **12**, 634–640 (2013)

[66] K. Kitagawa, N. Katayama, K. Ohgushi, M. Yoshida, and M. Takigawa, J. Phys. Soc. Jpn. **77**, 114709 (2008).

[67] K. Kitagawa et al., J. Phys. Soc. Jpn. **78**, 063706 (2009).

[68] Hidekazu Mukuda, Nobuyuki Terasaki, Nobukatsu Tamura, Hiroaki Kinouchi, Mitsuharu Yashima, Yoshio Kitaoka, Kiichi Miyazawa, Parasharam M. Shirage, Shinnosuke Suzuki, Shigeki Miyasaka, Setsuko Tajima, Hijiri Kito, Hiroshi Eisaki, Akira Iyo, Journal of the Physical Society of Japan, **78**, 084717 (2009).

[69] S. V. Borisenko, V. B. Zabolotnyy, D. V. Evtushinsky, T. K. Kim, I. V. Morozov, A. N. Yaresko, A. A. Kordyuk, G. Behr, A. Vasiliev, R. Follath, and B. Buchner, Phys. Rev. Lett. **105**, 067002 (2010).

[70] T. Kondo, A. F. Santander-Syro, O. Copie, C. Liu, M. E. Tillman, E. D. Mun, J. Schmalian, S. L. Bud'ko, M. A. Tanatar, P. C. Canfield, and A. Kaminski, Phys. Rev. Lett. **101**, 147003 (2008).

[71] T. Shimojima, F. Sakaguchi, K. Ishizaka, Y. Ishida, T. Kiss, M. Okawa, T. Togashi, C.-T. Chen, S. Watanabe, M. Arita, K. Shimada, H. Namatame, M. Taniguchi, K. Ohgushi, S. Kasahara, T. Terashima, T. Shibauchi, Y. Matsuda, A. Chainani, and S. Shin, Science **332**, 564 (2011).

[72] H. Kontani and S. Onari, Phys. Rev. Lett. **104**, 157001 (2010).

[73] R. M. Fernandes, M. G. Vavilov, and A. V. Chubukov, Phys. Rev. B **85**, 140512(R) (2012).

[74] Y. K. Li, X. Lin, Q. Tao, C. Wang, T. Zhou, L. Li, Q. Wang, M. He, G. Cao, and Z. A. Xu, New J. Phys. **11**, 053008 (2009).

[75] Y. K. Li, J. Tong, Q. Tao, C. Feng, G. Cao, W. Chen, F. C. Zhang, and Z. A. Xu, New J. Phys. **12**, 083008 (2010).

[76] Y. F. Guo, Y. G. Shi, S. Yu, A. A. Belik, Y. Matsushita, M. Tanaka, Y. Katsuya, K. Kobayashi, I. Nowik, I. Felner, V. P. S. Awana, K. Yamaura, and E. Takayama-Muromachi, Phys. Rev. B **82**, 054506 (2010).

[77] D. J. Singh, Phys. Rev. B **78**, 094511 (2008).

[78] Chen Fang, Hong Yao, Wei-Feng Tsai, Jiang Ping Hu, and Steven A. Kivelson, Phys. Rev. B **77**, 224509 (2008).

[79] M. A. McGuire et al., Phys. Rev. B **78**, 094517 (2008).

[80] Q. Huang, Y. Qiu, W. Bao, M. A. Green, J. W. Lynn, Y. C. Gasparovic, T. Wu, G. Wu, and X. H. Chen, Phys. Rev. Lett. **101**, 257003 (2008).

[81] Jennifer L. Niedziela, M. A. McGuire, and T. Egami, Phys. Rev. B **86**, 174113 (2012).

[82] A. A. Aczel, E. Baggio-Saitovitch, S. L. Budko, P. C. Canfield, J. P. Carlo, G. F. Chen, Pengcheng Dai, T. Goko, W. Z. Hu, G. M. Luke, J. L. Luo, N. Ni, D. R. Sanchez-Candela, F. F. Tafti, N. L. Wang, T. J. Williams, W. Yu, and Y. J. Uemura, Phys. Rev. B **78**, 214503 (2008).

[83] M. J. Han, Q. Yin, W. E. Pickett, and S. Y. Savrasov, Phys. Rev. Lett. **102**, 107003 (2009)

[84] T. Yildirim, Phys. Rev. Lett. **101** 057010 (2008).

[85] Q. Si and E. Abrahams, Phys. Rev. Lett. **101**, 076401 (2008).

[86] Jonathan Pelliciari, Yaobo Huang, Kenji Ishii, Chenglin Zhang, Pengcheng Dai, Gen Fu Chen, Lingyi Xing, Xiancheng Wang, Changqing Jin, Hong Ding, Philipp Werner, Thorsten Schmitt, arXiv:1607.04038 (2016).

[87] P. Dai, J. Hu and E. Dagotto, Nature Physics **8**, 709-718 (2012).

[88] N. Mannella, J. Phys.: Condens. Matter **26**, 473202 (2014).

[89] P. Vilmercati, A. Fedorov, F. Bondino, F. Offi, G. Panaccione, P. Lacovig, L. Simonelli, M. A. McGuire, A. S. M. Sefat, D. Mandrus, B. C. Sales, T. Egami, W. Ku, and N. Mannella, Phys. Rev. B **85**, 220503(R) (2012).

[90] S. Avci, O. Chmaissem, J.M. Allred, S. Rosenkranz, I. Eremin, A.V. Chubukov, D.E. Bugaris, D.Y. Chung, M.G. Kanatzidis, J.-P Castellan, J.A. Schlueter, H. Claus, D.D. Khalyavin, P. Manuel, A. Daoud-Aladine and R. Osborn, Nature Communications **5**, Article number: 3845 (2014).

[91] M. G. Kim, R. M. Fernandes, A. Kreyssig, J. W. Kim, A. Thaler, S. L. Bud'ko, P. C. Canfield, R. J. McQueeney, J. Schmalian, and A. I. Goldman Phys. Rev. B **83**, 134522 (2011).

[92] C. R. Rotundu, R. J. Birgeneau, Phys. Rev. B **84**, 092501 (2011).

[93] R. M. Fernandes, A. V. Chubukov and J. Schmalian, Nature Physics **10**, 97-104 (2014).

[94] P. J. Hirschfeld, M. M. Korshunov, and I. I. Mazin, Rep. Prog. Phys. **74**, 124508 (2011).

[95] A. V. Chubukov, Annu. Rev. Condens. Matter Phys. **3**, 57-92 (2012).

[96] E. Fradkin, S. A. Kivelson, M. J. Lawler, J. P. Eisenstein, and A. P. Mackenzie, Annu. Rev. Condens. Matter Phys. **1**, 153-178 (2010).

[97] S. A. Kivelson, E. Fradkin and V. J. Emery, Nature **393**, 550-553 (1998).

[98] S. Lederer, Y. Schattner, E. Berg and S. A. Kivelson, Phys. Rev. Lett. **114**, 097001 (2015).

[99] S. Avci, et al. Phys. Rev. B **85**, 184507 (2012).

[100] S. Kasahara, et al. Nature **486**, 382-385 (2012).

[101] R. Zhou et al., Nature Comm. **4**, 2265 (2013).

[102] Qisi Wang, Yao Shen, Bingying Pan, Yiqing Hao, Mingwei Ma, Fang Zhou, P. Steffens, K. Schmalzl, T. R. Forrest, M. Abdel-Hafiez, Xiaojia Chen, D. A. Chareev, A. N. Vasiliev, P. Bourges, Y. Sidis, Huibo Cao and Jun Zhao, Nature Materials **15**, 159–163 (2016).

[103] Xu, C., Muller, M. and Sachdev, Phys. Rev. B **78**, 020501(R) (2008).

[104] Jiang, S. et al. Phys. Rev. Lett. **110**, 067001 (2013).

[105] Nakajima, M. et al. Proc. Natl. Acad. Sci. USA **108**, 12238–12242 (2011).

[106] Dusza, A. et al. Europhys. Lett. **93**, 37002 (2011).

[107] Yi, M. et al. Proc. Natl Acad. Sci. USA **108**, 6878–6883 (2011).

[108] M. Fu, D. A. Torchetti, T. Imai, F. L. Ning, J.-Q. Yan, and A. S. Sefat, Phys. Rev. Lett. **109**, 247001 (2012).

[109] S. Nandi, M. G. Kim, A. Kreyssig, R. M. Fernandes, D. K. Pratt, A. Thaler, N. Ni, S. L. Bud'ko, P. C. Canfield, J. Schmalian, R. J. McQueeney, and A. I. Goldman, Phys. Rev. Lett. **104**, 057006 (2010).

[110] A. V. Chubukov, D. V. Efremov and I. Eremin, Phys. Rev. B **78**, 134512 (2008).

[111] I. Eremin and A. V. Chubukov, Phys. Rev. B **81**, 024511 (2010).

[112] L. Ma, G. F. Chen, Dao-Xin Yao, J. Zhang, S. Zhang, T.-L. Xia, and Weiqiang Yu, Phys. Rev. B **83**, 132501 (2011).

[113] L. Bossoni, P. Carretta, W. P. Halperin, S. Oh, A. Reyes, P. Kuhns, and P. C. Canfield, Phys. Rev. B **88**, 100503(R) (2013).

[114] L. Bossoni, M. Moroni, M. H. Julien, H. Mayaffre, P. C. Canfield, A. Reyes, W. P. Halperin, and P. Carretta, Phys. Rev. B **93**, 224517 (2016).

[115] Rafael M. Fernandes, Anna E. Böhmer, Christoph Meingast, and Jörg Schmalian, Phys. Rev. Lett. **111**, 137001(2013).

[116] C. L. Henley, Phys. Rev. Lett. **62**, 2056 (1989).

[117] Hyowon Park, Kristjan Haule, and Gabriel Kotliar Phys. Rev. Lett. **107**, 137007 (2011).

[118] C. Utfeld, J. Laverock, T.D. Haynes, S.B. Dugdale, J.A. Duffy, M.W. Butchers, J.W. Taylor, S.R. Giblin, J.G. Analytis, J.-H. Chu, I.R. Fisher, M. Itou, and Y. Sakurai, Phys. Rev. B **81** (2010), p. 064509.

[119] Neven Barišića, Mun K. Chan, Yuan Li, Guichuan Yu, Xudong Zhao, Martin Dressel, Ana Smontara, and Martin Greven, Proc. Natl. Acad. Sci. **110**, 30, 12235–12240 (2013).

[120] L. de' Medici, G. Giovannetti, and M. Capone, Phys. Rev. Lett. **112**, 177001 (2014).

[121] Patrick A. Lee, Naoto Nagaosa, and Xiao-Gang Wen, Rev. Mod. Phys. **78**, 17 (2006).

[122] D.J. Scalapino, Rev. Mod. Phys.**84**, 1383 (2012).

[123] Tom Timusk and Bryan Statt Reports on Progress in Physics, Volume **62**, Number 1 (1999).

[124] T. Wu, H. Mayaffre, S. Krämer, M. Horvatić, C. Berthier, W. N. Hardy, R. Liang, D. A. Bonn, and M.-H. Julien, Nature (London) **477**, 191 (2011).

[125] J. M. Tranquada, B. J. Sternlieb, J. D. Axe, Y. Nakamura, and S. Uchida, Nature (London) **375**, 561 (1995).

[126] L. Chaix, G. Ghiringhelli, Y. Y. Peng, M. Hashimoto, B. Moritz, K. Kummer, N. B. Brookes, Y. He, S. Chen, S. Ishida, Y. Yoshida, H. Eisaki, M. Salluzzo, L. Braicovich, Z.-X. Shen, T. P. Devereaux and W.-S. Lee, Nature Physics (2017); doi:10.1038/nphys4157

[127] G. Ghiringhelli et al., Science **337**, 821 (2012).

[128] Y. Y. Peng, R. Fumagalli, Y. Ding, M. Minola, S. Caprara, D. Betto, G. M. De Luca, K. Kummer, E. Lefrançois, M. Salluzzo, H. Suzuki, M. Le Tacon, X. J. Zhou, N. B. Brookes, B. Keimer, L. Braicovich, M. Grilli, G. Ghiringhelli, arXiv:1705.06165 (2017).

[129] Comin, R. et al. Science **343**, 390 (2014).

[130] Steven Reichardt, Michael Jurkutat, Robin Gühne, Jonas Kohlrautz, Andreas Erb, Jürgen Haase, arXiv:1710.01520 (2017).

[131] R. R. Urbano, B.-L. Young, N. J. Curro, J. D. Thompson, L. D. Pham, and Z. Fisk Phys. Rev. Lett. **99**, 146402 (2007).

[132] Y. Luo, L. Pourovskii, S. E. Rowley, Y. Li, C. Feng, A. Georges, J. Dai, G. Cao, Z. Xu, Q. Si and N. P. Ong, Nature Materials **13**, 777–781 (2014).

[133] Y. P. Wu, D. Zhao, A. F. Wang, N. Z. Wang, Z. J. Xiang, X. G. Luo, T. Wu, and X. H. Chen, Phys. Rev. Lett. **116**, 147001 (2016).

[134] *Heavy-Fermion Systems*, Prasanta Misra, Elsevier, First Edition (2008).

[135] K. Haule and G. Kotliar, New J. Phys. **11**, 025021 (2009).

[136] C. P. Slichter, *Principles of Magnetic Resonance, Third Enlarged and Updated Edition*, Springer Series In Solid-State Sciences (1996), Third Edition.

[137] A. Abragam, *Principles of Nuclear Magnetism*, (Oxford University Press), New York (1961).

[138] S. J. Blundell, Contemporary Physics Vol. **40**, Iss. 3, Pag. 175-192 (1999).

[139] P. Dalmas de Reotier and A. Yaouanc, J. Phys.: Condens. Matter **9**, 9113, (1997).

[140] I. Bakonyi, I. Kovács, I. Pócsik *Physica status solidi* (b) **114**, 609 (1982).

[141] W. D. Knight, Phys. Rev. **76**, 1259 (1949).

[142] D. R. Vij, *Handbook of Applied Solid State Spectroscopy*, (2006).

[143] F. Hammerath, *Magnetism and Superconductivity in Iron-based Superconductors as Probed by Nuclear Magnetic Resonance*, Springer Spektrum (2012).

[144] F. Bloch, W. W. Hansen, and M. Packard, Phys. Rev. **70**, 474 (1946).

[145] T. Farrar, E. D. Becker *Pulse and Fourier Transform NMR: Introduction to Theory and Methods*, Academic Press (1971).

[146] M. H. Levitt, *Spin Dynamics: Basics of Nuclear Magnetic Resonance*, second edition, John Wiley & Sons (2008).

[147] E. Fukushima, S. B. W Roeder, *Experimental pulse NMR: A nuts and bolts approach*, Addison-Wesley Publishing Company (1981).

[148] G. Lang, *Etude par RMN et μSR des propriéteés electroniques et magnétiques des cobaltates de sodium*, PhD thesis, Université Paris XI Orsay, (2007).

[149] A. U. B. Wolter, *Longitudinal and Transverse Magnetization in Low-Dimensional Molecule-Based Quantum Magnets*, PhD thesis, TU Braunschweig, (2005).

[150] A. G. Redfield, Phys. Rev. **98**, 1787 (1955).

[151] E. L. Hahn, Phys. Rev **50**, 580 (1950).

[152] M. Takigawa, N. Motoyama, H. Eisaki, and S. Uchida, Phys. Rev. B **57**, 1124 (1998).

[153] R. E. Walstedt, Phys. Rev. Lett. **19**, 146 (1967).

[154] R. E. Walstedt and S.-W. Cheong, Phys. Rev. B **51**, 3163 (1995).

[155] M. Takigawa, Phys. Rev. B **49**, 4158 (1994).

[156] W. Heitler, E. Teller, Proc. R. Soc. Lond. A **155** 629-639 (1936).

[157] J. Korringa, Physica **16**, 601 (1950).

[158] N. Bloembergen, E. M. Purcell, and R. V. Pound, Phys. Rev. **73**, 679 (1948).

[159] N. Bloembergen, E. M. Purcell, and R. V. Pound, Nature **160**, 475 (1947).

[160] A. Suter, M. Mali, J. Roos, and D. Brinkmann, Journal of Physics: Condensed Matter **10**, 5977 (1998).

[161] F. Hammerath, U. Gräfe, H. Kühne, P. L. Kuhns, A. P. Reyes, G. Lang, S. Wurmehl, B. Büchner, P. Carretta, and H.-J. Grafe, Phys. Rev. B **88**, 104503 (2013).

[162] Nan Lin Wang, Hideo Hosono, Pengcheng Dai, *Iron-based Superconductors: Materials, Properties and Mechanisms*, 1st Edition (2012).

[163] H.-J. Grafe, D. Paar, G. Lang, N. J. Curro, G. Behr, J. Werner, J. Hamann-Borrero, C. Hess, N. Leps, R. Klingeler, and B. Büchner, Phys. Rev. Lett. **101**, 047003, (2008).

[164] T. Moriya, *Spin Fluctuations in Itinerant Electron Magnetism*. Springer-Verlag, (1985).

[165] Y. Nakai et al.: New J. Phys. **11**, 045004 (2009).

[166] G. Lang, H.-J. Grafe, D. Paar, F. Hammerath, K. Manthey, G. Behr, J. Werner, and B. Büchner, Phys. Rev. Lett. **104**, 097001 (2010).

[167] H. Fukazawa, K. Hirayama, K. Kondo, T. Yamazaki, Y. Kohori, N. Takeshita, K. Miyazawa, H. Kito, H. Eisaki, A. Iyo, Journal of the Physical Society of Japan, **77**, 093706 (2008).

[168] G. Lang, L. Veyrat, U. Gräfe, F. Hammerath, D. Paar, G. Behr, S. Wurmehl, and H.-J. Grafe, Phys. Rev. B **94**, 014514 (2016).

[169] F. L. Ning, K. Ahilan, T. Imai, A. S. Sefat, M. A. McGuire, B. C. Sales, D. Mandrus, P. Cheng, B. Shen, and H.-H. Wen, Phys. Rev. Lett. **104**, 037001 (2010).

[170] M. Yashima, H. Nishimura, H. Mukuda, Y. Kitaoka, K. Miyazawa, P. M. Shirage, K. Kihou, H. Kito, H. Eisaki, and A. Iyo, J. Phys. Soc. Jpn. **78**, 103702 (2009).

[171] S. Oh, A. M. Mounce, S. Mukhopadhyay, W. P. Halperin, A. B. Vorontsov, S. L. Bud'ko, P. C. Canfield, Y. Furukawa, A. P. Reyes, and P. L. Kuhns, Phys. Rev. B **83**, 214501 (2011).

[172] S. Mukhopadhyay, S. Oh, A. M.Mounce, M. Lee, W. P. Halperin, N. Ni, S. L. Bud'ko, P.C. Canfield, A. P. Reyes and P. L. Kuhns, New Jour. of Phys. **11**, 055002 (2009).

[173] P. Carretta, R. De Renzi, G. Prando, S. Sanna, Physica Scripta **88**, 068504 (2013).

[174] G. Prando, O. Vakaliuk, S. Sanna, G. Lamura, T. Shiroka, P. Bonfà, P. Carretta, R. De Renzi, H.-H. Klauss, S. Wurmehl, C. Hess, B. Büchner, Phys. Rev. B **87**, 174519 (2013).

[175] R. Kubo and T. Toyabe, in *Magnetic Resonance and Relaxation*, ed. R. Blinc, p810, North-Holland, Amsterdam (1967).

[176] A. Maisuradze, R. Khasanov, A. Shengelaya and H. Keller, J. Phys.: Condens. Matter **21** (2009) 075701 (15pp).

[177] J. E. Sonier, J. H. Brewer, R. F. Kiefl, G. D. Morris, R. I. Miller, D. A. Bonn, J. Chakhalian, R. H. Heffner, W. N. Hardy, and R. Liang, Phys. Rev. Lett. **83**, 4156 (1999).

[178] B. Pümpin, H. Keller, W. Kündig, W. Odermatt, I. M. Savić, J. W. Schneider, H. Simmler, P. Zimmermann, E. Kaldis, S. Rusiecki, Y. Maeno, and C. Rossel, Phys. Rev. B **42**, 8019 (1990).

[179] E. H. Brandt, Rep. Prog. Phys. **58**, 1465 (1995)

[180] Aegerter, C. M., and Lee, S. L., Appl. Mag. Res. **13**, 75 (1997).

[181] M. Tinkham, *Introduction to Superconductivity: Second Edition*, Dover Publications, 2004.

[182] Y. J. Uemura, G. M. Luke, B. J. Sternlieb, J. H. Brewer, J. F. Carolan, W. N. Hardy, R. Kadono, J. R. Kempton, R. F. Kiefl, S. R. Kreitzman, P. Mulhern, T. M. Riseman, D. L. Williams, B. X. Yang, S. Uchida, H. Takagi, J. Gopalakrishnan, A. W. Sleight, M. A. Subramanian, C. L. Chien, M. Z. Cieplak, G. Xiao, V. Y. Lee, B. W. Statt, C. E. Stronach, W. J. Kossler, X. H. Yu, Phys. Rev. Lett. **62**, 2317 (1989).

[183] R. M. Fernandes, D. K. Pratt, W. Tian, J. Zarestky, A. Kreyssig, S. Nandi, M. G. Kim, A. Thaler, N. Ni, P. C. Canfield, R. J. McQueeney, J. Schmalian, A. I. Goldman, Phys. Rev. B **81**, 140501 (2010).

[184] R. M. Fernandes, J. Schmalian, Phys. Rev. B **82**, 014521 (2010)

[185] J. T. Park, D. S. Inosov, C. Niedermayer, G. L. Sun, D. Haug, N. B. Christensen, R. Dinnebier, A. V. Boris, A. J. Drew, L. Schulz, T. Shapoval, U. Wolff, V. Neu, X. Yang, C. T. Lin, B. Keimer, V. Hinkov, Phys. Rev. Lett. **102**, 117006 (2009).

[186] C. Bernhard, C. N. Wang, L. Nuccio, L. Schulz, O. Zaharko, J. Larsen, C. Aristizabal, M. Willis, A. J. Drew, G. D. Varma, T. Wolf, C. Niedermayer, Phys. Rev. B **86**, 184509 (2012).

[187] G. Prando, P. Bonfà, G. Profeta, R. Khasanov, F. Bernardini, M. Mazzani, E. M. Brüning, A. Pal, V. P. S. Awana, H.-J. Grafe, B. Büchner, R. De Renzi, P. Carretta, S. Sanna, Phys. Rev. B **87**, 064401 (2013)

[188] R. De Renzi, P. Bonfà, M. Mazzani, S. Sanna, G. Prando, P. Carretta, R. Khasanov, A. Amato, H. Luetkens, M. Bendele, F. Bernardini, S. Massidda, A. Palenzona, M. Tropeano, M. Vignolo, Supercond. Sci. Technol. **25**, 084009 (2012).

[189] R. Khasanov and Z. Guguchiam, Supercond. Sci. Technol. **28** 034003 (15pp) (2015).

[190] M. Bendele *et al.*, Physical Review B **81**, 224520, (2010).

[191] V. J. Emery and S. A. Kivelson, Nature **374**, 434 - 437 (1994).

[192] A. J. Millis, H. Monien and D. Pines, Phys. Rev. B **42**, 167 (1990).

[193] C. H. Pennington and C. P. Slichter, Phys. Rev. Lett. **66**, 381 (1991).

[194] M. Hücker et al., Phys. Rev. B **90**, 054514 (2014).

[195] A. P. Dioguardi, M. M. Lawson, B. T. Bush, J. Crocker, K. R. Shirer, D. M. Nisson, T. Kissikov, S. Ran, S. L. Bud'ko, P. C. Canfield, S. Yuan, P. L. Kuhns, A. P. Reyes, H.-J. Grafe, and N. J. Curro Phys. Rev. B **92**, 165116 (2015).

[196] E. D. Ostroff and J. S. Waugh, Phys. Rev. Lett. **16**, 1097 (1966).

[197] B. J. Suh, D. R. Torgeson, and F. Borsa, Phys. Rev. Lett. **71**, 3011 (1993).

[198] B. J. Suh, F. Borsa, and D. R. Torgeson, J. Magn. Res. Ser. **110**, 58 (1994).

[199] I. Yu and W. P. Halperin, Physical Review B **47**, 15830 (1993).

[200] B. Robertson, Phys. Rev. **151**, 273 (1966).

[201] R. C. Wayne and R. M. Cotts, Phys. Rev. **151**, 264 (1966).

[202] A. Z. Genack and A. G. Redfield, Phys. Rev. B **12**, 78 (1975).

[203] K. R. Gorny, O. M. Vyaselev, C. H. Pennington, P. C. Hammel, W. L. Hults, J. L. Smith, J. Baumgartner, T. R. Lemberger, P. Klamut, and B. Dabrowski, Phys. Rev. B **63**, 064513 (2001).

[204] V. F. Mitrović, H. N. Bachman, W. P. Halperin, A. P. Reyes, P. Kuhns, and W. G. Moulton, Phys. Rev. B **66**, 014511 (2002).

[205] A. W. Hunt, P. M. Singer, K. R. Thurber, and T. Imai, Phys. Rev. Lett. **82**, 4300 (1999).

[206] G. B. Teitel'baum, I. M. Abu-Shiekah, O. Bakharev, H. B. Brom, and J. Zaanen, Phys. Rev. B **63**, 020507 (2000).

[207] P. Chandra, P. Coleman, and A. I. Larkin, Phys. Rev. Lett. **64**, 88 (1990).

[208] P. Carretta, R. Melzi, N. Papinutto, and P. Millet, Phys. Rev. Lett. **88**, 047601 (2002).

[209] J. H. Chu et al., Science **329**, 824–826 (2010).

[210] M. A. Tanatar et al., Phys. Rev. B **81**, 184508 (2010).

[211] J. H. Chu, H.-H. Kuo, J. G. Analytis, I. R. Fisher, Science **337**, 710–712 (2012).

[212] I. R. Fisher, L. Degiorgi, Z. X. Shen, Rep. Prog. Phys. **74**, 124506 (2011).

[213] X. Lu, J. T. Park, R. Zhang, H. Luo, A. H. Nevidomskyy, Q. Si, P. Dai, Science **345**, 6197, pp. 657-660 (2014).

[214] C. Dhital, Z. Yamani, W. Tian, J. Zeretsky, A. S. Sefat, Z. Q. Wang, R. J. Birgeneau and S. D. Wilson, Phys. Rev. Lett. **108** 087001 (2012).

[215] E. C. Blomberg, A. Kreyssig, M. A. Tanatar, R. M. Fernandes, M. G. Kim, A. Thaler, J. Schmalian, S. L. Bud'ko, P. C. Canfield, A. I. Goldman, and R. Prozorov, Phys. Rev. B **85**, 144509 (2012).

[216] C. Dhital, T. Hogan, Z. Yamani, R. J. Birgeneau, W. Tian, M. Matsuda, A. S. Sefat, Z. Wang, and S. D. Wilson, Phys. Rev. B **89**, 214404 (2014).

[217] H.-H. Kuo, J. G. Analytis, J.-H. Chu, R. M. Fernandes, J. Schmalian, and I. R. Fisher, Phys. Rev. B **86**, 134507 (2012).

[218] W. J. Duncan, O. P. Welzel, C. Harrison, X. F. Wang, X. H. Chen, F. M. Grosche and P. G. Niklowitz, J. Phys.: Condens. Matter **22**, 052201 (2010).

[219] C. W. Hicks, M. E. Barber, S. D. Edkins, D. O. Brodsky, and A. P. Mackenzie, Review of Scientific Instruments **85**, 065003 (2014).

[220] De Souza, G., Serbena, F., Jurelo, A., Da Silva, S., Pinheiro, L., Dias, F., Canfield, P. (2016). On the determination of hardness and elastic modulus in BaFe2As2 lamellar-like material. Journal of Materials Research, **31**(10), 1413-1422, doi:10.1557/jmr.2016.166 (2016).

[221] L. Bossoni et al, EPL **102** 17005 (2013).

[222] T. Kissikov, R. Sarkar, M. Lawson, B. T. Bush, E. I. Timmons, M. A. Tanatar, R. Prozorov, S. L. Bud'ko, P. C. Canfield, R. M. Fernandes, N. J. Curro, arXiv:1704.03566, (2017).

[223] T. Kissikov, R. Sarkar, B. T. Bush, M. Lawson, P. C. Canfield, N. J. Curro, arXiv:1708.08501 (2017).

[224] Y. Mizukami, Y. Kawamoto, Y. Shimoyama, S. Kurata, H. Ikeda, T. Wolf, D. A. Zocco, K. Grube, H. v. Löhneysen, Y. Matsuda, and T. Shibauchi, Phys. Rev. B **94**, 024508 (2016).

[225] S.-L. Drechsler, H. Rosner, V. Grinenko, S. Johnston, arXiv:1701.00596 (2017).

[226] Felix Eilers, Kai Grube, Diego A. Zocco, Thomas Wolf, Michael Merz, Peter Schweiss, Rolf Heid, Robert Eder, Rong Yu, Jian-Xin Zhu, Qimiao Si, Takasada Shibauchi, and Hilbert v. Löhneysen Phys. Rev. Lett. **116**, 237003 (2016).

[227] S. Backes, H. O. Jeschke, and R. Valentí, Phys. Rev. B **92**, 195128 (2015).

[228] F. Hardy, A. E. Böhmer, L. de' Medici, M. Capone, G. Giovannetti, R. Eder, L. Wang, M. He, T. Wolf, P. Schweiss, R. Heid, A. Herbig, P. Adelmann, R. A. Fisher, C. Meingast, Phys. Rev. B **94**, 205113 (2016).

[229] J. Li, D. Zhao, Y. P. Wu, S. J. Li, D. W. Song, L. X. Zheng, N. Z. Wang, X. G. Luo, Z. Sun, T. Wu, X. H. Chen, arXiv:1611.04694 (2016).

[230] F. Hardy, A. E. Böhmer, D. Aoki, P. Burger, T. Wolf, P. Schweiss, R. Heid, P. Adelmann, Y. X. Yao, G. Kotliar, et al., Phys. Rev. Lett. **111**, 027002 (2013).

[231] Luca de' Medici and Massimo Capone, arXiv:1607:08468 (2016).

[232] Luca de' Medici, Phys. Rev. Lett. **118**, 167003 (2017).

[233] E. Civardi, M. Moroni, M. Babij, Z. Bukowski, and P. Carretta, Phys. Rev. Lett. **117**, 217001 (2016).

[234] Z. Bukowski, S. Weyeneth, R. Puzniak, J. Karpinski and B. Batlogg, Physica C **470**, S328 (2010).

[235] Elk code, version 3.3.17 and ff, http://elk.sourceforge.net

[236] J. P. Perdew, A. Ruzsinszky, G. I. Csonka, O. A. Vydrov, G E. Scuseria, L. A. Constantin, X. Zhou, and K. Burke, Phys. Rev. Lett. **100**, 136406 (2008).

[237] H. J. Monkhorst and J. D. Pack, Phys. Rev. B **13**, 5188 (1976).

[238] M. Methfessel and A. Paxton, Phys. Rev. B **40**, 3616 (1989).

[239] Y. Kobayashi, E Satomi, S. C. Lee, and M. Sato, J. Phys. Soc. Jpn. **79**, 093709 (2010).

[240] P. S. Wang, P. Zhou, J. Dai, J. Zhang, X. X. Ding, H. Lin, H. H. Wen, B. Normand, R. Yu, and W. Yu, Phys. Rev. B **93**, 085129 (2016).

[241] P. Butaud, P. Ségransan, C. Berthier, J. Dumas, and C. Schlenker, Phys. Rev. Lett. **55**, 253 (1985).

[242] J. H. Ross, Z. Wang, and C.P. Slichter Phys. Rev. Lett. **56**, 663 (1986).

[243] C. Berthier and P. Ségransan, in *Low-dimensional Conductors and Superconductors*, Eds. D.Jérome and L.G.Caron, (Plenum Pub., 1987), p.455.

[244] K.I. Kugel and D.I. Khomskii, Sov. Phys.-JETP **37**, 725 (1973).

[245] P. Carretta, M. Giovannini, M. Horvatić, N. Papinutto, and A. Rigamonti, Phys. Rev. B **68**, 220404(R) (2003)

[246] A. Ishigaki and T. T. Moriya, J. Phys. Soc. Jpn. **65**, 3402 (1996).

[247] A. Ishigaki and T. T. Moriya, J. Phys. Soc. Jpn. **67**, 3924 (1998).

[248] F. Hammerath, P. Bonfá, S. Sanna, G. Prando, R. De Renzi, Y. Kobayashi, M. Sato, and P. Carretta, Phys. Rev. B **89**, 134503 (2014).

[249] H. Alloul, T. Ohno and P. Mendels, Phys. Rev. Lett. **63**, 1700 (1989).

[250] B. Batlogg, H. Y. Hwang, H. Takagi, R.J. Cava, H.L. Kao and J. Kwo, Physica C **235-240**, 130 (1994).

[251] H. Ding, T. Yokoya, J.C. Campuzano, T. Takahashi, M. Randeira, M.R. Norman, T. Mochiku, H. Kadowaki and J. Giapintzakis, Nature **382**, 51 (1996).

[252] E. Gull, M. Ferrero, O. Parcollet, A. Georges, and A. J. Millis, Phys. Rev. B **82**, 155101 (2010).

[253] D.E. MacLaughlin, J.D. Williamson and J. Butterworth, Phys. Rev. B **4**, 60 (1971).

[254] R. J. Radtke, K. Levin, H.-B. Schüttler, and M. R. Norman, Phys. Rev. B **48**, 653(R) (1993).

[255] M. Sato, Y. Kobayashi, S. C. Lee, H. Takahashi, E. Satomi, and Y. Miura, J. Phys. Soc. Jpn. **79**, 014710 (2010).

[256] E. Satomi, S. C. Lee, Y. Kobayashi, and M. Sato, Journal of the Physical Society of Japan **79**, 094702 (2010).

[257] T. Kawamata, E. Satomi, Y. Kobayashi, M. Itoh, and M. Sato, J. Phys. Soc. Jpn **80**, 084720 (2011).

[258] S. Sanna, P. Carretta, P. Bonfà, G. Prando, G. Allodi, R. De Renzi, T. Shiroka, G. Lamura, A. Martinelli, and M. Putti, Phys. Rev. Lett. **107**, 227003 (2011).

[259] S. Sanna, P. Carretta, R. De Renzi, G. Prando, P. Bonfà, M. Mazzani, G. Lamura, T. Shiroka, Y. Kobayashi, and M. Sato, Phys. Rev. B **87**, 134518 (2013).

[260] P. Cheng, B. Shen, J. Hu, and H.-H. Wen, Phys. Rev. B **81**, 174529 (2010).

[261] J. Li, Y. F. Guo, S. B. Zhang, J. Yuan, Y. Tsujimoto, X. Wang, C. I. Sathish, Y. Sun, S. Yu, W. Yi, K. Yamaura, E. Takayama-Muromachiu, Y. Shirako, M. Akaogi, and H. Kontani, Phys. Rev. B **85**, 214509 (2012).

[262] R. Frankovsky, H. Luetkens, F. Tambornino, A. Marchuk, G. Pascua, A. Amato, H.-H. Klauss, and D. Johrendt, Phys. Rev. B **87**, 174515 (2013).

[263] G. S. Tucker, D. K. Pratt, M. G. Kim, S. Ran, A. Thaler, G. E. Granroth, K. Marty, W. Tian, J. L. Zarestky, M. D. Lumsden, S. L. Bud'ko, P. C. Canfield, A. Kreyssig, A. I. Goldman, and R. J. McQueeney, Phys. Rev. B **86**, 020503(R) (2012).

[264] M. Moroni, S. Sanna, G. Lamura, T. Shiroka, R. De Renzi, R. Kappenberger, M. A. Afrassa, S. Wurmehl, A. U. B. Wolter, B. Büchner, and P. Carretta, Phys. Rev. B **94**, 054508 (2016).

[265] G. Lamura, T. Shiroka, S. Bordignon, S. Sanna, M. Moroni, R. De Renzi, P. Carretta, P. K. Biswas, F. Caglieris, M. Putti, S. Wurmehl, S. J. Singh, J. Shimoyama, M. N. Gastiasoro, and B. M. Andersen, Phys. Rev. B **94**, 214517 (2017).

[266] F. Hammerath, M. Moroni, L. Bossoni, S. Sanna, R. Kappenberger, S. Wurmehl, A. U. B. Wolter, M. A. Afrassa, Y. Kobayashi, M. Sato, B. Büchner, and P. Carretta, Phys. Rev. B **92**, 020505(R) (2015).

[267] M. N. Gastiasoro, F. Bernardini, and B. M. Andersen, Phys. Rev. Lett. **117**, 257002 (2016).

[268] S. Kitagawa, Y. Nakai, T. Iye, K. Ishida, Y. Kamihara, M. Hirano, H. Hosono, Phys. Rev. B, **81**, 212502 (2010).

[269] H.-H. Klauss, H. Luetkens, R. Klingeler, C. Hess, F. J. Litterst, M. Kraken, M. M. Korshunov, I. Eremin, S.-L. Drechsler, R. Khasanov, A. Amato, J. Hamann-Borrero, N. Leps, A. Kondrat, G. Behr, J. Werner, and B. Büchner, Phys. Rev. Lett. **101**, 077005 (2008).

[270] S. Kitao, Y. Kobayashi, S. Higashitaniguchi, M. Saito, Y. Kamihara, M. Hirano, T. Mitsui, H. Hosono, M. Seto, J. Phys. Soc. Japan **77**, 103706 (2008).

[271] D. Bérardan, L. Pinsard-Gaudart, N. Dragoe, Journal of Alloys and Compounds, Volume **481**, Issues 1-2, 29 July 2009, Pages 470-472.

[272] C. Hess, A. Kondrat, A. Narduzzo, J. E. Hamann-Borrero, R. Klingeler, J. Werner, G. Behr, and B. Büchner, Europhys. Lett. **87**, 17005 (2009).

[273] H. Ikeda, R. Arita, and J. Kunes, Phys. Rev. B **81**, 054502 (2010).

[274] B. M. Andersen, P. J. Hirschfeld, A. P. Kampf, and M. Schmid, Phys. Rev. Lett. **99**, 147002 (2007).

[275] M. N. Gastiasoro and B. M. Andersen, Phys. Rev. Lett. **113**, 067002 (2014).

[276] A. A. Abrikosov and L. P. Gorkov, Zh. Eksp. Teor. Fiz. 39, 1781 (1960). Sov. Phys. JETP **1**2, 1243 (1961).

[277] G. Prando, P. Carretta, A. Rigamonti, S. Sanna, A. Palenzona, M. Putti, and M. Tropeano Phys. Rev. B **81**, 100508(R) (2010).

[278] M.-H. Julien, A. Campana, A. Rigamonti, P. Carretta, F. Borsa, P. Kuhns, A. P. Reyes, W. G. Moulton, M. Horvatic, C. Berthier, A. Vietkin and A. Revcolevschi, Phys. Rev. B **63**, 144508 (2001).

[279] M. Filibian, P. Carretta, T. Miyake, Y. Taguchi, and Y. Iwasa, Phys. Rev. B **75**, 085107 (2007).

[280] P. Carretta, A. Rigamonti and R. Sala, Phys. Rev. B **55**, 3734 (1997).

[281] H.Benner and J.P.Boucher in *Magnetic Properties of Layered Transition Metal Compounds* Ed. L.J. De Jongh, Kluwer Academic Pub. (1990).

[282] F. Massee, P. Oliver Sprau, Y.-L. Wang, J. C. S. Davis, G. Ghigo, G. Gu, W.-K. Kwok, Science Advances **1**, e1500033 (2015).

[283] T. Tamegai, T. Taen, H. Yagyuda, Y. Tsuchiya, S.Mohan, T. Taniguchi, Y. Nakajima, S.u Okayasu, M. Sasase, H. Kitamura, T. Murakami, T. Kambara and Y. Kanai, Supercond. Sci. Technol. **25**, 084008 (2012).

[284] G. P. Summers, E. A. Burke, D. B. Chrisey, M. Nastasi and J. R. Tesmer, Appl. Phys. Lett. **55**, 1469 (1989).

[285] F. Rullier-Albenque, P. A. Vieillefond, H. Alloul, A. W. Tyler, P. Lejay and J. F. Marucco, Europhys. Lett. **50** (1), pp. 81-87 (2000).

[286] Y. Nakajima, T. Taen, Y. Tsuchiya, T. Tamegai, H. Kitamura, and T. Murakami, Phys. Rev. B **82**, 220504(R) (2010).

[287] R. Prozorov, M. A. Tanatar, B. Roy, N. Ni, S. L. Bud'ko, P. C. Canfield, J. Hua, U. Welp and W. K. Kwok, Phys. Rev. B **81**, 094509 (2010)

[288] N. W. Salovich, Hyunsoo Kim, Ajay K. Ghosh, R. W. Giannetta, W. Kwok, U. Welp, B. Shen, S. Zhu, H.-H. Wen, M. A. Tanatar, and R. Prozorov, Phys. Rev. B **87**, 180502(R) (2013).

[289] F. Laviano, R. Gerbaldo, G. Ghigo, L. Gozzelino, G. P. Mikitik, T. Taen and T. Tamegai, Supercond. Sci. Technol. **27**, 044014 (2014).

[290] N. Haberkorn, Jeehoon Kim, B. Maiorov, I. Usov, G. F. Chen, W. Yu and L. Civale, Supercond. Sci. Technol. **27**, 095004 (2014).

[291] F. Ohtake, T. Taen, S. Pyon, T. Tamegai, S. Okayasu, Physics Procedia **58**, 122-125 (2014).

[292] K. J. Kihlstrom, L. Fang, Y. Jia, B. Shen, A. E. Koshelev, U. Welp, G. W. Crabtree, W.-K. Kwok, A. Kayani, S. F. Zhu, and H.-H. Wen, Appl. Phys. Lett. **103**, 202601 (2013).

[293] T. Taen, H. Yagyuda, Y. Nakajima, T. Tamegai, S. Okayasu, H. Kitamura, T. Murakami, F. Laviano, G. Ghigo, Physica C, **484**, 62 (2013).

[294] T. Taen, F. Ohtake, H. Akiyama, H. Inoue, Yue Sun, S. Pyon, T. Tamegai, and H. Kitamura, Phys. Rev. B **88**, 224514 (2013).

[295] N. Haberkorn, B. Maiorov, I. O. Usov, M. Weigand, W. Hirata, S. Miyasaka, S. Tajima, N. Chikumoto, K. Tanabe, and L. Civale, Phys. Rev. B **85**, 014522 (2012).

[296] Y. Mizukami, M. Konczykowski, Y. Kawamoto, S. Kurata, S. Kasahara, K. Hashimoto, V. Mishra, A. Kreisel, Y. Wang, P. J. Hirschfeld, Y. Matsuda, and T. Shibauchi, Nature Commun. **5**, 5657 (2014).

[297] R. Prozorov, M. Konczykowski, M. A. Tanatar, A. Thaler, S. L. Bud'ko, P. C. Canfield, V. Mishra, and P. J. Hirschfeld, Phys. Rev. X **4**, 041032 (2014).

[298] C. J. van der Beek, S. Demirdis, D. Colson, F. Rullier-Albenque, Y. Fasano, T. Shibauchi, Y. Matsuda, S. Kasahara, P. Gierlowski, and M .Konczykowski, J. Physics Conference Series **449**, 012023 (2013).

[299] K. Cho, M. Konczykowski, J. Murphy, H. Kim, M. A. Tanatar, W. E. Straszheim, B. Shen, H. H. Wen, and R. Prozorov Phys. Rev. B **90**, 104514 (2014)

[300] Kyil Cho, M. K. Teknowijoyo, M. A. Tanatar, Yong Liu, T. A. Lograsso, W. E. Straszheim, V. Mishra, S. Maiti, P. J. Hirschfeld, and R. Prozorov, Science Advances. **2**, e1600807 (2016).

[301] S. Teknowijoyo, K. Cho, M. A. Tanatar, J. Gonzales, A. E. Böhmer, O. Cavani, V. Mishra, P. J. Hirschfeld, S. L. Bud'ko, P. C. Canfield, and R. Prozorov Phys. Rev. B **94**, 064521 (2016).

[302] J. Li, Y. Guo, S. Zhang, Y. Tsujimoto, X. Wang, C. I. Sathish, S. Yu, K. Yamaura, and E. Takayama-Muromachi, Solid State Commun. **152**, 671 (2012).

[303] 8 Y. K. Li, X. Lin, Q. Tao, C. Wang, T. Zhou, L. Li, Q. Wang, M. He, G. Cao, and Z. A. Xu, New J. Phys. **11**, 053008 (2009).

[304] M. Moroni, L. Gozzelino, G. Ghigo, M. A. Tanatar, R. Prozorov, P. C. Canfield, P. Carretta, Phys. Rev. B **96**, 094523 (2017).

[305] J.F. Ziegler, SRIM code, http://www.srim.org/.

[306] M. A. Tanatar, N. Ni, A. Thaler, S. L. Bud'ko, P. C. Canfield, and R. Prozorov, Phys. Rev. B **82**, 134528 (2010).

[307] Mazzani, M., Bonfà, P., Allodi, G., Sanna, S., Martinelli, A., Palenzona, A., Manfrinetti, P., Putti, M. and De Renzi, R., Phys. Status Solidi B, **251**: 974-979 (2014).

[308] H. Alloul, J. Bobroff, M. Gabay, and P. J. Hirschfeld, Rev. Mod. Phys. **81**, 45 (2009).

[309] D. LeBoeuf, Y. Texier, M. Boselli, A. Forget, D. Colson, and J. Bobroff, Phys. Rev. B **89**, 035114 (2014).

[310] Y. Texier, Y. Laplace, P. Mendels, J. T. Park, G. Friemel, D. L. Sun, D. S. Inosov, C. T. Lin and J. Bobroff, EPL, **99**, 17002 (2012).

[311] P. Esquinazi , W. Hergert , D. Spemann , A. Setzer , and A. Ernst, Transaction on Magnetics **49** (8), 4668 (2013).

[312] T. Goko, A. A. Aczel, E. Baggio-Saitovitch, S. L. Bud'ko, P. C. Canfield, J. P. Carlo, G. F. Chen, Pengcheng Dai, A. C. Hamann, W. Z. Hu, H. Kageyama, G. M. Luke, J. L. Luo, B. Nachumi, N. Ni, D. Reznik, D. R. Sanchez-Candela, A. T. Savici, K. J. Sikes, N. L. Wang, C. R. Wiebe, T. J. Williams, T. Yamamoto, W. Yu, and Y. J. Uemura, Phys. Rev. B **80**, 024508 (2009).

[313] N. Papinutto, P. Carretta, S. Gonthier, and P. Millet, Phys. Rev. B **71**, 174425 (2005).

[314] A. P. Dioguardi, J. Crocker, A. C. Shockley, C. H. Lin, K. R. Shirer, D. M. Nisson, M. M. Lawson, N. apRoberts-Warren, P. C. Canfield, S. L. Bud'ko, S. Ran, and N. J. Curro, Phys. Rev. Lett. **111**, 207201 (2013).

[315] E. R. Andrew *Nuclear Magnetic Resonance*, Cambridge University Press (1956).

[316] C. Kittel *Introduction to solid state physics*, Wiley & S., 8th edition (2005).

[317] M. Horvatič, Journal of Physics: Condensed Matter **4**, 5811 (1992).

[318] L. Bossoni, *Dissipative and fluctuating effects in* $Ba(Fe_{1-x}Rh_x)_2As_2$ *iron-based superconductors*, Ph.d. thesis (2014).

[319] T. Moriya, J. Phys. Soc. Jpn. **18**, 516 (1963).

List of publications

1. F. Hammerath, **M. Moroni**, L. Bossoni, S. Sanna, R. Kappenberger, S. Wurmehl, A. U. B. Wolter, M. A. Afrassa, Y. Kobayashi, M. Sato, B. Büchner, and P. Carretta: "Enhancement of low-frequency fluctuations and superconductivity breakdown in Mn-doped $La_{1-y}Y_yFeAsO_{0.89}F_{0.11}$ superconductors", Phys. Rev. B **92**, 020505(R) (2015).

2. L. Bossoni, **M. Moroni**, M. H. Julien, H. Mayaffre, P. C. Canfield, A. Reyes, W. P. Halperin, and P. Carretta: "Persistence of slow fluctuations in the overdoped regime of $Ba(Fe_{1-x}Rh_x)_2As_2$ superconductor", Phys. Rev. B **93**, 224517 (2016).

3. **M. Moroni**, S. Sanna, G. Lamura, T. Shiroka, R. De Renzi, R. Kappenberger, M. A. Afrassa, S. Wurmehl, A. U. B. Wolter, B. Büchner, and P. Carretta: "Competing effects of Mn and Y doping on the low-energy excitations and phase diagram of $La_{1-y}Y_yFe_{1-x}Mn_xAsO_{0.89}F_{0.11}$ iron-based superconductors", Phys. Rev. B **94**, 054508 (2016).

4. E. Civardi, **M. Moroni**, M. Babij, Z. Bukowski, and P. Carretta: "Superconductivity Emerging from an Electronic Phase Separation in the Charge Ordered Phase of $RbFe_2As_2$", Phys. Rev. Lett. **117**, 217001 (2016).

5. G. Lamura, T. Shiroka, S. Bordignon, S. Sanna, **M. Moroni**, R. De Renzi, P. Carretta, P. K. Biswas, F. Caglieris, M. Putti, S. Wurmehl, S. J. Singh, J. Shimoyama, M. N. Gastiasoro, and B. M. Andersen: "Role of magnetic dopants in the phase diagram of Sm1111 pnictides: The case of Mn", Phys. Rev. B **94**, 214517 (2016).

6. **M. Moroni**, P. Carretta, G. Allodi, R. De Renzi, M. N. Gastiasoro, B. M. Andersen, P. Materne, H.-H. Klauss, Y. Kobayashi, M. Sato and S. Sanna: "Fast recovery of the stripe magnetic order by Mn/Fe substitution in F-doped LaFeAsO superconductors" , Phys. Rev. B **95**, 180501(R) (2017).

7. **M. Moroni**, L. Gozzelino, G. Ghigo, M. A. Tanatar, R. Prozorov, P. C. Canfield and P. Carretta: "Effect of proton irradiation on the normal state low-energy excitations of $Ba(Fe_{1-x}Rh_x)_2As_2$ superconductors", Phys. Rev. B **96**, 094523 (2017).